



UNIVERSIDADE ESTADUAL DE CAMPINAS
Faculdade de Engenharia Mecânica

THIAGO DESTRI CABRAL

**Development of Novel Optical Sensors and
Applications Based on Conventional and
Specialty Optical Fibers**

**Desenvolvimento de Novos Sensores Ópticos e
Suas Aplicações Baseados em Fibras Ópticas
Convencionais e Especiais**

CAMPINAS
2022

THIAGO DESTRI CABRAL

Development of Novel Optical Sensors and Applications Based on Conventional and Specialty Optical Fibers

Desenvolvimento de Novos Sensores Ópticos e Suas Aplicações Baseados em Fibras Ópticas Convencionais e Especiais

Thesis presented to the School of Mechanical Engineering of the University of Campinas in partial fulfillment of the requirements for the degree of Doctor in Mechanical Engineering, in the area of Mechatronics.

Tese apresentada à Faculdade de Engenharia Mecânica da Universidade Estadual de Campinas como parte dos requisitos exigidos para a obtenção do título de Doutor em Engenharia Mecânica, na Área de Mecatrônica.

Orientador: Prof. Dr. Éric Fujiwara

Coorientador: Prof. Dr. Cristiano Monteiro de Barros Cordeiro

ESTE TRABALHO CORRESPONDE À VERSÃO FINAL DA TESE DEFENDIDA PELO ALUNO THIAGO DESTRI CABRAL, E ORIENTADA PELO PROF. DR. ÉRIC FUJIWARA.

CAMPINAS
2022

Ficha catalográfica
Universidade Estadual de Campinas
Biblioteca da Área de Engenharia e Arquitetura
Rose Meire da Silva - CRB 8/5974

C112d Cabral, Thiago Destri, 1990-
Development of novel optical sensors and applications based on conventional and specialty optical fibers / Thiago Destri Cabral. – Campinas, SP : [s.n.], 2022.

Orientador: Éric Fujiwara.
Coorientador: Cristiano Monteiro de Barros Cordeiro.
Tese (doutorado) – Universidade Estadual de Campinas, Faculdade de Engenharia Mecânica.

1. Fibras óticas. 2. Fibras de cristal fotônico. 3. Sensor ótico. 4. Instrumentação. 5. Medidas óticas. I. Fujiwara, Éric, 1985-. II. Cordeiro, Cristiano Monteiro de Barros, 1973-. III. Universidade Estadual de Campinas. Faculdade de Engenharia Mecânica. IV. Título.

Informações Complementares

Título em outro idioma: Desenvolvimento de novos sensores ópticos e suas aplicações baseados em fibras ópticas convencionais e especiais

Palavras-chave em inglês:

Optical fibers

Photonic crystal fiber

Optical sensor

Instrumentation

Optical measurements

Área de concentração: Mecatrônica

Titulação: Doutor em Engenharia Mecânica

Banca examinadora:

Éric Fujiwara [Orientador]

Jonas Henrique Osório

Niederauer Mastelari

Marcos José Ferreira Carvalho

Daniel Pedro Willemann

Data de defesa: 30-11-2022

Programa de Pós-Graduação: Engenharia Mecânica

Identificação e informações acadêmicas do(a) aluno(a)

- ORCID do autor: <https://orcid.org/0000-0001-9399-9463>

- Currículo Lattes do autor: <http://lattes.cnpq.br/1658795104148366>

**UNIVERSIDADE ESTADUAL DE CAMPINAS
FACULDADE DE ENGENHARIA MECÂNICA**

TESE DE DOUTORADO ACADÊMICO

**Development of Novel Optical Sensors and
Applications Based on Conventional and
Specialty Optical Fibers**

**Desenvolvimento de Novos Sensores Ópticos e
Suas Aplicações Baseados em Fibras Ópticas
Convencionais e Especiais**

Autor: Thiago Destri Cabral

Orientador: Prof. Dr. Éric Fujiwara

Coorientador: Prof. Dr. Cristiano Monteiro de Barros Cordeiro

A Banca Examinadora composta pelos membros abaixo aprovou esta Dissertação/Tese:

Prof. Dr. Éric Fujiwara, Presidente
Faculdade de Engenharia Mecânica/UNICAMP

Dr. Jonas Henrique Osório
Instituto de Física “Gleb Wataghin”/UNICAMP

Prof. Dr. Niederauer Mastelari
Faculdade de Engenharia Mecânica/UNICAMP

Prof. Dr. Marcos José Ferreira Carvalho
Departamento de Engenharia Mecânica/IME

Prof. Dr. Daniel Pedro Willemann
Departamento de Engenharia de Pesca e Ciências Biológicas/CERES/UDESC

A Ata de Defesa com as respectivas assinaturas dos membros encontra-se no SIGA/Sistema de Fluxo de Dissertação/Tese e na Secretaria do Programa da Unidade.

Campinas, 30 de Novembro de 2022.

Acknowledgments

This study was financed in part by the The Brazilian National Council for Scientific and Technological Development (CNPq), grant #140375/2019-8. This study was financed in part by the Coordenação de Aperfeiçoamento de Pessoal de Nível Superior – Brasil (CAPES) – Finance Code 001. This study was financed in part by the São Paulo Research Foundation (FAPESP), grants #2017/25666-2 and 2018/10409-7.

I would also like to thank, in no particular order:

- All my fellow coauthors named in the List of Publications section of this document, for the effort, contribution, and dedication invested into making each publication featured in this thesis a solid journal worthy research piece.
- The long-time and ever-present friends: Bruno Travassos, João Paulo “Tiz”, Lucas de Camargo, Miguel Mendes, Victor Ugo Amarante, Alexandre Bittencourt de Sá, Jian Carlos Bonelli, Juan Filipi Garcês, Filipe Zanini Broetto, Estiven Sánchez Barrera, Mariana Tiemi Tamura and Nilton Branco, for the companionship and support over many years.
- The new friends I met in UNICAMP: Hugo Eugênio de Freitas, Stenio Aristilde, Arthur Valêncio, William de Petri, Marco César Prado Soares, Bruno Oliveira Ferreira, Arthur Clini, Lucas Hamada, Lucas “Tortuguita” Gomes, Yu Tzu Wu, Anderson Pitoli Breve, Leonardo José Ferreira Leite, Luiz Evaristo, Pedro Machado Lazari, and Julio Roberto Bartoli, for the companionship, intriguing lunch-time discussions, trips to Sergel and coffee-time laughs that contributed to make my time in Campinas a pleasant one.
- The awesome folks from ‘Whitesand’ (and ‘Spriggang’ aggregates), the old ‘Hokuten’, and other smaller circles on the critically acclaimed MMORPG Final Fantasy XIV and its expanded Free Trial including the entirety of A Realm Reborn base game and the award-winning Heavensward Expansion (special thanks to Yoshi-P and the dev team) for the fun times and helping me keep my sanity during the exhausting (but rewarding) experience that is pursuing a PhD, especially during the pandemic times.
- UNICAMP’s School of Mechanical Engineering and the “Gleb Wataghin” Institute of Physics for the access to the infrastructure needed to conduct this work.
- Professors Éric Fujiwara and Cristiano Cordeiro for the academic guidance.
- My Family, for all the support.

Resumo

Cada vez mais os sensores mecânicos e eletrônicos tradicionais estão sendo substituídos por sensores baseados em fibras ópticas uma vez que estas apresentam grande flexibilidade, fator de forma reduzido, imunidade à interferência eletromagnética e grande capacidade de multiplexação. A evolução da tecnologia de fibras ópticas e o advento de fibras microestruturadas trouxeram opções de design, funcionalização e aplicação virtualmente ilimitadas nas áreas de transmissão de dados, imageamento, iluminação e sensoriamento. Apesar disto, os sensores de fibra óptica comumente disponíveis no mercado hoje em dia fazem uso de interrogadores de alto custo como analisadores de espectro óptico, dependem de esquemas interferométricos complexos, ou ambos. Este trabalho explora uma gama de novos sensores baseados em fibras ópticas especiais, como sensores em fibras de cristal fotônico fabricadas em sílica, fibras de vidro opto-magnético, fibras com estruturas concatenadas, fibras poliméricas, fibras microestruturadas em biopolímero de agarose, e guias de onda de agarose dopadas com nanopartículas fluorescentes que foram desenvolvidos tendo em mente o uso de interrogadores de baixa complexidade e custo como alternativas aos sensores de fibra óptica tradicionais. A capacidade destes novos sensores de monitorar variáveis diversas é demonstrada, incluindo temperatura, deformação mecânica, curvatura, índice de refração, nível de líquido, campo magnético, potencial hidrogeniônico e taxa de evaporação de fluidos em microcanais. Tendo uma grande presença já estabelecida no meio comercial, sensores do tipo redes de Bragg também foram explorados para aplicações inéditas, como o desenvolvimento de anemômetros ópticos, monitoramento de válvulas de ar em adutoras de água, e obtenção de parâmetros de escoamentos multifásicos em mili/microcanais.

Palavras Chave: sensores de fibra óptica; sensores de fiber speckle; fibras ópticas especiais; fibras ópticas poliméricas; fibras ópticas biodegradáveis; redes de Bragg; nanopartículas fluorescentes.

Abstract

Fiber optic sensors are increasingly more prevalent in applications that were typically dominated by more traditional mechanical or electronic sensors, given the inherited advantages fiber sensors bring, such as increased flexibility, great multiplexing capability, small form-factor, and immunity to electromagnetic interference. The continued improvement of fiber optic technology and the advent of photonic crystal fibers resulted in virtually limitless options for designing and functionalizing optical fibers, allowing the development of a vast array of new applications for data transmission, imaging, and sensing. Despite that, optical fiber sensors already established for commercial applications typically make use of expensive interrogation equipment such as optical spectrum analyzers, are based on complex interferometric setups, or both. This thesis demonstrates several novel fiber sensors based on specialty optical fibers such as microstructured silica optical fibers, magneto-optic glass fibers, concatenated fiber structures, polymer fibers, agarose biopolymer structured optical fibers, and agarose waveguides doped with fluorescent nanoparticles, all developed with the mindset of enabling low-cost and low-complexity sensor interrogation setups as alternatives to the currently established commercial fiber probes. The fitness of these new probes to measure a wide array of physical and chemical variables is explored, including temperature, mechanical strain, curvature, refractive index, liquid level, magnetic field intensity, pH, and evaporation rate of fluids in microchannels. Already boasting a large presence for commercial solutions, fiber Bragg gratings-based sensors were also explored in novel applications, namely the development of all-optical anemometers, monitoring of air-vacuum valves in water adductor systems, and the assessment of multiphase flow parameters in mili/microchannels.

Key Words: Optical fiber sensors; fiber specklegram sensors; photonic crystal fibers; polymer optical fibers; biodegradable optical fibers; fiber Bragg gratings; fluorescent nanoparticles.

List of Publications

Publications discussed in this thesis (in order of appearance in the text):

CABRAL, T.D.; DA SILVA, L.E.; FUJIWARA, E.; CORDEIRO, C.M.B. **Fiber Specklegram Analysis for Monitoring Evaporation Inside a Capillary-like Optical Fiber**. Proc. LAWOFS 2019 (Rio de Janeiro, Brazil), 2019. http://www.sbmo.org.br/lawofs/Proceedings-LAWOFS_2019_final.pdf

Type: conference paper

My contributions: paper writing, fiber fabrication, sensing experiments, data analysis, discussion of the results.

FUJIWARA, E.; CABRAL, T.D.; CORDEIRO, C.M.B. **Optical Fiber Specklegram Sensors for Measurement of Liquids (Invited Paper)**. Proc. 2019 SBFoton IOPC (São Paulo, Brazil), 2019. <https://doi.org/10.1109/SBFoton-IOPC.2019.8910183>

Type: conference paper

My contributions: paper text review, capillary-like fiber fabrication, capillary-like fiber sensing experiments and data analysis, discussion of the results.

FUJIWARA, E.; DA SILVA, L.E.; CABRAL, T.D.; DE FREITAS, H.E.; WU, Y.T.; CORDEIRO, C.M.B. **Optical Fiber Specklegram Chemical Sensor for Based on a Concatenated Multimode Fiber Structure**. Journal of Lightwave Technology, v. 37(19), pp. 5041-5047, 2019. <https://doi.org/10.1109/JLT.2019.2927332>

Type: journal paper

My contributions: paper text review, fiber fabrication, data analysis review, discussion of the results.

SMITH, D.L.; NGUYEN, L.V.; OTTAWAY, D.J.; CABRAL, T.D.; FUJIWARA, E.; CORDEIRO, C.M.B.; WARREN-SMITH, S.C. **Machine learning for sensing with a multimode exposed core fiber specklegram sensor**. Optics Express, v. 30(7), pp. 10443-10455, 2022. <https://doi.org/10.1364/OE.443932>

Type: journal paper

My contributions: paper text review, sensing experiments, ZNCC data analysis, discussion of the results.

CABRAL, T.D.; FRANCO, D.D.; FUJIWARA, E.; NALIN, M.; CORDEIRO, C.M.B. **Magnetic Field Fiber Specklegram Sensor Based on Tb³⁺ Doped Magneto-Optical Glass Fibers with Very High Verdet Constants – IEEE Sensors Journal (UNDER REVIEW)**

Type: journal paper

My contributions: paper writing, sensing experiments, data analysis, discussion of the results.

FUJIWARA, E.; CABRAL, T.D.; SATO, M.; OKU, H.; CORDEIRO, C.M.B. **Agarose-based structured optical fibre**. Scientific Reports, v. 10(1), 7035, 2020. <https://doi.org/10.1038/s41598-020-64103-3>

Type: journal paper

My contributions: paper text review, sensing and waveguide characterization experiments with EF, data analysis review, discussion of the results.

CABRAL, T.D.; DA SILVA, L.E.; FUJIWARA, E.; NG, A.K.L; EBENDORFF-HEIDEPRIEM, H.; CORDEIRO, C.M.B. **Reusable polymer optical fiber strains sensor with memory capability based on ABS crazing**. Applied Optics, v. 58(20), pp. 9870-9875, 2019. <https://doi.org/10.1364/AO.58.009870>

Type: journal paper

My contributions: paper writing, sensing experiments, data analysis, discussion of the results.

AMATO, F.; SOARES, M.C.P.; CABRAL, T.D.; FUJIWARA, E.; CORDEIRO, C.M.B.; CRIADO, A.; PRATO, M.; BARTOLI, J. R. **Agarose-Based Fluorescent Waveguide with Embedded Silica Nanoparticle-Carbon Nanodot Hybrids for pH Sensing**. ACS Applied Nano Materials, v. 4(9), pp. 9738-9751, 2021. <https://doi.org/10.1021/acsnm.1c02127>

Type: journal paper

My contributions: paper text review, doped waveguide fabrication with MCPS, pH sensing experiments and data analysis with MCPS, discussion of the results.

FUJIWARA, E.; DELFINO, T. S.; CABRAL, T.D.; CORDEIRO, C.M.B. **All-Optical Fiber Anemometer Based on the Pitot-Static Tube**. IEEE Transactions on Instrumentation and Measurement, v. 69(4), pp. 1805-1811, 2019. <https://doi.org/10.1109/TIM.2019.2915392>

Type: journal paper

My contributions: paper text review, data analysis review, discussion of the results.

ARISTILDE, S.; SOARES, M.C.P.; CABRAL, T.D.; RODRIGUES, G.; FUJIWARA, E.; FRUETT, F.; CORDEIRO, C.M.B. **Measurement of Multiphase Flow by Tilted Optical Fiber Bragg Grating Sensor**. IEEE Sensors Journal, v. 21(2), pp. 1534-1539, 2021. <https://doi.org/10.1109/JSEN.2020.3016616>

Type: journal paper

My contributions: paper text review, data analysis review, discussion of the results.

DE AQUINO, G.A.; DE LUCCA, Y.F.L.; CABRAL, T.D.; LAZARI, P.M.; MARTIM, A.L.S.S.; FUJIWARA, E.; CORDEIRO, C.M.B.; DALFRÉ FILHO, J.G. **All-optical real-time monitoring of air/vacuum valves in water pipeline systems using fiber Bragg gratings**. Journal of the Brazilian Society of Mechanical Sciences and Engineering, v. 44, 5, 2022. <https://doi.org/10.1007/s40430-021-03310-z>

Type: journal paper

My contributions: paper writing, data analysis, discussion of the results.

Other works published during the PhD program (in chronological order):

FUJIWARA, E.; MACHADO, P.L.; OLIVEIRA, T.C.D.; SOARES, M.C.P.; CABRAL, T.D.; CORDEIRO, C.M.B. **Using the Smartphone as an Ubiquitous Platform for Implementing Optical Fiber Sensors**. Proc. 2019 SBFoton IOPC (São Paulo, Brazil), 2019. <https://doi.org/10.1109/SBFoton-IOPC.2019.8910250>

CABRAL, T.D.; FUJIWARA, E.; WARREN-SMITH, S.C.; EBENDORFF-HEIDEPRIEM, H.; CORDEIRO, C.M.B. **Multimode exposed core fiber specklegram sensor**. Optics Letters, v. 45(12), pp. 3212-3215, 2020. <https://doi.org/10.1364/OL.391812>

SOARES, M.C.P.; PERLI, G.; BERTUZZI, D.L.; CABRAL, T.D.; CORDEIRO, C.M.B.; ORNELAS, C.C.C.; BARTOLI, J.R.; FUJIWARA, E. **One-Step Synthesis of Fluorescent Carbon Nanodots from Two Widely Available Natural Sources**. Proc. OSA Advanced Photonics Congress (AP) 2020 (IPR, NP, NOMA, Networks, PVLED, PSC, SPPCom, SOF), paper JTh3G.4, 2020. <https://doi.org/10.1364/NOMA.2020.JTh3G.4>

CABRAL, T.D.; ZIMMERMANN, A.C.; WILLEMANN, D.P.; GONÇALVES JR, A.A. **Pipeline Bonded Joints Assembly and Operation Health Monitoring with Embedded FBG Sensors**. MDPI Engineering Proceedings, v. 2(1), 5, 2020. <https://doi.org/10.3390/ecsa-7-08208>

SOARES, M.C.P.; CABRAL, T.D.; LAZARI, P.M.; RODRIGUES, M.S.; RODRIGUES, G.S.; FUJIWARA, E. **Smartphone-Based Optical Fiber Sensor for the Assessment of a Fed-Batch Bioreactor**. MDPI Engineering Proceedings, v. 2(1), 26, 2020. <https://doi.org/10.3390/ecsa-7-08157>

SOARES, M.C.P.; CABRAL, T.D.; MENDES, B.F.; DA SILVA, V.A.; TAMBOURGI, E.B.; FUJIWARA, E. **Technical and Economic Viability Analysis of Optical Fiber Sensors for Monitoring Industrial Bioreactors**. MDPI Engineering Proceedings, v. 2(1), 57, 2020. <https://doi.org/10.3390/ecsa-7-08161>

SOARES, M.C.P.; CABRAL, T.D.; PERLI, G.; BRESSANIN, J.M.; BARTOLI, J.R. **Estimating Polymer Properties and Practicing Statistical Tools in Undergraduate Level through Simple Experiments**. Chemical Engineering Transactions, v. 86, pp. 1375-1380, 2021. <https://doi.org/10.3303/CET2186230>

CABRAL, T.D.; CORDEIRO, C.M.B.; FUJIWARA, E. **Enhancing the measurement range of laser speckle systems**. Microwave and Optical Technology Letters, v. 64(11), pp. 2110-2114, 2022. <http://doi.org/10.1002/mop.33388>

FUJIWARA, E.; CABRAL, T.D. **Optical fiber specklegram sensor for multi-point curvature measurements**. Applied Optics, v. 61(23), pp. 6787-6794, 2022. <https://doi.org/10.1364/AO.46450>

PERLI, G.; SOARES, M.C.P.; CABRAL, T.D.; BERTUZZI, D.L.; BARTOLI, J.R.; LIVI, S.; D.-RUMEAU, J.; CORDEIRO, C.M.B.; FUJIWARA, E.; ORNELAS, C. **Synthesis of Carbon Nanodots from Sugarcane Syrup, and Their Incorporation into a Hydrogel-Based Composite to Fabricate Innovative Fluorescent Microstructured Polymer Optical Fibers**. MDPI Gels, v.8(9), 553, 2022.. <https://doi.org/10.3390/gels8090553>

List of Figures

Figure 1 – Typical structure of an optical fiber. Adapted from (20).	29
Figure 2 – The condition for total internal reflection determines the acceptance cone to transmit incident light. Adapted from (20).	30
Figure 3 – Types of optical fibers by index profile and number of guided modes. Adapted from (20).	31
Figure 4 – Transverse electric field of a few guided modes extending past the core of an optical fiber (21).	34
Figure 5 – First few linearly polarized (LP) modes supported in a multimode optical fiber (22).	35
Figure 6 – Left: Cross-section drawing of a D-shaped optical fiber (30); Right: Schematic drawing of a fiber optic taper, adapted from (31).	36
Figure 7 – Cross-section of a single-material fiber with the core suspended in air by thin glass bridges (36).	37
Figure 8 – Scanning electron micrograph of the first reported photonic crystal fiber (38).	37
Figure 9 – Scanning electron micrographs of an index guided PCF (left) and photonic bandgap hollow-core PCF (41).	38
Figure 10 – Fabrication of a bandgap hollow-core fiber by the “stack and draw” method. A: primary preform obtained by stacking glass capillaries; B: first stage drawing of the preform into a “cane” of a few mm in diameter; C: optical image of the cross-section of the cane; D: micrograph of the finalized fiber (49).	38
Figure 11 – Intensity-based fiber optic displacement sensors. Left: Probe based on intensity of light reflected back into a fiber by a mirrored surface. Right: Probe based on transmission losses caused by microbending. (61).	40
Figure 12 – Temperature dependent luminescence of doped tellurite glass excited by a 980 nm laser source (65).	40
Figure 13 – Two realizations of fiber Fabry-Perot interferometers. Left: Air gap between two fiber pieces in a capillary tube (66). Right: Fiber tip Fabry-Perot interferometer with a flexible diaphragm (67).	41
Figure 14 – Left: Spectrum of a broadband light source coupled into a fiber with a Fabry-Perot interferometer. Right: Output reflection spectra of the fiber interferometer (68).	41

Figure 15 – (a): Concatenated multimode-no-core-multimode fiber structure for refractive index sensing. (b): Response of the sensor (in transmission) for liquids with refractive index between 1.3 and 1.42 (74).	42
Figure 16 – Transmission and reflection spectra from an FBG (81).	44
Figure 17 – Photograph of a fiber specklegram from a commercial multimode fiber. Light source is a 633 nm He-Ne laser, and the image was projected from the fiber end-face into a lens-less webcam using a 20× objective.	46
Figure 18 – Optical microscope images of (a): a sample of the capillary fiber, and (b): resin sealed capillary filled with water and red dye.	49
Figure 19 – Schematic of the experimental setup, a frame of the captured specklegram video is shown to the right along with a representation of the analysis window for the calculation of ZNCC. NDF = neutral density filter; M1/M2 = mirrors, L1/L2 = objective lenses (105).	50
Figure 20 – (a) Image of the liquid filled capillary fiber showing the air/liquid interface as observed by the microscope. (b) Observed output specklegram as captured by the webcam, dashed yellow rectangle represents the 200×200 pixels ZNCC analysis window.	50
Figure 21 - (a): Comparison of the Z curve over time for an air-filled capillary and a water filled capillary. (b): Combined displacement and Z data over time up to a maximum displacement of 40 μm, dashed red line is a linear fit of the displacement data (105).	51
Figure 22 – Z over time for displacements Δx up to (a): 20 μm, (b): 30 μm, (c): 40 μm, and (d): 50 μm (105).	52
Figure 23 – Average Final Z as a function of displacement. Dashed black line is a guide to the eyes, solid red line is a linear fit ($R^2 = 0.999$) of the for the 0 μm to 30 μm range (105).	52
Figure 24 – Optical microscope image of a capillary-like optical fiber with a Ge doped glass rod of ~40 μm in diameter attached to its inner wall.	53
Figure 25 – Schematic of the MNCM structure. Light from the MMF1 fiber core is coupled to the NCF section, where the MNC modes are excited as a function of the sample refractive index n_3 . Part of the light is coupled to MMF2 core, resulting in an output specklegram $I(x, y)$ which is processed to retrieve sample properties (107).	56
Figure 26 – Transmission spectra of the MNCM fibers in the air for different NCF lengths. The spectra were offset for the sake of visualization (107).	56
Figure 27 – Measurement of the water level. (a) Experimental setup: the no-core fiber (NCF) section of length L is immersed in the analyzed liquid of relative level h . (b) Sensor response	

as a function of h for the ZNCC referenced to $h = 0$ mm (Z_0) and $h = L = 30$ mm (Z_L). The solid lines are guides to the eye (107).	58
Figure 28 – Experimental setup for measuring the refractive index n_3 . LS: laser source; MMF: multimode fiber; MS: mode scrambler; FUT: no-core fiber section under test; $I(x,y)$: specklegram; CCD: camera; and PC: computer (107).	59
Figure 29 – Sensor response to the sample refractive index. (a) Near-field speckle field intensity for the NCF immersed in different liquids. The intensity values were normalized for the sake of visualization. (b) ZNCC values with the reference statuses set to the fiber immersed in water (Z_W) and ethanol (Z_E). The solid lines correspond to linear curve fittings ($R^2 > 0.98$). (107)..	61
Figure 30 – Variation of the ZNCC as a function of the sample temperature for the MNM probe placed in the air. The solid line is the linear curve fitting (107).	62
Figure 31 - (a) 3D model of the fiber preform – inset shows the cross-section view of the fiber; (b) optical microscope image of the fiber cross-section (108).	64
Figure 32 – Up: 3D model of the fiber bathing apparatus indicating its main features, such as alignment rails and a slot for a Peltier device. Down: Machined bathing apparatus with fiber holders and a Peltier device.	65
Figure 33 - Experimental setup used to characterize the ECF’s response to temperature and refractive index of fluids. NDF: Neutral density filter. M1, M2: mirrors. L1: 20× objective. L2: 40× objective (108).	66
Figure 34 – Output specklegram from the core of the ECF as captured by the webcam. The dashed yellow square indicates the 200×200 pixels region-of-interest for ZNCC calculation (108).	66
Figure 35 – Scatter plot of Z for a single video collected with the ECF. Blue dots are the datapoints, green line indicates average Z for the dataset and the orange lines are offsets of $\pm 3.5\sigma$ in relation to the average value.	67
Figure 36 – ECF response to length bathed in water. Blue curve is a quadratic fit of the data ($R^2 = 0.958$). (108).	68
Figure 37 – ECF response to bathing with distinct fluids: water, ethanol, 33% w/w glycerol solution and isopropyl alcohol (IPA). Blue curve is a quadratic fit of the data ($R^2 = 0.989$). (108).	69
Figure 38 – Setup modifications for assessing the ECF response to quasi-static temperature variations.	69

Figure 39 - Response of the ECF to quasi-static temperature variations for the fiber exposed to air (orange dots) and bathed in water (blue dots). Solid lines are quadratic fits of the data (108).	70
Figure 40 – Speckle field image processing: (a): output specklegram, (b): filtered image, and (c): level mask for the ECF bathed in water. (d), (e) and (f) show the equivalent analysis for the ECF bathed in air.....	71
Figure 41 - Response of the ECF probe (blue) to dynamic temperature variations (red). Temperature varies ± 1.0 °C over the baseline value (108).	72
Figure 42 – The glass preforms BGB-xTb: BGB-6Tb (a), BGB-8Tb (b) and BGB-10Tb (c). (110).	75
Figure 43 – Schematic drawing of the experimental setup. NDF: Neutral density filter; M1, M2: mirrors; FUT: Fiber under test; L1, L2: objective lenses. Graphic inset is the magnetic field intensity H produced by the coil as a function of the fed electrical current, solid line is a linear fit of the data ($R^2 = 0.999$). (110).	77
Figure 44 – Data analysis process showing the speckle pattern and 201×201 pixels ROI for unperturbed ($H = 0$ mT) state of the BGB-6Tb fiber.	77
Figure 45 – Z curves as H increases for specklegram videos collected with the BGB-8Tb fiber (a). Single video Z curve (silica MMF) highlighting the average value of Z (μ_z) and the standard deviation σ (b). (110).....	78
Figure 46 – Normalized fiber output intensity for $H = 0$ mT for the BGB-6Tb fiber as the analyzer (orange curve) or polarizer (blue curve) are allowed to rotate.	80
Figure 47 – Sensitivity to H for a BGB-6Tb fiber when using a polarizer + analyzer (black), or polarizer only (red). Solid lines are linear fits of the data (Black curve: $R^2 = 0.984$; Red curve: $R^2 = 0.995$). (110).	80
Figure 48 – Magnetic hysteresis test results. (a): Temporal evolution of μ_z for a commercial MMF showing a mirrored response for increasing and decreasing H . (b): μ_z as a function of H for the MMF subjected to the cyclic H . (c): Results for the BGB-6Tb fiber showing divergence between the increasing and decreasing H curves. (d): Diverge between datasets for the BGB-6Tb eliminated by redefining $I_0(x,y)$ for μ_z calculations.	82
Figure 49 – Response of each fiber to H . Solid lines are linear fits of the data. Dark blue triangles: MMF ($R^2 = 0.943$); red diamonds: BGB-6Tb fiber ($R^2 = 0.995$); green crosses: BGB-8Tb fiber ($R^2 = 0.995$); light blue asterisks: BGB-10Tb fiber ($R^2 = 0.997$).	83

Figure 50 – Sensitivity S as a function of the Verdet constant V of each fiber, showcasing the sharp increase in sensitivity for high V fibers. Solid line is a linear fit of the data ($R^2 = 0.989$). (110).	84
Figure 51 – (a) Fabrication of structured agarose fiber: boiled agar solution is poured into the mold, and the fiber is released after solidification in a refrigerator. (b) Detail of the fiber inside the mold with cross-section views of the mold edges and center, as well as the fiber end face: the glass tube supports the fiber structure whereas air holes are formed by the rods (181).	87
Figure 52 – Agarose-based structured optical fiber: (b) cross-section view of the end-face and (c) output speckle field of the core-guided modes. The fiber has 60 mm length, diameters of 0.64 mm, 2.5 mm, and 0.5 mm for core, cladding, and holes respectively, and bridges of ~ 0.08 mm width (181).	87
Figure 53 – Experimental setups for fiber sensing: (a) measurement of surrounding fluid droplet by speckle field analysis; (b) assessment of fluids inserted into all the fiber holes based on the average intensity of projected speckle pattern (181).	88
Figure 54 – Optical characterization: (a) refractive index of bulk agarose samples; (b) refractive index as a function of sucrose addition in a 2% w/v agarose samples; (c) output power spectra for agarose bulk and fibre samples, the inset shows the output spectrum of a 2% w/v agarose fibre; and (d) fibre optical loss at 633 nm obtained by the cut-back method (181).	90
Figure 55 – Sensing with the agarose structured fiber: (a) effect of surrounding fluid on the EZNCC. The sample dripping event is indicated by the vertical line. (b) Relative intensity values of the light transmitted by fiber core, cladding, and holes. Solid lines are guides to the eye, whereas the vertical line indicates the RI of 2% w/v agarose (181).	92
Figure 56 – (a) Schematic of the planar sample fabrication procedure; (b) Pictures of the clear (top) and bent (bottom) samples; (c) Transmission spectrum where typical absorption lines are observed (182).	95
Figure 57 – (a) 0.5 mm thick sample transmittance in its original state (clear), after bending and thermal treatment; (b) Absorbance due the whitening process and the residual absorbance after heating of the sample close to its glass transition temperature for 90 seconds. The signal discontinuities at 800 nm are due to the detector and grating change in the spectrometer (182).	96
Figure 58 – Optical microscope image of the ABS core, PMMA cladding fiber (182).	97
Figure 59 – Indentation test experimental setup, L1 and L2 are 20 \times objective lenses (182)... ..	98

Figure 60 – (a) Transmission loss as a function of indentation depth, the orange curve is a linear fit of the data ($R^2 = 0.997$). (b) Residual loss due to stress whitening when various indentation depths were reached, the blue curve is a linear fit of the data ($R^2 = 0.967$). (182).	99
Figure 61 – (a) Indentator device lightly touching the POF probe; (b) Visible stress-whitening occur as the indentator presses on the fiber; (c) Stress-whitening remains after removal of the load; (d) Stress-whitening spot vanishes after heating the fiber with a heat gun.	100
Figure 62 – Transmission spectrum of the crazed (red) and heat-recovered (green) fiber relative to the transmission in pristine condition (182).	100
Figure 63 – Residual loss due to whitening as a function of: (a) Macrobending Radius (R) and (b) Curvature (κ). The lines are fits (a: linear, b: quadratic) of the collected data (182).	101
Figure 64 – Tensile test experimental setup, L1 and L2 are 20× objective lenses.	102
Figure 65 – (a) Transmission loss as a function of Δl , the dotted line is a guide to the eyes; (b) Residual transmission loss at various values of Δl , the blue line is a fit of the data (182).	102
Figure 66 – Synthesis Routes of α -CDs, Amino-Terminated SiO_2 Nanoparticles, and Hybrids of α -CDs Coupled to a- SiO_2 (183).	105
Figure 67 – Fluorescence spectra of (a) α -CD and (b) silica-Cdots (183).	106
Figure 68 – Agarose Waveguide Doped with the Hybrids (183).	107
Figure 69 – (a) Setup for the pH evaluation using the aqueous hybrids dispersions. (b) Wavelength of maximum emitted fluorescence as a function of pH for the dispersions of hybrids. The inset shows the linear portion of the curve (pH ranging from 6 to 10). (183). .	108
Figure 70 – (a) Intensity of light transmitted by the waveguides (excitation with the supercontinuum laser). The dashed region corresponds to the fluorescence of the hybrids. (b) Wavelength of maximum emitted fluorescence as a function of pH for the agar waveguide. The inset shows the linear portion of the curve (pH 6–10). (183).	111
Figure 71 – Fluorescence spectra of the silica-Cdots hybrids at excitation wavelength of 403 nm (when dispersed in water and when occluded into the agarose matrix) for pH 4.3, exhibiting a red-shift between curves.	112
Figure 72 – Schematic drawing of the FBG inscribing process. M1, M2: Mirrors. PM: Phase Mask (257).	115
Figure 73 – Differential pressure diaphragm based on an $a \times b$ area, h thickness square plate with clamped edges and subjected to a uniformly distributed load q (255).	118
Figure 74 – CAD drawing of the fabricated Pitot-static tube. (a) Cross-sectional view. (b) Isometric view. 1: total pressure port. 2: static pressure port. 3: diaphragm support (255). ..	119

Figure 75 –Experimental setup. The Pitot-static tube inlet is aligned to the airflow speed U , causing the diaphragm to be deflected by the difference between the total and static pressures p_t and p_s , respectively. Then, the curvature of the FBG written in the SMF is measured by the optical interrogator (255).....	119
Figure 76 – Simulation of the diaphragm deflection in response to the airflow speed. (a) Deflection profile for $U = 36$ m/s, the colors indicate the magnitude of w . (b) Deflection profiles as a function of U . (c) Fiber radius of curvature, the inset shows the w values (squares) and the sine function curve fitting (red line) for $U = 36$ m/s. (d) Bragg wavelength shift as a function of the speed (the experimental data fitted by a degree-2 polynomial). (255).....	121
Figure 77 – FBG wavelength shift as a function of the airflow speed for different diaphragm parameters α (indicated in the legend). (255).....	121
Figure 78 – Sensor calibration curves: Bragg wavelength shift as a function of (a) airflow speed U and (c) U^4 . Experimental data fitted by polynomial functions, where R^2 is the coefficient of determination. The curve fitting residuals are shown in (b) and (d) for U and U^4 , respectively (255).	122
Figure 79 – Comparison between the airflow speeds measured by the fiber sensor U and the reference values U^* obtained by the U-tube manometer. (a) Variation of the U value and (b) measurement errors. In (b), the red line indicates the linear fit model applied to the data, whereas the black dotted line indicates the $U = U^*$ case (255).....	123
Figure 80 – Variation of surrounding refractive index as a function of time. The output spectra of TFBG shifts with the dispersed phase transport, making it feasible to evaluate the flow speed and estimate the continuous and dispersed substances (256).	126
Figure 81 – Optical fiber sensor: water-in-oil two-phase flow passes through the millifluidic device and changes the refractive index surrounding the TFBG. The speed of water droplets V_{Liq} is defined by the flow rates of continuous and dispersed phases. 3D sketch in the bottom-right shows the multiphase flow device (256).	127
Figure 82 – FBG sensor response to the surrounding refractive index n :(a) transmission spectra; (b) resonance dips around 1531.5 nm, the vertical line indicates $\lambda = 1531.36$ nm whereas the legend indicates n values; (c) transmission as a function of n , solid line is a linear curve fitting that excludes outliers. Transmission data was normalized for the sake of visualization (256).	128

Figure 83 – Measurement of water-in-oil flows: normalized intensity for (a) $q = 0.6$ and (b) $q = 0.5$, peaks and dips indicate the passage of water and oil slugs, respectively, along the TFBG. Flow profiles for (c) $q = 0.6$ and (d) $q = 0.5$, water slugs are colored with black dye (256)..	129
Figure 84 – Normalized intensity signals for (a) air-in-oil (dips indicate the passage of air slugs along the TFBG) and (b) water-in-air flows (peaks represent transport of water slugs). (256).	130
Figure 85 – 3D-printed TPU encased FBG sensor secured to the 3D-printed PLA support (257).	133
Figure 86 – Stress-Strain curve of 3D-printer filament grade TPU (257).	134
Figure 87 – Schematic drawing of hydraulic test bench. V1, V2 = gate valves. AVV = air/vacuum valve (257).	135
Figure 88 – Schematic drawing of the optical fiber sensor working principle. (a): Sensor at rest (no air flow). (b): Bending of the sensor due to the air and water droplets flow in a purging event. (c): Bending of the sensor during an air intake event. (d): PLA support and encased FBG sensor secured to the AVV (257).	137
Figure 89 – Response curves of the FBG sensor (red dots) and electronic pressure sensors (green dots). (a): During air purging events. (b): During air intake events (257).	138

List of Tables

Table 1 – Results of the speckle count for output specklegrams captured with the ECF bathed in water and in air.	71
Table 2 – Summary of sensor metrics including the Verdet constant V , deviation σ , sensitivity S and resolution ΔH for each tested fiber (110).....	83
Table 3 – Characteristics of hydrogel-based optical fibers and waveguides reported in the literature (181).	91
Table 4 – Physical properties of the TPU polymer (257).....	134

List of Abbreviations

- UV** – ultraviolet (light spectrum)
- IR** – infrared (light spectrum)
- VIS** – visible (light spectrum)
- FBG** – fiber Bragg grating
- NA** – numerical aperture (step-index fiber)
- NA_g** – numerical aperture (graded-index fiber)
- TE** – transverse electric (modes)
- LP** – linearly polarized (modes)
- HE** – hybrid electric (mode)
- HM** – hybrid magnetic (mode)
- PCF** – photonic crystal fiber
- OFS** – optical fiber sensor
- POF** – polymer optical fiber
- SPR** – surface plasmon resonance
- CSF** – Coreless-silica fiber
- LPG** – long period gratings
- USD** – United States Dollars (currency)
- FSS** – fiber specklegram sensor
- NIPC** – normalized inner-product coefficient (correlation metric)
- ZNCC** – zero-mean normalized cross-correlation (correlation metric)
- POC** – phase-only correlation (correlation metric)
- EZNCC** – extended-ZNCC (correlation metric)
- NDF** – neutral density filter
- MSM** – multimode-single-mode-multimode (concatenated fiber structure)
- SMF** – single-mode fiber
- NCF** – no-core fiber
- MNCM** – multimode-no-core-multimode (concatenated fiber structure)
- MMF** – multimode fiber
- OSA** – optical spectrum analyzer

MMI – multimodal interference
CCD – charge-coupled device
ROI – region-of-interest
LS – laser source
MS – mode scrambler
FUT – fiber under test
RI – refractive index
RIU – refractive index units
ECF – exposed core fiber
VIM – International Vocabulary of Metrology
IPA – isopropyl alcohol
MO – magneto-optical (glass)
PMMA – poly(methyl methacrylate)
DC – direct current
DI – deionized (water)
ABS – acrylonitrile butadiene styrene
ATR – attenuated total reflection
FTIR – Fourier-transform infrared spectroscopy
OTDR – optical time-domain reflectometry
PEG – poly(ethylene glycol)
QD – quantum dot
CD – carbon dot
APTES – 3-aminopropyltriethoxysilane
DMF – anhydrous dimethylformamide
EDC·HCl – 1-ethyl-3-(3-(dimethylamino)propyl) carbodiimide hydrochloride
NHS – N-hydroxysuccinimide
PL – photoluminescent (spectra)
PETG – poly(ethylene terephthalate)
LED – light emitting diode
XPS – x-ray photoelectron spectroscopy
PM – phase-mask
MEMS – micro-electro-mechanical system
TFBG – tilted fiber Bragg grating

AVV – air/vacuum valve

AWWA – American Water Works Association

TPU – thermoplastic polyurethane

PLA – polylactide

ISO – International Organization for Standardization

Table of Contents

1 INTRODUCTION.....	25
1.1 Motivation.....	25
1.2 Objectives	26
1.3 Chapter Summary	26
2 OPTICAL FIBERS FUNDAMENTALS	27
2.1 Optical communications and optical fibers: A brief history	27
2.2 Theoretical framework.....	29
2.3 Specialty optical fibers.....	36
3 OPTICAL FIBER SENSORS	39
3.1 Intensity based optical fiber sensors	39
3.2 Interferometric optical fiber sensors	41
3.3 Evanescent wave and surface plasmon sensors	42
3.4 Optical fiber gratings sensors.....	43
3.5 Fiber specklegram sensors	45
4 SENSORS BASED ON GLASS FIBERS	48
4.1 Specklegram based monitoring of evaporation inside capillary-like optical fibers.....	48
4.1.1 Materials and methods	48
4.1.2 Results and discussion.....	51
4.2 Fiber specklegram chemical sensor based on a concatenated fiber structure	54
4.2.1 Materials and methods	55
4.2.2 Results and discussion.....	57
4.3 Multimode exposed core fiber specklegram sensor.....	63
4.3.1 Materials and methods	63
4.3.2 Results and discussion.....	67

4.4 Tb ³⁺ doped fiber specklegram sensor for magnetic field sensing.....	72
4.4.1 Materials and methods	74
4.4.2 Results and discussion.....	78
5 SENSORS BASED ON (BIO)POLYMER FIBERS	85
5.1 Agarose-based structured optical fiber	85
5.1.1 Materials and methods	86
5.1.2 Results and discussion.....	89
5.2 Reusable polymer fiber strain sensor with memory capability based on ABS crazing ..	93
5.2.1 Materials and methods	94
5.2.2 Results and discussion.....	97
5.3 Agarose fluorescent waveguide with hybrid carbon/silica nanodots for pH sensing ...	103
5.3.1 Materials and methods	104
5.3.2 Results and discussion.....	107
6 FBG APPLICATION CASES.....	115
6.1 All-optical anemometer based on the pitot-static tube and fiber Bragg gratings	116
6.1.1 Materials and methods	117
6.1.2 Results and discussion.....	120
6.2 Tilted fiber Bragg gratings for measurement of multiphase flow.....	124
6.2.1 Materials and methods	125
6.2.2 Results and discussion.....	129
6.3 All-optical real-time monitoring of air/vacuum valves with fiber Bragg gratings	131
6.3.1 Materials and methods	133
6.3.2 Results and discussion.....	136
7 CONCLUSIONS	140
References	143

1 INTRODUCTION

1.1 Motivation

In the field of modern sensor technology, research and development efforts are primarily directed towards novel and reliable sensing solutions that can deliver higher sensitivity and accuracy than that of the state-of-the-art. Furthermore, secondary goals often gravitate towards lowering cost, decreasing form-factors and enhancing the robustness to environmental factors and sources of interference.

A steady influx of novel sensors and sensing systems is a foundational building block of modern technological and scientific advancement, as unraveling fundamental natural sciences phenomena requires increasingly more precise instruments, metrological standards need periodic refinements, and industries invest into quality control and process monitoring solutions to stay competitive in a global market. Given this context, optical fiber sensors have been a prolific object of study due to their inherent favorable characteristics, notably the ability to be tailored to respond to a wide variety of physical and chemical variables, small form-factor, immunity to electromagnetic interference and high multiplexing capability.

Despite their advantages, the current generation of commercial fiber optic sensors is still dependent on expensive interrogation equipment like optical spectrum analyzers, makes use of complicated interferometric setups, or both. However, new fiber sensors designed to replace well established mechanical and electronic sensors, and to fulfill roles where current sensor technology falters, are being researched and developed at an accelerated pace.

The current thesis then aims to explore this gap in the state-of-the-art of fiber sensing technology by investigating several novel optical fiber probes based on specialty fibers that are designed to make use of cheaper and simpler interrogation setups. This was achieved by making use of the combined infrastructures of the laboratories of Photonic Materials and Devices (School of Mechanical Engineering), and Specialty Optical Fibers (“Gleb Wataghin” Institute of Physics) in the State University of Campinas (UNICAMP), that allow for a high degree of freedom to design, manufacture, and validate new optical fiber sensor designs.

1.2 Objectives

The objective of this work can be summarized as the development and characterization of novel fiber optic probes to assess a diverse array of physical and chemical quantities, as well as exploring new applications for conventional optical fiber sensors (fiber Bragg gratings).

Reaching this goal involves manufacturing the fiber probes either in-house or with the help of partnering institutions, followed then by conducting extensive experimentation to characterize the response of the new sensors to physical and chemical quantities of interest in a controlled laboratory environment.

Optical fibers fabricated from a wide array of materials and dopants were investigated, and distinct interrogation techniques were chosen to collect sensor data as appropriate. Probe design was not restricted to conventional cylindrical core-cladding structures, but photonic crystal fibers, no-core fibers and concatenated fiber structures have been investigated as well.

1.3 Chapter Summary

This thesis is divided in seven chapters, including the current Introduction. Chapter 2 contains a literature review on optical fibers, detailing the fundamental theoretical framework and defining conventional and specialty fibers. Chapter 3 presents an overview on sensing with optical fibers and common types of fiber sensors, with an emphasis on fiber specklegram sensors as they comprise the main focus of this work.

Chapter 4 and 5 contains detailed information on novel optical fiber probes developed in the context of the author's doctorate studies, with Chapter 4 presenting probes based on glass fibers and Chapter 5 polymeric materials fibers. Chapter 6 relates to new application cases for traditional fiber Bragg gratings (FBG) sensors, and the Conclusions are contained in Chapter 7.

The studies presented in Chapters 4 through 6 are fruits of collaborative research work I (co)authored and that have been published in the international literature. For a breakdown of my contributions towards each of the featured studies please refer to the List of Publications section earlier in this document.

2 OPTICAL FIBERS FUNDAMENTALS

2.1 Optical communications and optical fibers: A brief history

Light and optical phenomena have fascinated mankind for millennia, with the earliest documented formal discussions on the nature of optical laws and vision dating back to ancient Greek philosophers in 400-300 BC, most notably with the publication of Euclid's *Optics* (1). Even before that, humans learned to use light to communicate and relay information, such examples are lighthouses, that can be traced to as early as ~660 BC (2), and fire and smoke beacons employed in the Great wall of China to warn about enemy invasions (3). Since these ancient times, optical communication methods continued to evolve in complexity and capability throughout history, tracking alongside advances in the optical sciences.

In the 2nd century BC, Greek engineers devised an optical telegraphy system in which letters of the Greek alphabet were listed in a 5×5 table and two groups of up to five torches (signaling row and column) could be used to send messages (4). Ancient Romans used polished metallic plates to convey signals by reflecting sunlight (5), a precursor to Carl Friedrich Gauss' heliotrope, an optical instrument used to mark the position of land surveyors using a mirror and telescope to reflect sunlight over great distances (6). The expansion of seafaring led to the development of specialized tools using the light from the oldest of beacons, the celestial bodies. Of note are the Arabian kamal from the late 9th century (7); astrolabes, which were invented around 150 BC for astronomical and surveying purposes but only employed for navigation from the 10th century onwards (8); and reflecting instruments such as the sextant by John Hadley and Thomas Godfrey in the 1700's (9).

Modern times saw the advent of the heliograph, an instrument created by Sir Henry Christopher Mance in 1869 that used sunlight and a mirror that could be quickly tilted or covered with a shutter, allowing the transmission of messages in Morse code in ranges of up to 100 miles without electrical power (10). Another interesting invention from the same time period was the photophone by Alexander Graham Bell in 1880, only 4 years after his successful demonstration of the telephone, this device employed a thin mirror connected to a mouthpiece to modulate sunlight by voice, a receiver would then capture the modulated reflected light and

convert it into sound again using a speaker, essentially functioning as a wireless optical telephone (11). This was the first device to use light as a carrier wave to transmit data (11).

Optical fibers themselves only emerged as long-distance carriers of light waves very recently as the culmination of several studies and advances in optics and optical materials. While the concept of total internal reflection was discussed as early as 1300 AD, it was not mathematically defined until the publication of Snell's Law in 1690 (12). It was then only in 1842 that the idea of using total internal reflection to guide light was first explored by Colladon and Babinet in the demonstration of a lighted laminar water fountain (12-14). In the following decades this demonstration inspired the creation of devices using glass rods or bundles of rods and fibers for illumination purposes and limited imaging applications (12). Even after Bell's demonstration of light as a carrier wave for the photophone in 1880, optical communications and fiber optic technology stagnated for almost a century as two big obstacles stood in the way of developing practical solutions for long range communications: lack of an adequate light source that could be modulated as a carrier wave; and glass fabrication processes at the time embedded several impurities leading to transmission losses exceeding 1000 dB/km (12,15).

The demonstration of the first laser in 1960 by Theodore Maiman (16) brought forward the needed paradigm shift to renew interest in optical communications, and soon, in 1964, engineers at Bell Labs suggested two designs of "beam waveguides" as transmission media for laser light: one comprised of long tubes with a series of focusing lenses, and a second using tubes with heated walls and filled with gas to create gas lenses (15). In parallel, fundamental research on the optical properties of glass aimed to reduce transmission losses to produce a more flexible and less bulky optical waveguide alternative, with Kao and Hockham pioneering a study in 1966 suggesting that fundamental light propagation mechanisms in glass provided an upper boundary of only 20 dB/km attenuation, provided the concentration of iron inclusions in the glass could be reduced to at least 1 part per million (17). This 20 dB/km attenuation figure was soon surpassed by engineers at Corning Glass in 1970 that produced silica fibers with a loss of 17 dB/km for the wavelength of 633 nm, and by 1985 low loss fibers with attenuation lower than 0.25 dB/km were already widespread commercially available (12,15).

These breakthroughs solidified the field of optical fiber communications, and nowadays all voice and data communications employ silica glass fibers at some point (12), the global production of optical fibers exceed 180 million km yearly (12), and the use of optical fibers has expanded past data transmission and into the realm of sensors and smart structures(18,19).

2.2 Theoretical framework

The traditional optical fiber is a cylindrical waveguide of reduced diameter (≤ 1 mm) and long lengths (few mm to several km range) fabricated from dielectric materials (glass and polymers) to confine and transmit optical signals from the ultraviolet (UV) to the infrared (IR) spectrum with low loss by means of total internal reflection (18,20). Light guidance by total internal reflection can be achieved by a fiber structure composed of a core with an index of refraction n_1 surrounded by a cladding with index of refraction $n_2 < n_1$, a buffer coating layer (usually polymeric) can also be present for mechanical protection, as illustrated in Figure 1.

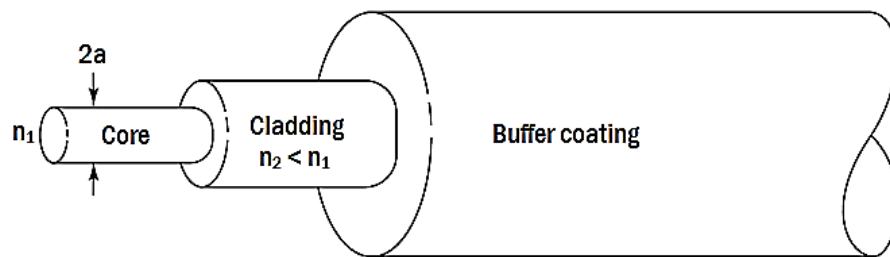


Figure 1 – Typical structure of an optical fiber. Adapted from (20).

Glass fibers are mostly fabricated from fused quartz glass (SiO_2). Dopants are added to the core, or core and cladding both, to slightly modify their refractive indexes so that $n_2 < n_1$ is satisfied. The most common dopants used to increase the refractive index of the core are GeO_2 and P_2O_5 , while B_2O_3 and Fluor can be added to the cladding to decrease its refractive index. For polymeric fibers, dissimilar polymers can be chosen as core and cladding materials (20).

Not all light directed at the fiber's core will be successfully coupled into the fiber and transmitted, depending on the incidence angle of light when it reaches the core/cladding interface it can either refract to the cladding or bounce back to the core by total internal reflection. Light refracted into the cladding will be heavily attenuated or radiated to the outside medium, effectively being lost (20).

Consider a ray of light coming from an external medium with refractive index n and reaching the fiber core with an incidence angle θ_0 , as shown in Figure 2. This ray will be reflected in the core/cladding interface if it satisfies the total internal reflection condition set by Snell's law, in which $\sin(\phi) \geq n_2/n_1$, with ϕ being the incidence angle in the core/cladding interface (20).

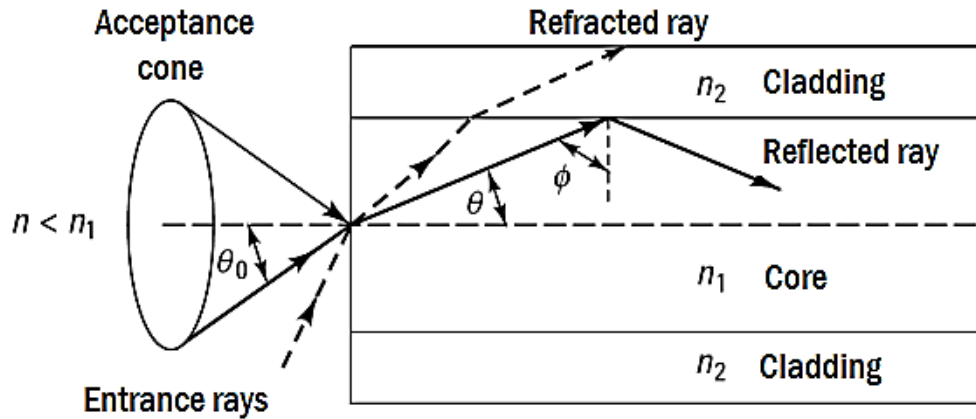


Figure 2 – The condition for total internal reflection determines the acceptance cone to transmit incident light. Adapted from (20).

Performing the inverse calculation from Snell's law, it is possible to determine the maximum permitted value for θ_0 , defining an acceptance cone for light to be successfully launched into the fiber:

$$n \cdot \sin(\theta_{0,max}) = \sqrt{n_1^2 - n_2^2} \approx n_1 \sqrt{2\Delta} ; \Delta = 1 - n_2/n_1 \quad (2.1)$$

The quantity $\sqrt{n_1^2 - n_2^2}$ in Equation (2.1) is usually referenced as the Numerical Aperture (NA) of the optical fiber, and the right-hand side approximation is valid for an index of refraction contrast $\Delta \ll 1$. Typically, for a given n_1, n_2 is chosen such that Δ is 0.01 (20).

An optical fiber that has a core with a constant index of refraction n_1 , such as the one represented in Figure 2 is referred to a step-index fiber. Optical fibers can also be fabricated such as the refractive index of the core has a maximum value n_1 at the center and gradually decays to n_2 following a power-law profile. This second type of fibers are referred to as graded-index fibers, and in this case the numerical aperture NA_g and index contrast Δ_g are given by Equations (2.2) and (2.3) respectively (20):

$$NA_g = \sqrt{n_1^2 - n_2^2} \cdot \sqrt{1 - (r/a)^\alpha} \quad (2.2)$$

$$\Delta_g = \frac{n_1^2 - n_2^2}{2n_1^2} \quad (2.3)$$

where a is the radius of the core, r is the radial distance from the center of the fiber ($0 \leq r \leq a$), and α is the exponent of the power function used to generate the index profile. Figure 3

shows the difference between step-index and graded-index fibers, along with the refractive index profile (on the left) and typical diameters for glass fibers (on the right).

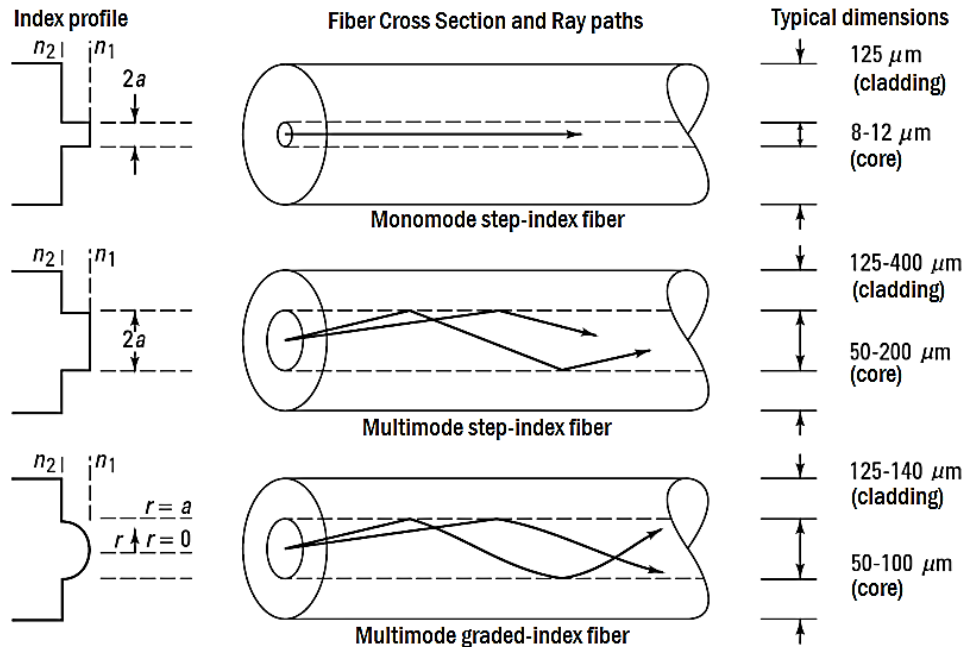


Figure 3 – Types of optical fibers by index profile and number of guided modes. Adapted from (20).

All particularities of light propagation in optical fibers (such as the “modes” shown in Figure 3) cannot be fully comprehended with only geometrical optics however, and this problem must be approached from the perspective of electromagnetic wave propagation theory.

For the boundary conditions of optical fibers (dielectric materials, linear and isotropic, no free charges or electrical current), Maxwell’s equations assume the following configuration (20):

$$\nabla \times \mathbf{E} = -\frac{\partial \mathbf{B}}{\partial t} \quad (2.4)$$

$$\nabla \times \mathbf{H} = \frac{\partial \mathbf{D}}{\partial t} \quad (2.5)$$

$$\nabla \cdot \mathbf{D} = 0 \quad (2.6)$$

$$\nabla \cdot \mathbf{B} = 0 \quad (2.7)$$

where \mathbf{E} and \mathbf{H} , are the electric and magnetic fields, and \mathbf{D} and \mathbf{B} are the electric and magnetic flux densities. In cylindrical coordinates (r, ϕ, z) , for waves propagating in the z axis of the waveguide ($\mathbf{E} = \mathbf{E}_0(r, \phi)e^{j(\omega t - \beta z)}$; $\mathbf{H} = \mathbf{H}_0(r, \phi)e^{j(\omega t - \beta z)}$), Equation (2.4) yields (20):

$$\frac{1}{r} \left(\frac{\partial E_Z}{\partial \phi} + jr\beta E_\phi \right) = -j\mu\omega H_r \quad (2.8)$$

$$j\beta E_r + \frac{\partial E_Z}{\partial r} = j\mu\omega H_\phi \quad (2.9)$$

$$\frac{1}{r} \left(\frac{\partial}{\partial r} (rE_\phi) - \frac{\partial E_r}{\partial \phi} \right) = -j\mu\omega H_z \quad (2.10)$$

in turn, Equation (2.5) then yields:

$$\frac{1}{r} \left(\frac{\partial H_z}{\partial \phi} + jr\beta H_\phi \right) = j\epsilon\omega E_r \quad (2.11)$$

$$j\beta H_r + \frac{\partial H_z}{\partial r} = -j\epsilon\omega E_\phi \quad (2.12)$$

$$\frac{1}{r} \left(\frac{\partial}{\partial r} (rH_\phi) - \frac{\partial H_r}{\partial \phi} \right) = j\epsilon\omega E_z \quad (2.13)$$

where β and ω are the wave's propagation constant and angular frequency, and ϵ and μ are the dielectric constant and permeability of the fiber material respectively. By rearranging Equations (2.8) through (2.13) it is possible to write the electric and magnetic field components E_r , E_ϕ , H_r and H_ϕ as functions of E_Z and H_Z , by which point substituting into Equations (2.10) and (2.13) returns the following differential equations (20):

$$\frac{\partial^2 E_Z}{\partial r^2} + \frac{1}{r} \frac{\partial E_Z}{\partial r} + \frac{1}{r^2} \frac{\partial^2 E_Z}{\partial \phi^2} + (\omega^2 \epsilon \mu - \beta^2) E_Z = 0 \quad (2.14)$$

$$\frac{\partial^2 H_Z}{\partial r^2} + \frac{1}{r} \frac{\partial H_Z}{\partial r} + \frac{1}{r^2} \frac{\partial^2 H_Z}{\partial \phi^2} + (\omega^2 \epsilon \mu - \beta^2) H_Z = 0 \quad (2.15)$$

These equations can be solved using the variable separation method: taking Equation (2.14) for example it is possible to write (20),

$$E_Z = AF_1(r)F_2(\phi)F_3(z)F_4(t) \quad (2.16)$$

where A is a constant and F_1 through F_4 are single variable functions.

The components pertaining to z and time t are given by $F_3(z)F_4(t) = e^{j(\omega t - \beta z)}$, and the circular symmetry of the waveguide makes it so that F_2 is a periodic function of the form $F_2(\phi) = e^{j\nu\phi}$ where ν is an integer (20). Substituting in Equation (2.16) then results in the following expression for E_z (20):

$$\frac{\partial^2 F_1}{\partial r^2} + \frac{1}{r} \frac{\partial F_1}{\partial r} + \left(\omega^2 \epsilon \mu - \beta^2 - \frac{\nu^2}{r^2} \right) F_1 = 0 \quad (2.17)$$

An analogous procedure can be followed to derive an expression for H_z . Equation (2.17) is a Bessel's differential equation with a family of solutions given by Bessel functions. Each solution to Equation (2.17) describes a wave with a distinct electrical field distribution that is guided by the optical fiber, referred as a "mode", meaning that the energy from a single light wave entering the fiber can be coupled into several different linearly superposed modes that propagate simultaneously along the fiber (20). There are several important implications that can be observed from modal analysis and the guided wave equations in optical fibers (20,21), such as that:

- i) Each guided mode has a slightly different propagation constant β , meaning they follow distinct paths inside the optical fiber, experience an "effective" refractive index in the core that is slightly distinct from n_1 and by consequence their wavelengths are also slightly different and smaller than it would be in the vacuum.
- ii) When multiple modes are present, light will travel down the fiber as a wave packet and given (i) the packet will tend to broaden over time (known as modal dispersion) and fall out of phase, so the shape of the transverse energy distribution of the linear superposition of modes is not constant and will change along the z axis of the fiber.
- iii) Each mode also has a distinct diameter, and the modal energy distribution is not completely confined to the core but can extend to the cladding (Figure 4) and even to the external medium depending on the cladding thickness. The portion of the transverse field that penetrates past the core is referred to as the Evanescent Field.

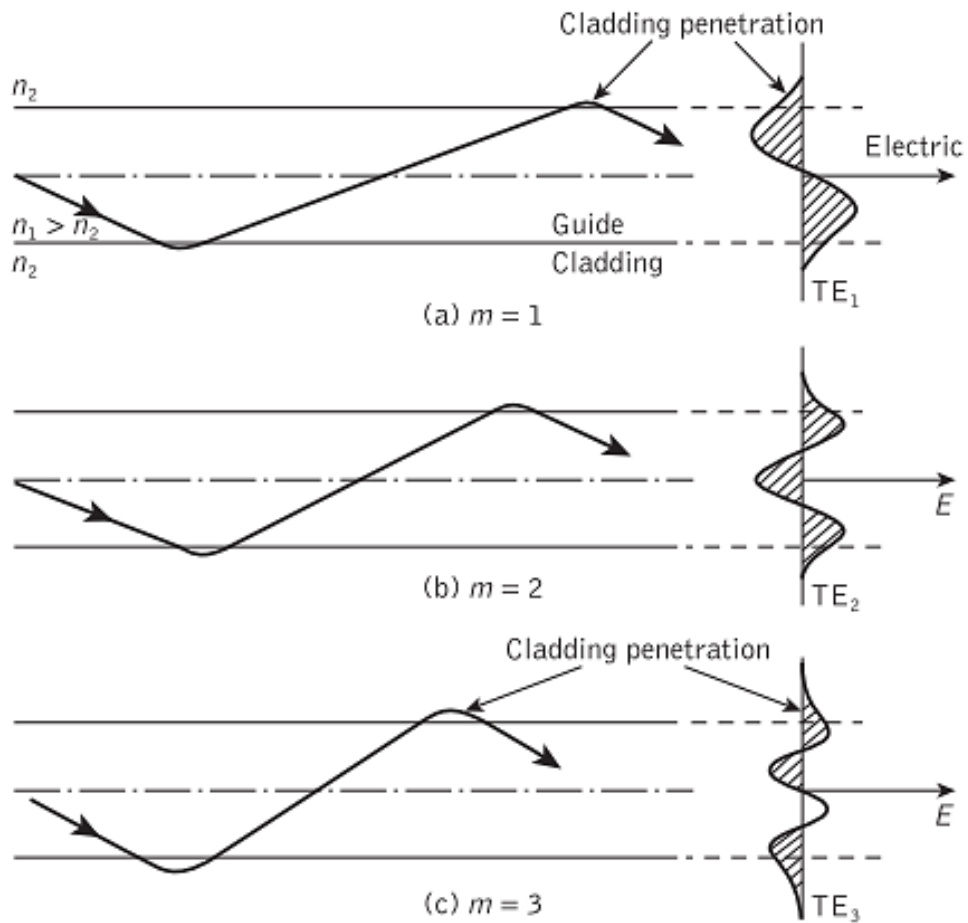


Figure 4 – Transverse electric field of a few guided modes extending past the core of an optical fiber (21).

Figure 5 shows a few examples of the intensity distribution of E_z for the first few linearly polarized guided modes. As it can be seen in both Figure 4 and Figure 5, modes are named and numbered according to the characteristics of the E_z distribution. In Figure 4 there are transverse electric (TE) modes ordered (mode number m) accordingly to the number of nodes (zeros) in E_z , while in Figure 5 the linearly polarized (LP) modes are classified with two sub-indices for the number of peaks in E_z in the azimuthal and radial directions. The solutions to equations (2.4) and (2.5) in optical fibers also lead to modes with coupled electric and magnetic fields, called hybrid modes, or HE/HM modes, that also use the sub-index pair notation (20,21,22).

The higher the mode number the largest is the mode diameter, resulting in lower “order” (mode number) modes presenting less cladding penetration, while higher order modes have more of their energy outside the fiber core, with the smallest mode being the gaussian profile of LP_{01} . As discussed previously, light traveling in the cladding are more heavily attenuated, and as such high order modes tend to disappear the longer the length of the fiber is. This implies that for a sufficiently small core size only the gaussian profile LP_{01} mode (often referred as

‘fundamental mode’) will be supported. A fiber that supports only one mode is a single-mode fiber, and fibers that guide multiple modes are multimode fibers, as shown in Figure 3 (20,21).

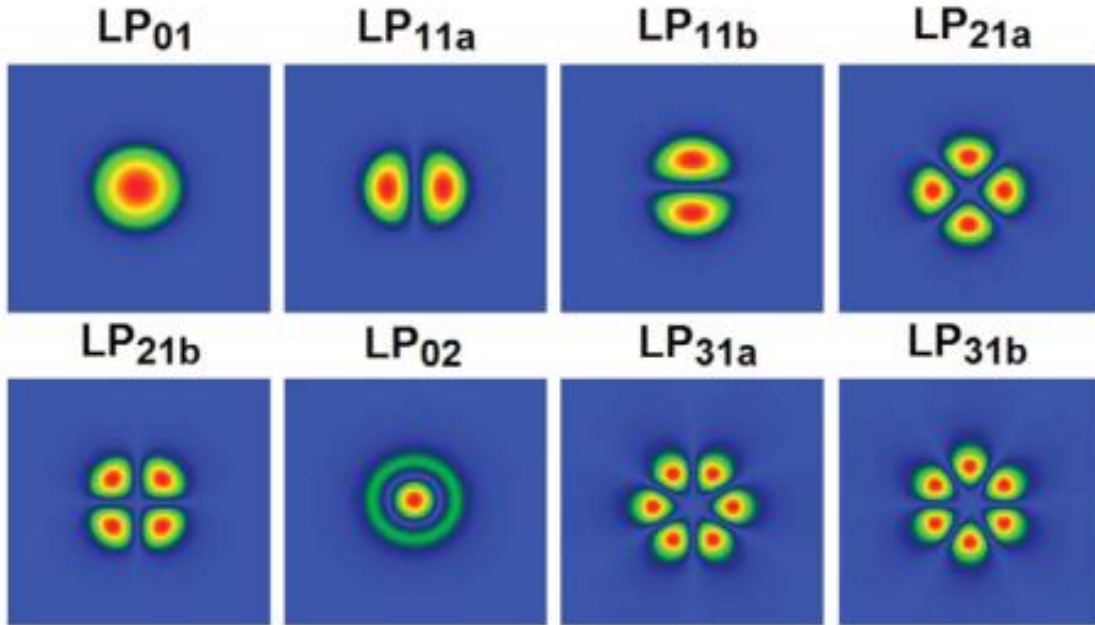


Figure 5 – First few linearly polarized (LP) modes supported in a multimode optical fiber (22).

The total number of supported modes M for a step-index fiber, M_g for a graded-index fiber can be estimated using Equations (2.18) and (2.19) respectively (20):

$$M \approx \frac{V^2}{2} \quad (2.18)$$

$$M_g \approx \frac{\alpha}{\alpha + 2} \cdot \frac{V^2}{2} \quad (2.19)$$

where α is again the exponent of the power function used to generate the graded index profile, and V is the Normalized Frequency defined as (20):

$$V = \left(\frac{2\pi a}{\lambda} \right) NA \quad (2.20)$$

where λ is the wavelength of the light being launched into the fiber, a the core radius and NA is the numerical aperture of the fiber. The approximations given by Equations (2.18) and (2.19) are valid for large values of V , and if $V \leq 2.405$ the fiber will only support the fundamental mode. It is important to note that since the normalized frequency V has a dependency on λ , the classification as a single-mode or multimode fiber is then relative to the wavelengths of the

light signals launched into the fiber for a given application, and the fiber parameters a and NA can be tweaked accordingly. Finally, for a multimode step-index fiber, the average fraction of the optical power that is guided in the cladding can be estimated as $1.25 \times M^{-0.5}$ (20).

2.3 Specialty optical fibers

There is not a closed definition of what constitutes a specialty optical fiber, rather the term is used as a “catch-all” for any fiber that deviates from the more standard fiber structures described in the previous section. These deviations can be related to the materials used in the fiber fabrication, such as modified SiO_2 glasses doped with fluorine for deep UV fibers (23), tellurite glass fibers for supercontinuum generation (24) and mid-IR transmission (25), among other materials (26,27), or fibers with liquid cores (28) and gas-filled hollow-core fibers (29). Another “class” of specialty fibers are fibers with non-standard geometries, such as D-shaped fibers (30) (Figure 6, left), tapered fibers (31) (Figure 6, right), and multi-core fibers (32).

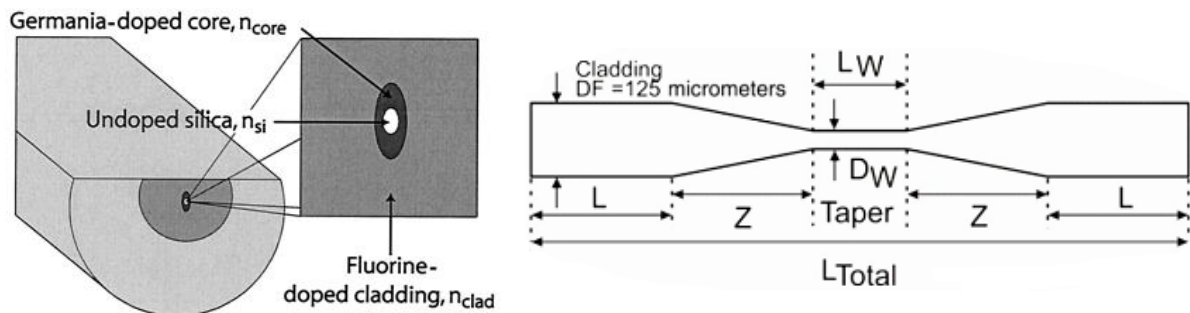


Figure 6 – Left: Cross-section drawing of a D-shaped optical fiber (30); Right: Schematic drawing of a fiber optic taper, adapted from (31).

Perhaps the most well-known specialty fibers are Photonic Crystal Fibers (PCFs), also known as “holey fibers” or “microstructured fibers”. PCFs are optical fibers in which the cladding contains several air holes to allow guidance on single-material pure silica fibers – although nowadays PCFs with other materials (33-35) have also been demonstrated – or in fibers with hollow cores. The concept of using air holes in the cladding to produce single-material silica fibers started being explored only a few years after the demonstration of the first low-loss glass fibers, and in 1974 Kaiser & Astle (36) developed a pure fused silica fiber where

the core is surrounded by big airholes and supported by very thin glass bridges (Figure 7), this concept is now usually referred to as Suspended Core Fibers (37).

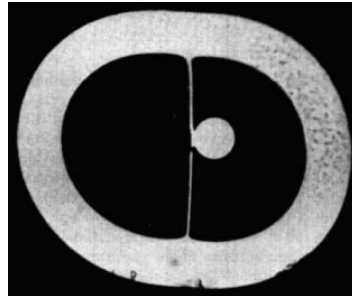


Figure 7 – Cross-section of a single-material fiber with the core suspended in air by thin glass bridges (36).

The term “photonic crystal fiber” itself was only coined in 1996 by Knight *et al.* (38) when reporting a new undoped all-silica optical fiber with a solid core surrounded by a cladding containing several small air holes in a hexagonal pattern (Figure 8). Although the entire fiber was fabricated in single-material pure silica, light is still guided in the core since the presence of the air holes lowers the average refractive index in the cladding region (38). In contrast with these “index-guided” PCFs, the careful arrangement of cladding air hole pattern allows for hollow-core fibers in which the core, also an air hole (albeit of a larger diameter), supports the guidance of light through the photonic bandgap effect or anti-resonance, *i.e.*, the periodic structure of the cladding effectively acts as a cylindrical Bragg mirror that does not allow light with certain wavelengths to leave the core (39-41). Figure 9 is a side-by-side comparison of scanning electron micrographs of an index-guided PCF (left) and a photonic bandgap PCF (right). As PCF design possibilities are virtually limitless, microstructured fibers have been shown to exhibit varied interesting properties such as single-mode guidance for all wavelengths (42), guiding in the terahertz regime (43) and near zero group velocity dispersion (44).

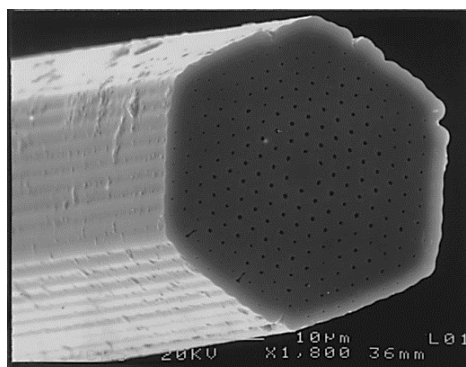


Figure 8 – Scanning electron micrograph of the first reported photonic crystal fiber (38).

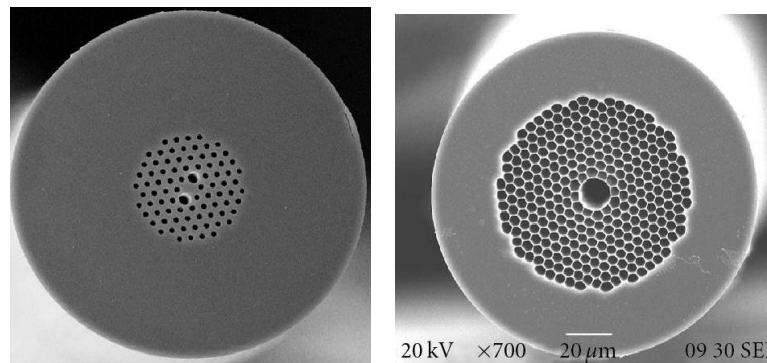


Figure 9 – Scanning electron micrographs of an index guided PCF (left) and photonic bandgap hollow-core PCF (41).

Fabrication of specialty fibers and PCFs is typically achieved by fiber drawing methods, where a “preform” – a larger diameter precursor with roughly the same geometry as the final desired fiber – are fed into a high-temperature furnace to be made malleable and are then drawn (pulled) out at a constant speed. By adjusting the preform feed speed and the drawing speed the final diameter of the fiber can be tweaked (20,21). Preforms for PCF fabrication can be prepared by extrusion (45), sol-gel casting (46), injection molding and drilling (47), 3D printing (48), or most commonly by stacking glass rods and capillaries inside a larger diameter tube (49) as shown in Figure 10.

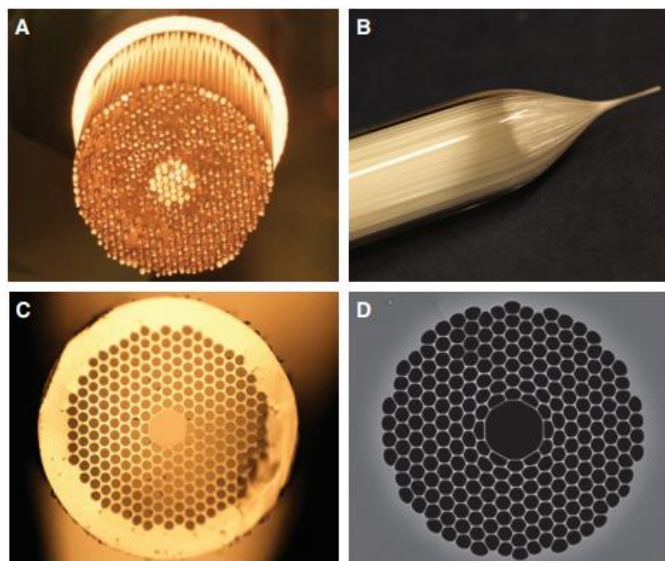


Figure 10 – Fabrication of a bandgap hollow-core fiber by the “stack and draw” method. A: primary preform obtained by stacking glass capillaries; B: first stage drawing of the preform into a “cane” of a few mm in diameter; C: optical image of the cross-section of the cane; D: micrograph of the finalized fiber (49).

3 OPTICAL FIBER SENSORS

Due to the great flexibility potential on the fabrication of optical fibers, as discussed in the previous chapter, optical fiber sensors (OFS) is an incredibly extensive field of research and several books can be written only on the fundamentals and introductions (18,50,51) on each branching subject of the topic in question.

Optical fibers can be used as sensors whenever a fiber is designed so that a physical, chemical or other variable of interest can be made to produce a repeatable and quantifiable modulation of the light guided in the fiber, be it an intensity modulation, phase modulation, modal energy redistribution, polarization changes or spectral shifts (18,50,51). Applications wise, several OFS have been successfully demonstrated for chemical and biological sensing (52), strain and temperature sensing (53), smart structures and structural health monitoring (19,54), refractive index sensing (55), electrical current sensing (56), magnetic field sensing (57), microfluidics applications (58), vibrations and displacement sensing (59), etc.

The ever-increasing prevalence of OFS displacing more traditional electronic sensors is not only due to their design flexibility, but most importantly due to inherent advantages such as their compactness, immunity to electromagnetic interference, high multiplexing capabilities and presenting no electrical safety concerns (18,50,51). It is also worth noting that when selecting the optical fiber material for sensing applications, compared to glass fibers the polymer optical fibers (POF) tend to be cheaper, easier to handle, are more flexible (able to withstand strains in excess of 30% without breakage), and present a much higher elastic limit (10%) in comparison to glass (1%), for the tradeoff of significantly higher transmission losses and more restrictive operating temperature and humidity conditions (60).

3.1 Intensity based optical fiber sensors

As the name indicates, these kinds of OFS are based on modulating the intensity of light that is transmitted down, or reflected back, an optical fiber. They tend to be simpler and historically find applications for mechanical measurements (18,61), such as displacement by

placing an optical fiber in front a movable reflecting surface and measuring the back-reflected intensity as a function of the distance between the fiber and the surface (Figure 11, left) or by sandwiching the fiber between movable corrugated surfaces that push on the fiber leading to transmission losses by the formation of microbends (Figure 11, right) (61).

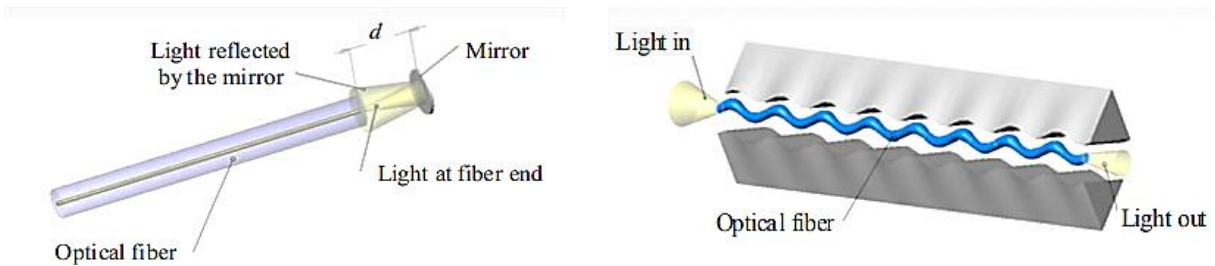


Figure 11 – Intensity-based fiber optic displacement sensors. Left: Probe based on intensity of light reflected back into a fiber by a mirrored surface. Right: Probe based on transmission losses caused by microbending. (61).

More recently intensity-based probes have seen renewed interest for biosensing applications by incorporating luminescent or selectively light absorbing materials that respond to biochemical compounds (62). Biochemical sensing and nanofluid characterization have also been realized using quasi-elastic light scattering based fiber probes (63,64). As an interesting recent example Yang *et al.* (65) demonstrated a temperature probe for chemical reactions that consists of a fluorescent $\text{Er}^{3+}/\text{Yb}^{3+}$ co-doped tellurite glass wire spliced to a single-mode fiber. When a 980 nm laser source is coupled into the fiber the co-doped glass exhibits a luminescence in the visible range with peaks at 522 nm and 544 nm, as temperature increases the intensity of the 522 nm peak diminishes and of the 544 nm peak increases (Figure 12). Temperature can be inferred by assessing the intensity ratio between luminescence peaks.

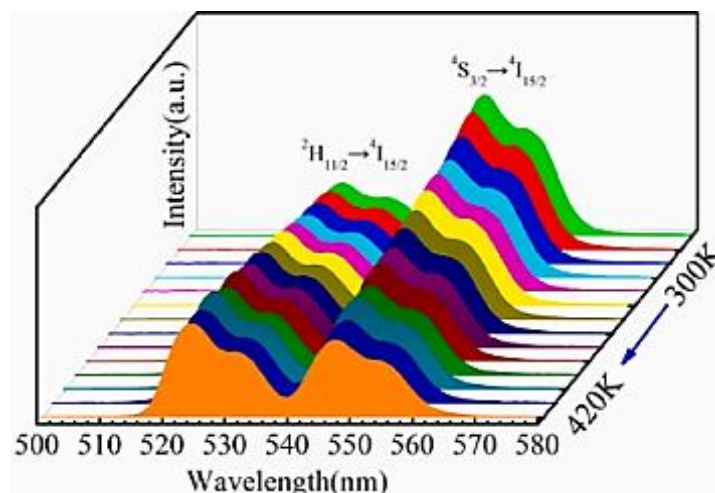


Figure 12 – Temperature dependent luminescence of doped tellurite glass excited by a 980 nm laser source (65).

3.2 Interferometric optical fiber sensors

This category is comprised of sensors based on the implementation of optical fiber interferometers. One of the most common examples are fiber Fabry-Perot interferometers (66-68), which are resonant cavities comprised of two consecutive (semi-)reflective surfaces and can be realized in optical fibers by, for example, creating an air gap between two pieces of optical fiber encapsulated in a glass capillary (Figure 13, left), or creating an air gap between the tip of an optical fiber and a flexible membrane (Figure 13, right).

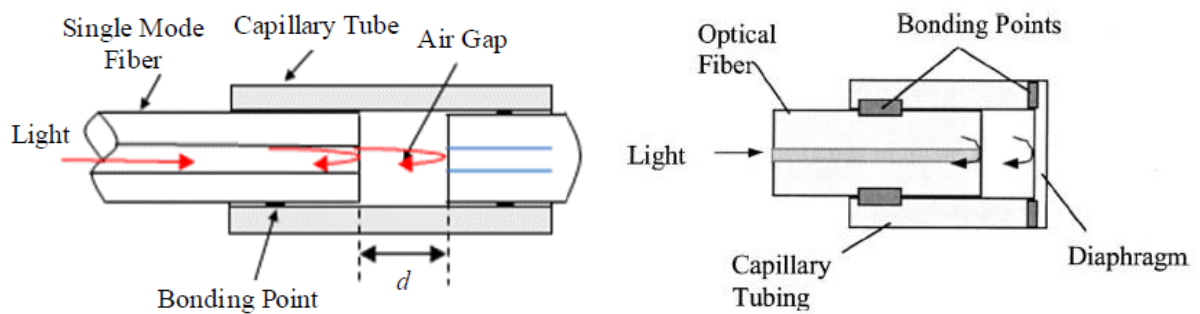


Figure 13 – Two realizations of fiber Fabry-Perot interferometers. Left: Air gap between two fiber pieces in a capillary tube (66). Right: Fiber tip Fabry-Perot interferometer with a flexible diaphragm (67).

When a broadband light source (Figure 14, left) is coupled into the fiber, the output of the fiber Fabry-Perot, which can be interrogated both in transmission or reflection, exhibits a series of transmission/reflection peaks and valleys (Figure 14, right). Using Equation (3.1), the length d of the Fabry-Perot cavity can be determined from the wavelength of two consecutive peaks or valleys, λ_1 and λ_2 , of the output spectrum (68).

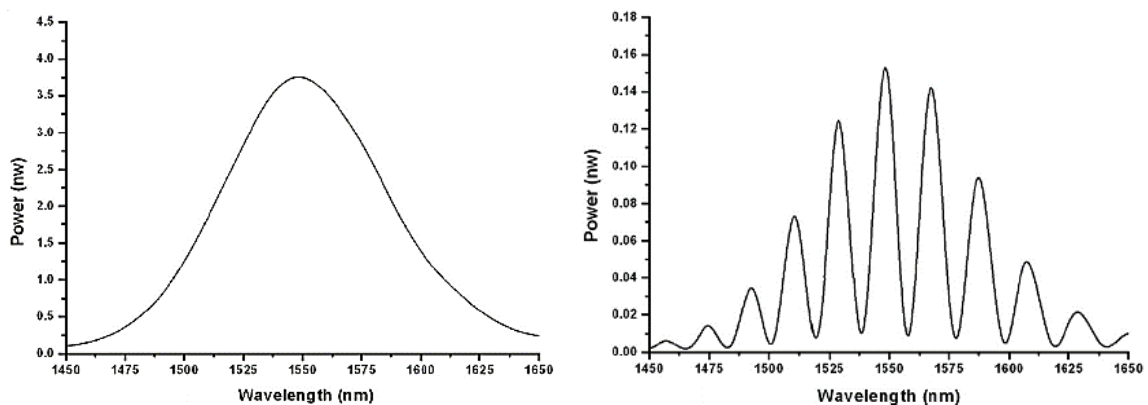


Figure 14 – Left: Spectrum of a broadband light source coupled into a fiber with a Fabry-Perot interferometer. Right: Output reflection spectra of the fiber interferometer (68).

$$d = \frac{\lambda_1 \lambda_2}{2(\lambda_2 - \lambda_1)} \quad (3.1)$$

Through monitoring changes in the cavity length d it is possible to use the fiber Fabry-Perot interferometer as a strain, temperature, pressure or displacement sensor (69). Other examples of interferometric fiber optic probes are distributed strain and temperature sensors using Mach-Zehnder interferometers with optical frequency domain reflectometry interrogation setups (70), and fiber optic gyroscopes based on the Sagnac interferometer (71).

3.3 Evanescent wave and surface plasmon sensors

As discussed previously in Section 2.2, light guided in an optical fiber is not entirely contained in the core, but part of the optical power penetrates the cladding as evanescent waves. Equation (2.17), the Bessel differential equation, must be solved for both the core and the surrounding medium, which is usually the cladding (20,21). This interaction between the guided waves in the core of the waveguide and its surroundings can be exploited for sensing applications in various ways: suspended core fibers can be used in gas and liquids sensing applications (72,73), or no-core fiber (solid single-material rods) segments can be incorporated in concatenated fiber structures (Figure 15) to allow localized evanescent wave probing of refractive index of liquids among other applications (74).

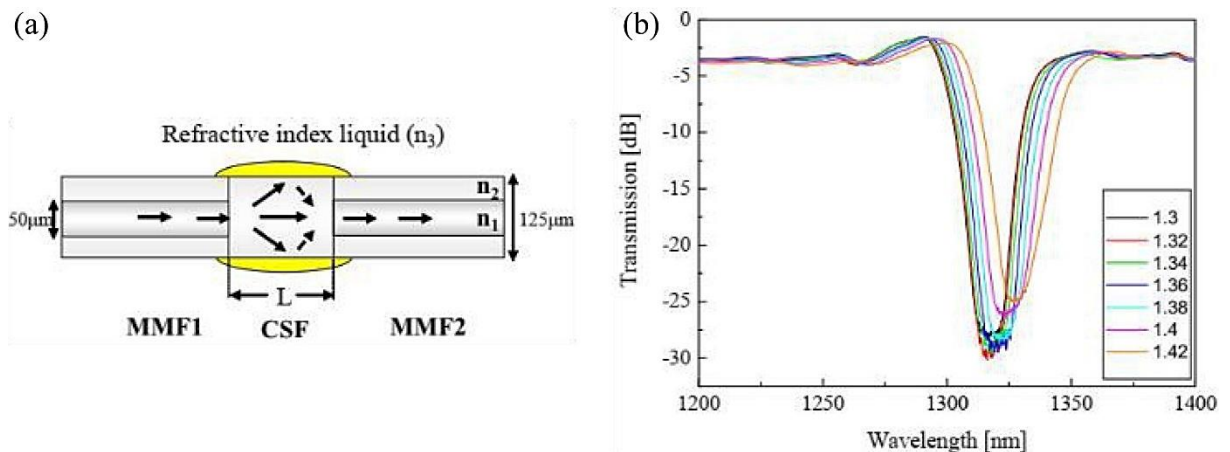


Figure 15 – (a): Concatenated multimode-nocore-multimode fiber structure for refractive index sensing. (b): Response of the sensor (in transmission) for liquids with refractive index between 1.3 and 1.42 (74).

The sensitivity and selectivity of sensors based in evanescent waves can also be augmented by making use of the surface plasmon resonance (SPR) phenomenon. In SPR fiber probes metallic materials such as gold and silver are deposited in the surface of the fiber, the evanescent waves from the waveguide interacts with the free electrons on the metal surface stimulating the emission of surface plasmon waves, which in turn creates a feedback response with the evanescent waves (74). SPR sensors have been demonstrated for multiple applications, including refractive index sensors (74), chemical sensors (75) and biosensing (76).

3.4 Optical fiber gratings sensors

Optical fiber gratings are periodic modulations of the refractive index of the fiber's core or cladding, this can be achieved by mechanical means (*e.g.* pressing on a fiber with a corrugated plate (77)) or, more commonly, photo-inscribed into a fiber due to the inherent photo-sensitivity of GeO₂ doped fibers to UV radiation (78,79). There are 3 main classifications of fiber gratings according to their period. Fiber Bragg gratings (FBGs) have a period in the order of hundreds of nanometers and act as a narrow-band spectral mirror by coupling a forward-propagating core mode to a backwards propagating one (78). Gratings with periods of the order of hundreds of μm to a few mm are referred as long period gratings (LPGs) and can couple a lower order forward-propagating core mode to a forward propagating cladding mode (leading to a heavy attenuation band) or another forward-propagating mode of a higher order (79). Finally, rocking filters are a special type of LPG, usually obtained by twisting the fiber during the grating inscription, that promotes coupling between orthogonally polarized modes (80).

Due to their simplicity, ability for being interrogated both in transmission and reflection, and high multiplexing capability, FBGs have a significantly stronger presence both in the scientific literature and commercially available end-products (18,78), and as such they will be briefly discussed in more detail in this section. Figure 16 is a schematic representation of the FBG operation principle. A broadband input source is coupled into the fiber, as light passes through the FBG a narrow-band signal is coupled in reflection, and the transmitted signal shows a dip in the same wavelength range. The peak reflection wavelength is referred as the Bragg wavelength, λ_B , and is given by Equation (3.2):

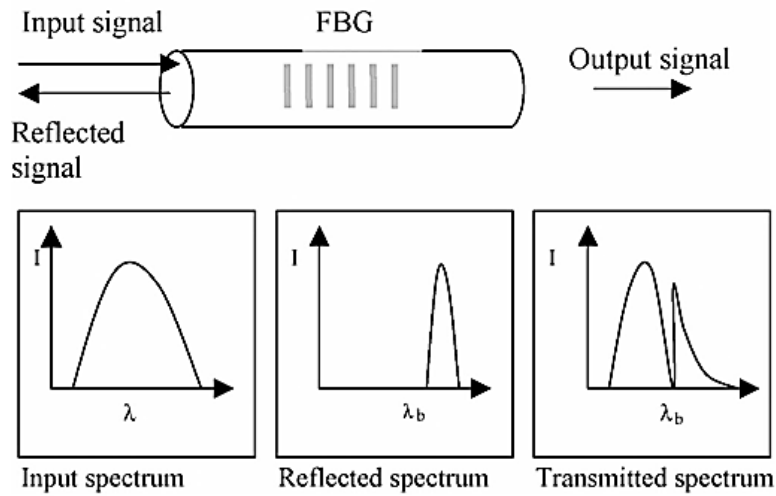


Figure 16 – Transmission and reflection spectra from an FBG (81).

$$\lambda_B = 2n_{eff}\Lambda \quad (3.2)$$

where n_{eff} is the effective refractive index for the core fundamental guided mode and Λ is the grating period (81). Mechanical or thermal loads experienced by the FBG will shift λ_B as they impact n_{eff} through the thermo-optical and photo-elastic effects, and Λ through thermal expansion and mechanical strain, so that (81):

$$\frac{\Delta\lambda_B}{\lambda_B} = (\alpha_F + \xi_F)\Delta T + (1 - \rho_e)\varepsilon \quad (3.3)$$

where α_F , ξ_F and ρ_e are the coefficient of thermal expansion, thermo-optic coefficient, and the effective photo-elastic constant of the fiber material respectively, ΔT is the temperature change experienced by the FBG and ε the applied longitudinal mechanical strain. Typical sensitivity values for GeO₂ doped silica fibers are ~ 13 pm/°C and 1.2 pm/ $\mu\varepsilon$ (81).

As they are sensitive to both mechanical strain and temperature, FBGs tend to often be explored for structural health monitoring and related applications (81-83), but the temperature cross-sensitivity needs to be compensated, which is also a highly active research topic (84). While interrogation cost can be relatively high (commonly based on Optical Spectrum Analyzers), the cost per measurement point can be drastically lowered by multiplexing FBGs in a single fiber. Furthermore, low-cost FBG interrogator setups with price points as low as USD 2,000.00 are also detailed on the literature and can be assembled using readily available commercial components (85-87). For this reason, new FBG based monitoring applications were also investigated in this thesis.

3.5 Fiber specklegram sensors

A significant portion of the sensors developed in the context of this work and reported in Chapters 4 and 5 are fiber specklegram sensors (FSSs), this is owed in part to the fact that from all the fiber sensors discussed in this chapter, FSSs are possibly the ones that boast the highest combined sensing versatility and sensitivity. This is in a sense also a double-edged sword, as will be discussed in this section.

The term ‘fiber specklegram’ sensor was proposed by Wu, Yin & Yu in 1991 to formally classify an emerging type of fiber sensors in which the output intensity is subjected to relative modal phases in multimode fibers, boasting high sensitivity comparable to interferometric fiber sensors but with simpler interrogation setups (88). According to the earlier discussion in Section 2.2, the solution of the Maxwell Equations led to the conclusion that various guided modes can exist simultaneously in a multimode optical fiber. To put this in perspective, applying Equations (2.18) and (2.20) to a multimode step-index fiber with a core diameter of 50 μm (Figure 3), refractive index contrast $\Delta = 0.01$ and a λ of 633 nm returns a normalized frequency V of 51.13 and an estimated number of guided modes of $M = 1307$. All the guided modes are linearly superposed, and the spatial distribution of the complex amplitude $A(x,y)$ of the electric field obtained by the interferometric superposition of M modes over the x - y plane is given by (89):

$$A(x, y) = \sum_{m=0}^{M-1} a_m(x, y) \exp[j\phi_m(x, y)] \quad (3.4)$$

where a_m and ϕ_m are the amplitude and phase distribution of the m -th mode, the intensity $I(x,y)$ distribution of the projected fiber output is then (89):

$$I(x, y) = \sum_{m=0}^{M-1} \sum_{n=0}^{M-1} a_m a_n \exp[j(\phi_m - \phi_n)] \quad (3.5)$$

From Equation (2.14) it is evident that the output $I(x,y)$ profile, that can be perceived by the eyes or measured by a camera (Figure 17), contains information on amplitude and phase difference between guided modes, *i.e.*, the output intensity is subjected to the relative modal phases (88,89). Any disturbance to the fiber status or guiding conditions will be reflected in the solutions of the Bessel differential equations, impacting the propagation constants β that satisfy

the guiding condition, leading to changes in the number of guided modes, as well as the amplitude and phase distribution of the modes, with the ultimate consequence that the disturbance will manifest itself in the spatial distribution of $I(x,y)$ (88-90). In short, FSSs are as sensitive as interferometric based sensors to a wide array of variables that can affect the guiding conditions *simultaneously*, this confers FSSs with high versatility and sensitivity at the same pace extra care must be given to avoid cross-sensitivity with undesired variables.

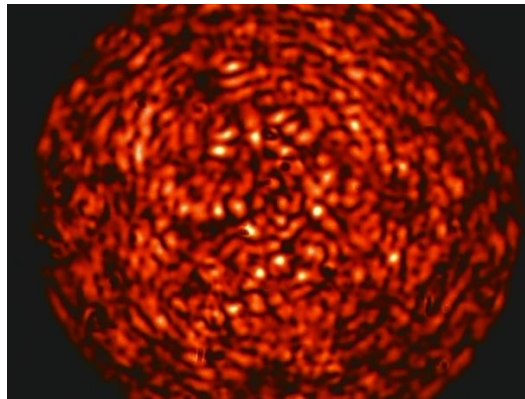


Figure 17 – Photograph of a fiber specklegram from a commercial multimode fiber. Light source is a 633 nm He-Ne laser, and the image was projected from the fiber end-face into a lens-less webcam using a 20× objective.

For the best results when working with fiber specklegram based sensors, a good speckle contrast is desirable. From Equation (3.5) and Figure 5 one can infer that the larger the number of modes supported in a fiber, the more complex and granular the speckle pattern will become. Indeed, the maximum number of degrees of freedom in a fiber speckle distribution is given by the number of guided modes M (91), and therefore the speckle contrast increases as the optical power from the laser source is coupled into a larger number of guided modes in the waveguide. It is demonstrable that as M increases, the number of speckle granules N_{sp} in a fiber specklegram steadily achieves parity with M (92), and while exciting the maximum theoretical number of modes a fiber can support is not feasible in practice, introducing misalignments in relation to the core when launching light into the FSS and using mode scramblers helps maximize the number of excited modes (92,93).

Measuring with FSSs is realized by quantifying the change in $I(x,y)$ caused by the variable of interest by comparing specklegrams for various fiber states. Different techniques for tracking the specklegram changes are currently available, including statistical analysis (90), morphological image processing (94), entropy analysis (95), machine learning (96), and correlation metrics (89). In particular, the latter has comparatively simpler implementation, allows for low cost experimental setups and is capable to quantify subtle deviations in the output

speckle pattern, yielding improved response as achieved by, for example, the normalized inner-product coefficient NIPC (97) and the zero-mean normalized cross-correlation coefficient ZNCC (89). FSSs have been successfully demonstrated for various applications such as structural health monitoring, tactile sensors, security and surveillance, measuring displacement, vibration, viscosity, strain, heart rate, among others (98-103).

In this thesis, specklegram images and videos will be analyzed using correlation coefficient Z of the Zero Mean Normalized Cross-Correlation (ZNCC), defined as (89):

$$Z = \frac{\sum \sum (I_0 - \bar{I}_0)(I - \bar{I})}{[\sum \sum (I_0 - \bar{I}_0)^2 \sum \sum (I - \bar{I})^2]^{1/2}} \quad (3.6)$$

where I and I_0 are the 2D intensity map for the fiber subjected to a load and in the reference condition respectively, while \bar{I} and \bar{I}_0 and the average intensity for each of those maps respectively. While many other correlation metrics could be adopted for this, such as the NIPC or the phase-only correlation (POC), ZNCC was chosen as it demonstrably has equivalent performance to the other competing metrics but with the advantage of being insensitive to intensity fluctuations of the laser source, making it more robust (89,97).

Despite the robustness advantage, it is important to highlight that ZNCC is subject to the limitations expected for normalized correlation metrics. The values returned by Equation (3.6) are limited between 1 and 0 which can lead to a limitation of a sensor's dynamic range due to the saturation of the metric, and, as Z is returning a similarity score between random-like patterns, the response curve of Z to a variable of interest is expected to be non-linear. To avoid this issue, the extended-ZNCC (EZ) metric will be used in this work to analyze some specklegram datasets. EZ is a non-saturating metric defined as (104):

$$EZ = Z_0 \mp \left\{ \frac{\sum \sum (I_0 - \bar{I}_0)(I - \bar{I})}{[\sum \sum (I_0 - \bar{I}_0)^2 \sum \sum (I - \bar{I})^2]^{1/2}} - 1 \right\} = Z_0 \mp (Z - 1) \quad (3.7)$$

in which Z_0 is a cumulative offset. Every time the calculation of Z crosses a pre-set threshold τ , the current value of Z gets appended to Z_0 , the last load state specklegram I is set as the new reference state I_0 and calculations resume. This process is repeated until the dataset is fully processed resulting in a continuous EZ curve with no upper or lower boundary. The plus or minus sign is there so the value of EZ can be set to either increase or decrease to better pair the behavior of the metric with that of the variable affecting the specklegram probe (104).

4 SENSORS BASED ON GLASS FIBERS

Optical fiber sensors developed in the context of this thesis that were fabricated from glass preforms are compiled in this chapter. Several research papers have been either published or submitted for publication based on the work presented here, namely references (105) and (106) pertaining to Section 4.1, (107) for Section 4.2, (108) and (109) for Section 4.3, and (110) for Section 4.4. Figures in this chapter are for the most part reused or adapted from the listed publications. Additional information and figures not included in the published manuscripts (due to article length restrictions, for example) may also be presented, deepening further the discussion on these sensors.

4.1 Specklegram based monitoring of evaporation inside capillary-like optical fibers

Measuring evaporation in microchannels and capillary structures is relevant in several applications, such as in evaporative cooling devices and porous coating technologies (111,112). Optical fibers can be used as a medium for carrying and analyzing fluids via microchannels intrinsic to the fiber. Even though liquid sensing with fiber devices such as Photonic Crystal Fibers is a prolific research topic (113), a simpler approach based on capillary-like fibers can be used (114,115). Here, a new approach for monitoring the evaporation of a liquid inside a capillary-like fiber is discussed. The fiber was filled with the fluid sample and light launched into the capillary wall. Light travels down the capillary and interacts with the fluid, producing changes in output fiber speckle pattern that was then processed in order to retrieve the displacement of the air/liquid interface.

4.1.1 Materials and methods

The probe consisted of a hollow glass capillary tube with an outer diameter of $\sim 250 \mu\text{m}$ and inner diameter of $\sim 200 \mu\text{m}$ (Figure 18a). It was drawn from a $6 \times 3 \text{ mm}$ industrial grade fused silica tube preform. Drawing parameters were furnace temperature $1902 \text{ }^\circ\text{C}$, preform feed

speed 1.5 mm/min and drawing speed 0.80 m/min. A constant manometric pressure of 0.4 kPa was maintained inside the tube by injecting inert argon gas to prevent the walls from collapsing.

A piece of the capillary fiber approximately 55 mm long was filled with fluid by attaching it to a hypodermic needle and syringe containing water with red food coloring. To avoid unwanted loss of fluid by leakage or evaporation both sides of the glass capillary fiber were sealed by injecting and hardening photocurable resin, as shown in Figure 18b.

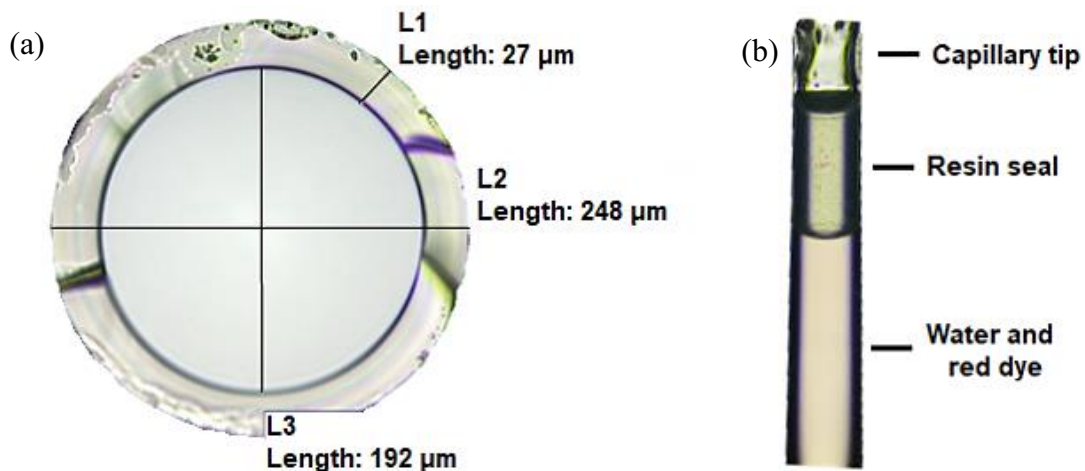


Figure 18 – Optical microscope images of (a): a sample of the capillary fiber, and (b): resin sealed capillary filled with water and red dye.

A schematic of the experimental setup is depicted in Figure 19. Light from a He-Ne laser source ($\lambda = 633 \text{ nm}$) shone through a neutral density filter (NDF) and was directed to the sensing fiber by the mirrors M1 and M2. Objective lenses L1 (20 \times) and L2 (40 \times) were mounted on precision translation stages and launched the light into the sensing fiber as well as focused the output speckle pattern into the exposed CCD of a webcam. A microscope was used to monitor the movement of the liquid inside the sensing fiber. Both the webcam and the microscope camera were connected to a computer via USB cables for data acquisition. Figure 20a is a picture of the air/liquid interface as seen by the microscope, and Figure 20b is the projection of the output fiber specklegram as captured by the webcam. Specklegram video was captured in AVI format, 15 fps and 800 \times 600 pixels resolution.

With an average wall thickness of 25 μm and proper choice of the filling fluid for refractive index contrast with glass, the capillary behaves as a highly multimode waveguide for the light from the He-Ne source. The guided modes interact with the fluid through evanescent waves, and as the liquid/air interface moves inside the capillary the output specklegram changes in response to the dynamically shifting guiding conditions. Changes to the specklegram were

quantified by evaluating the ZNCC from a 200×200 pixels window slightly off-centered in relation to the capillary wall thickness (dashed-line yellow rectangle in Figure 20b).

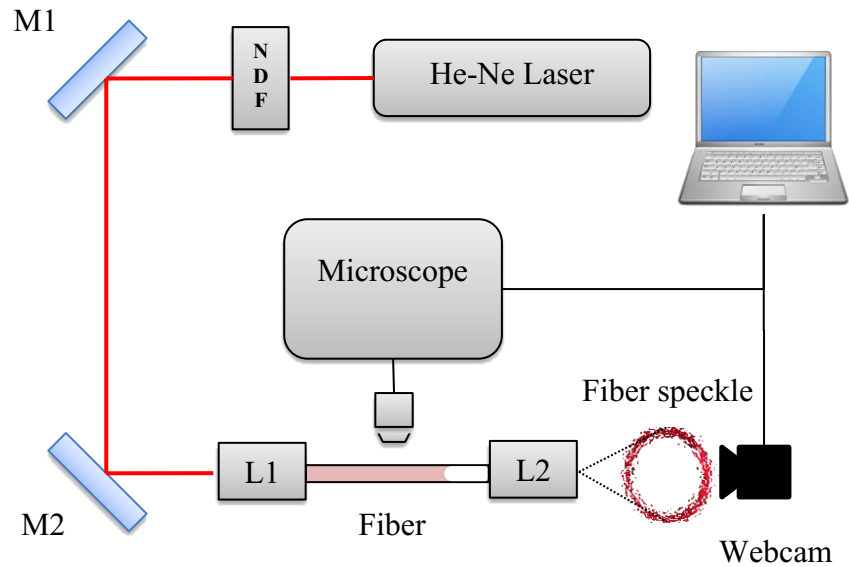


Figure 19 – Schematic of the experimental setup, a frame of the captured specklegram video is shown to the right along with a representation of the analysis window for the calculation of ZNCC. NDF = neutral density filter; M1/M2 = mirrors, L1/L2 = objective lenses (105).

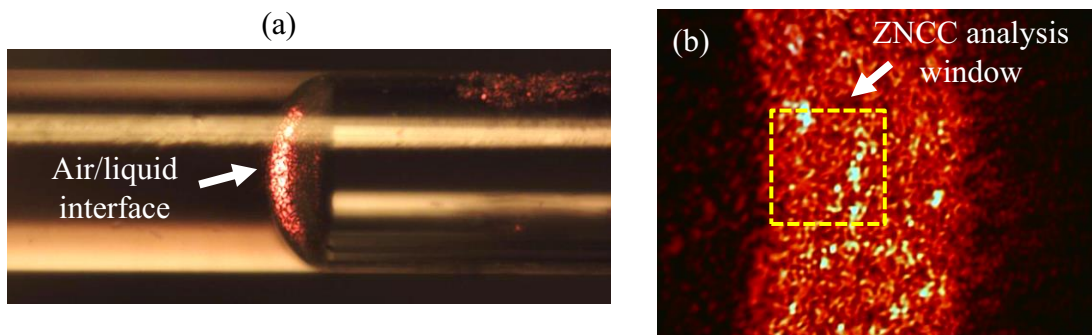


Figure 20 – (a) Image of the liquid filled capillary fiber showing the air/liquid interface as observed by the microscope. (b) Observed output specklegram as captured by the webcam, dashed yellow rectangle represents the 200×200 pixels ZNCC analysis window.

The He-Ne laser was let stabilize for about an hour before starting the experiments. One of the sealed extremities of the sensing fiber containing a liquid of interest was then cleaved out and the fiber carefully placed between the lenses, open side facing the webcam. A LabVIEW routine was used to capture and save images of the meniscus with the microscope camera. Overlays for image count and a scale for measuring the movement of the meniscus were also included in the LabVIEW routine.

4.1.2 Results and discussion

First the temporal evolution of the correlation coefficient Z for a capillary filled with air and one filled with fluid were compared to determine if the probe is indeed sensitive to the displacement of the liquid/air interface, this comparison is shown in Figure 21a. Without the filling liquid Z is very stable and remains higher than 0.995 (solid black line, the small initial dip at $t = 0$ seconds from $Z = 1.00$ is due to the webcam video capture noise), that is, guiding conditions remain constant and so does the output specklegram. A clearly distinct behavior was observed for the liquid filled capillary (red line), with Z steadily decreasing with time, demonstrating the probe produces a direct response to the evaporation of the filling fluid.

The general behavior of Z in relation to the displacement (Δx) of the liquid/air interface can be observed by plotting both Z and Δx over time (t) in the same graphic. This is shown in Figure 21b for a Δx of 40 μm over a Δt of 450 s. As can be observed, Z exhibits a fairly linear response over time with good correspondence to Δx . Note that Δx is the relative displacement observed during the timespan of a single experiment, and not the absolute position of the air/liquid interface in relation to the unsealed tip of the capillary, with Z computed accordingly.

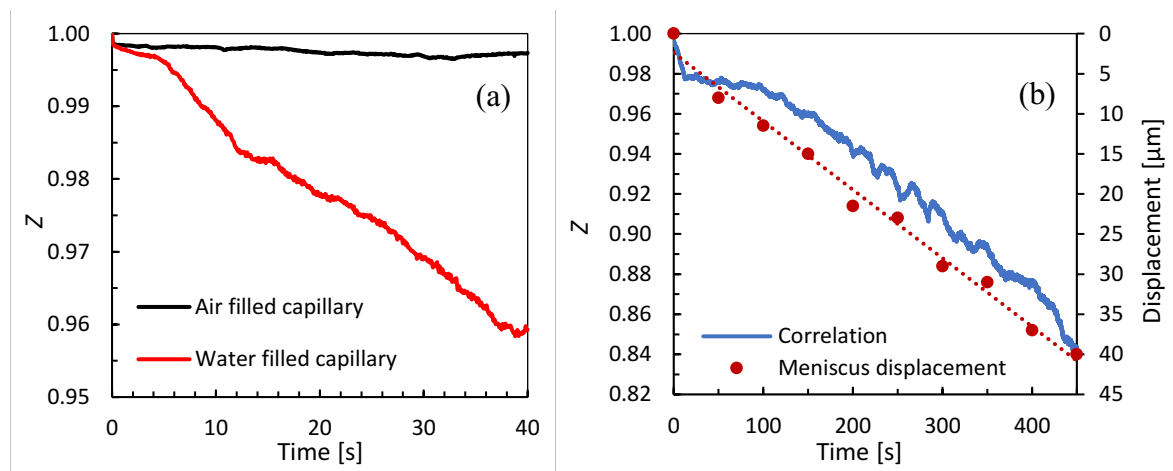


Figure 21 - (a): Comparison of the Z curve over time for an air-filled capillary and a water filled capillary. (b): Combined displacement and Z data over time up to a maximum displacement of 40 μm , dashed red line is a linear fit of the displacement data (105).

Several more tests were performed in sequence for Δx values of 20, 30, 40 and 50 μm , two repetitions per Δx value for a total of 8 experiments. The results are presented in Figure 22. Finally, by taking the average final Z value for each set of tests in Figure 22 it is possible to plot Z as a function of Δx in Figure 23.

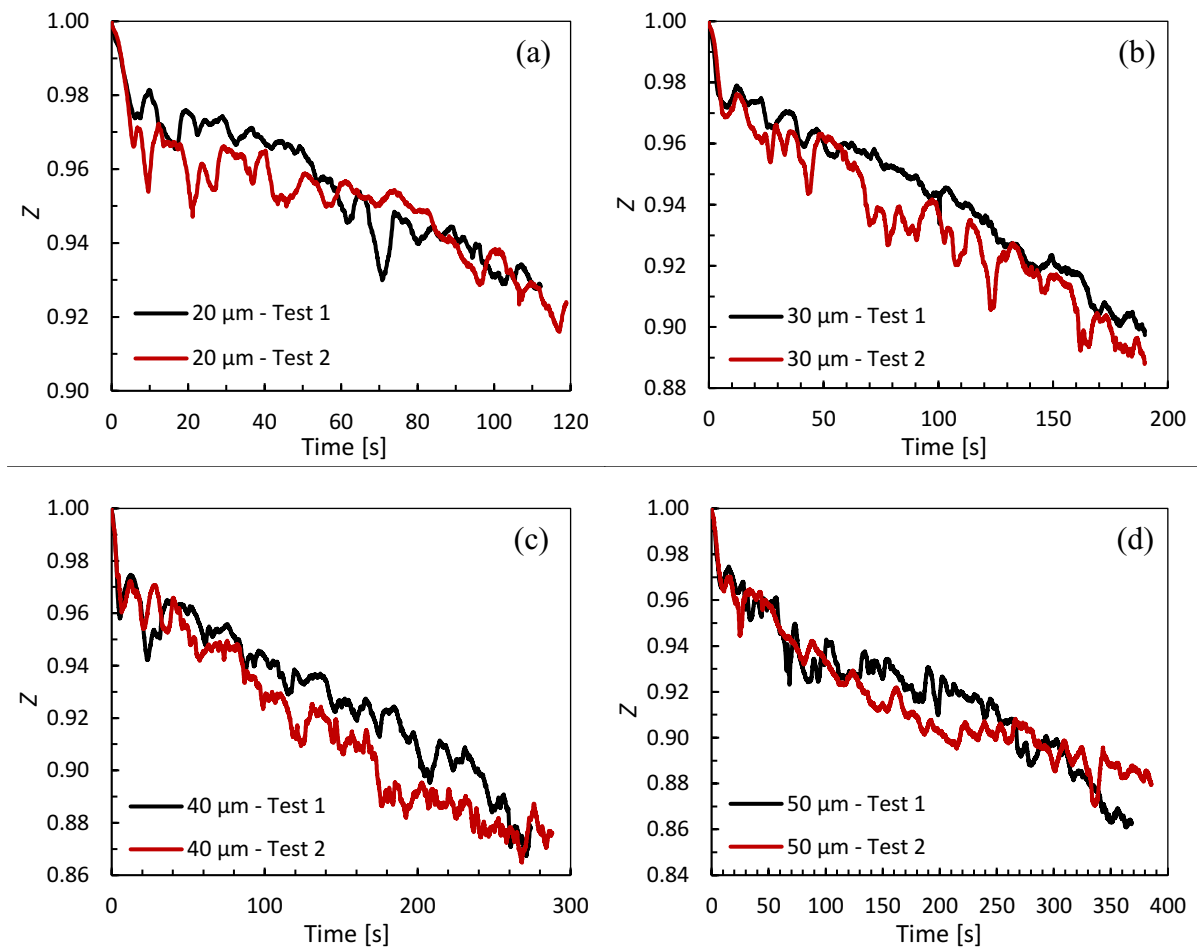


Figure 22 – Z over time for displacements Δx up to (a): 20 μm , (b): 30 μm , (c): 40 μm , and (d): 50 μm (105).

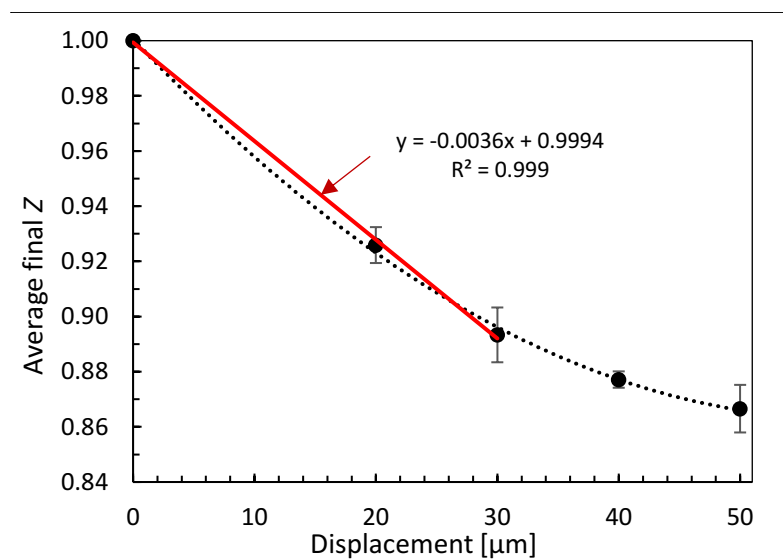


Figure 23 – Average Final Z as a function of displacement. Dashed black line is a guide to the eyes, solid red line is a linear fit ($R^2 = 0.999$) of the for the 0 μm to 30 μm range (105).

As is evident in Figure 22, the correlation curves are fairly noisy, but have well defined slopes with Z decaying in a linear like fashion with Δx . Specklegram probes are sensitive to any changes in guiding conditions, so factors like imperfections in the capillary geometry, water microdroplets attached to the inner surface of the capillary, possible interactions of higher order guided modes with water vapor inside the microtube and localized evaporative cooling can all affect the specklegram in hard-to-quantify ways. One more detail of note is that even though the analysis window for ZNCC calculations was placed nearer to the inner wall of the capillary, some response to interactions between the guided modes and the external medium of the probe are also expected.

Despite the non-linear response observed for the full 0 – 50 μm tested Δx range in Figure 23 (dashed black line), when limiting the analysis to the 0 – 30 μm Δx range the response is linear (red solid line, $R^2 = 0.999$), exhibiting a sensitivity $S = -3.6 \times 10^{-3} \mu\text{m}^{-1}$. Assuming a Z resolution of 5×10^{-3} (89), the limit of detection in the linear response range is then 1.4 μm .

One possible solution to improve the stability of the probe's response and shield it from external factors is to introduce a Germanium doped glass rod fixed to the inner wall of the glass microtube, as illustrated in Figure 24.

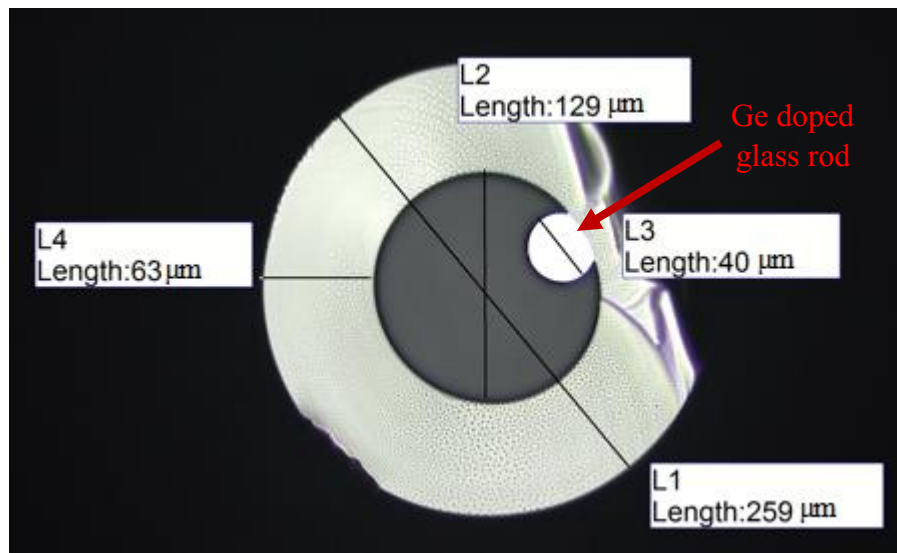


Figure 24 – Optical microscope image of a capillary-like optical fiber with a Ge doped glass rod of $\sim 40 \mu\text{m}$ in diameter attached to its inner wall.

Just as a regular optical fiber, the refractive index contrast between fused silica glass and Ge doped glass will prevent light launched in the Ge doped rod from leaking into the glass tube, strongly limiting the interaction between guided modes and the external medium to the

interface between the rod and the fluid contained inside the capillary. As of the writing of this document prototypes of this modified probe (such as the one in Figure 24) have been fabricated but there was not yet an opportune moment to conduct extensive laboratory testing.

4.2 Fiber specklegram chemical sensor based on a concatenated fiber structure

Even though the assessment of liquid samples with optical fiber sensors can be accomplished by means of several techniques, including all-fiber reflectometers (116), fiber Bragg gratings (117), long-period gratings (118), surface plasmon resonance (119), multimodal interferometers (120), tapers and microfibers (121), and photonic crystal fibers (122), most of these approaches rely on complex fabrication procedures and expensive interrogation schemes.

Currently, a few examples of fiber chemical sensors based on the speckle field analysis have been reported. In (123) a multimode-single-mode-multimode (MSM) hetero core structure was designed so the refractive index of the surrounding medium modulates the fiber modes guided through the single-mode fiber (SMF) cladding, affecting the output specklegram. Another approach consists of using a no-core fiber (NCF) fiber as the sensor probe: since the number and the average size of light speckles depend on the fiber numerical aperture, the external refractive index can be estimated by specklegram morphological analysis (92). Biochemical measurements can also be carried out with a functionalized fiber taper, allowing for DNA detection by speckle field correlation (124). Ultimately, in (99) a vibration transducer was used to obtain the frequency response of a reservoir filled with the assessed sample, therefore the liquid can be identified based on its viscosity value. Nevertheless, most of these sensors present a limited response in terms of measurement range because the sensitivity drastically decreases as the refractive index of the sample deviates from the fiber one.

In this context, an optical fiber specklegram chemical sensor based on a concatenated multimode-no-core-multimode (MNCM) structure is presented here. The modal interference in the NCF section depends on the refractive index of the surrounding liquid, so the output speckle field can be processed by correlation techniques to retrieve information regarding the sample properties, such as refractive index, temperature, and liquid level. Conversely to the previous works (125), in this study the MNCM structure is interrogated based on the speckle field analysis instead of the transmission spectrum, presenting improved sensitivity and dynamic

range, and requiring simpler instrumentation. Furthermore, as the proposed sensor explores the light interaction in the NCF section rather than the cladding of a single-mode fiber (123), the coupling efficiency between the higher-order modes of the NCF exposed to the surrounding media and the core-propagating modes of the output multimode fiber is higher, therefore the specklegram is more sensitive to the external refractive index differences.

4.2.1 Materials and methods

Consider the MNCM structure depicted in Figure 25, formed by a pair of multimode fibers (MMF) – with core and cladding radii and refractive indexes a , b , n_1 and n_2 , respectively – connected to a NCF fiber (refractive index n_2 , radius b , and length L). The light from the MMF1 core is coupled to the NCF section, so a number of modes M_{NC} are excited depending on the NCF radius b , the surrounding refractive index n_3 , and the wavelength λ . For a fiber supporting a large number of modes and assuming that the power is equally distributed to all modes, M_{NC} can be estimated for a step-index fiber by Equation (2.18). The excited modes in the NCF segment are coupled to the core and cladding modes of the MMF2 fiber. Neglecting the contribution of the cladding modes and the reflections in the NCF-MMF2 interface, and assuming that the fibers are in the absence of vibration, bending, and temperature variations, the changes in the specklegram produced by MMF2 can be correlated to the external index n_3 experienced by the NCF section.

The MNCM structure was fabricated by joining a 125 μm diameter no-core fiber (drawn from a pure silica rod) to a pair of step-index MMF (62.5/125 μm core/cladding diameters, ~ 2 m length) using a Fujikura 12R fusion splicer. The transmission spectra were evaluated with a supercontinuum white light source (SuperK Compact, NKT Photonics) by means of an optical spectrum analyzer (OSA AQ-6315, Yokogawa) for NC section lengths ranging from 30 to 60 mm and the fiber surrounded by the air ($n_3 \approx 1$). As observed in Figure 26, the resonance dips produced by the multimodal interference (MMI) experience a blue shift as the NCF length L increases. The rejection wavelength values λ_d do not exactly match the values reported in (125) probably due to differences in the MMFs core dimensions and deviations in L , but the trends of the curves corroborate the reference. In particular, the dip observed at 1454 nm for $L = 60$ mm is related to the reimaging of the MMI.

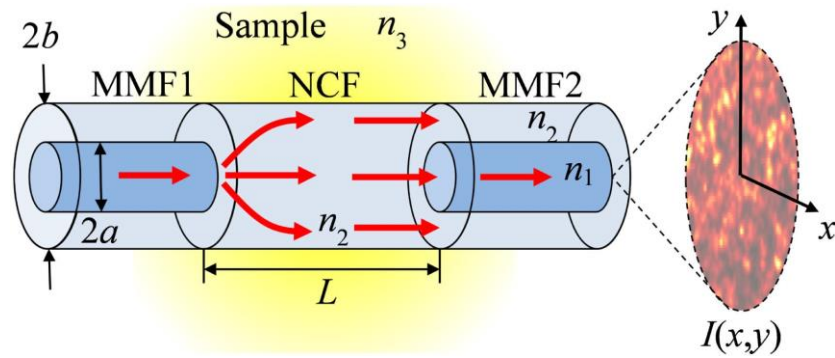


Figure 25 – Schematic of the MNCF structure. Light from the MMF1 fiber core is coupled to the NCF section, where the MNC modes are excited as a function of the sample refractive index n_3 . Part of the light is coupled to MMF2 core, resulting in an output specklegram $I(x, y)$ which is processed to retrieve sample properties (107).

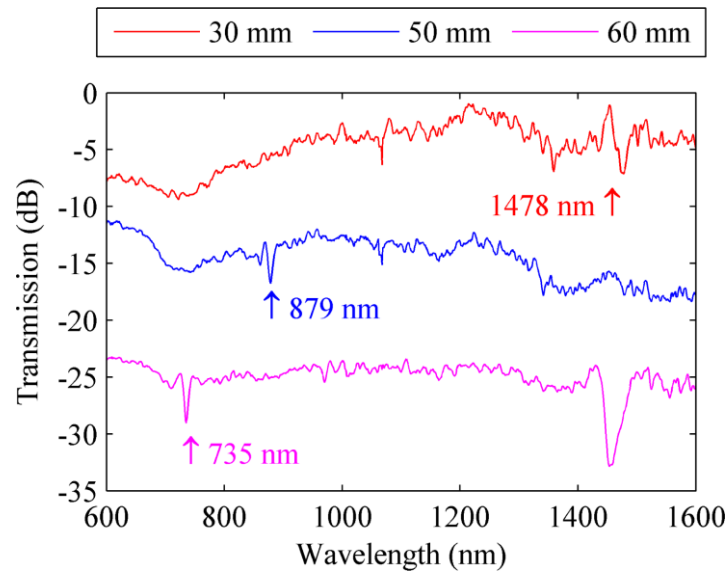


Figure 26 – Transmission spectra of the MNCF fibers in the air for different NCF lengths. The spectra were offset for the sake of visualization (107).

Variations in the external refractive index affect the coupling between the NCF modes to the core and cladding modes of MMF2, changing the magnitude and wavelength of the rejection dips. At the resonance, the output field of the NCF is characterized by an intensity halo in the borders of the waveguide, indicating that most of the light is transmitted as evanescent modes, which are more sensitive to n_3 but reduces the coupling efficiency between the NCF and the MMF2 core (125). On the other hand, since no significant dips were observed at ~ 633 nm for the tested NCF lengths, the speckle field changes in response to n_3 can be related to variations in the beat length, given that L is fixed (126). In practice, even though the specklegram experiences the effect of MMI, in the proposed MNCF setup the sensing principle is more associated to the modulation of MNC by n_3 , as it directly influences the number of

modes that are effectively coupled to the MMF2 core. With respect to the probe length, albeit the use of longer NCF segments can increase the physical contact with the liquid refractive index, thus theoretically improving the sensitivity, in practice it is preferable to choose shorter NCF fiber sections because the exposed fiber segment is too susceptible to the extraneous variables such as temperature and vibration, making the system less robust and difficult to implement. Therefore, all experiments were conducted with an $L = 30$ mm NCF.

The specklegram images obtained during experimentation were converted to grayscale and reduced to a square 201×201 pixels region-of-interest (ROI) for removing the speckle boundary effects. Next, the ROI was denoised by a 2D wavelet transform using the Daubechies db4 function, and finally the specklegram changes were evaluated with the ZNCC by routines developed in MATLAB. All experiments were conducted at room temperature, with the system mounted on a vibration-free table and in the absence of external illumination.

4.2.2 Results and discussion

An important feature of hetero-core structures is the ability to change their spectral response proportionally to the ratio of fiber length surrounded by the analyzed liquid, making such devices effective for continuous level measurements (127). In order to investigate the specklegram sensor response, the optical fiber was placed inside a 10 mm diameter, 60 mm height cylindrical vessel by maintaining the waveguide straight in vertical orientation, as illustrated in Figure 27a. The output near-field specklegram from the MMF2 is expanded with another objective ($20 \times$ magnification, $NA = 0.40$), and then is detected by a CCD camera (uEye IDS UI-2230SE-C HQ, 1024×768 pixels resolution, 15 fps).

DI water was carefully supplied by means of a micropipette to gradually submerge the NCF section and the experiments were repeated 5 times by varying h from 0 to 30 mm in increments of 3 mm. The ZNCC was evaluated by choosing the reference status I_0 as the NCF section in the air ($Z_0, h = 0$ mm) or completely immersed in water ($Z_L, h = 30$ mm). As observed in Figure 27b, the correlation coefficient increases as the liquid level approaches the reference condition, and even though the sensor response is not linear within the full range, it is possible to combine information from Z_0 and Z_L curves to retrieve h . The maximum sensitivities are $dZ_0/dh = (4.90 \pm 0.76) \times 10^{-2} \text{ mm}^{-1}$ (~ 0.20 mm resolution) for the $0 \leq h \leq 15$ mm range, and $dZ_L/dh = (4.70 \pm 0.66) \times 10^{-2} \text{ mm}^{-1}$ (~ 0.21 mm resolution) for $15 < h \leq 30$ mm. For comparison,

multi-modal interferometers assisted by FBG have been reported with < 0.1 mm resolution and linear response for 50 mm range (127,128), but such approaches demand additional fiber processing and more complex interrogation systems.

The difference in the surrounding media caused by the fiber immersion fraction generates a physical discontinuity in the waveguide. The dissimilar NCF sections work as a pair of modal filters, each transfer function corresponding to the NCF subjected to the air or to the liquid, in which the maximum number of guided modes depends on n_3 and the immersed length h . Indeed, the variations in the speckle field distribution occur because the liquid level defines the propagation distances and the phase changes experienced by the several modes of each NCF segment (129). Moreover, the low sensitivity regions observed at the NCF extremities ($h = 0$ and 30 mm) are due to the core's diameters mismatch in the MMF1-NCF and NCF-MMF2 couplings. The propagating light modes are not fully excited in the waveguide transitions (130), just as the effective number of modes modulated by the external media, therefore the speckle-gram changes are mitigated in comparison to the other regions, consequently, the practical level dynamic range is shorter than the NCF length L .

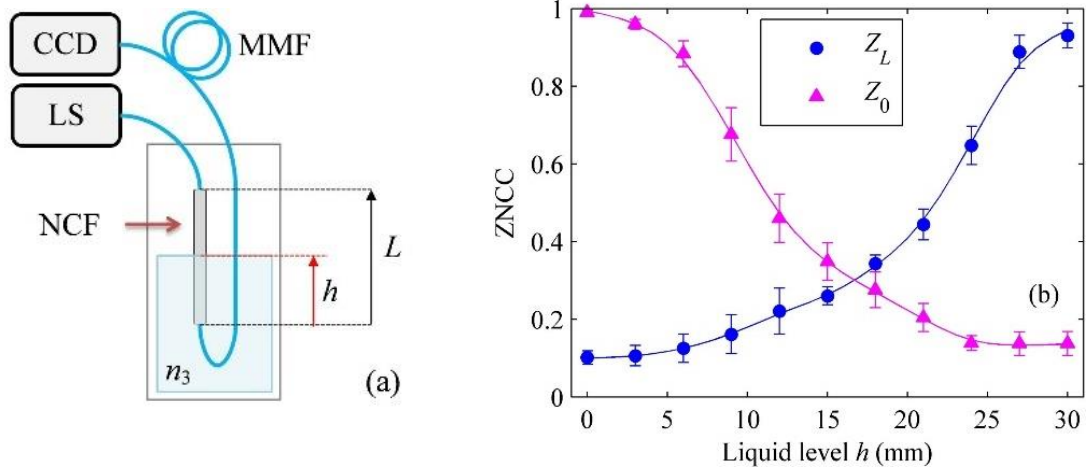


Figure 27 – Measurement of the water level. (a) Experimental setup: the no-core fiber (NCF) section of length L is immersed in the analyzed liquid of relative level h . (b) Sensor response as a function of h for the ZNCC referenced to $h = 0$ mm (Z_0) and $h = L = 30$ mm (Z_L). The solid lines are guides to the eye (107).

The evaluation of the MNCM structure sensitivity to the external refractive index n_3 was conducted by placing the no-core fiber section in a cylindrical silica glass reservoir (10 mm diameter and 70 mm length), which was filled with ethanol-DI water solutions prepared with different concentrations. The measurement setup is depicted in Figure 28. The MMF1 is subjected to a mode scrambler (a custom-made microbending transducer with 1 mm periodicity,

50 mm length, and 0.5 mm preload) for improving the power distribution, whereas the stripped, 30 mm length NCF is placed in the test environment. The liquid was gradually poured into the chamber, whereas the setup was kept static during the measurements with the fiber straight to avoid extraneous specklegram modulation. The fiber was also carefully cleaned using isopropanol between measurements and dried using a bulb blower to guarantee that the NCF section is only surrounded by the air before pouring the next sample.

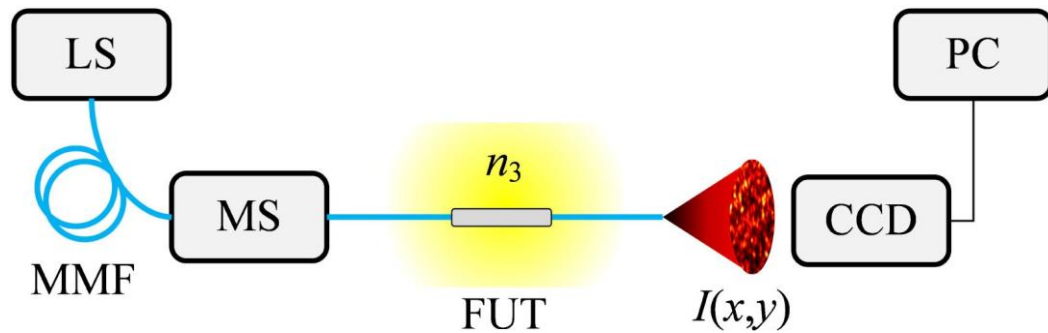


Figure 28 – Experimental setup for measuring the refractive index n_3 . LS: laser source; MMF: multimode fiber; MS: mode scrambler; FUT: no-core fiber section under test; $I(x,y)$: specklegram; CCD: camera; and PC: computer (107).

The variation of the near-field specklegram image $I(x,y)$ is shown in Figure 29a for the NCF section immersed in water ($n_3 = 1.333$), 16 wt% ethanol solution ($n_3 = 1.344$), and pure ethanol ($n_3 = 1.361$). The specklegram changes are related to the modulation of the number of guided modes in the NCF MNC, which is a function of n_3 through Equation (2.18). Even though it is not trivial to characterize the morphological characteristics of the speckle field as carried out in (92), the sensor response can be quantified in terms of the ZNCC values computed by adopting the reference statuses as the fiber immersed in water and in ethanol, Z_W and Z_E , respectively. The results are depicted in Figure 29b, where the data points correspond to the average of 3 experiments. The correlation coefficient is reduced as n_3 deviates from the reference condition, so Z_W and Z_E present complementary behaviors.

The sensitivity for the sensor referenced to water evaluated for a 95% confidence interval is $dZ_W/dn_3 = 18.7 \pm 2.5 \text{ RIU}^{-1}$ (refractive index units). Considering a $\Delta Z = 0.01$ resolution on the evaluation of the ZNCC, the system practical resolution is $\Delta n_3 = 0.01/18.7 = 5.35 \times 10^{-4} \text{ RIU}$. In case of Z_E , the sensitivity and resolution are $dZ_E/dn = 16.4 \pm 3.1 \text{ RIU}^{-1}$ and $\Delta n_3 = 0.01/16.4 = 6.1 \times 10^{-4} \text{ RIU}$, respectively. The sensor characteristics for Z_W and Z_E are practically equivalent, indicating that both references can be used for determining the calibration curve. Moreover, the sensor presented reliable results in terms of repeatability

according to the random uncertainties contained in the error bars of Figure 29b, with maximum standard deviations of 0.06 and 0.02 for Z_W and Z_E , respectively.

One may notice that the proposed MNCM structure is capable to detect refractive indexes values very different from silica ($n_2 \approx 1.45$), in contrast to the previously reported MSM fiber specklegram sensor, in which the response is non-linear, and the dynamic range is restricted to $n_3 > 1.38$ (123). The present device also exceeds the former chemical sensor based on the speckle field morphological processing (92), in which a ~ 0.003 RIU resolution for the $1.33 \leq n_3 \leq 1.45$ range was achieved. More-over, even though the tapered specklegram sensor reported in (124) exhibited higher sensitivity for low solute concentrations, it must be stressed that the MNCM structure is more mechanically robust and simpler to fabricate. Ultimately, the specklegram MNCM sensor can be compared to the multimodal interferometer described in (125): the transmission spectrum analysis yielded a $\sim 4.37 \times 10^{-4}$ RIU average resolution for the $1.30 \leq n_3 \leq 1.44$ range, but the sensor response becomes nonlinear as n_3 equals n_2 . Regarding the $1.33 \leq n_3 \leq 1.36$ interval, the resolution is decreased to 0.01 RIU, which is lower than the specklegram approach.

In practice, the dynamic range of the FSS is limited by the numerical aperture in the NCF section and by the saturation of the correlation function. Once the former governs the number of excited modes in the no-core fiber, fewer modes are coupled to the MMF2 fiber core as n_3 approaches n_2 , thus affecting the power and the number of light peaks in the output speckle field (92). Particularly, the interference condition also depends on the length of the NCF segment (131), so the specklegram visibility can be improved by adjusting the MNCM probe characteristics during the fabrication. Furthermore, MNC also decreases with the numerical aperture, causing the attenuation of the output speckle distribution. Although the ZNCC algorithm compensates the intensity fluctuations by subtracting the average value, the output power is expected to be lower in case of a reduced number of modes because a significant part of the optical signal will be lost in the NCF segment, hindering the sensitivity of the correlation analysis (89). On the other hand, the dynamic range can be enhanced by implementing EZNCC calculations as described in Chapter 3 to avoid the correlation saturation issue. Alternative methods also include the morphological processing (132) and recursive division (98) of the speckle field image, but it must be stressed that the measurement range is still limited by the numerical aperture of the NCF, *i.e.* the correlation analysis will be less responsive for n_3 values closer to n_2 .

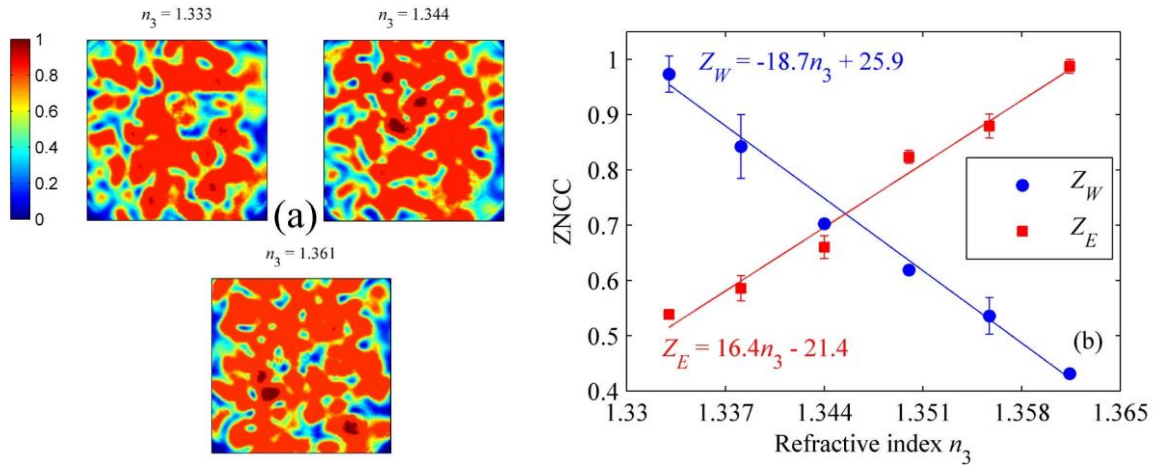


Figure 29 – Sensor response to the sample refractive index. (a) Near-field speckle field intensity for the NCF immersed in different liquids. The intensity values were normalized for the sake of visualization. (b) ZNCC values with the reference statuses set to the fiber immersed in water (Z_W) and ethanol (Z_E). The solid lines correspond to linear curve fittings ($R^2 > 0.98$). (107).

Finally, it is worth noticing that the temperature affects the sensor response by means of the sample and the silica thermo-optic coefficients, dn_3/dT and dn_2/dT , respectively. As the former is related to variations of the liquid refractive index due to temperature changes, the latter plays a role in the heat transfer mechanism from the environment to the fiber material. The temperature influence also relates to the thermal expansion, and photo-elastic properties of the fiber material (133). In particular, the silica NCF is expected to be less sensitive to temperature fluctuations than the germanosilicate fiber due to a lower thermo-optic coefficient (125), so the thermally induced n_2 deviations in the silica probe are less critical. On the other hand, the number of guided modes in the NCF section is affected by the temperature-dependent refractive indexes of the silica waveguide and the external medium (134), consequently, the output speckle field distribution changes even for minor temperature fluctuations.

Since the guiding conditions in the NCF section depends on both n_2 and n_3 (125), the light coupled to MMF2 is expected to be affected by temperature fluctuations, consequently changing the output specklegram and inducing errors in the liquid level estimation. In case of the chemical sensing, the thermal effect must be compensated for properly resolving the sample refractive index dependence. A straightforward approach consists in using a reference arm subjected to the same thermal load, so the changes in the ZNCC value due to the variations of sample composition and temperature can be discerned by comparing both output specklegrams (124). Alternatively, it is possible to implement an automatic compensation scheme by setting a threshold ZNCC value in the reference arm, causing the sensor characteristics to be restored whenever the temperature fluctuation exceeds a critical value (104).

For investigating the thermal sensitivity of the FSS, the NCF section surrounded by the air was heated from the room temperature (~ 26 °C) up to 35 °C by means of an infrared lamp (PAR38 Phillips, 150 W). A type K thermocouple positioned in the vicinity of the MNCM fiber was employed to continuously monitor the sample temperature T , whereas the probe was kept suspended in the environment to avoid the specklegram changes induced by mechanical or thermal conduction effects. The variation on the ZNCC value as a function of T is depicted in Figure 30. The correlation coefficient presents a linear decrease for $26 \leq T \leq 36$ °C, yielding $dZ/dT = (7.14 \pm 0.07) \times 10^{-2}$ °C $^{-1}$ sensitivity and 0.14 °C resolution. As a comparison, in (125) a 9.6 pm/°C sensitivity and ~ 10 °C resolution (given a 0.1 nm spectral resolution) was reported for the 25 – 300 °C range by using a spectral MNCM interferometer, whereas in (135) a bent Ge-doped NCF provided 6.5 nm/°C sensitivity and ~ 0.02 °C resolution in the 51 – 65 °C range.

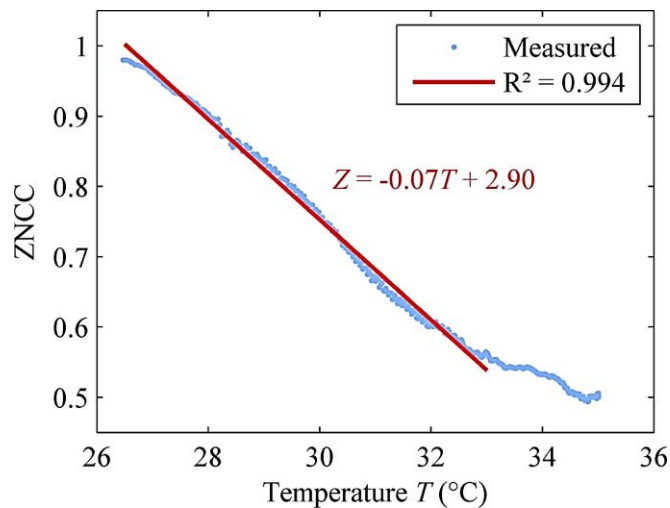


Figure 30 – Variation of the ZNCC as a function of the sample temperature for the MNCM probe placed in the air. The solid line is the linear curve fitting (107).

An optical fiber specklegram sensor based on the MNCM structure was demonstrated. The system presented 18.7 RIU $^{-1}$, 0.07 °C $^{-1}$, and 0.05 mm $^{-1}$ sensitivities comparable to other reported multimodal interferometers based on more complicated interrogation schemes. The proposed device also takes advantage of the intrinsic specklegram sensors features, making it possible to improve the system characteristics according to the application. On the other hand, the sensor performance is still limited by the speckle field sensitivity to extraneous effects such temperature changes, in this sense further studies will focus on the enhancement of the sensor characteristics, as well as its application in practical measurements.

4.3 Multimode exposed core fiber specklegram sensor

Since the first reported photonic crystal fibers, the concept has been refined and iterated upon for various applications. Suspended core fibers found many applications in fluid and gas sensing due to the high fraction of mode energy located in the air holes, and eventually fibers with periodically exposed cores were proposed to solve practical problems with introducing fluids in suspended core fibers (136). The first fully exposed core fiber (ECF) was later demonstrated with a lateral slot running along all fiber length (137), this result opened a new route to design and explore waveguides that are simultaneously robust, sensitive to the external medium and easily accessed. Since then, ECFs have been explored for various physical and chemical sensing applications (138-142).

Until recently, exclusively single-mode or few-modes ECFs were explored (137-142), this work was the first demonstration of a novel fiber specklegram sensor (FSS) based on an original highly multimode ECF concept with a lateral slot that runs along the full extension of the fiber. This new design allowed for the first time the interrogation of ECFs as fiber specklegram sensors, which are particularly interesting for their ability to achieve high sensitivity with simple and low-cost interrogation setups (143,144). Here the performance of the probe was evaluated for measuring temperature, refractive index and liquid level (length of fiber bathed in fluid).

4.3.1 Materials and methods

Fabrication of the exposed core fiber was conducted in the facilities of the Institute for Photonics & Advanced Sensing and School of Physical Sciences, University of Adelaide, Australia. Fiber samples were then shipped to Brazil for testing in UNICAMP.

The fiber preform was prepared by drilling a 150 mm long, 21 mm thick pure silica rod using the same technique reported for few-modes ECF in (145). An ultrasonic CNC milling machine was used to drill six holes in a hexagonal pattern with a missing hole in the center to form the fiber core. The diameter d of the air holes was 2.8 mm and the hole-to-hole pitch ratio Λ 3.2 mm, translating to a core diameter of 3.6 mm and preform d/Λ of 0.875. The minimum gap between adjacent holes was 0.4 mm. A diamond endmill was then used to open a 1 mm wide slot on the surface of the preform to expose one of the holes to the external environment.

Figure 31 shows a 3D rendering of the fiber preform modeled using AutoDesk Inventor and an optical microscope image of the drawn fiber, note that the fiber was illuminated from below making the core shine bright white.

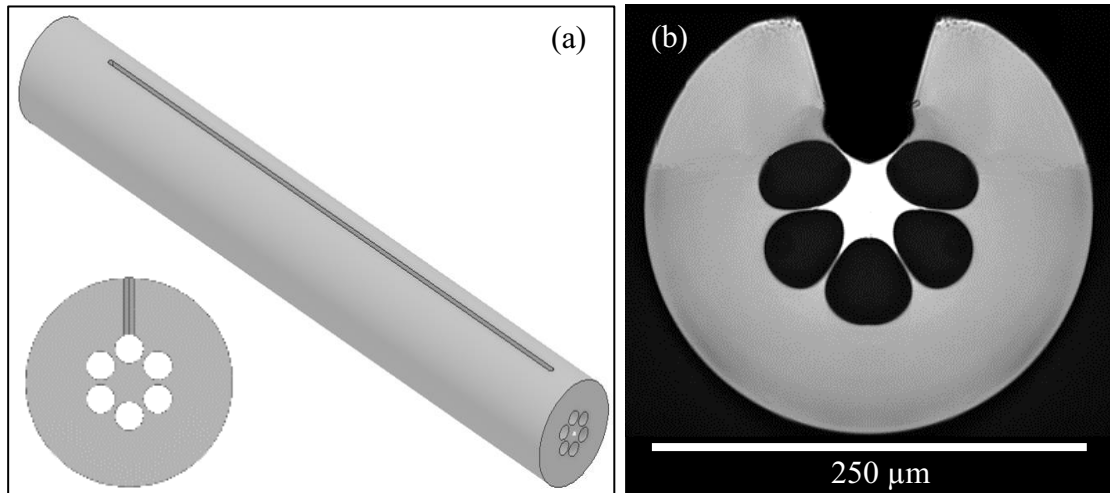


Figure 31 - (a) 3D model of the fiber preform – inset shows the cross-section view of the fiber; (b) optical microscope image of the fiber cross-section (108).

Drawing to an optical fiber was realized in a single stage using a draw tower, with an overall size reduction of $80\times$. The preform had both ends fused to silica tubes for easier handling and to help locate the structure within the furnace hot zone. Drawing was realized at $2005\text{ }^{\circ}\text{C}$, with a feed rate of 0.8 mm/min and a typical pulling rate of $5\text{ to }10\text{ m/min}$. To increase d/Λ a 12 mbar positive pressure was applied in the preform holes during drawing. Expanding the holes helps to better confine the optical mode as light is guided through total internal reflection due to index contrast between the silica core and holey cladding, reducing confinement loss. The drawn fiber has external diameter of $\sim 250\text{ }\mu\text{m}$, core size of $\sim 35\text{ }\mu\text{m}$ and d/Λ of approximately 0.96 .

The lateral slot provides an external fluid direct access to the fiber core, allowing for the interaction between the fluid and core-guided modes through their evanescent fields. As the fluid substitutes an air hole, the mean refractive index (RI) of the cladding changes, and by consequence the effective RI of the guided modes is also affected (146-148). The fiber is sensitive to the refractive index of the fluid, which manifests as changes in the output specklegram of the fiber core as the number of core-guided modes, and the energy distribution among them, is altered by the presence of the fluid. In order to expose the ECF to a fluid of interest in a controlled fashion a fiber bathing apparatus (Figure 32) was designed and machined

out of a single aluminum block. The apparatus has alignment rails for fiber holders, as well as for positioning on top of a XYZ precision linear stage. In its underside there is a clearance for a Peltier device for temperature control, whereas the upper surface contains a cross-shaped bathing area 25 mm long by 10 mm deep intercepting the fibers path. The side-lobes in the bathing area allows for easier introduction on removal of fluid without disturbing the ECF.

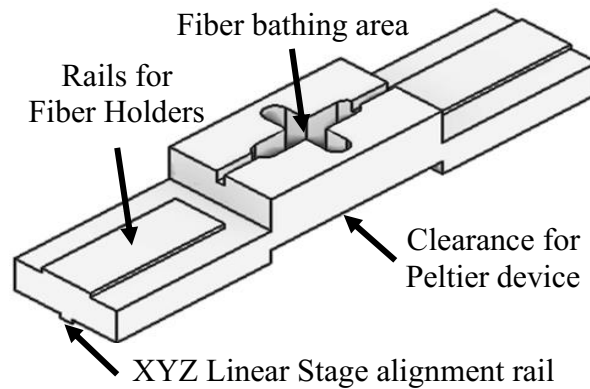


Figure 32 – Up: 3D model of the fiber bathing apparatus indicating its main features, such as alignment rails and a slot for a Peltier device. Down: Machined bathing apparatus with fiber holders and a Peltier device.

The experimental setup is depicted in Figure 33 and is similar to that of Figure 19 in sub-section 4.1.1. Light from a He-Ne laser (633 nm, 5 mW) passed through a neutral density filter (NDF) and was redirected by mirrors (M1, M2) to a 20 \times objective lens (L1). Lens L1 coupled the laser light into the fiber, which was secured to the bathing apparatus, while a 40 \times objective (L2) focused the output speckle pattern to the CCD of a webcam. Light was launched into the core by aligning the laser beam with the axis of the fiber, centering it in relation to the core and adjusting the focus so the beam and the core diameters coincide in the plane of entry. Video was captured at 800 \times 600 pixels resolution and 15 frames per second. A Peltier device was positioned directly below the fiber bathing area to control the temperature, with thermal contact facilitated by a thin layer of thermal grease. To provide a quantifiable metric for specklegram shifts ZNCC was used, it was calculated from a 200 \times 200 pixels region-of-interest (ROI) positioned as shown in Figure 34.

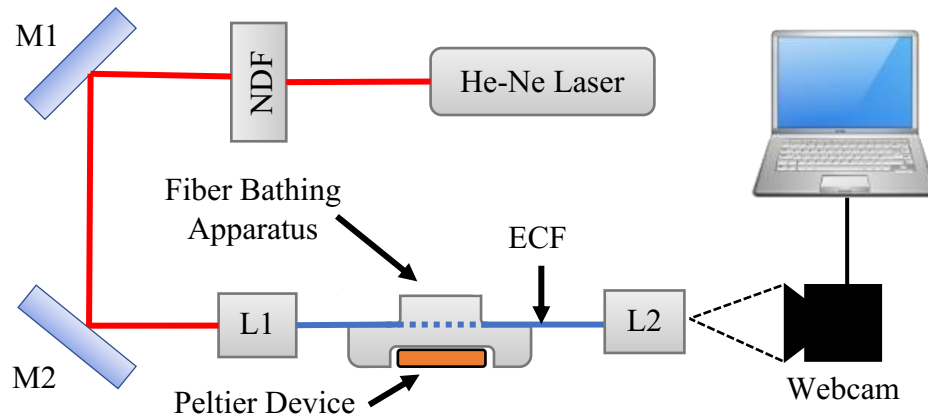


Figure 33 - Experimental setup used to characterize the ECF's response to temperature and refractive index of fluids. NDF: Neutral density filter. M1, M2: mirrors. L1: 20× objective. L2: 40× objective (108).

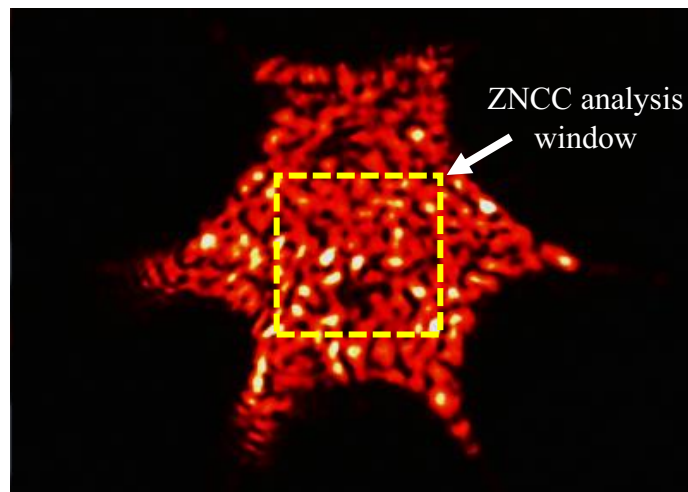


Figure 34 – Output specklegram from the core of the ECF as captured by the webcam. The dashed yellow square indicates the 200×200 pixels region-of-interest for ZNCC calculation (108).

In this study, each data point presented in the results contained in Section 4.3.2 is the mean Z (μ_z) for a ~ 10 seconds video (~ 150 frames). While the precision of Z is given by the bit size of the floating-point variable used in the computations, in practice the intrinsic electronic noise of the webcam, combined with external sources of noise pose a practical boundary for the ZNCC resolution due to data dispersion. It is worth noting this approach to determining the resolution of the probe based on noise is noted in Section 4.14 of the International Vocabulary of Metrology (VIM) (149). To determine a sensible resolution metric firstly the standard deviation for each datapoint was calculated. Let's look at, for example, the distribution of Z for all frames of a video collected with the ECF bathed in water at 26.0 °C calculated using as a reference the probe bathed in water at 23.0 °C, as indicated by the blue dots in Figure 35. In this example, μ_z is 0.3273 and the standard deviation σ is 5.9×10^{-4} . For a 99.9% expected

fraction of Z values in range of μ_z it is possible to use the boundary $\mu_z \pm 3.5\sigma$ (150). In Figure 35, the horizontal green line represents μ_z while the orange lines are $\mu_z \pm 3.5\sigma$. The lower and upper boundaries created by the orange lines easily contain most, if not all, ZNCC data.

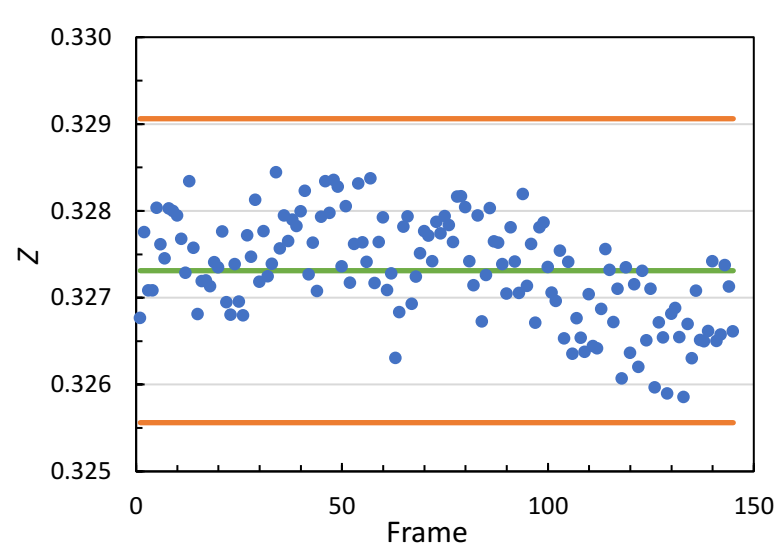


Figure 35 – Scatter plot of Z for a single video collected with the ECF. Blue dots are the datapoints, green line indicates average Z for the dataset and the orange lines are offsets of $\pm 3.5\sigma$ in relation to the average value.

When analyzing the entire data space for this study (all videos), the average value of σ is around 5.0×10^{-4} , the upper and lower boundaries then become $\mu \pm 1.75 \times 10^{-3}$, which is an interval with a width of 3.5×10^{-3} . To accommodate for datasets with higher σ values such as the provided example in Figure 35, 5×10^{-3} was chosen as a conservative estimate for the width of the interval in which the true value of μ_z is expected to be contained, so effectively 5×10^{-3} is the practical ZNCC resolution. This value was then converted into temperature, refractive index or bathed length resolutions as appropriate.

4.3.2 Results and discussion

To evaluate the response of the probe when a span of fiber is submerged in fluid, the bathing apparatus was substituted for a 100 mm long, 25 mm wide solid aluminum block. The block's surface was made rough by sanding with a sandpaper to prevent water from pooling due to the surface tension. Fine lines were drawn on the block, dividing it into 5 mm long sections. A ~ 110 mm long fiber piece was placed on top of the block and secured in place by applying adhesive clay to the first and last sections. Water was then added to the block section

by section. Data was recorded from no water in contact with the fiber (submerged length = 0 mm) to use as reference for ZNCC calculations, and up to a submerged length of 50 mm in increments of 5 mm. Figure 36 is a plot of the experimental data, μ_z is observed to drop as the fiber is progressively submerged in water. As the response is non-linear, resolution was computed for each step, returning maximum and median values of 0.12 mm and 0.40 mm respectively. Mean sensitivity over the 0.0 – 50.0 mm bathed length range was -0.015 mm^{-1} .

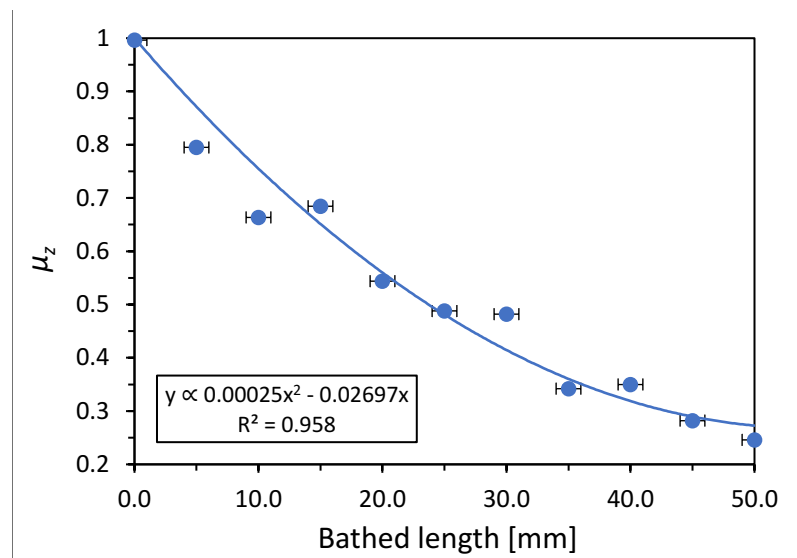


Figure 36 – ECF response to length bathed in water. Blue curve is a quadratic fit of the data ($R^2 = 0.958$). (108).

Afterwards, utilizing the fiber bathing apparatus, a ~130 mm fiber piece was bathed (submerged length = 25 mm) in multiple liquids with distinct refractive indexes – water ($n = 1.3330$), ethanol ($n = 1.3632$), 33% w/w glycerol solution ($n = 1.3747$) and isopropyl alcohol (IPA, $n = 1.3772$) – and the value of μ_z for each bathing fluid was recorded (ZNCC reference set as the undisturbed fiber in air). Refractive index for each fluid was measured using a digital handheld refractometer (Palm Abbe PA202, Misco, 589.29 nm). The results are depicted in Figure 37, the ECF exhibits a mean resolution of 4.6×10^{-4} RIU, higher than sensors based on conventional multimode fibers (107), and mean sensitivity of -10.97 RIU^{-1} . As can be observed from these metrics, the air-referenced fiber is very sensitive in the 1.33-1.37 RI range, making it attractive for biomedical applications (151-154). Measurement range can be adjusted by choosing a different reference fluid for ZNCC calculations. It is also important to notice that, in Figure 36, for a 25 mm submerged length a ZNCC of approximately 0.5 was observed, which coincides with the value for water obtained using the bathing apparatus in Figure 37. As these

measurements were conducted independently, it demonstrates that the ECF produces repeatable and reliable results.

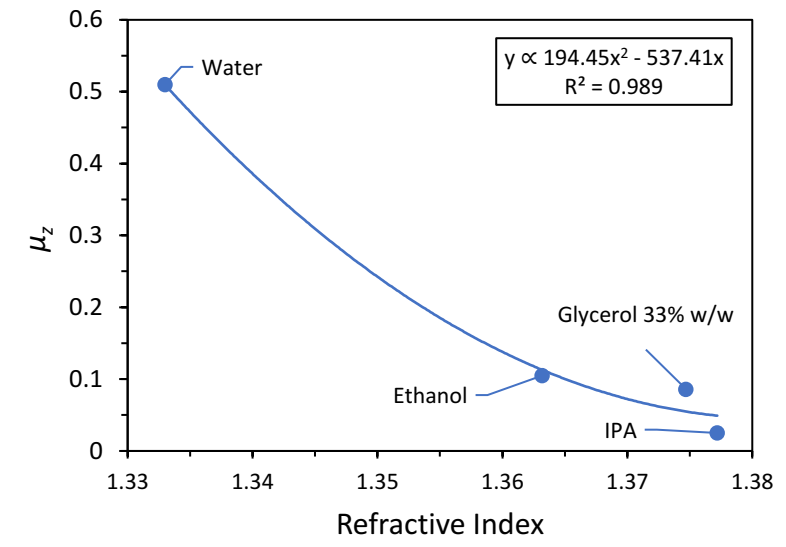


Figure 37 – ECF response to bathing with distinct fluids: water, ethanol, 33% w/w glycerol solution and isopropyl alcohol (IPA). Blue curve is a quadratic fit of the data ($R^2 = 0.989$). (108).

Finally, the temperature response of the ECF was assessed, there is also special interest in evaluating the thermal response of speckle-based probes since cross-sensitivity can be an issue in experimentation. First, the ECF response was characterized for quasi-static temperature variations. To avoid evaporation of the bathing fluid and losing heat to the surrounding air, the bathing area was sealed with aluminum tape. A type K thermocouple was inserted in one of the side-lobes of the bathing area through the tape to assess temperature, as illustrated in Figure 38. Heat energy was introduced slowly into the system using the Peltier device.

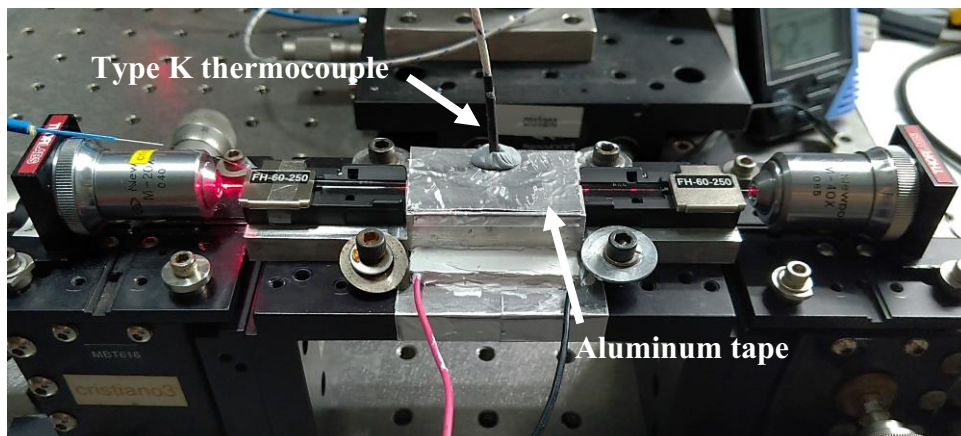


Figure 38 – Setup modifications for assessing the ECF response to quasi-static temperature variations.

This experiment was conducted for both air and water baths to observe the influence of the thermo-optic coefficient of the fluid in the probe's response. Heating rate was approximately $0.1\text{ }^{\circ}\text{C}/\text{min}$ and, after each step of $0.5\text{ }^{\circ}\text{C}$, the temperature was let stabilize for 2 minutes before collecting data. Figure 39 shows the response curves for water and air, ZNCC was referenced at $22.5\text{ }^{\circ}\text{C}$ for both fluids. For a 5×10^{-3} ZNCC resolution, maximum and median temperature resolutions for a 130 mm long fiber piece are $0.017\text{ }^{\circ}\text{C}$ and $0.030\text{ }^{\circ}\text{C}$ respectively for water, and $0.017\text{ }^{\circ}\text{C}$ and $0.027\text{ }^{\circ}\text{C}$ for air. Mean sensitivity over the $23\text{ }^{\circ}\text{C} - 28\text{ }^{\circ}\text{C}$ range is $-0.19\text{ }^{\circ}\text{C}^{-1}$ for water and $-0.20\text{ }^{\circ}\text{C}^{-1}$ for air.

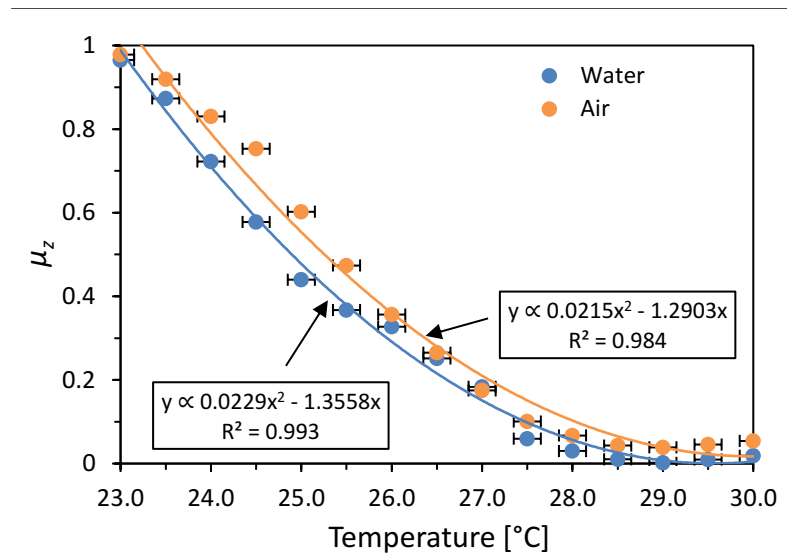


Figure 39 - Response of the ECF to quasi-static temperature variations for the fiber exposed to air (orange dots) and bathed in water (blue dots). Solid lines are quadratic fits of the data (108).

Despite water's thermo-optic coefficient ($-7.71\times 10^{-5} - 633\text{ nm}$) being two orders of magnitude higher than air's ($-9.73\times 10^{-7} - 633\text{ nm}$), the results are roughly equivalent. This similarity between both curves indicates that the thermal response of the ECF is most likely dominated by the glass, with a thermo-optic coefficient of $8.80\times 10^{-6} @ 633\text{ nm}$ (156). This can be explained in part by the large multimode core leading to a relatively small optical energy fraction in the evanescent field in contact with fluid in the exposed core.

Furthermore, by estimating the number of guided modes by counting speckles, no significant difference in number of guided modes was observed for the fiber bathed in air or water. The number of modes can be estimated from the number of light speckles, the output speckle field images acquired by the CCD camera were processed according to the method described in (92): firstly, color images are converted to grayscale and filtered by 2D wavelet transform (Daubechies db4). Then, image features are enhanced by Law's texture energy

method using 5×5 pixels level masks, and the number of speckles is counted from the binary masks (large areas are segmented into smaller ones using an opening operation). Analyzed images for ECF bathed in water and air are depicted in Figure 40, whereas the results are summarized in Table 1.

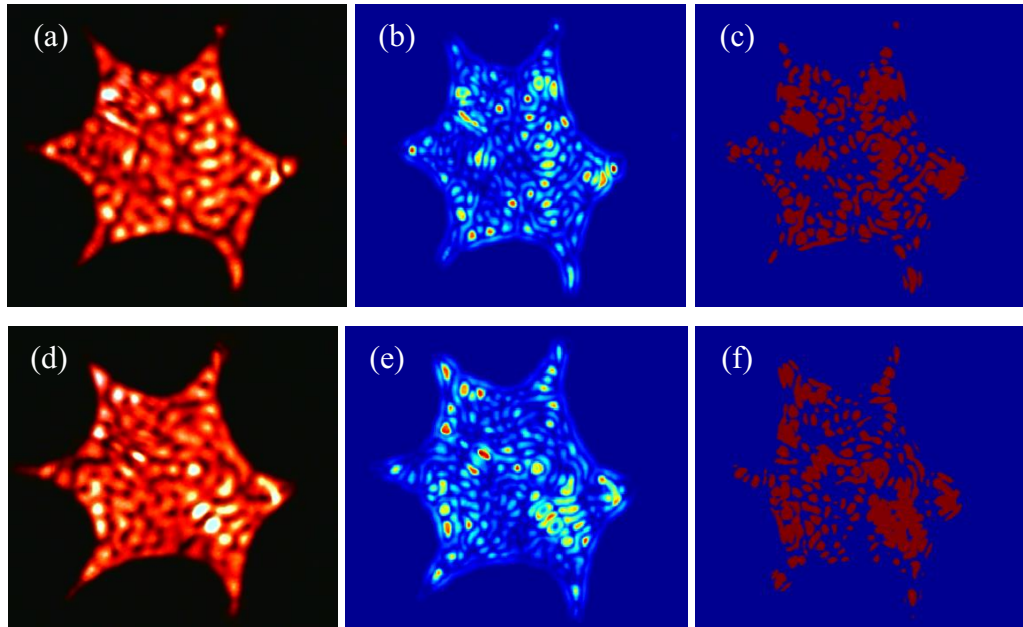


Figure 40 – Speckle field image processing: (a): output specklegram, (b): filtered image, and (c): level mask for the ECF bathed in water. (d), (e) and (f) show the equivalent analysis for the ECF bathed in air.

Table 1 – Results of the speckle count for output specklegrams captured with the ECF bathed in water and in air.

Sample	Number of speckles
Water 1	135
Water 2	141
Air 1	146
Air 2	147

As shown in Table 1, the number of excited modes for both cases were around 150, orders of magnitude lower than the theoretical maximum supported by the fiber, which can be estimated with Equation (2.8) as ~ 5000 for water and ~ 12000 for air at 633 nm. Thus, a plausible hypothesis is that the response is then caused by changes in the relative phase between modes and modal energy redistribution induced by the temperature variations.

Finally, a dynamic non-monotonic temperature test was conducted. As the response observed before for water and air are equivalent, air was used to avoid unwanted fiber

movement from convection currents in water. For a more accurate dynamic temperature measurement, the thermocouple was replaced with a fiber Bragg grating (FBG) sensor interrogated by a 1 pm (~ 0.077 °C) resolution system (HBM FS42-01-010-420). Figure 41 shows the evolution of Z over time and the corresponding air temperature curve. As can be observed, ZNCC closely follows the temperature curve for temperature variations of around ± 1.0 °C over the 23.2 °C baseline (cross-correlation = 0.999). As ZNCC cannot be higher than 1 (it is a correlation metric), the reference was set as the lowest recorded temperature (~ 22.2 °C @ 450 seconds), to avoid mirroring of the Z curve.

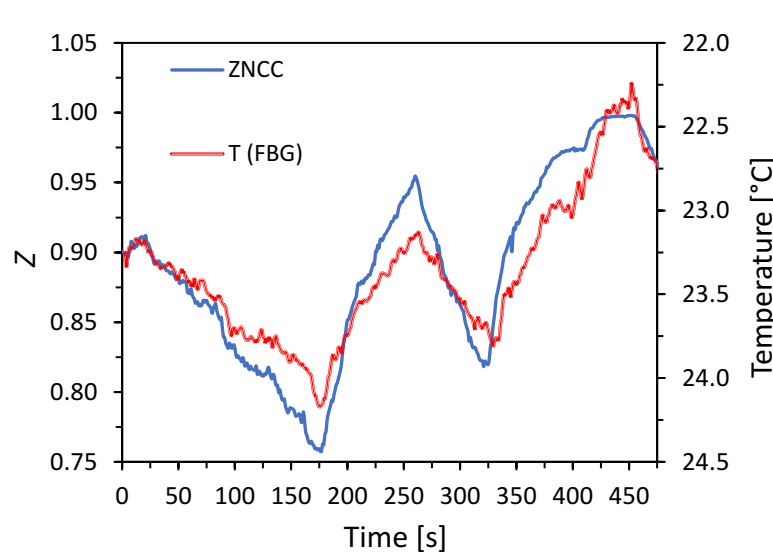


Figure 41 - Response of the ECF probe (blue) to dynamic temperature variations (red). Temperature varies ± 1.0 °C over the baseline value (108).

A highly multimode exposed core fiber and its use as a versatile specklegram sensor for practical sensing of fluids was demonstrated. The probe exhibited competitive sensitivity and resolution metrics when compared to traditional sensors or specialty PCF/ECF sensors already reported in the literature (141,151,157,158), while at the same time utilizing a simpler and low-cost interrogation setup.

4.4 Tb³⁺ doped fiber specklegram sensor for magnetic field sensing

Magnetic sensors are necessary for several technological and medical applications, including storage hard disks, distance meters for aircrafts and automobiles navigation, and brain

function mapping. Particularly, the development of devices for measuring magnetic fields finds applications in biomedics, security, non-destructive testing, among other industrial uses. Nowadays, several OFS setups for magnetic measurements (including field, force, and electric current) have been proposed, such as Faraday effect sensors (159), fiber strain gauges based on magnetostrictive materials (160), structured fibers immersed in ferrofluids for surrounding refractive index modulation (161), and photonic crystal fibers filled with ferromagnetic colloids (162). Despite their notable sensing capabilities, these approaches still present drawbacks in terms of expensive interrogation setups, and complex fiber processing steps in case of structured fibers.

In this context, as discussed throughout this thesis, fiber specklegram sensors (FSS) are promising alternatives. A few schemes for magnetic measurements with FSSs have been demonstrated in the specialized literature, for instance, a cantilever device based on a nickel-jacketed fiber is used for assessing the magnetic field produced by a solenoid (163). The fiber is bent with the increase of the coil driving current and the sensor response is interrogated by superimposing the speckle patterns. Despite the simplicity, the fabrication of metallic jackets or coatings involves laborious procedures, and the sensor detection capabilities are limited by the resolution of the Young's fringes (164). Another case is comprised of Faraday rotation sensors in which the speckle field is spatially rotated as a function of the applied magnetic field as demonstrated for a few-modes fiber (165). However, the specklegram changes are subtle and difficult to measure in case of an ordinary silica fiber, so complicated waveguides modifications, such as a graphene coating (166), would be required to improve the sensing capabilities. Similarly, a speckle-based sensor utilizing a fused quartz rod instead of a glass fiber was demonstrated for magnetic field measurements (167). The speckle pattern is generated by directing laser light through a ground glass diffuser, the quartz rod is placed before the diffuser and inside a solenoid. By subjecting the quartz rod to a magnetic field, the polarization of the laser light rotates due to the Faraday effect, resulting in a small change to the speckle pattern that can be quantified with digital image correlation techniques. However, the sensitivity of the reported setup is still low, with a correlation change of less than 0.05 for a change of the applied magnetic field intensity of up to 200 G (20 mT).

One possible approach to solve for both sensitivity and complexity is using optical fibers with simple structures and high Verdet constants, to maximize the Faraday rotation effects on the speckle pattern. To this end, no-core fibers fabricated from magneto-optical (MO) glass doped with Terbium oxide (Tb_4O_7) can be employed (168,169). In recent years, magneto-

optical glasses with high Verdet constant values have been on the forefront of optics, photonics and spintronics research (170,171), with works reported for glasses containing Tb^{3+} , Dy^{3+} , Pr^{3+} and Gd^{3+} ions (172-174), for applications such as electrical current optical fiber sensors (175) and optical isolators (176).

This section demonstrates a novel high-sensitivity FSS for assessing the magnetic field intensity using no-core optical fibers fabricated from terbium-doped magneto-optical glass with very high Verdet constants, making it possible to greatly increase the specklegram response to the applied magnetic field. To the best of knowledge, at the time of writing this thesis, this is the first practical demonstration of a magnetic field FSS based on magneto-optical glass.

4.4.1 Materials and methods

Fabrication of the MO fibers was conducted in part in UNESP Araraquara – Brazil and in part in COPL, Laval University, Canada. The first step involved the selection of three glass compositions based on the glass system $(100-x)(41GeO_2-25B_2O_3-4Al_2O_3-10Na_2O-20BaO)-xTb_4O_7$ (BGB- xTb), where x represents the concentration of Tb_4O_7 (in mol %). The glass preforms containing 6, 8 and 10 mol % were prepared and labeled as BGB-6Tb, BGB-8Tb and BGB-10Tb, respectively, Figure 42(a-c).

The punctual choice of these glass compositions to prepare the glassy preforms and, subsequently, to draw the MO fibers fabrication were based on the highest thermal stability parameters ($\Delta T = T_x - T_g$, where T_x is the crystallization temperature and T_g the glass transition temperature) of them, equal 257 °C (6Tb), 305 °C (8Tb) and 241 °C (10Tb) (169). Three glass preforms were prepared by the melt-quenching method from the 30 g batch of glasses. The glass compositions were melted in an induction furnace using a platinum crucible at 1450 °C for 1 h, under a flow rate of 30 mL/min of N_2 . The glass rods were obtained using a cylindrical stainless-steel mold 100 mm long and of 10 mm diameter. Initially, before the melt-quenching process, the mold was pre-heated for 2 h at 50 °C below T_g for three different glass compositions: BGB-6Tb (at 535 °C), BGB-8Tb (555 °C) and BGB-10Tb (592 °C).

After the melting processes, the glass rods (preforms) were annealed for 6 h at 50 °C below T_g and cooled at a rate of 0.5 °C/min for a time of 17.5 h to reach room temperature. Subsequently the cooling process, the preforms were polished gradually using SiC papers with different granulometries (600 to 1200 grit). In the last step, the BGB- xTb preforms were mounted into the drawing tower, and the drawing procedures were started around 700-750 °C

depending on glass composition ($T_g + 115$ °C). To improve the mechanical properties of materials, the MO fibers were coated with a low-index UV-cured poly(methyl methacrylate) (PMMA) polymer. The diameters of BGB-6Tb, BGB-8Tb and BGB-10Tb fibers are 125, 237 and 206 μm , respectively.

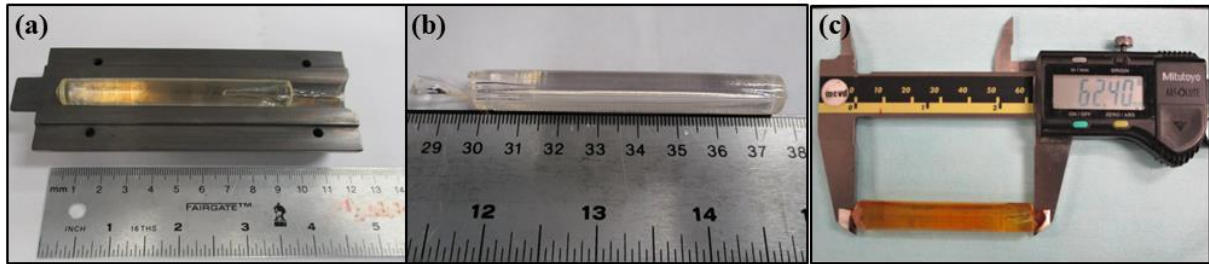


Figure 42 – The glass preforms BGB-xTb: BGB-6Tb (a), BGB-8Tb (b) and BGB-10Tb (c). (110).

The working principle of the probe is as follows. When linearly polarized light is transmitted through a dielectric material subjected to a magnetic field, a rotation of the polarization plane is observed through the Faraday effect. The magnitude of the rotation is dependent on the properties of the dielectric material and its thickness, and the intensity of the magnetic field as given by $\theta = V \cdot H \cdot L \cdot \cos(\alpha)$, where θ is the angle of rotation, V the material's Verdet constant, H the intensity of the magnetic field, L is the length of dielectric subjected to said field, and α is the angle between the directions of the magnetic field and light propagation (165). In this work, the axis of the optical fiber is aligned with the direction of the magnetic field so that $\cos(\alpha) \approx 1$. In the case of dielectric waveguides where few modes can be coupled and propagate simultaneously, this results in a rotation of the intensity distribution profile of each mode, consequently rotating the speckle pattern (177). However, since each guided mode has a different propagation constant (β) and not all modes conserve the polarization of the input light, in the presence of an external magnetic field H the polarization corrections to the propagation constants are not uniform and the magnitude of the rotation θ is different for each mode, with higher order modes experiencing increasingly smaller Faraday rotations (165).

It follows that for highly multimode waveguides the combined effects of the non-uniform Faraday rotations between lower and higher order modes produce morphological changes to the speckle pattern that does not manifest as a simple rotation of the starting pattern in the absence of the magnetic field (165). Furthermore, it has been demonstrated that for optical fibers fabricated from magneto-optical materials, the mode coupling coefficients are sensitive to the magnitude and direction of applied magnetic fields which will also impact the speckle

morphology through polarization mode conversion and changing the energy distribution between modes (171). To summarize, for a regular dielectric material or waveguide the spatial distribution of the specklegram intensity profile, $I(x,y)$, is sensitive to an external magnetic field H through the Faraday effect (167), though this effect is very small due to the typically low values of the Verdet constant. This response to an external magnetic field can then be sharply increased by using magneto-optical waveguides, such as the optical fibers detailed in this work, by the virtue of having intrinsically higher Verdet constants and, potentially, through the influence of the magnetic field on the multimode coupling coefficients, resulting in much more sensitive magnetic field FSS.

The experimental setup is depicted in Figure 43. The light emitted by a He-Ne laser source (633 nm) shines through a neutral density filter and is directed by a pair of mirrors to a linear polarizer and a 20× objective lens that launches the light into the fiber under test ($L_{\text{fiber}} \approx 140$ mm). A 100 mm long coil with ~ 200 turns (house made) connected to a benchtop adjustable DC power supply (Hikari, HF-3203S), and the magnetic field strength is set by varying the current supplied to the coil. Finally, the output nearfield specklegram is focused by a second 20× objective lens to the CCD element of a lensless webcam (Creative Labs Inc., VF0230), captured in AVI video format (800×600 pixels, 15 fps) and subsequently processed by routines programmed in MATLAB.

The optical fiber sensor was characterized by evaluating the speckle field changes as a function of H for different concentrations of Tb_4O_7 in the glass composition. The obtained results are also compared to the response of a regular commercial silica multimode fiber (62.5 $\mu\text{m}/125$ μm core/cladding diameters). The magnetic field intensity produced by the coil as a function of driving electrical current (Figure 43, inset) was obtained using a Model 425 Gaussmeter equipped with an axial Hall-effect probe (Lake Shore Cryotronics), by inserting the probe in the center of the coil and computing the average value over the coil's length. The relation between the magnetic field intensity H and the current fed to the coil is linear ($R^2 = 0.999$), with an angular coefficient of 2.5×10^{-3} mT/mA. All experiments were conducted at fixed room temperature on a mechanically isolated optical table and avoiding the influence of external illumination.

ZNCC was to quantify the specklegram changes, and the calculations were made for a ROI of 201×201 pixels positioned roughly at the center of the fiber (Figure 44). When discussing the results in the next section the datapoints represent the average value of Z (μz) for

each video. The metric ΔZ , defined as $\Delta Z = 1 - \mu_Z$, which gives a quick reference on how much Z has changed from the reference condition, is also used when convenient.

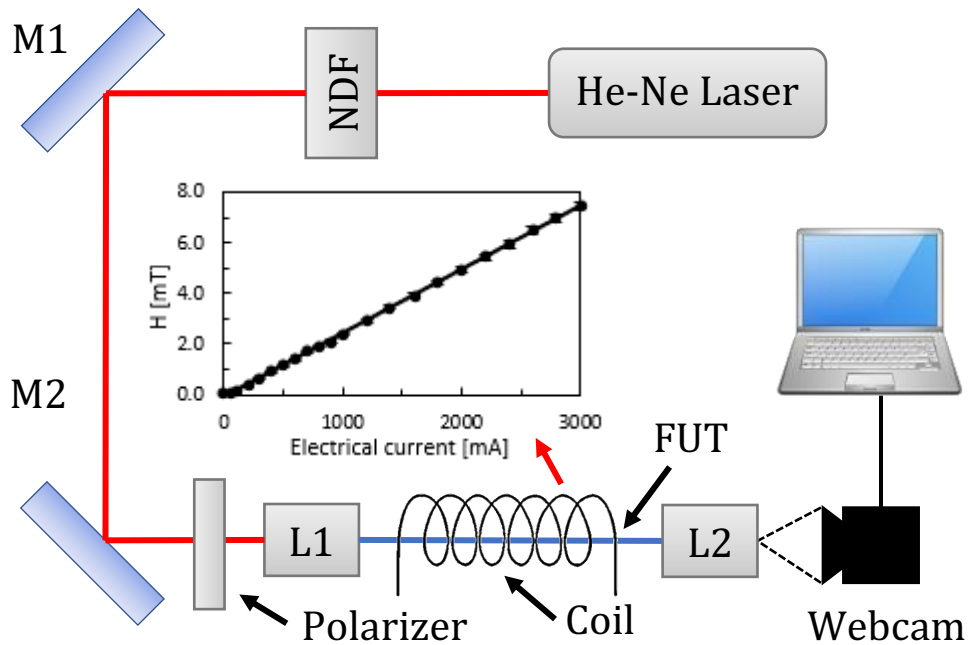


Figure 43 – Schematic drawing of the experimental setup. NDF: Neutral density filter; M1, M2: mirrors; FUT: Fiber under test; L1, L2: objective lenses. Graphic inset is the magnetic field intensity H produced by the coil as a function of the fed electrical current, solid line is a linear fit of the data ($R^2 = 0.999$). (110).

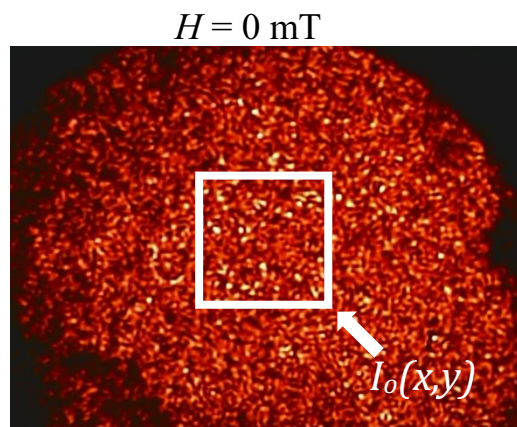


Figure 44 – Data analysis process showing the speckle pattern and 201 × 201 pixels ROI for unperturbed ($H = 0$ mT) state of the BGB-6Tb fiber.

As discussed previously, the ZNCC is more robust than other image comparison techniques as it compensates the brightness fluctuations, this characteristic along with the polarizer positioned between the laser and the fiber probe ensures a very stable experimental

environment, where Z calculations are insensitive to both intensity and polarization fluctuations (as they will also manifest as small intensity fluctuations due to the presence of the input polarizer) of the laser source.

4.4.2 Results and discussion

For each tested fiber one reference specklegram video for $H = 0$ mT (current = 0 mA) and 25 more videos with electric current steps of 100 mA up to 2500 mA ($H = 6.16$ mT) were collected. The magnetic field is kept constant for the full duration of each video, which was of ~ 10 seconds (150 frames). Z was calculated for all frames, with $I_0(x,y)$ set as the intensity distribution in the ROI for the first frame of the reference video. As shown in Figure 45a (for the BGB-8Tb fiber) Z decreases as H increases, once the speckle pattern deviates from the unperturbed condition in response to the presence of the magnetic field.

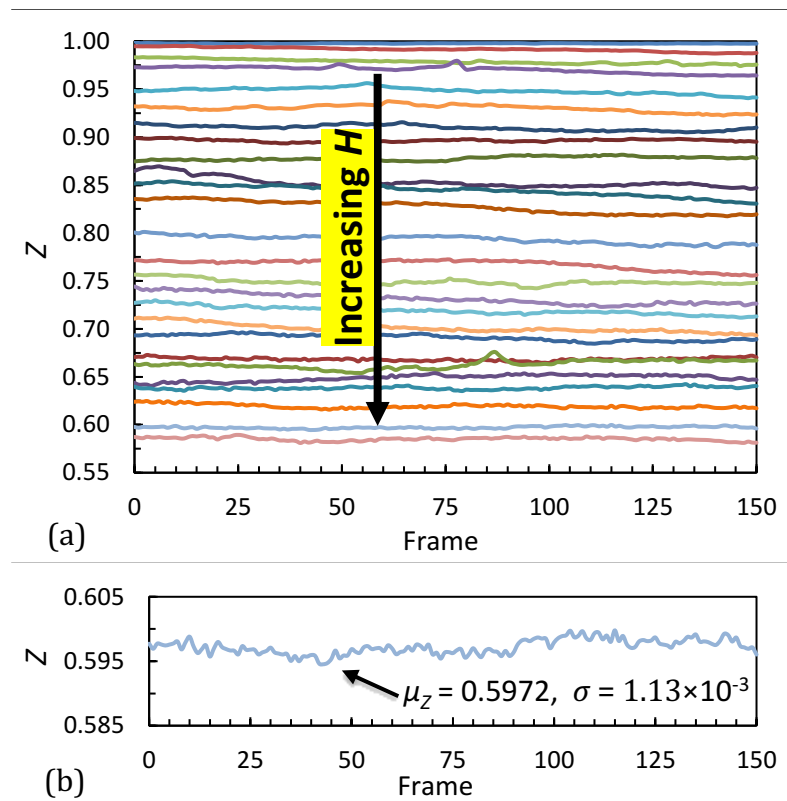


Figure 45 – Z curves as H increases for specklegram videos collected with the BGB-8Tb fiber (a). Single video Z curve (silica MMF) highlighting the average value of Z (μ_Z) and the standard deviation σ (b). (110).

Looking at the Z curve for a single video, Figure 45b, it is observable that the data closely follows a horizontal line. A practical limit for the resolution of Z can be determined by

first computing the standard deviation (σ) of each curve, then calculating the average standard deviation and finally correcting it to the sample size by dividing it by \sqrt{n} , where $n = 26$ is the number of videos per dataset. This quantity, here referred as $\bar{\sigma}$, was calculated separately for each probe and used to determine the resolution of the probes for measuring H .

To evaluate if heating of the coil when subjected to a relatively high current (> 2000 mA) could induce a temperature crosstalk signal on Z by heating the FSS, the specklegram of a regular MMF was recorded for the coil powered with a 2500 mA current. A ΔZ of 3.13×10^{-3} was observed after ~ 4 min (3500 frames). As can be seen in Figure 45b this is of the same order of magnitude as σ for a Z curve, and since the time to collect a full dataset for a FSS is not too dissimilar (~ 8 min), during most of which the current will be much lower than 2500 mA, any temperature effects related to a possible electrical heating were deemed negligible.

A. Specklegram polarization and influence on sensitivity

The polarization state of the output specklegram was also investigated by slightly modifying the experimental setup depicted in Figure 43. The webcam and computer were substituted by a photodetector (Thorlabs PDA55) connected to an oscilloscope (Tektronix DPO 4104), and a second linear polarizer (analyzer) was introduced between the lens L2 and the photodetector. By allowing the polarizer or the analyzer to freely rotate, it is possible to get a general evaluation of the output specklegram polarization from the intensity measured by the photodetector. For this end an automatic rotating mount (Newport NSR1) was employed. Results of this experiment for the BGB-6Tb fiber are depicted in Figure 46.

It is evident that the laser source is highly linearly polarized, as the intensity reaching the photodetector can be almost completely extinguished by rotating the input polarizer (blue curve), blocking off the laser light from reaching the fiber. On the other hand, as the analyzer rotates, the contrast of the orange curve is much lower, with the minimum intensity still reaching about half maximum, suggesting a moderately elliptical polarization state for the output speckle pattern. This is expected, as the no-core magneto-optical fibers are highly multimode and were not fabricated with polarization maintaining features.

As previously discussed, different modes will experience dissimilar Faraday rotations in response to a magnetic field, and modal energy distribution will also be affected as the mode-coupling coefficients are also sensitive to the magnitude and orientation of H . Contrasting this

information with the findings showcased in Figure 46, the inclusion of an analyzer will eliminate the contribution of many modes in the spatiotemporal characteristics of $I(x,y)$, which can impact the sensitivity of the probe.

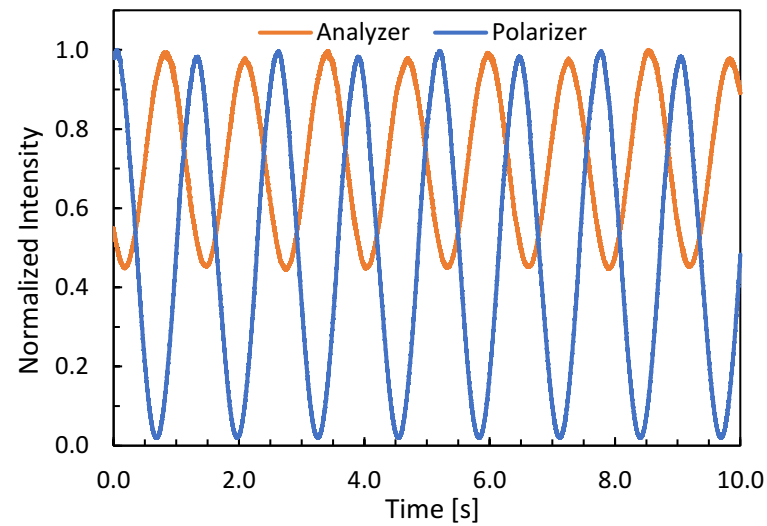


Figure 46 – Normalized fiber output intensity for $H = 0$ mT for the BGB-6Tb fiber as the analyzer (orange curve) or polarizer (blue curve) are allowed to rotate.

This possibility was investigated by collecting two full datasets of 26 videos using the BGB-6Tb fiber, one with only the input polarizer included in the experimental setup and the second with both polarizer and analyzer, with the analyzer angle set for peak output intensity. The results of this experiment are summarized in Figure 47.

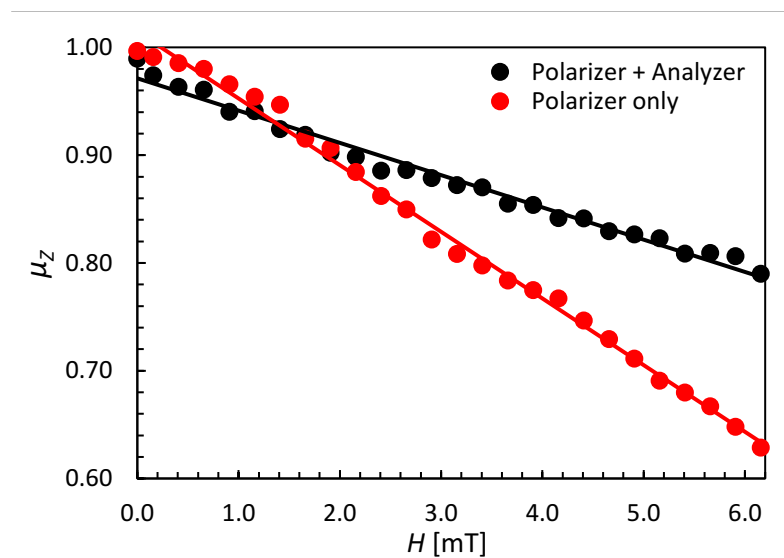


Figure 47 – Sensitivity to H for a BGB-6Tb fiber when using a polarizer + analyzer (black), or polarizer only (red). Solid lines are linear fits of the data (Black curve: $R^2 = 0.984$; Red curve: $R^2 = 0.995$). (110).

An impact on the sensitivity between configurations is clearly visible. For an input polarizer only (red) a sensitivity $d\mu_z/dH$ of $-6.18 \times 10^{-2} \text{ mT}^{-1}$ was observed ($R^2 = 0.995$), while the inclusion of an analyzer (black) decreases the sensitivity to $-2.99 \times 10^{-2} \text{ mT}^{-1}$ ($R^2 = 0.984$), a $\sim 52\%$ reduction. This is most likely due to a sharp reduction on the number of modes contributing to $I(x,y)$. All experiments going forward were conducted with input polarizer only to maximize sensitivity.

B. Magnetic hysteresis

Magnetic materials can present magnetization hysteresis loops when submitted to cyclic fields if saturation occurs (178). Due to this phenomenon, it is of interest to study this behavior in magnetic field probes to minimize errors (179,180).

To study this behavior in the magnetoptic glass fiber probes, two sets of experiments were conducted. First a regular commercial MMF was tested as a reference, a series of specklegram videos were collected in which the electrical current fed to the coil steadily increases (and, by consequence, H) from 0 to 2400 mA in steps of 200 mA, afterwards the current was decreased in steps of -200 mA from 2400 mA back to zero. The “temporal” evolution of μ_z , i. e., μ_z per video is depicted in Figure 48a, as it can be observed the μ_z curves for increasing and decreasing H are approximately mirrored in relation to each other, and when plotted against H instead, the curves approximately coincide (Figure 48a). This shows that the response of the MMF does not exhibit magnetic hysteresis, which is to be expected since it does not contain added magnetic ions in the glass composition.

On the other hand, when the same experiment was conducted for the BGB-6Tb fiber – this time with steps of 100 mA, from 0 mA to 2500 mA and back to 0 mA for better detail – it resulted in loading (increasing H) and unloading (decreasing H) curves that diverge from each other, Figure 48c, indicating that the presence of the magnetic ions in the glass composition leads to some sort of hysteresis in the response. However, it was also observed that this issue can be avoided by re-referencing the ZNCC calculations, i.e., if $I_0(x,y)$ is chosen as the 0 mA specklegram video at the start of the test for the determination of μ_z for the Increasing H curve, and the specklegram video for 2500 mA is used as $I_0(x,y)$ for calculating μ_z of the Decreasing H curve, then μ_z match again (Figure 48d). A more in-depth investigation of the mechanisms that lead to this behavior will be conducted in later studies.

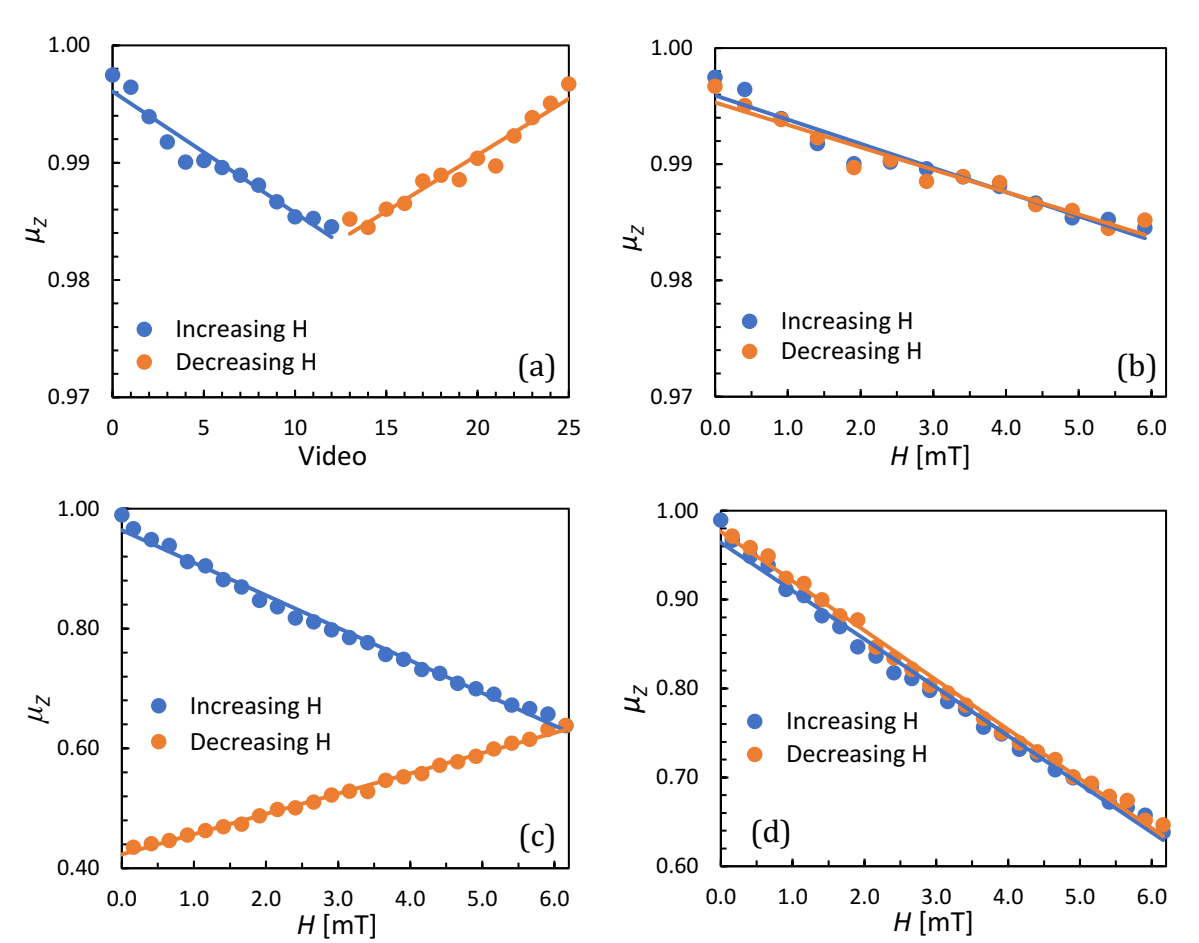


Figure 48 – Magnetic hysteresis test results. (a): Temporal evolution of μ_z for a commercial MMF showing a mirrored response for increasing and decreasing H . (b): μ_z as a function of H for the MMF subjected to the cyclic H . (c): Results for the BGB-6Tb fiber showing divergence between the increasing and decreasing H curves. (d): Diverge between datasets for the BGB-6Tb eliminated by redefining $I_0(x,y)$ for μ_z calculations.

C. Characterization of the fiber probes

The response of all Tb^{3+} doped fibers to H was then evaluated, alongside with a regular commercial MMF for comparison purposes using the procedures detailed earlier (one reference specklegram video for $H = 0$ mT, plus 25 with electric current steps of 100 mA up to 2500 mA, $H = 6.16$ mT). Results in terms of ΔZ as a function of H (in mT) are compiled in Figure 49.

Compared to the doped fibers, the response of the conventional MMF presents itself almost as a horizontal line, clearly demonstrating a great sensitivity increase for MO glasses with Tb^{3+} ions. All response curves exhibited good linearity (solid lines), with R^2 of 0.943, 0.995, 0.995 and 0.997 for the MMF, BGB-6Tb, BGB-8Tb and BGB-10Tb fibers respectively. The respective sensitivities ($S = d\Delta Z/dH$) are $1.49 \times 10^{-3} \text{ mT}^{-1}$, $6.18 \times 10^{-2} \text{ mT}^{-1}$, $7.01 \times 10^{-2} \text{ mT}^{-1}$

and $8.78 \times 10^{-2} \text{ mT}^{-1}$, a $\sim 59\times$ increase from the MMF to the BGB-10Tb fiber. The respective deviations $\bar{\sigma}$ are of 8.39×10^{-5} , 5.75×10^{-4} , 6.38×10^{-4} and 1.17×10^{-3} .

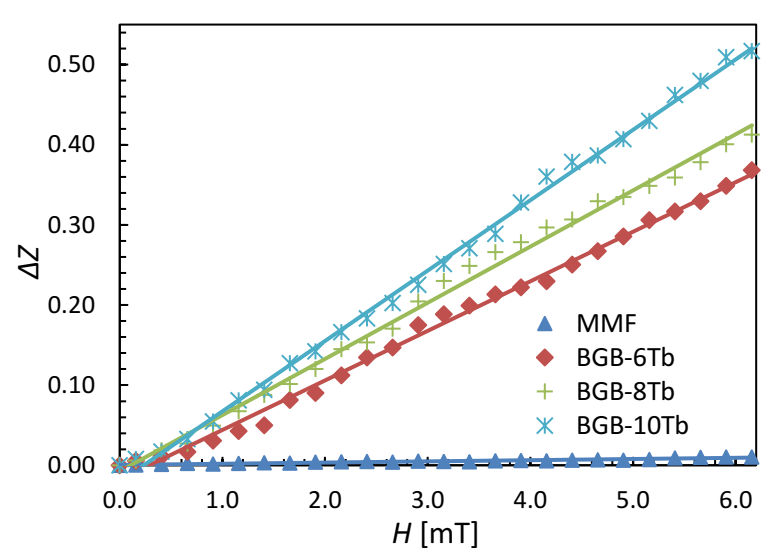


Figure 49 – Response of each fiber to H . Solid lines are linear fits of the data. Dark blue triangles: MMF ($R^2 = 0.943$); red diamonds: BGB-6Tb fiber ($R^2 = 0.995$); green crosses: BGB-8Tb fiber ($R^2 = 0.995$); light blue asterisks: BGB-10Tb fiber ($R^2 = 0.997$).

Considering a ΔZ resolution of $2\bar{\sigma}$ for a $\sim 95\%$ confidence level, the resolution of the probes can be estimated as $\Delta H = 2\bar{\sigma}/S = 0.11 \text{ mT}$, $1.86 \times 10^{-2} \text{ mT}$, $1.82 \times 10^{-2} \text{ mT}$ and $2.65 \times 10^{-2} \text{ mT}$ for the MMF, BGB-6Tb, BGB-8Tb and BGB-10Tb fibers respectively. For quick reference and ease of comparison all these metrics are compiled in Table 2. The increase in sensitivity as a function of the Verdet constant (V) of the fibers is also shown as a scatter plot in Figure 50, highlighting a good linearity between the quantities ($R^2 = 0.989$) with dS/dV of $1.31 \times 10^{-6} \text{ m/rad}$.

Table 2 – Summary of sensor metrics including the Verdet constant V , deviation $\bar{\sigma}$, sensitivity S and resolution ΔH for each tested fiber (110).

Fiber	V [rad/Tm] @ 650 nm	$\bar{\sigma}$	S [mT ⁻¹]	ΔH [mT]
MMF	3.7	8.39×10^{-5}	1.49×10^{-3}	0.11
BGB-6Tb	53.1	5.75×10^{-4}	6.18×10^{-2}	1.86×10^{-2}
BGB-8Tb	58.8	6.38×10^{-4}	7.01×10^{-2}	1.82×10^{-2}
BGB-10Tb	68.3	1.17×10^{-3}	8.78×10^{-2}	2.65×10^{-2}

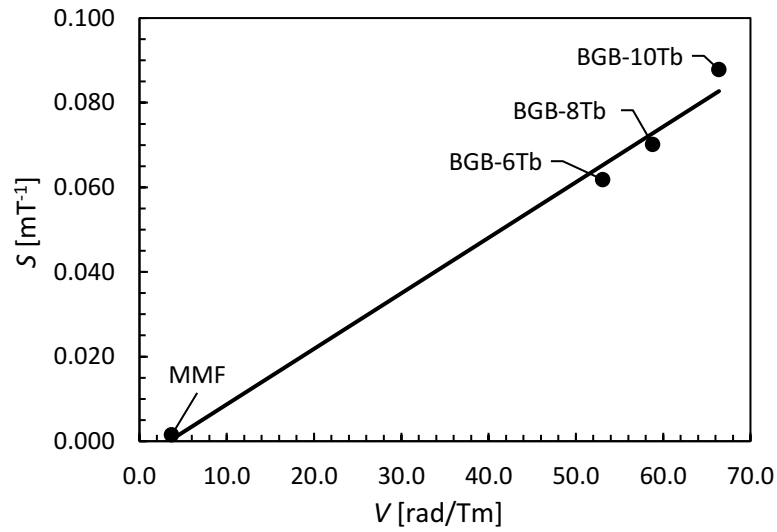


Figure 50 – Sensitivity S as a function of the Verdet constant V of each fiber, showcasing the sharp increase in sensitivity for high V fibers. Solid line is a linear fit of the data ($R^2 = 0.989$). (110).

In comparison to the other FSS, in (163) the authors reported a ~ 0.8 mm/mA sensitivity regarding the Young's fringes measurement using a solenoid, whereas in (165) it was achieved a $\sim 0.04^\circ/\text{mT}$ detection capability with the assessment of the specklegram rotation through polarization-based techniques. Even though the latter present linear response for a broader dynamic range (100 mT), the practical resolution is probably limited to $0.1/0.04 = 2.5$ mT and the implemented interrogation scheme is more complicated than the proposed one. Concerning the other types of OFS, the Faraday-effect sensor reported in (159) provided $\sim 28.1^\circ/\text{T}$ sensitivity for up to 3.2 T, whereas the magnetostrictive approach shown in (160) yielded $5.61 \mu\text{T}/\sqrt{\text{Hz}}$ resolution within the 1.22 to 2.53 mT range. Ultimately, the photonic crystal fiber filled with ferrofluid developed in (162) resulted in a maximum resolution of $\sim 9 \mu\text{T}$ for ≤ 60 mT.

5 SENSORS BASED ON (BIO)POLYMER FIBERS

In the same vein as the previous chapter, this chapter discusses fiber sensors fabricated using polymeric materials, be it agarose biopolymer (Sections 5.1 and 5.3) or plastics (Section 5.2). Publications based on these works have also been made, namely reference (181) pertaining to Section 5.1, (182) for Section 5.2 and (183) for Section 5.3. Figures in this chapter are for the most part reused or adapted from the listed publications. Additional information and figures not included in the published manuscripts is also presented when possible.

5.1 Agarose-based structured optical fiber

Biocompatible and biodegradable optical fibers are emerging, breakthrough technologies for enabling the assessment and manipulation of biological systems by their interaction with light. Such devices are eligible as implantable probes for in vivo measurements (184,185) and endoscopes for medical imaging (186), being completely absorbed by the organism after their use. Another promising application is the monitoring of biochemical variables, wherein the waveguide can be used both as the sensing probe and encapsulation medium for microorganisms (187). Moreover, localized and controlled light incidence is suitable for optical actuation purposes such as neuronal stimulation through optogenetics (188).

In this context, waveguides made of hydrogels present remarkable characteristics in terms of tailoring optical and mechanical properties of the material by controlling the polymer/water content, yielding transparency, flexibility, and stability (189,190). Fabrication is usually simpler than other fiber types (191,192), and hydrogels are also suitable for functionalization by embedding biomolecules in the material pores as well as for cell encapsulation (189). For instance, slab waveguides made of poly(ethylene glycol) (PEG) coupled to standard optical fibers were developed for detecting heavy metal ions in vivo, either by encapsulating cells or embedding fluorescent nanoparticles (188,193). Hydrogel-based fibers were also conceived with PEG core and alginate cladding structure to assess blood oxygen saturation (184) and glucose concentration (194). Another approach is comprised of an

alginate-acrylamide multimode fiber by adjusting the numerical aperture according to the acrylamide concentration, presenting sensitivity to refractive index and strain (195).

Besides the aforementioned hydrogels, agarose exhibits excellent biocompatibility and provides excellent physical and biochemical conditions for cell encapsulation and nutrients permeation (184,196). Agarose presents low-cost, food-grade characteristics, thermo-reversible gelation, and high transparency in the visible range, whereas the refractive index can be increased by adding sugar to the hydrogel solution (196,197). In previous reports, a gelatin core, agarose cladding planar waveguide was fabricated by spin coating to obtain devices with core thickness ranging from 2 μm to 2 mm, providing practical transmittance in the visible spectrum over 50 mm length (198). Another approach comprised of a $130 \times 130 \mu\text{m}^2$ rib waveguide made of agarose through soft lithography method, with the ability to encapsulate living cells (187). However, as the time of this study there was no mention of agar-based optical fibers in the literature to the best of knowledge.

This study then reports a novel structured optical fiber made of food-grade agarose. This was the first realization of an agar-based fiber in contrast to the previous planar and rib waveguides, comprising a straightforward fabrication method to produce devices eligible for in vivo imaging and light delivery, as agar is biocompatible and edible. Moreover, this was the first structured hydrogel fiber reported in the literature.

5.1.1 Materials and methods

The fabrication method (Figure 51) of the structured agarose fiber consisted of pouring food-grade agarose solution into a glass mold (inner diameter of 3 mm) with six internal rods (diameter of 0.5 mm). The rods were arranged in symmetrical fashion and fixed to the external tube using polymer holders, whereas central rods connected to the extremities supported the structure and created the fiber core. Food-grade agar powder was added to distilled water and heated in a hot plate (IKA R Basic KT/C). The solution was continuously agitated at $\sim 100^\circ\text{C}$ for 2 min. Then, the temperature lowered to $\sim 80^\circ\text{C}$ and the sample kept at rest for 2 min to remove air bubbles. After pouring the liquid agar solution inside the mold, the tube was sealed with Teflon tape and cooled in a refrigerator until the sample becomes solid. Finally, the rods were carefully removed to form the air holes, the fiber was pushed from the mold, and the end faces cleaved using a razor blade.

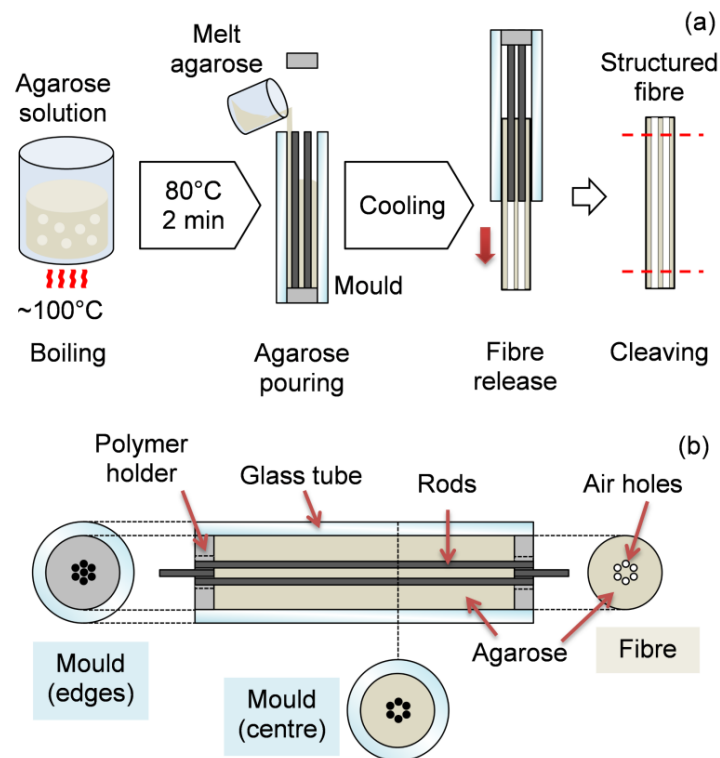


Figure 51 – (a) Fabrication of structured agarose fiber: boiled agar solution is poured into the mold, and the fiber is released after solidification in a refrigerator. (b) Detail of the fiber inside the mold with cross-section views of the mold edges and center, as well as the fiber end face: the glass tube supports the fiber structure whereas air holes are formed by the rods (181).

A multimode optical fiber made of 2% w/v agarose is shown in Figure 52a/b. To demonstrate the guiding capabilities, light from a HeNe laser illuminates the fiber core, producing the far-field speckle-like pattern observed in Figure 52c. Likewise microstructured glass fibers, light is confined to the core due to the refractive indexes difference between air holes and the fiber material. Cladding and holes follow the mold dimensions (~ 2.5 mm and ~ 0.5 mm, respectively) whereas the core (~ 0.64 mm diameter) is supported by ~ 0.08 mm width agar bridges, suggesting that the size could be reduced by tailoring mold geometry accordingly.

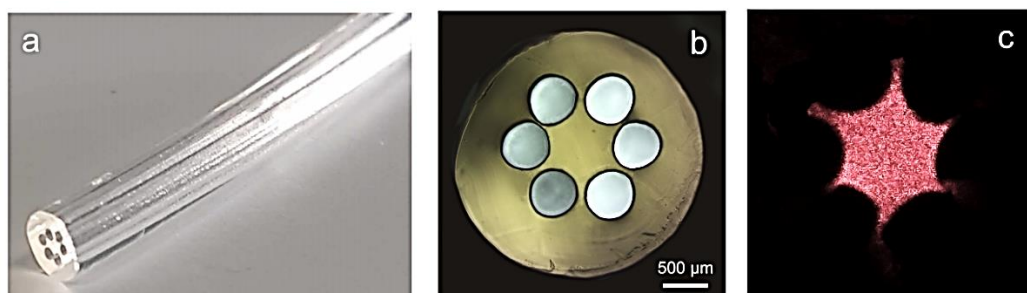


Figure 52 – Agarose-based structured optical fiber: (b) cross-section view of the end-face and (c) output speckle field of the core-guided modes. The fiber has 60 mm length, diameters of 0.64 mm, 2.5 mm, and 0.5 mm for core, cladding, and holes respectively, and bridges of ~ 0.08 mm width (181).

Regarding the experimental setup, for measurements of surround fluids the setup depicted in Figure 53a was used. The 2% w/v agarose fiber was inserted in a plastic tube with a small aperture for dripping the sample and to prevent liquid from flowing into the air holes. Droplets were poured using a micropipette, which is enough for covering the exposed cladding surface without displacing the fiber. Light from a HeNe laser was coupled to the fiber core using a 40× objective, and the output beam expanded by a 20× lens into the CCD of a camera. Several propagating modes are excited because of the core dimensions, and the interference between these multiple modes produces an output speckle pattern. The acquired speckle patterns were then processed using ZNCC and EZNCC implementations in MATLAB that converts the speckle field images to grayscale, reduce them to a square 201×201 pixels region-of-interest and apply a 2D discrete wavelet transform (Daubechies db4) filter before performing the correlation calculations. As for the assessment of liquids or gases inserted into the airholes of the structured agarose fiber, a 2% w/v agarose fiber core was filled with the analyzed sample by immersing the fiber tip into the liquid and using a syringe attached to the other end face for drawing fluids inside the air cavities. This procedure is repeated until all holes are completely filled with liquid and no air bubbles can be observed. Subsequently, the fiber was cleaved, and the core is excited with a HeNe laser, while the output beam expanded by a 10× objective was projected on a screen and captured by a CCD camera, as shown in Figure 53b. Finally, the normalized speckle field intensities in the core, cladding, and holes were evaluated by the same image processing routines as before.

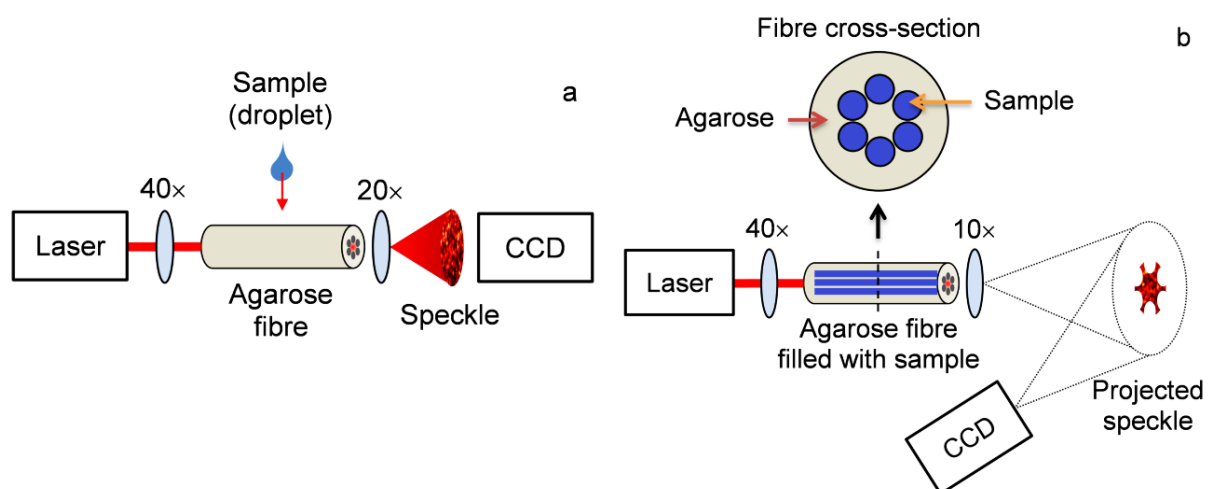


Figure 53 – Experimental setups for fiber sensing: (a) measurement of surrounding fluid droplet by speckle field analysis; (b) assessment of fluids inserted into all the fiber holes based on the average intensity of projected speckle pattern (181).

5.1.2 Results and discussion

The optical characteristics of the structured fiber depend on the composition of agar solution. For instance, Figure 54a and b show the effect of concentration on the refractive index (RI) of bulk agarose samples. The experiments were conducted for pure agar (0 to 4% w/v) as well as for sucrose addition to 2% w/v agarose solutions. The refractive index was measured in a MISCO PA202 Palm Abbe refractometer with 1×10^{-4} RIU resolution at 589.29 nm. Samples were prepared by diluting agar powder in 50 mL of distilled water, with a further addition of food-grade sucrose into the boiled agarose solutions. The solidified materials were then cut into ~ 1 mm side cubes and carefully placed over the refractometer detector to avoid air interfaces. RI increases linearly with concentration, yielding $\sim 1.4 \times 10^{-3}$ and $\sim 3.1 \times 10^{-3}$ RIU/g (RI unit per gram) enhancement for agarose and sucrose respectively, making it feasible to adjust the fiber light guiding characteristics.

The transmission spectra of bulk samples were measured with a Hitachi U-3000 spectrophotometer (± 0.3 nm accuracy within the 190 to 900 nm range) using 10 mm path length quartz cuvettes. Agar solutions with different concentrations were solidified inside the cuvettes and analyzed using DI water as a reference. For agarose fibers, an NKT Photonics SuperK Compact supercontinuum source was used to illuminate a 30 mm long fiber, the light was collected by a multimode fiber and then measured with a Yokogawa AQ-6315 optical spectrum analyzer (~ 0.05 nm resolution from 350 to 1750 nm). As noticed in Figure 54c, the transmitted power in the visible range decreases with agar concentration. In addition, besides the possible waveguide losses, water absorption bands were also observed in the structured fiber spectrum at 950 nm and >1200 nm (199).

Finally, Figure 54d shows the optical loss for 2% w/v agarose fibers evaluated by the cut-back method using the HeNe laser and a u-Eye IDS UI-2230SE-C HQ CCD camera (1024 \times 768 pixels). The input and output powers were calculated as the average pixel values in grayscale. The experiments were performed for 30 mm length, 2% w/v agar fibers placed on a microscope slide and cleaved in steps of ~ 5 mm. The loss in dB/cm was evaluated by fitting the experimental data with a linear function, yielding 3.23 dB/cm (attenuation coefficient of 0.74 cm^{-1}). This result is significantly lower than the 13 dB/cm reported for agarose rib waveguides (187) but higher than the obtained for alginate-based fibers (0.45 dB/cm) (193). Nevertheless, the lowest optical losses are expected at ~ 800 nm and ~ 1100 nm due to the improved

transmittance at this wavelength, as shown in Figure 54c. It must be stressed that the 3.23 dB/cm loss is still high in comparison to glass and polymer fibers, and fabrication is also restricted by the mold dimensions, so it is not possible to produce kilometers of fibers like in preform drawing towers. Nevertheless, short fiber segments can be coupled to silica launching and collecting fibers to be used in laboratory setups for biochemical sensing and light delivery.

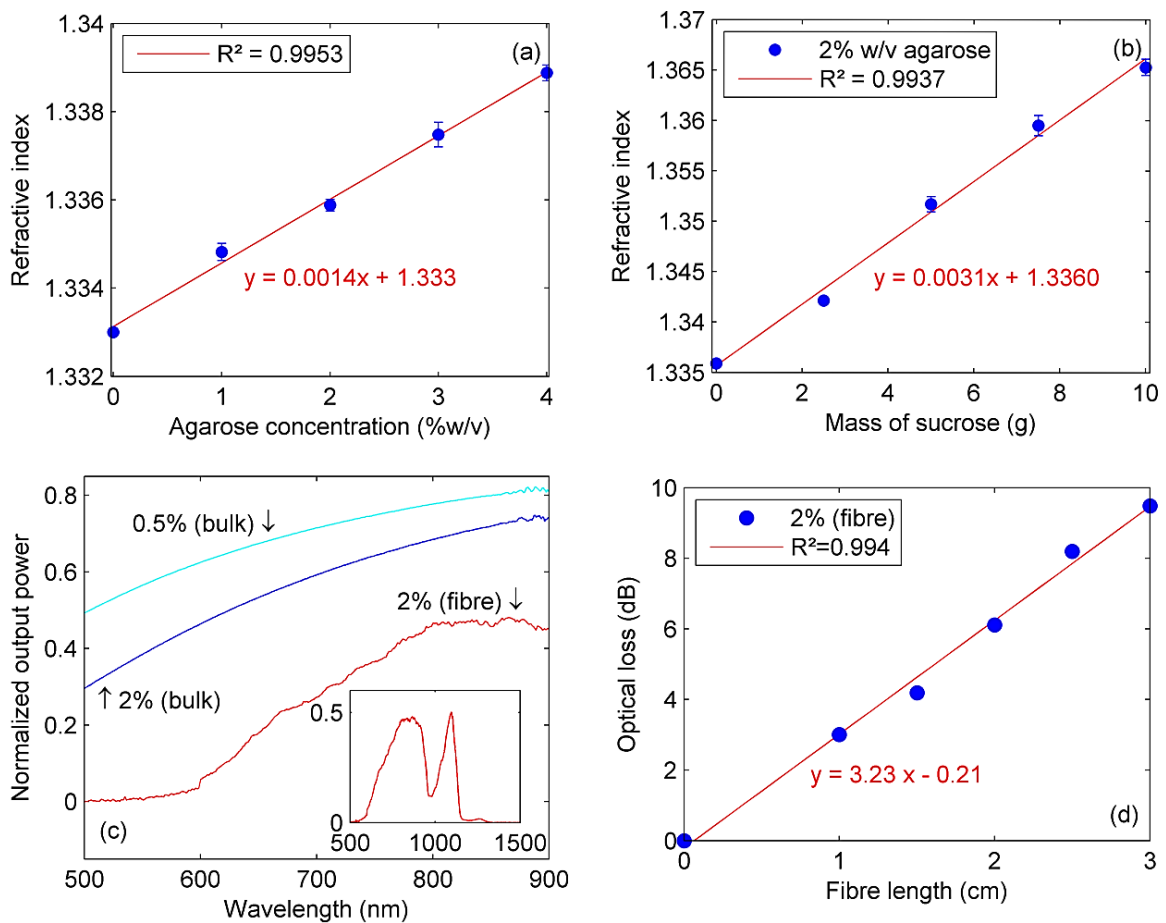


Figure 54 – Optical characterization: (a) refractive index of bulk agarose samples; (b) refractive index as a function of sucrose addition in a 2% w/v agarose samples; (c) output power spectra for agarose bulk and fibre samples, the inset shows the output spectrum of a 2% w/v agarose fibre; and (d) fibre optical loss at 633 nm obtained by the cut-back method (181).

For the sake of comparison, Table 1 summarizes the characteristics of hydrogel fibers and planar waveguides reported in previous works. The optical loss for the structured fiber is compatible with other agarose and alginate-based devices, but fiber dimensions must be reduced to improve light guiding and coupling conditions. On the other hand, larger cores are suitable for speckle field interrogation, as the increased number of guided modes produces a more granular and thus sensitive output speckle pattern.

Table 3 – Characteristics of hydrogel-based optical fibers and waveguides reported in the literature (181).

Ref	Material	Type	Dimensions	Optical Loss
This	Agarose	Structured fiber	0.64 mm core, 2.5 mm cladding (diameter)	3.23 dB/cm (633 nm)
(187)	Agarose	Rib waveguide	130×130 μm^2 (cross-section area)	13 dB/cm (633 nm)
(198)	Gelatin core, agarose cladding	Planar waveguide	2 μm –2 mm core (thickness)	N/A
(188)	Polyethylene glycol diacrylate (PEGDA)	Planar waveguide	1×4 mm^2 (cross-section area)	0.17–0.68 dB/cm (450–550 nm)
(193)	PEGDA	Planar waveguide	1.1×5 mm^2 (cross-section area)	1.7–2.8 dB/cm (450–750 nm)
(184)	PEGDA core, alginate cladding	Fiber	0.2–1 mm core, 0.4–1.2 mm cladding (diameter)	0.3 dB/cm (492 nm)
(200)	PEGDA core, alginate cladding	Fiber	0.2–2 mm core, 0.3–2.2 mm cladding (diameter)	2.6–8.3 dB/cm (532 nm)
(194)	PEGDA core, alginate cladding	Fiber	0.2–2 mm core, 0.3–2.2 mm cladding	1–6 dB/cm (532 nm)

The ability of agarose to undergo structural changes under temperature, humidity, and pH variations makes the structured fiber suitable for optical sensing purposes. For example, Figure 55a presents the fiber response to surrounding fluids. A fluid sample (water or acetone) is dripped on the 2% w/v agar fiber excited with HeNe laser, whereas the output speckle field was monitored during 1 min by the camera. Subtle variations in acquired images are quantified with EZNCC. The correlation coefficient decreases continuously in case of the waveguide subjected to the air, which is associated to a gradual volume reduction by syneresis (201), *i.e.*, slight fiber geometry deviations affect the core modes distribution, leading to spatiotemporal changes in the speckle pattern. On the other hand, adding a water droplet yields an abrupt variation followed by a slow decrease of the EZNCC signal, whereas acetone produced a faster decay tendency. Disregarding the initial variation, caused mostly by mechanical disturbance, the subsequent speckle field drift can be explained by agarose swelling due to water absorption, or shrinkage related to dehydration with acetone. These results corroborate the behavior of bulk agar samples, wherein absolute volume changes obtained by immersion in water are less noticeable than those observed for acetone (201). Therefore, one may apply the agarose fiber as a consumable chemical sensor: regarding an *in vivo* application, for example, the optical

signal decay rate due to the fiber degradation could be related to biochemical parameters in-loco for investigating diseases.

An alternative to the previous sensing method is measuring the effect of fluids inserted into the air holes. A 2% w/v agarose fiber ($n = 1.336$) is filled with air ($n \approx 1.000$), water ($n = 1.333$), and ethanol ($n = 1.361$). Average intensities in the core, cladding, and holes are shown in Figure 55b. The refractive index difference between 2% w/v agar ($n = 1.336$) and air ($n \approx 1.000$) causes the light to be highly confined to the core, as expected. Conversely, the RI of water ($n = 1.333$) is quite similar to the agar one, therefore power is leaked through the suspending agarose bridges and is partially coupled to the holes and cladding, increasing their respective relative intensity values (202). Finally, regarding ethanol, leaked light is fairly coupled into the holes because the RI in this region ($n = 1.361$) becomes greater than the surrounding agar substrate. Therefore, it is demonstrated that fluid samples can be identified by comparing the relative intensities observed for each region of the projected fiber speckle field. It is worth noticing that sensitivity and measurement range can be enhanced by adjusting the composition of agarose solution (*i.e.*, the RI value), so the optical fiber would be capable to assess a variety of substances. Furthermore, functionalization of agarose is also possible, expanding the range of detectable chemical and biological agents (203,204). Alternatively, one may investigate the transmitted spectrum of core-propagating modes since part of the light wave travels as evanescent fields that interact with the filled holes.

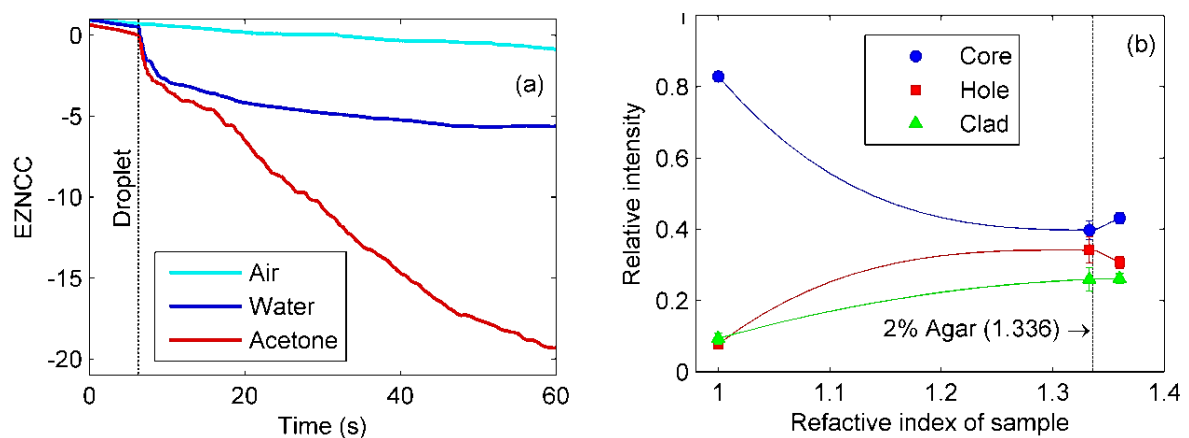


Figure 55 – Sensing with the agarose structured fiber: (a) effect of surrounding fluid on the EZNCC. The sample dripping event is indicated by the vertical line. (b) Relative intensity values of the light transmitted by fiber core, cladding, and holes. Solid lines are guides to the eye, whereas the vertical line indicates the RI of 2% w/v agarose (181).

One promising application yet to be explored is using the agarose fiber simultaneously as an optical sensor and growth medium for microorganisms. Both excitation and fluorescent lights can be guided through the structured fiber core, making it simple to evaluate the spectral response under different environmental conditions. The waveguide may be designed as a disposable sample unit containing the necessary nutrients and immobilized cells, which could be promptly coupled to the optical instrumentation (spectrometer or microscope) for practical analyses. Besides the prospective uses for in vivo imaging and light delivery, the agarose fiber may also be suited for chemical measurements based on the sensitivity provided by the waveguide material and the holey structure, with potential applications for in vivo monitoring as the agar is biocompatible and edible. Moreover, the fiber can also be used as a substrate for cell immobilization and as a growth medium, so the biochemical properties can be assessed through the interaction between the sample and the transmitted light. Future works will be focused on optimizing the structured fiber design to minimize the transmission losses, characterizing additional fiber properties such as nonlinear refractive index and group velocity dispersion, and investigating its biochemical sensing capabilities in practical scenarios.

5.2 Reusable polymer fiber strain sensor with memory capability based on ABS crazing

Plastic optical fibers (POF) can present intrinsic “memory effects” when subjected to large strains (205,206) or high temperatures (205,207), in which the effects of the load are still observable when interrogating the fiber after the load is removed. Nonetheless, little attention was given to the reversibility of the memory effect (205). It has been observed to vanish over time under continued application of the load (206), or to be non-reversible and attributed to thermal degradation (207). This work was started on the premise to learn how to harness this memory effect and ways to reverse it to produce reusable sensors.

Polymeric materials under mechanical loads can deform by three mechanisms, shear yielding, crazing or cracking (208). Glassy polymers and rubber-toughened glassy polymers are craze-prone polymers, meaning craze initiation is possible when a critical stress/strain is reached in the material (209,210). When crazing occurs the amorphous polymer chains undergo localized flowing, forming fine semi-crystalline fibrils bridging nanometric voids (208,211), this high spatial frequency density modulation results in a strong scattering of incident light due

to the associated refractive index modulation (208), leading to a characteristic whiteish color. This effect is known as stress whitening and has been an ample object of study regarding polymer materials both for aesthetic and mechanical/chemical performance reasons (212-214). It has also been suggested that stress whitening can be exploited for experimental stress analysis (215). Methods on reversing stress whitening can also be found in specialized literature, including pulling stress whitened samples in a hydrostatic pressure environment at room temperature (216), and heating the polymer above its recrystallization temperature (217).

As acrylonitrile butadiene styrene (ABS) is a rubber-toughened (styrene) glassy polymer, and, as such, is craze prone (209,210), combined with the fact that it is a thermoplastic, it can be readily reworked by heating the polymer above its glass transition temperature (218). This implicates that the crazing can be reversed by heating the affected area as proposed in (217). ABS being a thermoplastic also enables working it into plastic optical fibers in a draw tower, and so it was chosen for use in this study. To the best of the author's knowledge this was the first time such a sensor was reported in the literature.

5.2.1 Materials and methods

The proposed POF sensor consists of a step-index fiber with a polymethylmethacrylate (PMMA) cladding and an ABS core. The optical properties of ABS were characterized prior to the fiber fabrication by utilizing a test piece prepared from a 60 mm long ABS filament piece heated to 150°C for one hour while being pressed among two microscope slides with a top weight Figure 56a. A flat 0.5 mm thick sample was produced (Figure 56b, top), allowing the material to be optically characterized in the visible and infrared. Figure 56c shows the attenuated total reflection (ATR) FTIR measurement (PerkinElmer, Spectrum 400, resolution 4 cm⁻¹) where the typical ABS absorption lines could be observed at 1602, 1452, 966, 759 and 698 cm⁻¹ (219). It should be noted that the proportions of acrylonitrile, butadiene and styrene can vary from brand to brand, impacting the strength of each absorption line.

To characterize the optical response of the sample subjected to large strains, the planar sample was manually bent multiple times until severe stress whitening due the crazing formation was observed (Figure 56b, bottom) (208-211). The transmittance signal from 350 to 2200 nm was measured with an UV-VIS spectrometer (Agilent, Cary 5000). Data from the same sample in three different situations are presented in Figure 57a: i) original state (clear), ii) after bending and, iii) after bending and subsequent heating at 105 °C for 90 seconds.

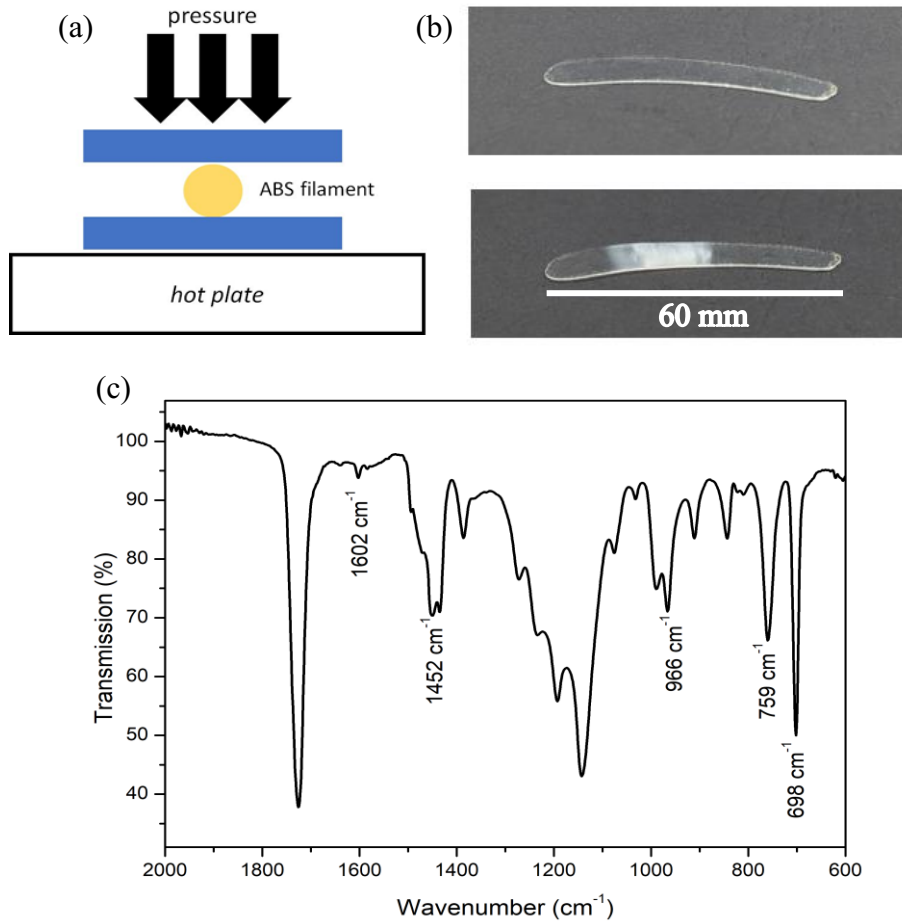


Figure 56 – (a) Schematic of the planar sample fabrication procedure; (b) Pictures of the clear (top) and bent (bottom) samples; (c) Transmission spectrum where typical absorption lines are observed (182).

From this data the absorbance due to the whitening ($A_{whitening}$) and the residual absorbance ($A_{residual}$) of the sample after being heated were calculated with Eq. (5.1) and Eq. (5.2) respectively:

$$A_{whitening} = -\log_{10} \left(\frac{T_{bent}}{T_{clear}} \right) \quad (5.1)$$

$$A_{residual} = -\log_{10} \left(\frac{T_{bent+heated}}{T_{clear}} \right) \quad (5.2)$$

where T_{clear} , T_{bent} and $T_{bent+heated}$ are the transmittance signals shown in Figure 57a. As clearly observed in Figure 56b (bottom), the occurrence of crazing strongly scatters the visible light, leaving the characteristic whitish appearance (stress whitening). This induces a high loss in the visible range, with absorbance values ranging from 0.65 to 1.7 (transmittance from 21% to 2%) in the wavelength interval from 400 to 650 nm. As the loss due to whitening is related

to scattering, which shows strong wavelength dependence, it should be negligible at longer wavelengths. The result shown in Figure 57b corroborates that indicating an absorbance as low as 0.037 at 2000 nm. While the wavelength dependency observed in the transmission and absorbance curves for the crazed ABS suggest that the wavelength of the light signal propagating along a fiber with an ABS core can significantly tune the sensitivity to applied loads, it is important to consider how the presence of a cladding influences the general spectral response of the fiber, as discussed further in Section 5.1.2.

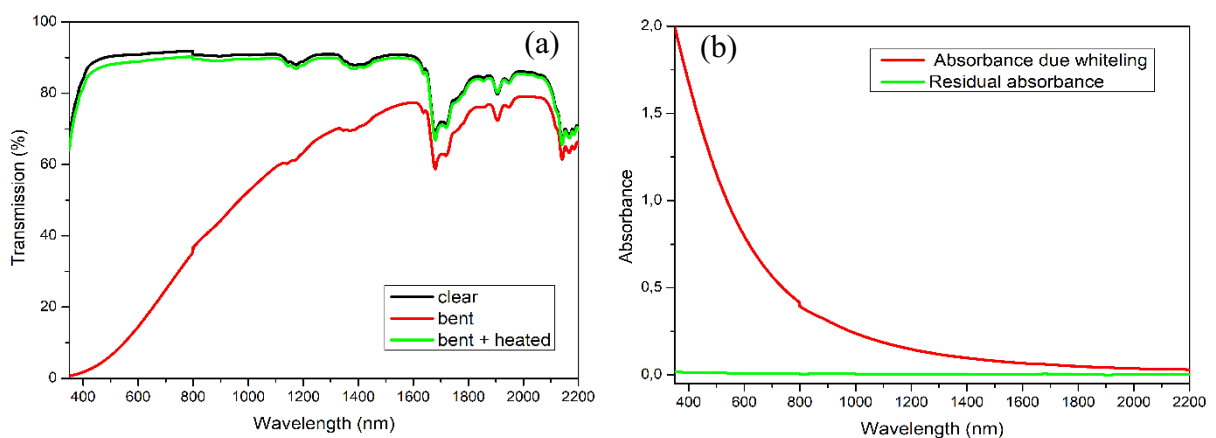


Figure 57 – (a) 0.5 mm thick sample transmittance in its original state (clear), after bending and thermal treatment; (b) Absorbance due the whitening process and the residual absorbance after heating of the sample close to its glass transition temperature for 90 seconds. The signal discontinuities at 800 nm are due to the detector and grating change in the spectrometer (182).

After heating the planar sample with a temperature close to the material glass transition temperature, the sample recovers its transparency. Residual absorbance is lower than 0.013 for the studied wavelength range. Transmittance of the recovered sample is higher than 96% of the transmittance of the original sample in the whole studied wavelength range.

As for the fiber probe, it was fabricated by drilling a hole with diameter of 1.8 mm through a 70 mm diameter PMMA cylinder, introducing a 1.75 mm thick 3D-printer ABS filament in the drilled hole and pulling the preform on a POF draw tower in a two-step process. Step 1 reduced the diameter of the preform from 70 mm to 10 mm, whereas step 2 further reduced the diameter down to the fiber's final dimensions. Drawing parameters for step 2 were: furnace temperature of 210 °C, 5 mm/min preform feed speed and around 1 m/min drawing speed. Figure 58 shows an optical microscope image of the fabricated PMMA/ABS fiber. The ABS core has a diameter of ~ 200 μm , and the cladding a diameter of ~ 650 μm .

It is worth noting that both the PMMA cylinder and 3D-printer ABS filament are commercial grade materials obtained from local suppliers, different compositions offered by distinct suppliers may impact the susceptibility of the fiber to undergo stress whitening.

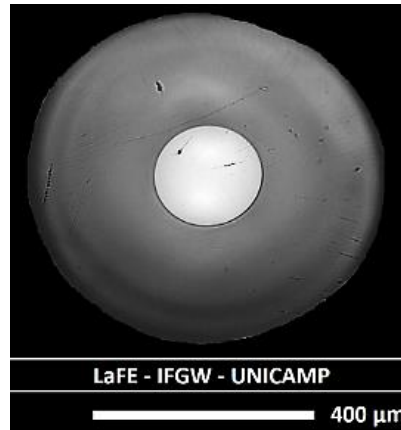


Figure 58 – Optical microscope image of the ABS core, PMMA cladding fiber (182).

5.2.2 Results and discussion

A possible application for these reversible probes is in structural health monitoring. Thermal recuperation of initial conditions also increases the expected life cycle of the probe, ensuring it can continue to provide accurate data after more thorough assessment of the abnormal events has been performed, which would not be possible with conventional silica fibers (due to fiber breakage) or non-recoverable POFs (loss of sensitivity, measurement range and/or calibration). These characteristics, combined with the intrinsic lightweight and electromagnetic interference immunity of POFs, are highly desirable in structural health monitoring applications, from civil infrastructure to the oil and gas or aerospace industry. In practical applications structures are subjected to a combination of various loading sources, such as tensile and flexural loads. To this effect the response of the proposed POF strain sensor was characterized for three distinct mechanical loading conditions: indentation (transverse compressive load), flexural load (macro-bending), and tensile load.

A. Indentation Test

In the indentation test a 150 mm long fiber piece was subjected to a controlled transverse compressive load to its middle point. Figure 59 is a sketch of the experimental setup: light from

a white light source was launched into the test fiber with a 20× objective lens (L1), while the transmitted light passed through an iris diaphragm to isolate the light traveling through the fiber core and was focused into a photodiode power sensor (Thorlabs, S120C) using a second 20× lens (L2). The photodiode was connected to a power meter to collect the transmitted power data, and the indentator device consists of a small steel piece with a rounded edge secured to a vertically mounted precision linear guide controlled by a step motor.

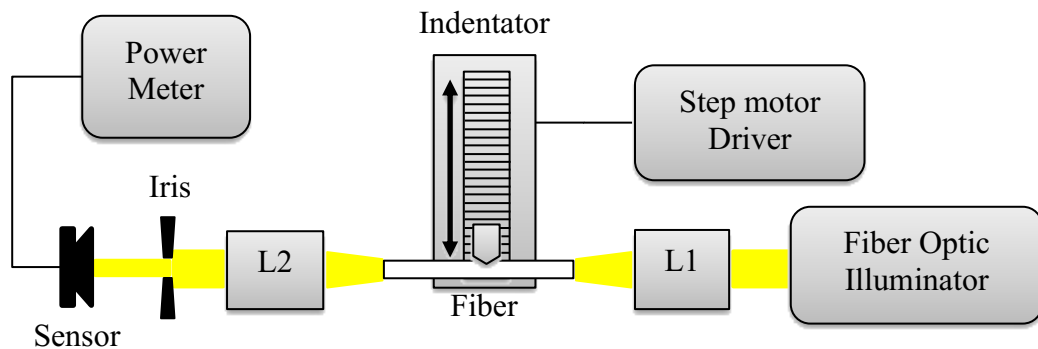


Figure 59 – Indentation test experimental setup, L1 and L2 are 20× objective lenses (182).

Firstly, the position of the indentation head was adjusted manually so it gently touched the surface of the fiber, then the step motor driver was turned on and the current position of the indentation head was set as the zero point. Afterwards the indentation head progressively pressed down on the fiber in steps of 0.01 mm until a depth of 0.25 mm was reached, afterwards steps of 0.02 mm were used instead. Transmitted power data was collected for each step.

Figure 60a shows the transmission loss observed as the indentation head pressed down on the fiber, no transmission loss is observed for an indentation depth lower than 0.05 mm, this can be attributed to a small clearance between the indentation head and the fiber after the manual positioning. The orange line in Figure 60a is a linear fit of the data in the $0.10 \text{ mm} \leq \text{indentation depth} \leq 0.65 \text{ mm}$ range. Whitening became visually observable at an indentation depth of 0.15 mm, at this point the indentation head was returned to the 0.05 mm position to collect data on the residual power loss caused by the whitening. More data on the residual loss was collected after reaching indentation depths of 0.25, 0.35, 0.45, 0.55, and 0.65 mm. Figure 60b is a plot of the residual loss due to stress whitening as a function of the indentation depth, the blue line is a linear fit of the data. As can be observed, total transmission loss under stress and residual transmission loss both vary linearly with the indentation depth ($R^2 = 0.997$ and

0.967 respectively). As an indentation probe the fiber exhibits a transmission loss of $16.28 \text{ dB}\cdot\text{mm}^{-1}$ during the application of the load, and a residual loss (memory) of $3.95 \text{ dB}\cdot\text{mm}^{-1}$.

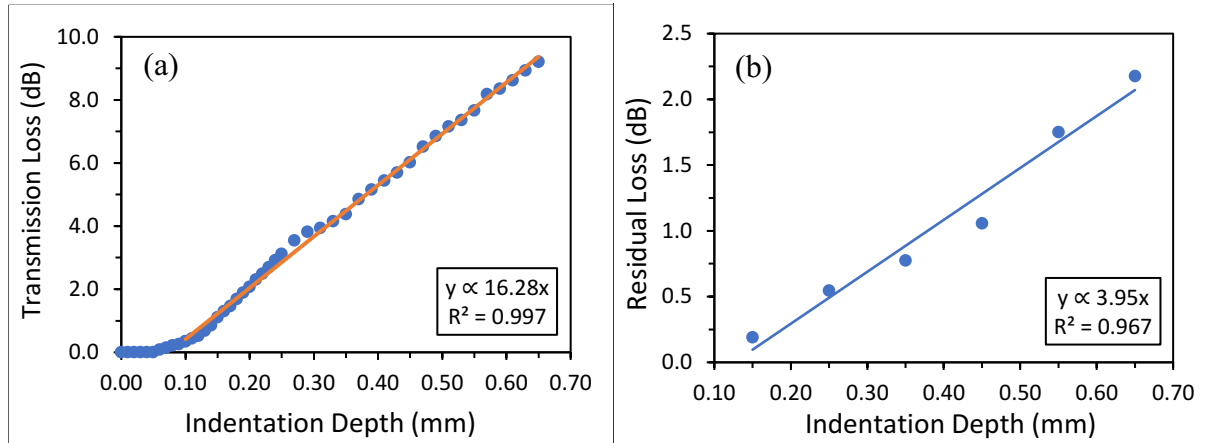


Figure 60 – (a) Transmission loss as a function of indentation depth, the orange curve is a linear fit of the data ($R^2 = 0.997$). (b) Residual loss due to stress whitening when various indentation depths were reached, the blue curve is a linear fit of the data ($R^2 = 0.967$). (182).

Spectral transmittance of the fiber core in the 450 – 750 nm range was assessed during the indentation tests by replacing the sensor for a fiber optic cable connected to a spectrometer. The transmission spectrum for a PMMA/ABS fiber in pristine condition was measured to be used as the reference, then the indenter was used to press on the pristine fiber until significant whitening was observed. Afterwards, the stress-whitened area was heated using a heat gun set to $100 \text{ }^\circ\text{C}$, returning the material to almost pristine condition. This procedure is illustrated in Figure 61. The obtained transmission curves were normalized to the reference transmission spectrum for the fiber in pristine condition. Figure 62 shows then the transmission curves of the fiber core after whitening was observed (in red) and after heat was applied (green). As before, a significant attenuation of the transmitted signal in the visible range due to crazing and a good recovery of the pristine ABS transmission properties after the application of heat can be observed. The attenuated transmission spectrum profile differs from the ones observed in Figure 57 for this wavelength range, presenting a more uniform transmission loss instead of a slope. This difference might arise as light guided through the POF and scattered in the core can be reflected at the core/cladding and cladding/air interface and coupled back into the core. Changes in the waveguide geometry and non-uniform whitening of the core induced by the transverse load are also contributing factors for this behavior. Some residual loss remains after the fiber is heat-treated. This is not due to residual stress whitening, but to changes to the waveguide

geometry introduced by the indentation process. Nonetheless the heat-treatment partially restores the geometry of the POF (217), contributing for a longer lifespan of the probe.

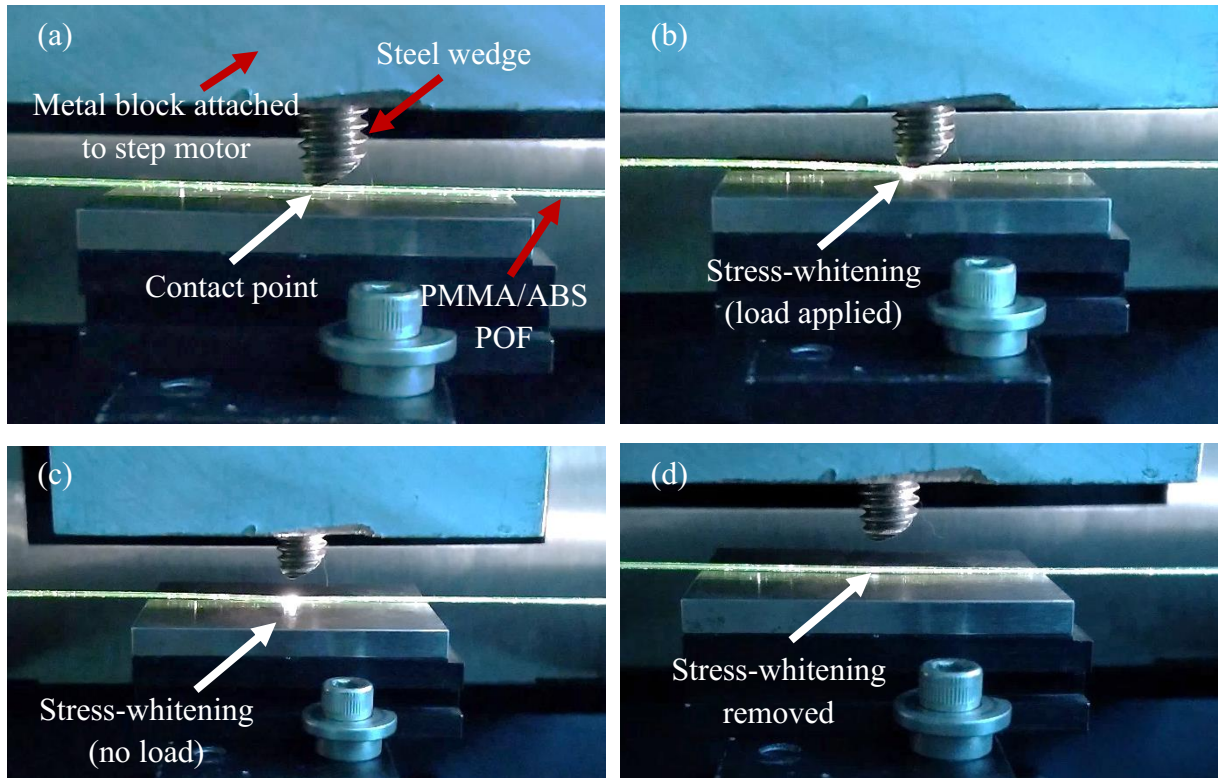


Figure 61 – (a) Indentator device lightly touching the POF probe; (b) Visible stress-whitening occur as the indentator presses on the fiber; (c) Stress-whitening remains after removal of the load; (d) Stress-whitening spot vanishes after heating the fiber with a heat gun.

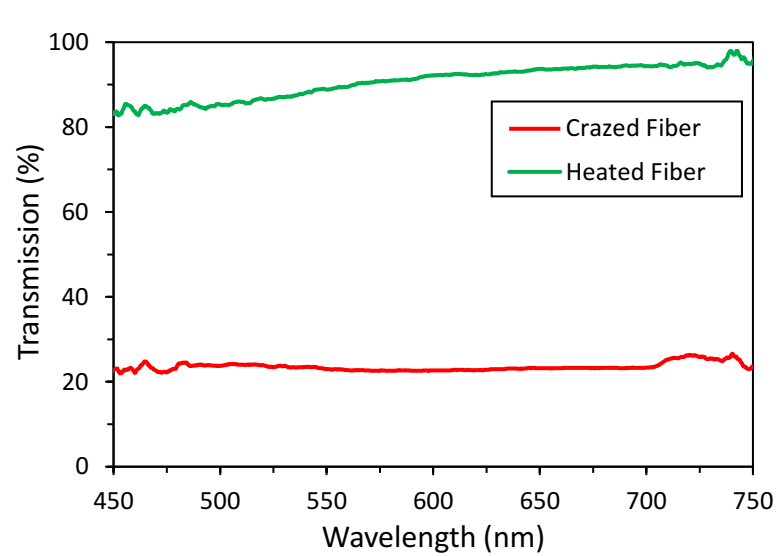


Figure 62 – Transmission spectrum of the crazed (red) and heat-recovered (green) fiber relative to the transmission in pristine condition (182).

B. Macrobending Test

In this experiment the indentator was removed, the fiber would be taken out of its support, bent at a desired bending radius with the help of a printed template, straightened, and put back in place for interrogation. The fiber was bent starting with a radius of curvature (R) of 22.5 mm and decreasing in steps of 2.5 mm until a minimum R of 10 mm. Figure 63 summarizes the results with plots of the Residual Loss (due to stress whitening, straight fiber) in relation to R and Curvature ($\kappa = 1/R$). While the residual transmission loss presents a linear response ($R^2 = 0.993$) for in terms of R , the general behavior of the probe under a macrobending load is better understood by looking at the data plotted as a function of κ . As κ increases from zero (fiber perfectly straight) the residual loss rapidly increases as the ABS core develops crazes, and as the curvature becomes more intense the number of crazes starts to saturate.

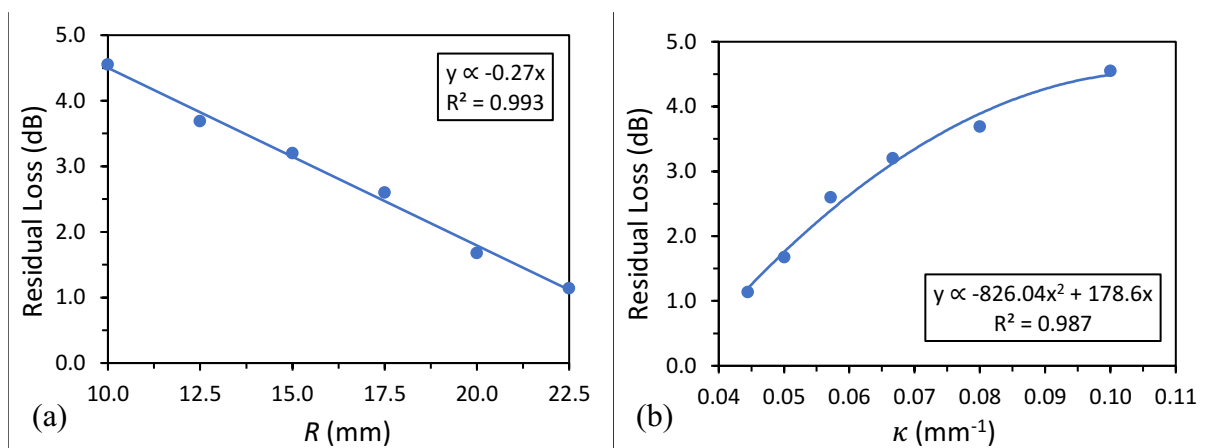


Figure 63 – Residual loss due to whitening as a function of: (a) Macrobending Radius (R) and (b) Curvature (κ). The lines are fits (a: linear, b: quadratic) of the collected data (182).

C. Tensile Test

Finally, the optical response of the fiber under tensile stress was studied. The tensile test setup is a repurposing of the setup used for the indentation test, the precision linear translation stage, now placed horizontally on the table, has one extremity of the fiber mounted on it, as shown in Figure 64. After firmly securing a 150 mm long fiber piece with cyanoacrylate-based adhesive, the fiber was subjected to a uniaxial tensile load by moving the translation stage to pull the fiber.

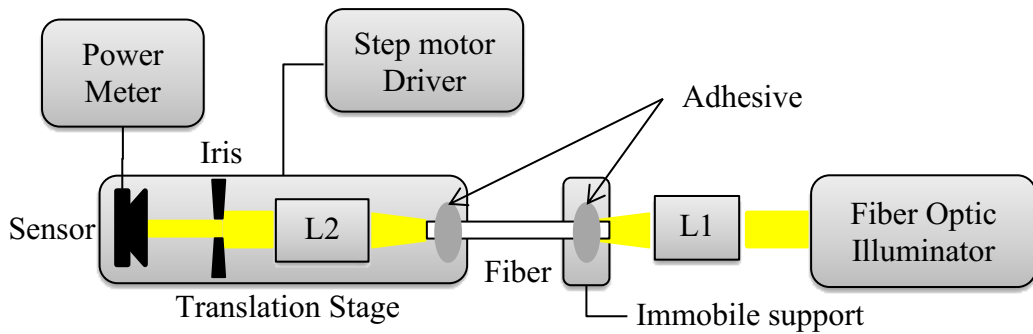


Figure 64 – Tensile test experimental setup, L1 and L2 are 20× objective lenses.

The translation stage was moved in steps of 0.01 to 0.05 mm, and a Δl of 0.10 mm was chosen as a baseline to evaluate the residual loss. Residual loss data was collected after reaching Δl values of 0.30 mm, 0.40 mm, 0.60 mm and 0.70 mm by returning to the baseline Δl (0.10 mm) in order to alleviate the tensile load. Figure 65a shows the transmission loss observed as the fiber was pulled by the translation stage, while Figure 65b is a plot of the residual loss due to the stress whitening caused by the tensile load. As can be noted in Figure 65a, an increase in the transmission loss occurs after the stress relief and reload cycles at $\Delta l = 0.40$, 0.60 and 0.70 mm, suggesting the PMMA/ABS fiber probe is very sensitive to cyclic loading (fatigue stress). Upon reaching a Δl of 0.90 mm the transmitted power started to steadily decay over time while the load on the fiber remained constant, dropping by a third of its initial value (at $\Delta l = 0.90$ mm) in the span of a few minutes. This indicates that at this point the tensile stress in the fiber may have exceeded the ultimate tensile strength for the PMMA/ABS composition, onsetting the necking phenomenon (220).

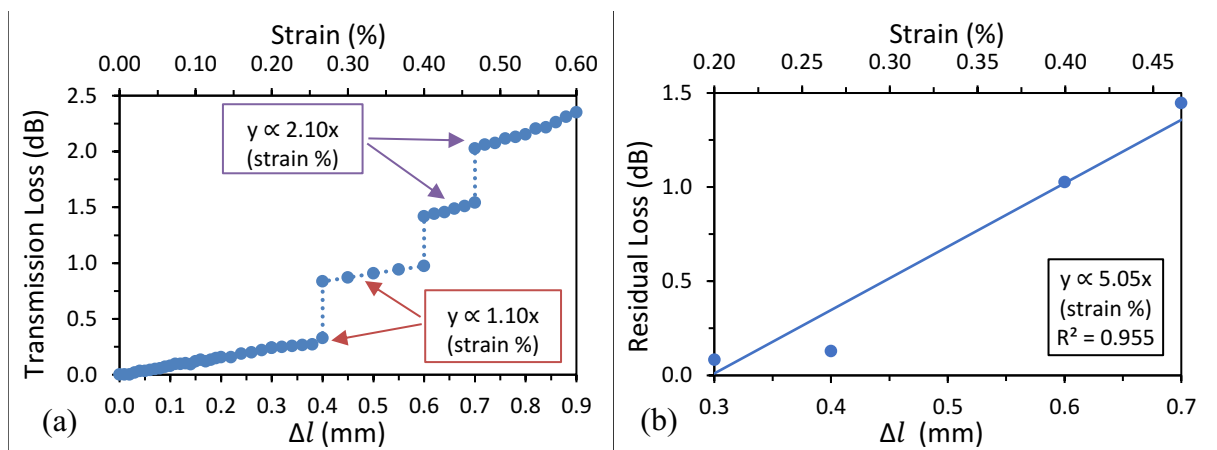


Figure 65 – (a) Transmission loss as a function of Δl , the dotted line is a guide to the eyes; (b) Residual transmission loss at various values of Δl , the blue line is a fit of the data (182).

During the application of the tensile load the POF probe exhibited a transmission loss of ~ 1.10 dB/strain% for a $\Delta l \leq 0.60$ mm and ~ 2.10 dB/strain% for the 0.60 to 0.90 mm range, respectively. A residual loss (memory) of 5.05 dB/strain% was observed. The memory sensitivity to tensile strain is comparable to what has been reported in previous works such as (205) and (206), with the advantage of having a much simpler interrogation setup (intensity detection in this work \times OTDR).

The behavior of the PMMA/ABS fiber under tensile stress can be investigated in further detail with access to a tensile testing machine to enable complete control of the applied stress and strain rate. Securing the fiber to a robust substrate, such as a standard tensile test specimen, will also significantly improve test results by inhibiting necking along the fiber. The observed spikes in the transmission loss after relief-reload cycles also present an interesting possibility of utilizing the proposed POF sensor as a fatigue life indicator.

5.3 Agarose fluorescent waveguide with hybrid carbon/silica nanodots for pH sensing

As discussed previously, the properties of hydrogels in suffering volumetric variations as a response to different parameters, including pH, temperature, ionic strength, and concentration of analytes, such as glucose, proteins, and DNA enable their use in sensing applications. These applications in industrial biotechnology, environmental monitoring, and biosensing can be also increased by doping the polymeric matrix with luminous agents. The doping strategy is based on the variation of the pattern of the light transmitted by the waveguide due to luminescence and other light–matter interaction phenomena. Studies have shown, for example, the possibility of producing step-index cylindrical optical fibers by coating a poly(ethylene glycol) (PEG) core with an alginate layer. These materials allowed the guiding of light inside living tissues and were doped with fluorophores and Au nanoparticles. Both types of doping allowed the sensor to selectively detect avidin (184). A PEG optical fiber was also doped with functionalized CdTe quantum dots (QDs) for monitoring Fe^{3+} (221). Meantime, practical applications of these devices are still limited by the fact that inorganic nanoparticles such as the semiconductor QDs usually present high toxicity (188), which can be overcome by their substitution by carbon nanodots (CDs) (222).

These carbon nanodots are materials emerging from the family of carbon nanotechnology (as well as graphene, fullerene, and carbon nanotubes), which present quasi-spherical morphology and sizes lower than 10 nm (222,223). They are constituted by a carbonaceous core with plenty of functional groups on the surface, such as hydroxyls, amines, and carboxylic acids, allowing their solubility in polar solvents. The peculiar behavior of carbon nanodots is their fluorescence, which arises from molecular domains that are formed during the synthesis that is carried out at high temperature (222-229). This luminescent behavior of CDs may be modulated by different factors, especially the excitation wavelength (224), pH (230), and solvent used (231). Moreover, the surroundings of the particles are responsible for the stabilization of the fluorophore electronic states, and red-shifted emissions are expected when the neighboring particles stabilize such states (solvatochromic effect) (232).

Due to these unique peculiarities, CDs find applications into several fields, such as biomarking, bioimaging, drug delivery, optoelectronics (226,229), covalent asymmetric catalysis (233), photocatalysis, renewable energies (226), luminescence down shifting, and solar concentrator devices (234-236). The advantages of CDs compared to inorganic QDs (considered superior fluorescence emitters) also include the fact that they are low-cost and environmentally safe materials (222) and show good biological and biocompatibility properties, being excreted in urine (226,227). Moreover, they present chemical robustness and high solubility in water and are easily doped and chemically modified (228). Also, previous studies showed that CDs can be easily fabricated in domestic microwave ovens using sugar cane syrup, a low-cost and renewable source (237).

In this study, carboxylic acid carbon nanodots, obtained from the thermolysis of citric acid, were used to produce amorphous nanohybrids by coupling CDs to silica and were tested for pH detection, leading to a simple and scalable method for obtaining an innovative green and disposable optical pH sensor. These nanoparticles were occluded into agarose to produce a waveguide with intrinsic fluorescence. The use of the hybrids instead of the net CDs is related to their physical properties: since the hybrid nanoparticles present slightly higher densities and are less hygroscopic, they are easier to manipulate under the larger scales of the hydrogel.

5.3.1 Materials and methods

The synthesis of the hybrid nanodots was conducted in the Department of Chemical and Pharmaceutical Sciences, University of Trieste, Italy, and then shipped to Brazil for embedding

in the hydrogel waveguide and conducting pH sensing experiments. Carboxylic acid terminated carbon nanodots, denominated here as α -CDs, were synthesized from the thermolysis of 200 g of citric acid (Fluka, 99.5%). The synthesis was performed in a muffle furnace under atmospheric air at 180 °C for 40 h, as reported by Martindale *et al.* (238). Amino-functionalized silica nanoparticles (a-SiO₂), in their turn, were prepared from commercial amorphous fumed silica nanoparticles treated with 3-aminopropyltriethoxysilane (APTES). Briefly, 206 mg of commercial fumed nanosilica (Aerosil 300, synthetic amorphous silica, average primary particle size ~7 nm, Evonik) previously dried for 2 days at 105 °C was added to ethanol (50 mL), and the mixture was stirred for 3 min. Then, APTES (5 mL, Sigma-Aldrich) was added and sonicated for 5 min, and the dispersion was stirred at room temperature (*r.t.*) and overnight (*o.n.*). After this step, the mixture was purified by centrifugation, and was then dispersed in ethanol (procedure repeated three times). The dispersion was lyophilized, leading to the a-SiO₂ nanoparticles. Then, the hybrid silica-CDots were synthesized through an amidic coupling reaction between a-SiO₂ and carboxyl-rich α -CD, as depicted in Figure 66. For this last synthesis, 223 mg of α -CDs dispersed in 10 mL of anhydrous dimethylformamide (DMF) was mixed with 50 mg of a-SiO₂ under an inert environment (Ar) and with 200 mg (1.04 mmol) of 1-ethyl-3-(3-(dimethylamino)propyl) carbodiimide hydrochloride (EDC·HCl, Alfa Aesar). An amount of 120 mg (1.04 mmol) of N-hydroxysuccinimide (NHS, Sigma-Aldrich) was also added. Finally, this mixture was sonicated for 10 s and stirred at 70 °C for 2 days at *r.t.* DMF was removed through azeotropic distillation with toluene under reduced pressure, and Milli-Q water was added. To purify the product, two cycles of centrifugation (20 min at 3000 rpm) were performed, followed by freeze-drying.

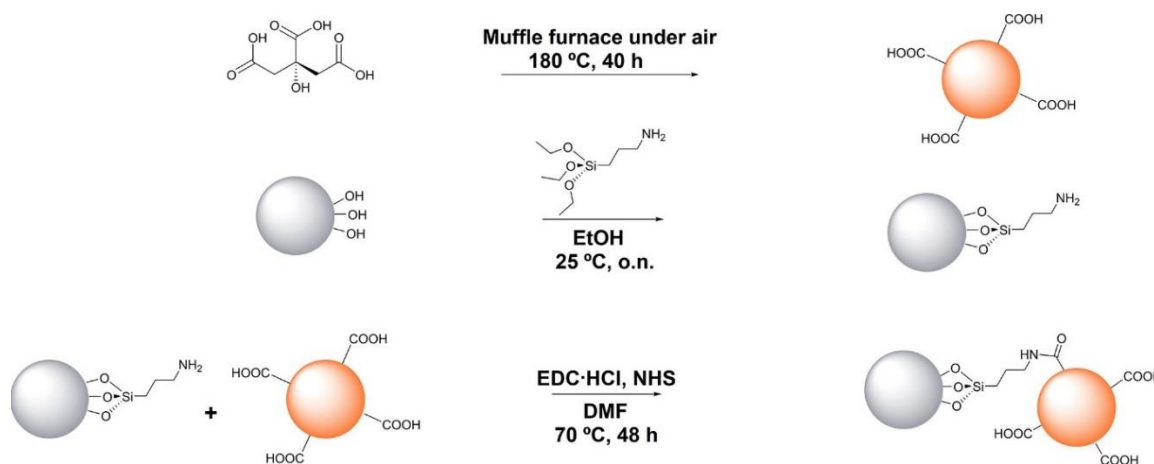


Figure 66 – Synthesis Routes of α -CDs, Amino-Terminated SiO₂ Nanoparticles, and Hybrids of α -CDs Coupled to a-SiO₂ (183).

The photoluminescent emission spectra of α -CDs recorded in water (Figure 67a) show a maximum emission at 465 nm when the sample is irradiated at 360 nm. When the excitation wavelength changed from 360 to 440 nm, an emission dependency with the excitation was observed with a concomitant loss of intensity. The photoluminescent (PL) spectra of the silica-Cdots in water (Figure 67b), in turn, show approximately the same behavior. The emission is dependent on the excitation wavelength, but the coupling caused an increase in the noise of the intensity signal. The maximum fluorescence intensity is still observed when the sample is excited by 360 nm (and still corresponds to the emission at 465 nm). It indicates that there is no loss of the stability of the excited state of the fluorescent agent caused by the silica coupling (232). Moreover, the fluorescence emission peak of the hybrids shifts from 465 to 513 nm (green) when the excitation changes from 360 to 430 nm. The peak intensities also decrease as they red-shift, a behavior previously observed for other CDs (237,238). The organic groups present on the surface of the CDs significantly affect the fluorescence properties (223,238).

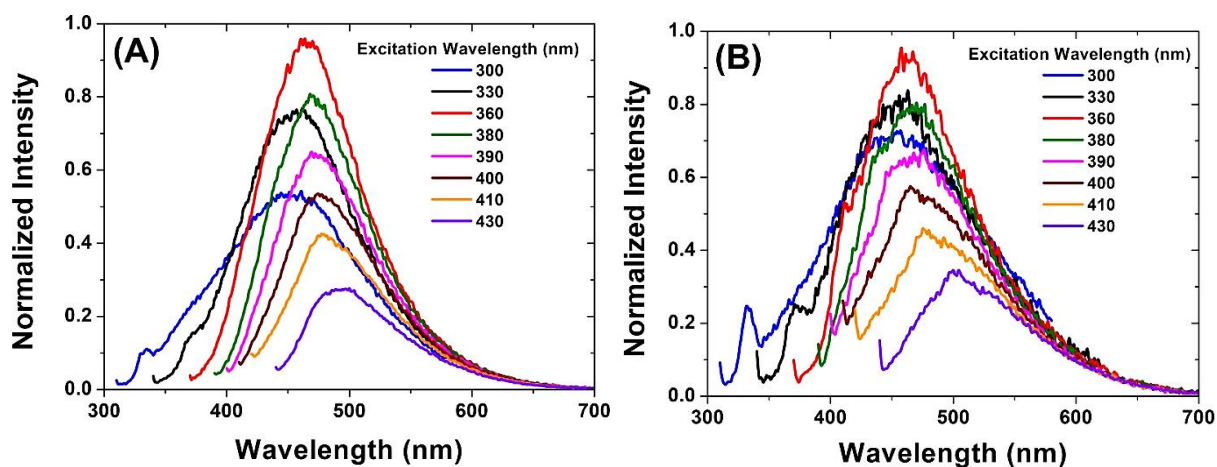


Figure 67 – Fluorescence spectra of (a) α -CD and (b) silica-Cdots (183).

Two types of waveguides were prepared by gelling precursor solutions containing agarose in DI water. The first solution contained 300.0 mg of agarose (food grade, acquired in a local market) and 31.0 mg of hybrids (silica-Cdots) dispersed in 10 mL of water, resulting in concentrations of 30.0 g/L (agarose) and 3.10 g/L (hybrids). The second solution was fabricated for comparison: it contained the same concentration of agarose in DI water (30.0 g/L), but no nanoparticles. The solutions were heated close to their boiling points for initiating the agarose thermal-curing process. Immediately after boiling starts, the precursor dispersions were poured into 3D-printed cylindrical molds (7 mm inner diameter) made of glycol-modified poly(ethylene terephthalate) (PETG) filament. The molds were sealed on their end-faces, and

left *o.n.* in the refrigerator at ~ 10 °C for curing. After removing the sealing, the hydrogel was left to dry under ambient conditions, so the loss of water diminishes its diameter and provides the loss of contact with the inner walls. After being removed, the formed materials are again put in contact with DI water for recovering the original diameter.

The refractive indexes (RIs) of both the agar and the agar with occluded hybrids were evaluated with a MISCO PA 202 refractometer (Palm Abbe), with a 589.29 nm high-precision LED. All samples were measured at ~ 25 °C and room atmosphere. For this, small volumes of the preheated precursor solutions (heated until boiling) were dropped on the sample window. The reading of the RI was performed after the curing and thermal stabilization of the system at 25 °C. The obtained refractive indexes were $n = 1.3334$, which is very close to the DI water's index ($n = 1.3330$, evaluated using the same equipment). This is due to the high adsorption of H₂O on the hydrophilic polymers and on the hybrids' surfaces. This value is also higher than the air's ($n \approx 1$), so light may be guided through total internal reflection, as in conventional optical fibers (this is represented in Figure 68).

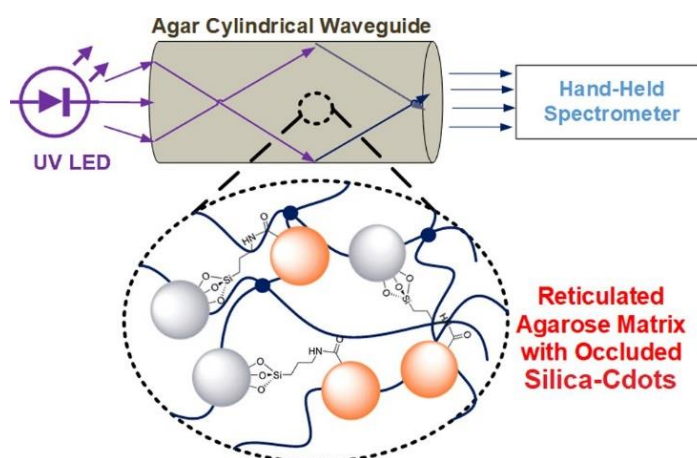


Figure 68 – Agarose Waveguide Doped with the Hybrids (183).

5.3.2 Results and discussion

Due to the presence of carboxylic groups, the possibility of applying the hybrids for pH assessment was evaluated. The use of silica–Cdots hybrids for pH monitoring tests has advantages because they are easy-to-handle powders, as they are less hygroscopic than α -CDs. Besides, silica-based nanoparticles doped with fluorophores are interesting hybrid nanosystems that intrinsically combine the mechanical proper-ties of silica with the optoelectronic properties of carbon nanodots.

A. pH Response of Silica-Cdots in Aqueous Dispersion

The pH-monitoring tests with aqueous dispersions of silica– Cdots (initial pH of 4.30) were performed according to the setup shown in Figure 69a. Briefly, the dispersions had the pH modified by first adding NaOH, and then the pH was reduced with HCl (both solutions 0.01 M). For each tested pH, the dispersions were introduced into cuvettes and were irradiated with a 403 nm LED to have the emission spectra analyzed. The wavelengths corresponding to the peaks of maximum emitted intensities were retrieved, and data were correlated to the pHs. The results are shown in Figure 69b. They were fitted by a cubic polynomial relating the maximum wavelength to the pH (wavelength = $467.23 + 20.17(\text{pH}) - 3.45(\text{pH})^2 + 0.20(\text{pH})^3$, adjusted $R^2 = 0.91$), proving that it is possible to optically monitor the acidity. The inset of Figure 69b shows a portion of the curve between pHs 6 and 10, which can be fitted by a linear polynomial ($R^2 = 0.95$). The sensitivity of the liquid phase silica–Cdots dispersions for this range is of 4.53 nm/(pH unit). Moreover, one can notice that, as the pH gets closer to 2, the curve reaches a signal baseline. It leads to a drop in sensitivity and makes it difficult to perform readings for more acidic media. As the pH is raised to 12, in turn, one can observe an increase in both the noise of the observed fluorescence spectra and the dispersion of data in Figure 69b. Besides that, the fluorescence was observed to be stable and reversible regarding the pH. It is also interesting to note that the increase in pH leads to a red-shift of the emitted fluorescence.

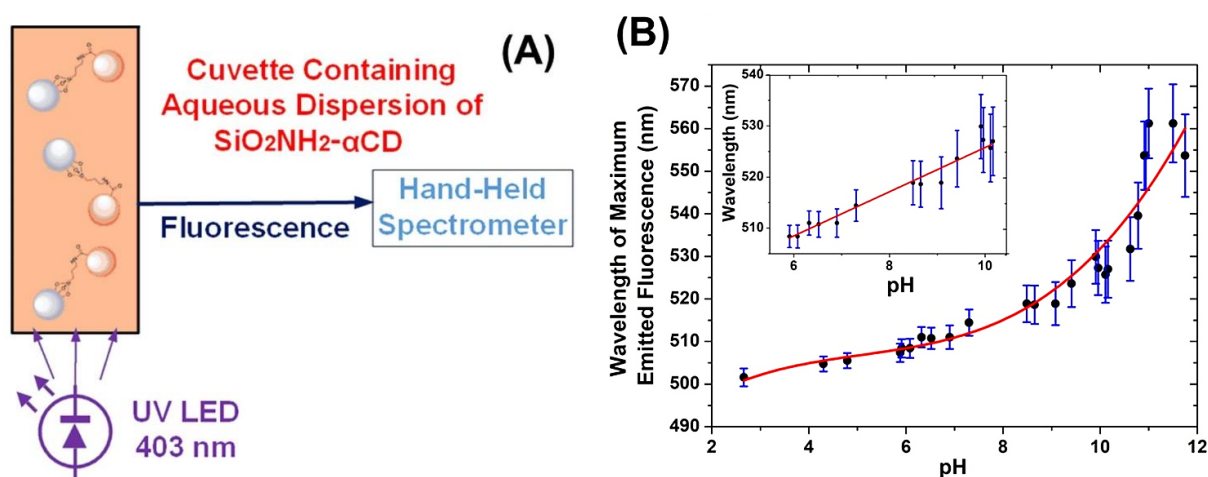


Figure 69 – (a) Setup for the pH evaluation using the aqueous hybrids dispersions. (b) Wavelength of maximum emitted fluorescence as a function of pH for the dispersions of hybrids. The inset shows the linear portion of the curve (pH ranging from 6 to 10). (183).

This red-shift verified when increasing the pH may be interpreted in terms of the interactions between the nanoparticles and the solvent, which results in modifications of the excited-state stability. According to Sciortino *et al.* (239), CDs emission energies show a notable and systematic dependence on solvent characteristics, as well as a strong response of the photoexcited particles to the presence of hydrogen bonds. As a consequence, CDs may be used as solvent polarity nanoprobe to monitor neighboring ions and molecules. The authors verified that the CDs' emission blue-shifts as the solvent polarity is reduced. The lowest wavelength was observed for water due to the stabilization effect of the hydrogen bonds. Their conclusion was that both the nitrogen and carboxylic acid groups that may be present on the CDs' surfaces act as efficient hydrogen-bond acceptors. This is due to their electron lone pairs, and thus, the fluorescence mechanism is closely related to the presence of these groups on the subnanometric surface shell around the carbon nuclei (239). In turn, Bano *et al.* (240) used latex as the raw material for the production of CDs containing carboxylic acid groups on their surfaces. They verified that the increase in the medium's acidity led to the protonation of the carboxylic surface groups of the dots. Consequently, the particles' negative charges decreased (or were even neutralized) in lower pHs, and the colloidal dispersions lost stability. This ultimately resulted in the aggregation of the CDs and in the extinction of the fluorescence (240). A similar effect was observed by Chandra *et al.* (241), but it was analyzed in terms of the UV–VIS absorbance spectrum: in basic media, the deprotonation of the surface acid groups of CDs caused an intense decrease in the radiation absorption.

In the current case, the silica–Cdots present chemical and structural differences compared to the α -CDs, which may impact their interactions with the solvent. The most important ones are the slightly superior dimensions of the particles which affects the sizes of the dynamic cavities/first solvent shells (242,243), and the fact that there may be fewer carboxylic groups, since $-\text{COOH}$ reacts with a-SiO_2 . On the other hand, Figure 66 shows the presence of other lone pairs on the hybrid surfaces. There are lone pairs from the amide group (the bond between SiO_2 and α -CD), the $\text{Si}-\text{O}-$ bonds between silica and α -CD, and other $-\text{Si}-\text{OH}$ and $-\text{Si}-\text{O}-\text{Si}-$ groups that may exist, since these defects are commonly observed on SiO_2 surfaces (244,245). Therefore, the surface groups of the silica–Cdots hybrids selectively detect Na^+ or Cl^- ions present in the controlled pH solutions. The main chemical groups of the hybrids, identified by XPS, are the COOH of the carbon nanodots (α -CDs), the $\text{NH}-(\text{C}=\text{O})$ from the amide group (the bond between SiO_2 and α -CD), the $\text{Si}-\text{O}-$ bonds between silica and α -CD, and other $-\text{Si}-\text{OH}$ and $-\text{Si}-\text{O}-\text{Si}-$ groups and $\text{Si}-\text{O}$. The wavelength

of the fluorescence emitted from the hybrids, measured at the highest emission intensity, is selectively shifted and quenched because of the interactions among the hybrids' surface groups and ions in the aqueous solution. At this moment, considering that the pH of the initial aqueous solution is clearly acidic, 4.30, and that there are still several groups capable of hydrogen bonding stabilizing the excited states, it can be considered that the hybrids behave as the other acidic carbon nanodots cited (239-241). Therefore, analogous conclusions can be made for the results of wavelength shifts with the pH depicted in Figure 69: as the pH gets more basic, the deprotonation of the carboxylic groups of the hybrids' surfaces increases their negative charges and, consequently, enhances the hydrogen-bond interactions between the particles and the solvent (water). Since this effect causes the stabilization of the fluorophores, the red-shift is observed (239,246). The possibly lower number of $-\text{COOH}$ groups is not necessarily a problem here: it is known that basic pHs (higher than 10) usually deprotonate colloidal and nanostructured silica's silanol groups (244,247,248), increasing the hybrids' charges.

B. pH Response of Doped Agarose Waveguide

The light transmission spectra of both the doped waveguide and of the agar containing no nanoparticles were obtained by transmitting a supercontinuum laser through the materials (Figure 70a). Afterwards the waveguides were submitted to tests with the 403 nm LED, the same source used for pH detection in the aqueous phase. Since both the agarose and the hybrids are very hygroscopic, by immersing the waveguides into solutions of known pH the readings take no longer than 30 s to stabilize when base or acid is added. Thus, the waveguides were kept immersed and under stirring (25 °C, room temperature) to ensure the homogeneity of the aqueous medium. Again, the pH was first raised to ~ 12 (addition of 0.01 M NaOH), and then reduced to ~ 2 (dropping of 0.01 M HCl). When the pH reading got stable after a given addition of NaOH or HCl, the waveguide was rapidly excited with the LED to have its fluorescence spectrum collected. It is important to mention that the wavelength interrogation is independent from the total amount of fluorophores, an important advantage of this approach compared to intensity-based sensing techniques (52,249). Therefore, it was not necessary to correlate the measurements with the added acid/base volumes. All of the datapoints shown in Figure 70b were collected under the same temperature and atmospheric air conditions. Then, the modifications of the spectra could be correlated to the changes in solvent polarity, as in the other mentioned reports (239-243).

Figure 70b summarizes the correlation between the wavelengths of the maximum emitted intensity (the peaks) and the pHs of the aqueous media where the doped waveguides were immersed. Contrary to what was observed for the aqueous dispersions (Figure 69b), the agar waveguides show a critical point for the results, which is again probably due to the interactions between the hybrids and the hydrogel matrix (246). The critical point corresponds to the initial situation: it is the pH of the water initially in equilibrium with the agar, 5.59, which was used to keep the device swollen before adding NaOH or HCl. It was observed that the wavelengths of maximum intensity present reversibility regarding pH. The results were again fitted by a third-degree polynomial correlating the maximum wavelength to the pH, given by $\text{wavelength} = 474.21 + 48.50(\text{pH}) - 7.03(\text{pH})^2 + 0.30(\text{pH})^3$, adjusted $R^2 = 0.83$. As in Figure 69b, Figure 70b (inset) shows a linear portion corresponding to the pH range from 6 to 10 ($R^2 = 0.84$). The sensitivity for this range is of $-5.61 \text{ nm}/(\text{pH unit})$. The derivative of this polynomial is negative, contrary to that observed for the aqueous dispersions. Despite the fact that no clear baseline was reached, the light intensity signals suffer substantial decreases as the pH gets closer to 2 or 12, indicating that the sensor is inadequate for monitoring pHs beyond these values. This pH range, however, is wider than the one obtained by Zhang *et al.* (250) (pHs from 2 to 7). It is also wider than the range achieved by Chen *et al.* (251), they obtained a system able to detect pHs from 3.0 to 11.0, but using a more complicated sensing strategy (ratiometric analysis).

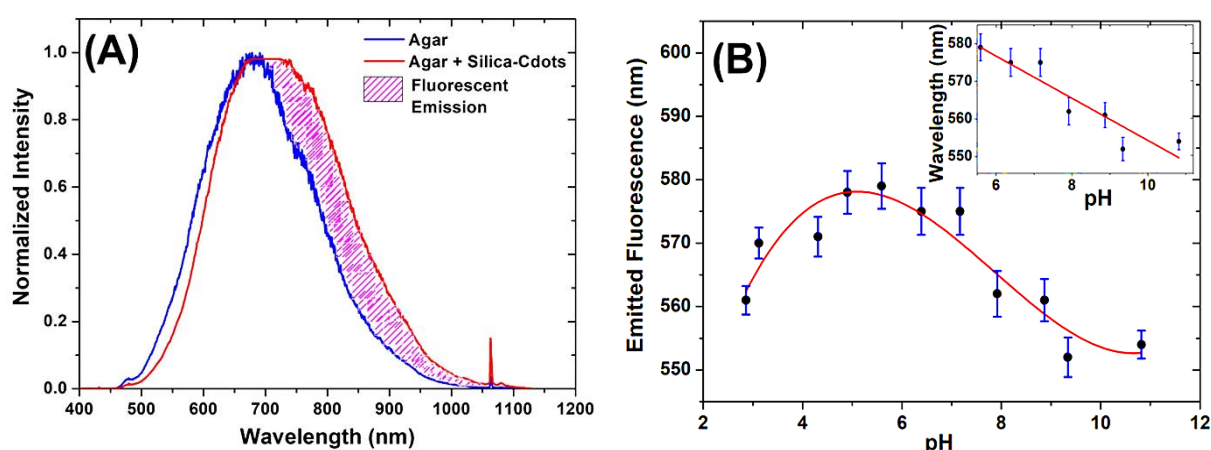


Figure 70 – (a) Intensity of light transmitted by the waveguides (excitation with the supercontinuum laser). The dashed region corresponds to the fluorescence of the hybrids. (b) Wavelength of maximum emitted fluorescence as a function of pH for the agar waveguide. The inset shows the linear portion of the curve (pH 6–10). (183).

Interesting conclusions are also obtained when comparing, for a same pH, the fluorescence spectrum collected for the doped waveguide with the one obtained for the aqueous dispersion of silica-Cdots (*i.e.*, when comparing the spectra used for obtaining the information

in Figure 70b and Figure 69b). An example of the general observed behavior is shown in Figure 71, where the spectra collected for pH 4.30 are compared.

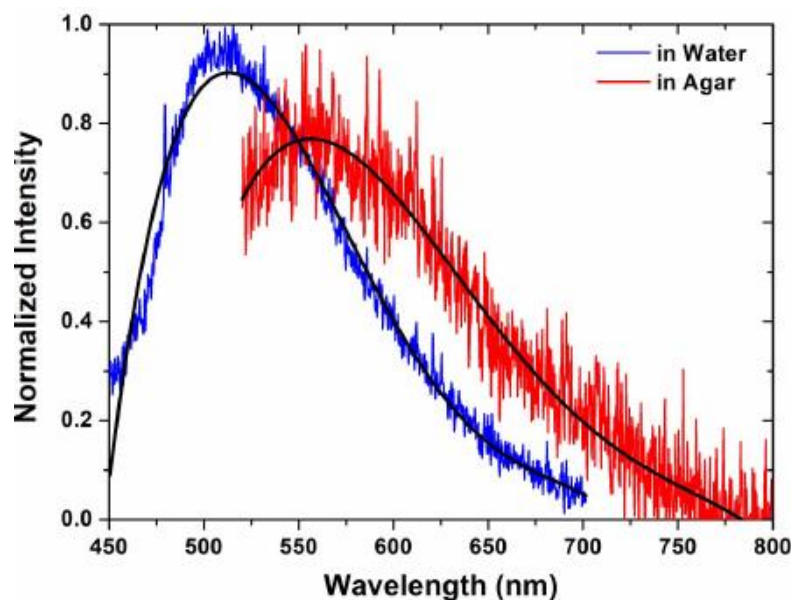


Figure 71 – Fluorescence spectra of the silica-Cdots hybrids at excitation wavelength of 403 nm (when dispersed in water and when occluded into the agarose matrix) for pH 4.3, exhibiting a red-shift between curves.

Figure 71 shows that the peak (maximum intensity of fluorescence) of the hybrids occluded into the hydrogel matrix is red-shifted compared to the one observed for the aqueous dispersion of silica-Cdots. This indicates an increase in the stability of the excited states (232,246,249), and this same shift was observed for all the other pHs. The solvatochromic shifts resulting from the enclosure of fluorescent species into rigid media are complex phenomena, as extensively discussed by other researchers (232,239-243,246,249). The observed shifts depend, for example, on the method used for preparing the matrix and on the particular technique applied to the incorporation of the fluorophores (232). For soluble polymers, in particular, an increase in the medium's polarity or in the intensity of the solute-matrix hydrogen-bond interactions may result in the reduction of the energy difference between the ground and the excited states, red-shifting the emission (232). Thus, the red-shift observed in Figure 71 may be explained analogously as performed by other authors who analyzed the increase in the nanoparticles' excited-state stability when the CDs are incorporated into hydrogel matrixes with plenty of oxygen and hydroxyl groups. For PVA, for example, the matrix networks form many hydrogen bonds with the polar groups of CDs, stabilizing the emissive states (246). This same phenomenon is expected to take place between the agarose's C-OH and C-O-C groups (252)

and the silica–Cdots' oxygen and nitrogen groups. According to Jiang *et al.* (246), in some hydrogels, these interactions may be so intense that they even result in composites showing phosphorescence or delayed fluorescence.

C. Further Considerations

It is interesting to notice that the applied setup (Figure 68) could be easily adapted to perform the online evaluation of the pH directly in the liquid medium. This would be done by transporting the light with external optical fibers: one fiber would guide the light from the LED to one extremity of the agar waveguide, and a second one would collect it at the end-face and guide it to the optical analyzer. However, this was not realized for the moment as it would not allow the evaluation of the sensor capability in retaining information even when it is removed from the assessed medium. This last analysis is particularly important, since there are several practical applications where a waveguide capable of retaining the medium information is required. In a biomedical environment, for example, it may be necessary to remove the sensor from the medium to analyze other parameters besides pH. This situation has been reported and analyzed in studies where hydrogel matrixes are simultaneously used as waveguides and as scaffolds for growing cells (184,188), with the need for cell counting. In the standard counting procedure, samples are periodically collected from the analyzed biosystem to be observed and counted on the microscope using specific devices, such as the Neubauer chamber (63). If the waveguides can be removed and their volumes are known, the chamber may be substituted by the waveguide itself. Then, the cellular environment is not disturbed, reducing the risk of causing cell death during counting (184,188). As Figure 70b showed, the pH information was actually retrieved by the silica–Cdots/agarose waveguide when it was removed from the aqueous medium. Therefore, since the waveguide can be removed and analyzed off-line, this novel device has potential for monitoring other important biochemical parameters in addition to pH (*e.g.*, the number of cells or the morphological characteristics of the doped agar).

A final important comparison to be performed is with commercial pH meters. As mentioned, a decrease of the detected fluorescence intensity as the pHs got closer to 12 was observed, preventing the detection beyond this condition. However, many commercial pH meters also show loss of signal intensity or difficulties in evaluating very alkaline media. Indeed, it is widely known that the traditional devices may lose precision when submitted to such conditions (253,254). That is because these devices commonly show substantial

interference caused by the presence of Na^+ ions for pHs > 12 (they interpret Na^+ as H^+ ions) (253). As a solution to this problem, many manufacturers provide tables correlating the detected pH to the ionic concentrations and estimating reading corrections, or they indicate devices specifically designed for higher pH ranges or more drastic operational conditions (254).

Lastly, the recovery of fluorescent silica–Cdots hybrids embedded into the agarose, after being discarded, is technically feasible. Since the agarose is biodegradable, it can be solubilized in water and the hybrids separated by centrifugation.

6 FBG APPLICATION CASES

Finally, this chapter discusses new application cases for fiber Bragg gratings sensors written in conventional optical fibers. As before, publications based on these work have been made, namely reference (255) pertaining to Section 6.1, (256) for Section 6.2 and (257) for Section 6.3. Figures in this chapter are for the most part reused or adapted from the listed publications. Additional information and figures not included in the published manuscripts is also presented when possible.

The FBG sensors used in the following studies were made in-house, using the phase-mask technique. In this setup (Figure 72), light from a continuous-wave 266 nm UV laser (Quantel Q-Smart 450) is directed at a single-mode telecom grade optical fiber by a pair of mirrors (M1 and M2). Along the optical path, the laser beam passes through a cylindrical lens that reshapes the circular beam into a line, and a phase-mask (PM), a diffraction grating designed to shine the laser light into the fiber as a periodic pattern (period λ). Prior to this procedure, the fiber was hydrogenated using a pressure chamber with a Hydrogen rich atmosphere to enhance the UV photosensitivity of the fiber (78,258). The inscribing of the FBG was monitored using a Portable BraggMETER (FS42, HBM) optical interrogator with a 1 pm wavelength resolution, an all-in-one portable interrogation unit with a built-in laser source, a touch display for data visualization, and an optical spectrum analyzer with a 100 nm measurement range (centered in 1550 nm) to obtain the power distribution over wavelength of the FBG reflection signals.

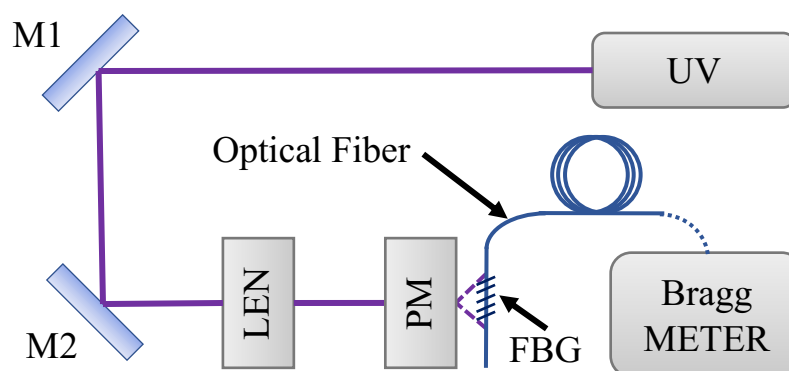


Figure 72 – Schematic drawing of the FBG inscribing process. M1, M2: Mirrors. PM: Phase Mask (257).

6.1 All-optical anemometer based on the pitot-static tube and fiber Bragg gratings

The assessment of airflow speed is essential for several technological applications, such as the navigation control in both crewed and unmanned aircrafts, validation of aerodynamic simulation studies, monitoring and maintenance of turbines in wind farms, and prevention of icing events in electric power transmission towers and lines. Currently, a variety of sensors have been proposed for measuring the airflow speed, including the Pitot-static pressure probe (259), thermal anemometers (260), integrated MEMS anemometers (261), laser Doppler interferometer (262), time-of-flight ultrasonic wave transducers (263), and piezoelectric films for both speed estimation and energy harvesting applications (264). Even though some of these systems are commercially available, such devices present drawbacks in terms of vulnerability to harsh environments and electromagnetic noise, complex construction, and high relative cost (265,266), issues that optical fiber sensors can work around.

Different optical fiber anemometers setups have been reported in the literature. In (267), a reflection-type sensor is used for measuring the wind speed in a turbine. The light from an emitting polymer optical fiber is coupled to the receiver fiber when the incident wave hits the reflecting surface of a slotted cylinder attached to the turbine rotor, so the speed can be retrieved by counting the detected optical pulses. Another approach consists of a cantilever-type transducer based on a tapered fiber Michelson interferometer (268). In (269), a modal interferometer is designed by splicing single-mode fibers (SMFs) with a core offset. The sensor probe is covered with a silver coating and then subjected to the assessed flow. Since the probe temperature is increased due to the high-power laser source, the heat transfer induced by the cooling airflow can be correlated to the interference spectrum shift. Optical fiber thermal anemometers can also be developed by using fiber Bragg gratings (FBGs) in substitution to the hot-wire probes (265). Finally, in (270), the pressure difference in a Venturi meter is monitored using a distributed Bragg reflector fiber laser mounted on a diaphragm. Conversely, this approach requires the use of a specialty fiber and a complex interrogation method. Moreover, pressure transducers based on FBG attached to circular diaphragms have been demonstrated by using metallic (271) or rubber membranes (272), allowing for the assessment of different ranges of pressure difference. On the other hand, no results were reported regarding the application of such sensors in the airflow monitoring, so the development of a sensitive and straightforward anemometer based on an FBG diaphragm can provide a feasible alternative to the

aforementioned expensive and complex setups. Also, in spite of the high sensitivity, these setups require laborious and costly coating procedures, as well as complicated interrogation setups, which can be a limiting factor regarding practical applications.

Given this discussion, here a practical OFS for measuring the air-flow speed is reported. The pressure difference assessed by a 3-D-printed Pitot-static tube was detected by means of a diaphragm with a mounted FBG sensor, so the airflow could be retrieved from the fiber curvature response, thus providing the sensitive and repeatable results. In contrast to the current fiber anemometers, the system was designed with a commercially available fiber and optical interrogator, whereas the transducer structure was completely fabricated by 3-D-printing, yielding a straightforward and less-invasive method for assessing the airflow speed.

6.1.1 Materials and methods

The Pitot-static probe is a device comprised of a central port aligned to the streamline for assessing the total pressure p_t and adjacent holes normal to the flow for static pressure p_s measurements. This type of instrument presents advantages over the obstruction meters and the thermal anemometers since it is more compact, robust, and generate low disturbance to the airflow (273). Assuming a uniform, steady flow and neglecting the mechanical losses, the fluid velocity U is correlated with the pressure difference $\Delta p = p_t - p_s$ by the conservation of energy, yielding

$$U = \left(\frac{2\Delta p}{\rho} \right)^{1/2} \quad (6.1)$$

where ρ is the fluid density (273).

The pressure difference Δp is assessed by means of a diaphragm, converting the mechanical load into displacement. Consider a thin clamped rectangular plate with an area $a \times b$ and thickness h , as shown in Figure 73. For the coordinate system (x, y) with the origin at the center of the diaphragm, the deflection $w(x, y)$ due to a uniform load q is given by (274):

$$w = K \frac{4qa^4}{\pi^5 D} \sum_m^{\infty} \frac{(-1)^{(m-1)/2}}{m^5} \cos\left(\frac{m\pi x}{a}\right) \times \left(1 - \frac{\alpha_m \tanh(\alpha_m) + 2}{2 \cosh(\alpha_m)} \cosh\left(\frac{m\pi y}{a}\right) + \frac{1}{2 \cosh(\alpha_m)} \frac{m\pi y}{a} \sinh\left(\frac{m\pi y}{a}\right) \right) \quad (6.2)$$

where $m = 1, 3, 5, \dots, am = m\pi b/2a$, K is the correction factor for the nonlinearities of the diaphragm material and flow conditions, and the flexural rigidity D is

$$D = \frac{Eh^3}{12(1 - \nu^2)} \quad (6.3)$$

where E and ν are Young's modulus and Poisson's coefficient of the plate material, respectively.

For measuring the deflection w , the optical fiber is mounted on the membrane surface by aligning the FBG section to the center of the structure, so it is possible to assume that the fiber bending is equal to the deflection profile (*i.e.*, the applied pressure difference). The Bragg wavelength shift $\Delta\lambda$ is correlated with the radius of curvature R by

$$\Delta\lambda = \lambda(1 - p_e)\delta \frac{1}{R} \quad (6.4)$$

where p_e is the photoelastic coefficient of the fiber material and δ is the distance from the neutral axis. Therefore, the FBG sensor response can be used to determine the pressure difference in the Pitot-static tube and, consequently, obtain the airflow speed.

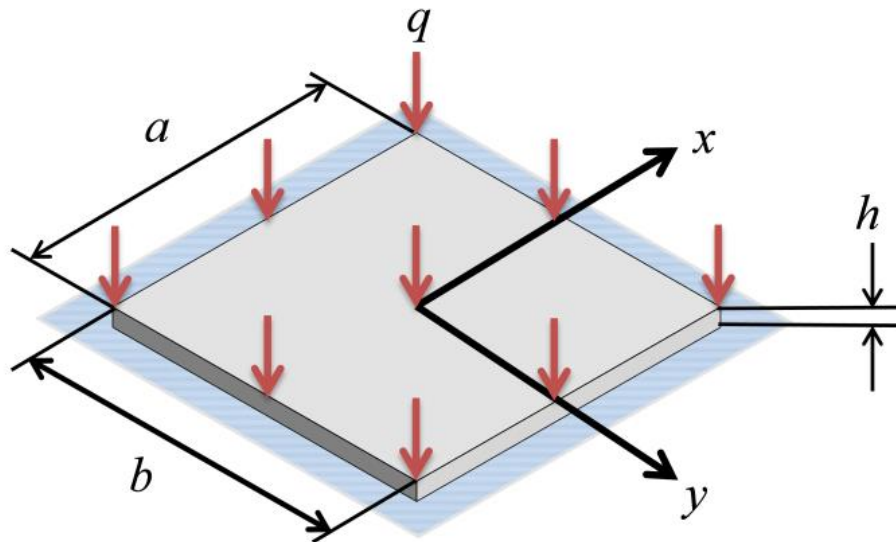


Figure 73 – Differential pressure diaphragm based on an $a \times b$ area, h thickness square plate with clamped edges and subjected to a uniformly distributed load q (255).

The Pitot-static probe was 3-D-printed using a polyethylene terephthalate glycol filament according to the geometry shown in Figure 74. A $25 \times 25 \text{ mm}^2$ area, $\sim 0.2\text{-mm}$ thickness square diaphragm made of a latex rubber was used to detect the pressure difference, whereas the deflection was assessed by an FBG firmly attached to the membrane surface.

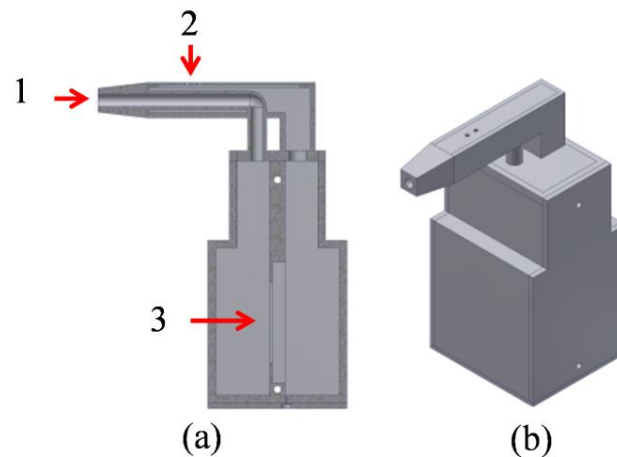


Figure 74 – CAD drawing of the fabricated Pitot-static tube. (a) Cross-sectional view. (b) Isometric view. 1: total pressure port. 2: static pressure port. 3: diaphragm support (255).

The experimental setup is shown in Figure 75. The Pitot-static tube was mounted inside the working section of an AF100 Subsonic Wind Tunnel (TecQuipment Ltd.) with the probe inlet aligned to the streamline. The airflow can be adjusted until the rated value of 36 m/s, whereas the nominal pressure difference is monitored by a preinstalled Pitot-static probe connected to a U-tube manometer with 1-mm H₂O (9.8 Pa) resolution. The fiber sensor was interrogated using an FS42 Optical Interrogator (HBM FiberSensing) that scans the optical spectrum in the C-band and automatically identifies the reflection peaks corresponding to the FBGs, so the intensity and the wavelength of those peaks are recorded and then correlated with the input wind speed conditions.

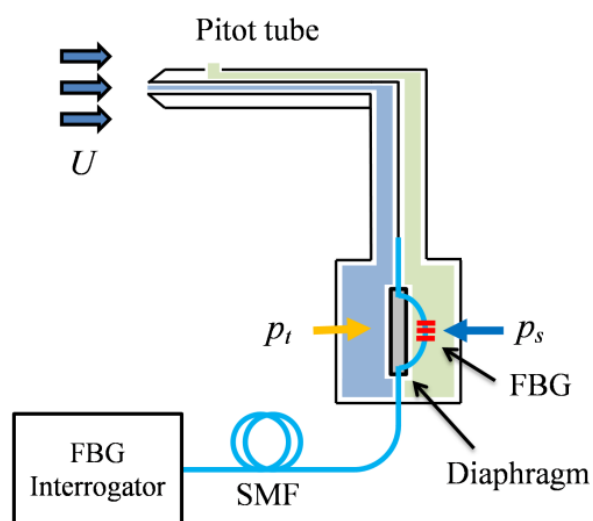


Figure 75 –Experimental setup. The Pitot-static tube inlet is aligned to the airflow speed U , causing the diaphragm to be deflected by the difference between the total and static pressures p_t and p_s , respectively. Then, the curvature of the FBG written in the SMF is measured by the optical interrogator (255).

6.1.2 Results and discussion

A. Simulation of the Probe

The sensor model given by Equations (6.1) – (6.4) was simulated in MATLAB for $a = b = 25$ mm. The diaphragm was modeled as $h = 0.2$ mm, $E = 1.51$ MPa, and $\nu = 0.5$ – latex rubber material (275). The load was assumed to be spatially uniform, *i.e.*, $q = -\Delta p$, using $\rho \cong 1.20$ kg/m³ for the air at 20 °C and $K = 3 \times 10^{-4}$. The fiber radius of curvature R was estimated by approximating the 1-D deflection profiles $w(x,0)$ to sine functions of the form $w(x) = A \sin(Bx + C)$; therefore, the R value at $(0,0)$ can be evaluated by

$$R = \frac{[1 + (w')^2]^{3/2}}{w''} \Big|_{x=0} \cong AB^2 \sin C \quad (6.5)$$

where A , B , and C are the coefficients obtained by curve fitting and the prime denotes the derivative with respect to x . Consequently, the Bragg wavelength shift was calculated from Eq. (6.4) by using $p_e = 0.22$, $\delta = 62.5$ μm for a silica SMF (276), and $\lambda = 1550$ nm. The deflection profiles $w(x)$ as a function of the airflow speed U are shown in Figure 76a/b. As expected, the maximum value occurs at the plate center because the membrane is clamped by all borders, and the magnitude of the deflection peak value increases with U^2 since it is proportional to the pressure difference. The variation of the radius of curvature is shown in Figure 76c, where the inset presents the sine function curve fitting applied to the simulated w data. Finally, the Bragg wavelength shift $\Delta\lambda$ is shown in Figure 76d. It is observed that the sensor has lower sensitivity for $U \leq 20$ m/s since the diaphragm curvature imposed by the input load Δp is not sufficient to cause a considerable fiber strain.

The sensitivity and the measurement range can be improved by choosing the diaphragm material and thickness in order to decrease the flexural rigidity D value or by enlarging its dimensions a , so the deflection effect can be enhanced for lower airflow speeds. For example, given $\hat{A} = K4a^4/(\pi^5 D)$ the parametric amplitude, thus, the deflection profile $w(x)$ has a peak value of $A = \alpha \hat{A} q$, where α is a constant. The effect of the diaphragm parameters on the sensor response can be estimated by simulating the correlation between $\Delta\lambda$ and U for different α values, as shown in Figure 77. However, even though the sensitivity can be theoretically improved by increasing a and reducing h , in practice, the operation limits will be bounded by the Pitot-static tube physical dimensions and the mechanical strength of the diaphragm material.

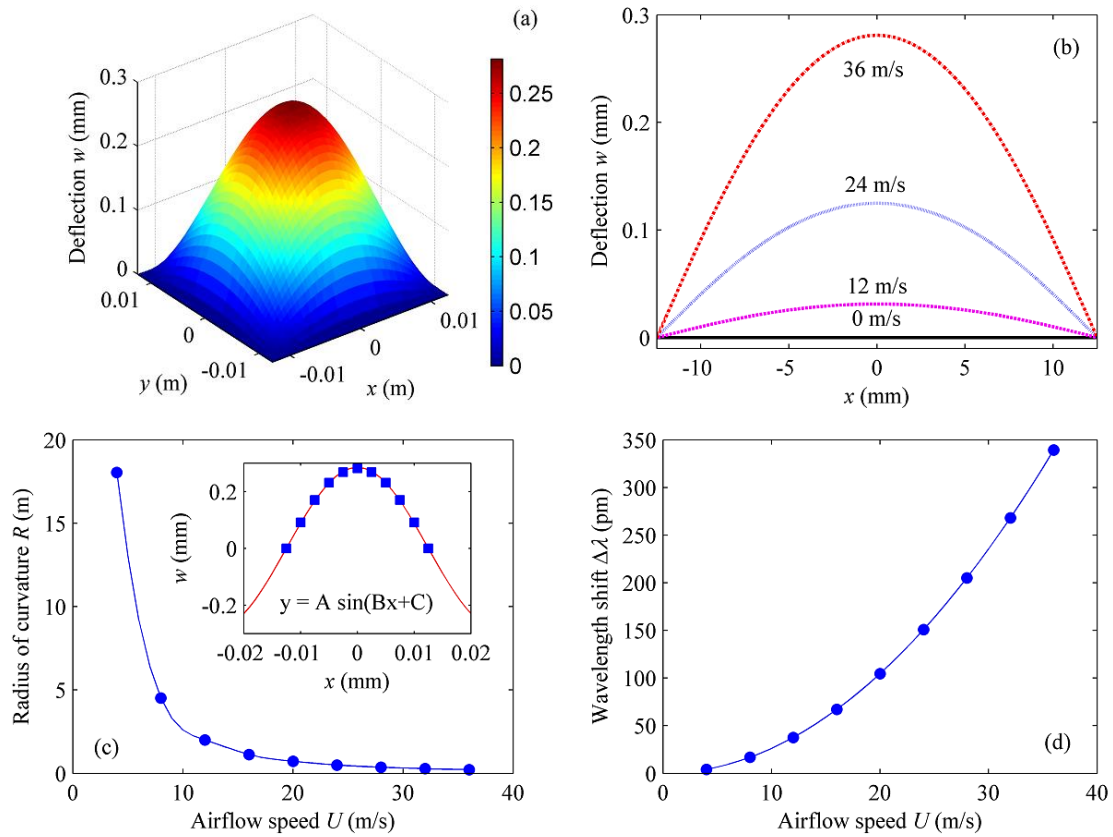


Figure 76 – Simulation of the diaphragm deflection in response to the airflow speed. (a) Deflection profile for $U = 36$ m/s, the colors indicate the magnitude of w . (b) Deflection profiles as a function of U . (c) Fiber radius of curvature, the inset shows the w values (squares) and the sine function curve fitting (red line) for $U = 36$ m/s. (d) Bragg wavelength shift as a function of the speed (the experimental data fitted by a degree-2 polynomial). (255).

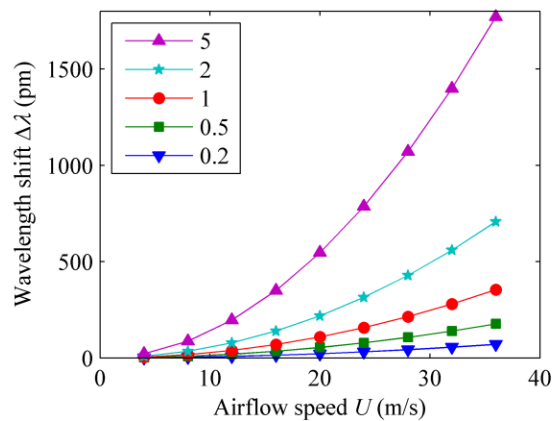


Figure 77 – FBG wavelength shift as a function of the airflow speed for different diaphragm parameters α (indicated in the legend). (255).

B. Experimental Results

The sensor calibration curve was obtained by varying the airflow speed in steps of ~ 0.7 m/s and then acquiring the optical signal and the nominal pressure values after the flow

stabilization. Then, the pressure difference was converted into speed value and correlated with the Bragg wavelength shift. Finally, the sensor measurements were validated by subjecting the device to several cycles of airflow increase and decrease within the linear operation range. In this case, the $\Delta\lambda$ value was applied to estimate the airflow speed based on the calibration curve, which was further compared with the reference values. The effect of the airflow speed in the FBG response is presented in Figure 78a. As predicted by the simulation, it was not possible to correctly retrieve the wavelength shifts for $U < 20$ m/s because the input pressure was not sufficient to deflect the diaphragm, so the fiber curvature was practically negligible. Although the sensor response is not linear, it presents a more sensitive range for $28 \leq U < 36$ m/s, yielding a ~ 24.9 pm/(m/s) sensitivity and 0.04 m/s resolution considering the 1 pm resolution of the FBG interrogator. The curve fitting residuals are shown in Figure 78b, thus resulting in a maximum absolute value of 15.56 pm (0.62 m/s) and a standard deviation of the mean of 5.59 pm (± 0.42 m/s measurements uncertainties for a 95% confidence interval). The differences between the calibration curves obtained in the simulation and experimental results can be explained due to the fact that the theoretical model did not consider the changes in the membrane thickness owing to deformation, which can affect the deflection profile and, consequently, the FBG response.

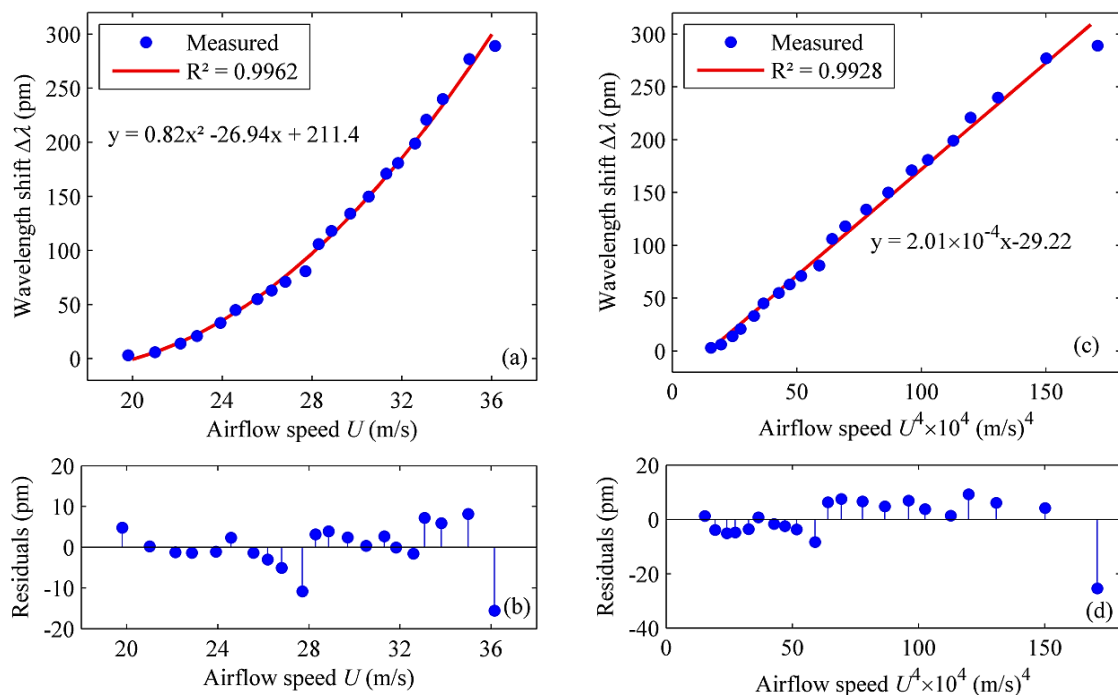


Figure 78 – Sensor calibration curves: Bragg wavelength shift as a function of (a) airflow speed U and (c) U^4 . Experimental data fitted by polynomial functions, where R^2 is the coefficient of determination. The curve fitting residuals are shown in (b) and (d) for U and U^4 , respectively (255).

For the sake of convenience, the sensor calibration curve was linearized in terms of $\Delta\lambda$ as a function of U^4 (Figure 78c), yielding $2.01 \times 10^{-4} \text{ pm}/(\text{m/s})^4$ sensitivity for the 20–36 m/s range. Regarding the residuals (Figure 78d), a 25.40 pm maximum absolute value was obtained, as well as a 7.70 pm standard deviation value [$\pm 0.80 \times 10^5 (\text{m/s})^4$ measurements uncertainties for a 95% confidence interval]. The results are comparable to a previously reported diaphragm-based optical fiber airflow sensor (270), but the interrogation method adopted in this work is much simpler to implement. Moreover, even though higher sensitivities were obtained with structured fiber sensors (266,277), it must be stressed that in addition to the complex procedures involved in the fabrication of the sensing probe, the measurement range of such devices is limited to lower airflow speeds ($< 10 \text{ m/s}$).

Once the linearized calibration curve was obtained, the sensor performance was validated for the assessment of a variable input wind speed (Figure 79). The measurements were performed based on the calibration curve shown in Figure 78c, whereas the output U^4 values were converted to U for more straightforward analysis. The fiber sensor was capable of measuring the airflow speed with good repeatability, as observed in the cyclic loads. The absolute error can be evaluated by the difference between the obtained speed values U and the reference ones U^* , yielding an average error of 0.98 m/s. This offset can be explained by the possible misalignment of the Pitot tube inlet in relation to the streamline, so the fiber sensor and the U-tube manometer were not exactly subjected to the same pressure difference.

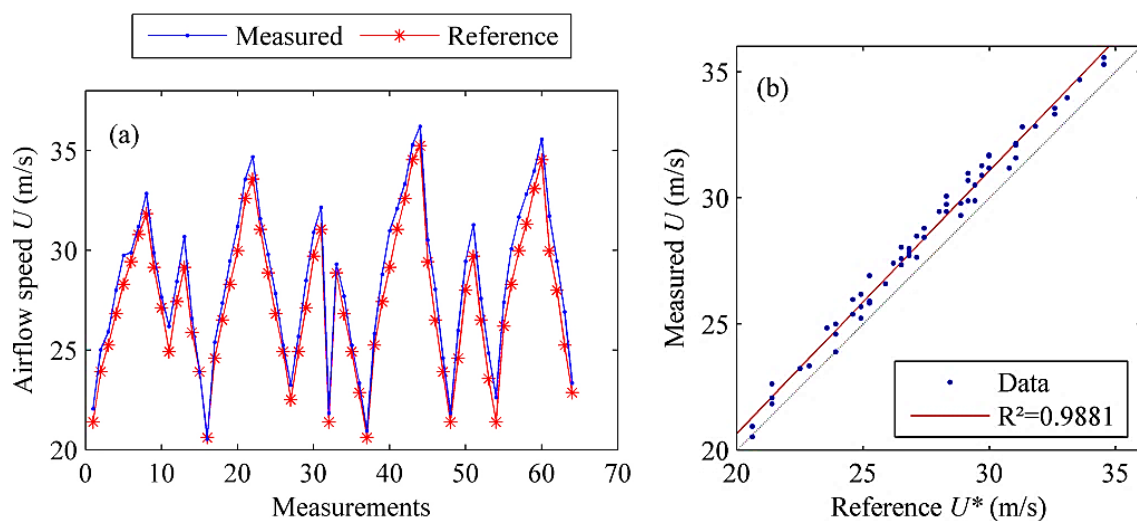


Figure 79 – Comparison between the airflow speeds measured by the fiber sensor U and the reference values U^* obtained by the U-tube manometer. (a) Variation of the U value and (b) measurement errors. In (b), the red line indicates the linear fit model applied to the data, whereas the black dotted line indicates the $U = U^*$ case (255).

Even though the device is not presently able to properly detect airflow speeds lower than 20 m/s, it is worth noticing that the dynamic range can be extended by changing the diaphragm design, which is comprised of: 1) increasing the square membrane dimensions a ; 2) reducing the thickness h ; or 3) choosing a material with adequate E and ν values. Another approach consists in using of OFSs with higher bending sensitivity, such as in-fiber interferometers, surface-core fibers, and fiber specklegram sensors, but there is a tradeoff between the measurement capabilities and the robustness of such devices. Thus, in contrast to the previously reported optical fiber anemometers, the proposed device utilizes a simple and straightforward design based on the 3-D-printed parts and can be implemented using commercially available FBG interrogators. In addition, further developments are still required for enhancing the measurement capabilities regarding practical applications in aerospace and wind power, including the study of the transducer placement, the compensation of temperature effect, the evaluation of the membrane degrading due to repeated loads, and the miniaturization of the interrogation unit into an embedded hardware; therefore, those topics will be explored in further developments on this study.

6.2 Tilted fiber Bragg gratings for measurement of multiphase flow

Multiphase flows comprise the simultaneous transport of immiscible substances as dispersed and continuous phases. Examples of such systems occur in the oil and gas industry, during the extraction of light and heavy oils containing dispersed elements like minerals, gases, and water, in nuclear reactors, as well as in biomedical applications, microreactors and clinical analyses. Measuring multiphase systems involves the detection of flow rate and velocity, temperature, and concentration (278). Even though several methods are currently available, such as imaging and computer-vision based systems, ultrasonic, capacitive, and electronic sensors, and spectroscopy analyses (278-281), there are limitations in terms of processing time, portability, robustness, and implementation costs (280,281). Therefore, optical fiber sensors emerge as suitable alternatives due to their intrinsic advantages and the inertness of silica to several chemical and biological agents (282). Different setups of optical fiber sensors for assessing two-phase flows have been proposed. For instance, reflection-type sensors estimate velocity and geometry of dispersed slugs based on the reflected light intensity, which can be

accomplished using either standard or specialty fiber probes (283,284). Velocity and concentration of droplets interacting with evanescent field can be monitored by microfibers transverse to the flow direction according to a complex interrogation setup (285). Photonic crystal fibers are also eligible for trapping volumes of liquids and sense their characteristics as the droplets flow through air holes, however, it may be difficult to clean clogged fibers (286,287). A grid of multiple fiber Bragg gratings (FBG) was proposed to track the passage of dispersed volumes based on mechanical stimulation, but this approach does not provide chemical characterization (288). Ultimately surrounding droplets can be detected using exposed FBG (289) or long-period gratings (LPG) (290), even though these methods require additional fiber processing and are restricted to periodical flows.

Tilted fiber Bragg gratings (TFBG) figure then as feasible alternatives to FBG and LPG sensors, exhibiting high sensitivity to external RI changes and intrinsic temperature-compensation capability (291,292). The analysis of two-phase systems by TFBG was demonstrated in surface tension (293) and flow measurements (294,295), but such methods usually require metallic coatings and rely on spectral analysis. Even though current fiber interrogation hardware is capable to provide fast wavelength scanning and peak/dip detection, such devices present relatively high cost and complexity. As an alternative, the study detailed in this section demonstrated a TFBG-based two-phase flow sensor with single-wavelength detection. A millifluidic device is used to produce controlled droplets that stimulate the TFBG, so the flow characteristics are assessed from the output intensity signal. In contrast to current approaches, the proposed system employs a simplified interrogation system based on a single photodetector so that the response time only depends on the sampling rate of the data acquisition hardware.

6.2.1 Materials and methods

Tilted fiber Bragg gratings, like regular FBGs, are comprised of periodical RI changes along the core length, but in a TFBG the diffraction template is slanted with respect to the fiber axis. The TFBG then couple core-propagating modes to a set of cladding high-order modes, creating resonances in the transmission spectrum toward shorter wavelengths. Since the evanescent field of cladding modes interacts with the external medium, resonance dips are red-shifted as the surrounding RI n approaches the cladding effective index, making TFBG sensors suitable for chemical measurements (291,292).

The resonance wavelength λ_i of the i -th cladding mode is given by the phase-matching condition:

$$\lambda_i = (n_{co} + n_{cl}^i) \frac{\Lambda}{\cos \theta} \quad (6.6)$$

where n_{co} and n_{cl}^i are the effective indexes of the core and the i -th cladding mode, respectively, Λ is the grating periodicity, and θ is the tilt angle (291). Regarding a TFBG subjected to longitudinal two-phase flow, wherein n_C and n_D denote the material RI of continuous and dispersed phases, respectively, the surrounding index varies with time as the dispersed phase passes along the grating. Since typical methods assess the output spectrum for quantifying shifts in the resonance wavelengths (292), velocity measurements in flowing droplets are restricted by the scanning frequency of the optical spectrum analyzer (OSA) or interrogation hardware. An alternative comprises choosing a fixed transmission wavelength λ so that the TFBG works as a tunable notch filter, therefore, variations of output light intensity $I(t)$ as a function of $n(t)$ can be measured in real-time using a photodetector connected to an oscilloscope or data acquisition card. Consequently, for a grating length L , the average flow speed V can be evaluated from the temporal features of $I(t)$ (296), as shown in Figure 80, whereas each phase is identifiable based on the respective RI values. Assuming that $I(t)$ has an average time period T , the flow speed is estimated by $V = L/T$.

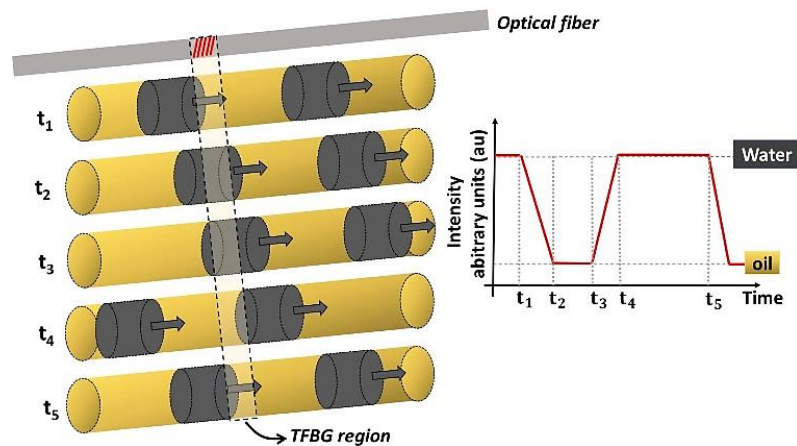


Figure 80 – Variation of surrounding refractive index as a function of time. The output spectra of TFBG shifts with the dispersed phase transport, making it feasible to evaluate the flow speed and estimate the continuous and dispersed substances (256).

An outline of the fiber sensor system is depicted in Figure 81. A light source excites the single-mode fiber whereas a detector measures the output light filtered by the TFBG. A section of the optical fiber was inserted into a transparent, T-junction millifluidic device, the waveguide

placed parallel to the flow direction. Syringe pumps controlled the input flow rates of the continuous and dispersed phases to create a two-phase flow profile. Furthermore, a transverse static camera performed optical tracking measurements for comparative analyses. The TFBG was fabricated by phase-mask technique as explained previously, yielding $\Lambda = 535.6$ nm, $L = 4$ mm and $\theta = 6^\circ$. The millifluidic device was obtained by stereolithography using a 3D printer (Formlabs) and transparent photopolymer resin, resulting in channel length and cross-section area of 30 mm and 1 mm^2 , respectively. The optical fiber was stretched and centered inside the channel, then, lateral accesses were sealed using a photocurable resin.

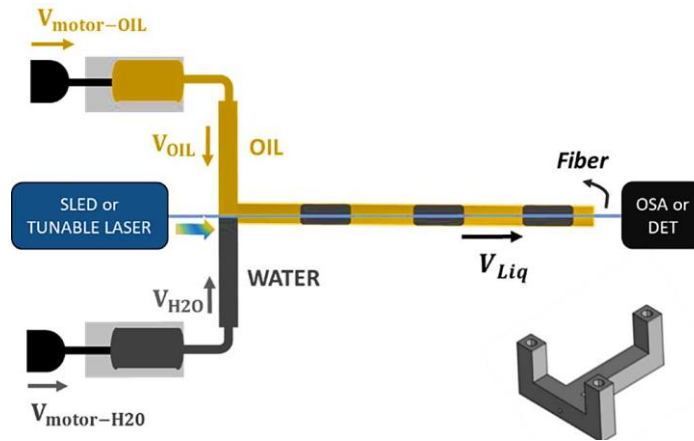


Figure 81 – Optical fiber sensor: water-in-oil two-phase flow passes through the millifluidic device and changes the refractive index surrounding the TFBG. The speed of water droplets V_{Liq} is defined by the flow rates of continuous and dispersed phases. 3D sketch in the bottom-right shows the multiphase flow device (256).

The sensor response to the surrounding index was characterized by immersing the TFBG in glycerin solutions ($1.33 \leq n \leq 1.47$). The fiber was excited with a superluminescent diode source, whereas the transmitted light was measured by an OSA. Based on the output transmission range, it is possible to choose a particular λ value for implementing the single-wavelength interrogation scheme. Afterwards, the fiber sensor was applied to assess two-phase flows using a tunable laser source and a photodetector. The syringe pumps of the millifluidic device were empirically adjusted to establish a periodical slug flow by setting the ratio q according to Equation (6.7):

$$q = \frac{Q_d}{Q_c} \quad (6.7)$$

where Q_d and Q_c are the flow rates of dispersed and continuous phases, respectively (297). The plungers were driven by linear stepper motors so that the translational velocity and dimensions of the syringe tube define the flow rates. Intensity signals were acquired by an oscilloscope at

100 Hz sampling rate and processed in a computer for evaluating the flow characteristics. The results were validated by concomitant optical tracking measurements. The sensor response was investigated for samples comprised of air ($n = 1.00$), DI water ($n = 1.33$), and vegetable oil ($n = 1.47$), as typically conducted in liquid-liquid and gas-liquid studies (298). All the experiments were carried at room temperature, the fiber and millifluidic device were cleaned between measurements using isopropyl alcohol to avoid contamination. Figure 82a shows the TFBG transmission spectra for different samples, indicating that resonance dips red-shift and then vanish when n equals the refractive index of silica (~ 1.47), as expected.

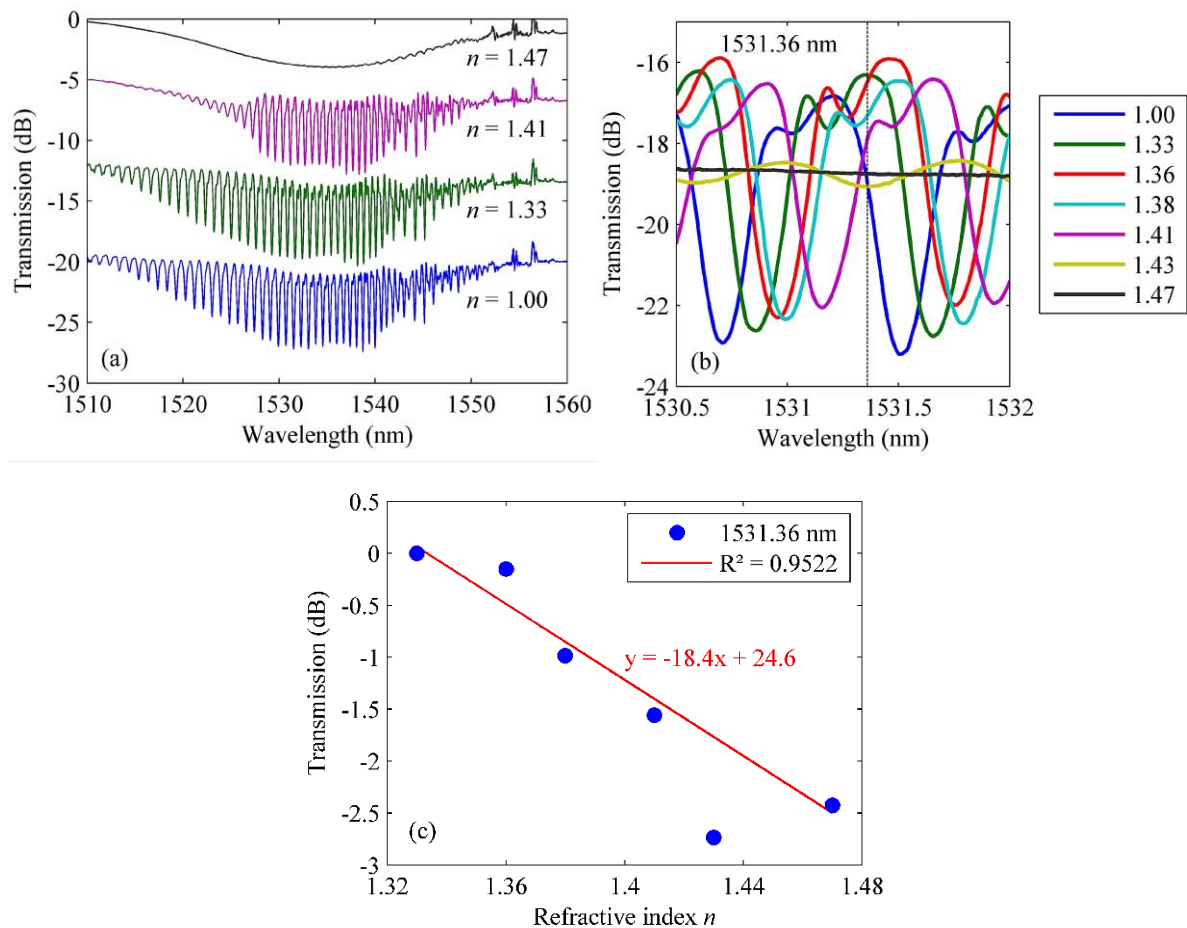


Figure 82 – FBG sensor response to the surrounding refractive index n :(a) transmission spectra; (b) resonance dips around 1531.5 nm, the vertical line indicates $\lambda = 1531.36$ nm whereas the legend indicates n values; (c) transmission as a function of n , solid line is a linear curve fitting that excludes outliers. Transmission data was normalized for the sake of visualization (256).

Using water as the reference, maximum resonance occurs at ~ 1531 nm, Figure 82b, therefore the closest neighboring peak at $\lambda = 1531.36$ nm was adopted for single-wavelength interrogation. Water slugs were marked using small volumes of dye for improving

visualization: prior measurements indicated that deviations in the sample refractive index caused by the dye are negligible. Although the sensor response becomes non-monotonic, it is feasible to discern water from oil and air based on the variation of -2.5 dB in the output intensity. The calibration curve for $1.33 \leq n \leq 1.47$ is depicted in Figure 82c, yielding an average sensitivity of -18.4 dB/RIU (refractive index units). Alternatives for tailoring the sensor dynamic range comprise adjusting λ according to the assessed medium (n_C and n_D values) or using a dual-wavelength scheme to resolve for ambiguities.

6.2.2 Results and discussion

The sensor response to water-in-oil flows (*i.e.*, water dispersed in oil) for ratios $q = 0.6$ and 0.5 is shown in Figure 83. The light intensity $I(t)$ fluctuates over time and achieves maximum value when a water slug passes by the grating: based on the reference wavelength chosen in Figure 82, the RI of water ($n_D = 1.33$) increases the transmission signal in contrast to the oil ($n_C = 1.47$).

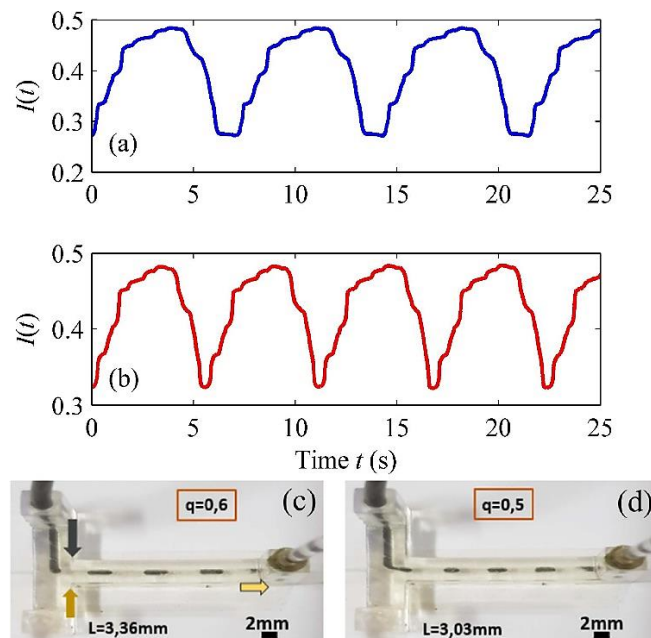


Figure 83 – Measurement of water-in-oil flows: normalized intensity for (a) $q = 0.6$ and (b) $q = 0.5$, peaks and dips indicate the passage of water and oil slugs, respectively, along the TFBG. Flow profiles for (c) $q = 0.6$ and (d) $q = 0.5$, water slugs are colored with black dye (256).

By adjusting q , it is possible to control the length of water slugs as well as the velocities of both phases (299): reducing q implies in increasing the speed of continuous phase and,

therefore, the frequency of periodical signal $I(t)$. As to the temporal analyses of Figure 83, recalling the TFBG length $L = 4$ mm, the evaluated period and average speed for $q = 0.6$ are $T = 7.16$ s and $V = 0.56$ mm/s, respectively, whereas the ratio $q = 0.5$ provides $T = 5.64$ s and $V = 0.71$ mm/s. These values corroborate with the optical tracking measurements, in which $V = 0.55$ mm/s and 0.68 mm/s were obtained for $q = 0.6$ and 0.5 , respectively, resulting in a maximum relative error of 4.4%. Transitions in $I(t)$ are not abrupt even though the substances are immiscible with discrepant refractive indexes since the resonance dip shifts depend on the proportion of water and oil surrounding the grating for a given time, as shown by the model depicted in Figure 80, but the intensity profile is expected to change depending on the flow speed and the detector sampling rate.

Regarding the measurement of air-in-oil flow (air is the dispersed phase), Figure 84a, deviations in the output intensity are more subtle in amplitude than the water-in-oil case because of the RI of dispersed and continuous phases produce a coincident transmission level at 1531.36 nm (difference of ~ 0.25 dB), which makes the sensor less sensitive in this case. Indeed, one may change the reference wavelength to increase the sensitivity regarding assessed phases: as noticed in Figure 82b, choosing the dip for $n = 1.00$ at $\lambda \approx 1531.5$ nm produce a difference of ~ 4.4 dB in comparison to the transmission for $n = 1.47$.

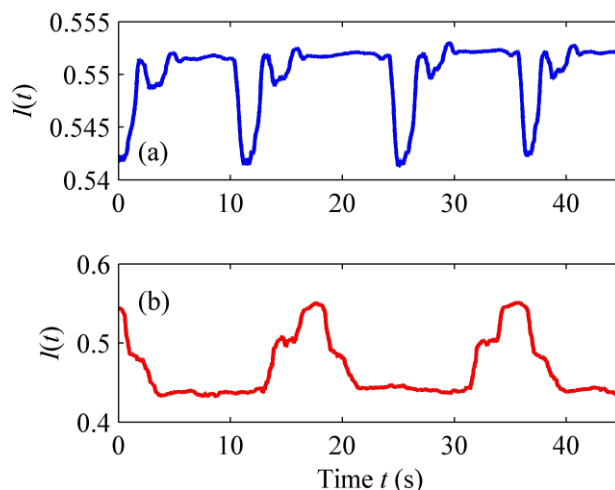


Figure 84 – Normalized intensity signals for (a) air-in-oil (dips indicate the passage of air slugs along the TFBG) and (b) water-in-air flows (peaks represent transport of water slugs). (256).

Nevertheless, the TFBG is capable to discern between both phases, resulting in an average flow speed of $V = 0.34$ mm/s ($T = 11.83$ s). The peaks observed during phases transitions are due to the non-monotonic characteristic of the sensor calibration curve for $n \leq 1.33$, as well as to small air bubbles formed during the droplet transport (297). As for water-in-

air flow, water slugs manifest as intensity peaks (Figure 84b) because of the distinct transmission level observed in Figure 82b, even though the RI of air extrapolates the calibration curve. The average period and speed are 17.96 s and 0.22 mm/s, respectively. Despite the $I(t)$ signal indicates that the continuous phase may be confused with oil due to the similar intensity values, it must be stressed that the sensor can be calibrated for other RI ranges by adjusting the interrogation wavelength λ .

In conclusion, by using the TFBG and single-wavelength detection scheme, it is possible to track the temporal evolution of liquid or gas slugs flowing through a continuous phase, wherein the response time depends only on the sampling frequency of the data acquisition hardware. Even though a tunable laser source was employed for the sake of convenience, a simpler approach would consist in using a single-mode longitudinal distributed feedback laser diode for exciting the fiber at a specific wavelength. In this case, a resonance dip can be adjusted (through tailoring the TFBG tilt angle) to match the laser emission so that the interrogation system can be realized with low-cost, ordinary telecom components. The evaluation of flow speed is also similar to the well-established optical tracking methods, but the proposed system does not require transparent tubes or colored fluids and is simpler to compute than image processing approaches (281). Furthermore, it is worth noticing that the sensor response is affected by the temperature as the surrounding fluids and the fiber material present characteristic thermo-optic coefficients, changes in n_{co} and n_{cl}^i shift the resonance wavelengths and affect the output intensity range. Nevertheless, thermal fluctuations can be compensated with a single TFBG by monitoring the Bragg reflection peak λ_B of the core mode, which is insensitive to the surrounding RI in contrast to the cladding modes resonances (292). Therefore, one may implement a dual-wavelength scheme to assess λ and λ_B simultaneously and correct the calibration curve in real-time, so no reference fibers are required with such setup.

6.3 All-optical real-time monitoring of air/vacuum valves with fiber Bragg gratings

Knowledge of both water and airflow is crucial in developing adequate models for water pipeline system sizing (300). To regulate the airflow in water lines, operators install several air valves along the length of the pipeline. Among the available airflow solutions, one commonly

employed is the air/vacuum valve (AVV), two-way mechanical devices that allow for both the expulsion of air when the pipeline is filled with water, and entrance of air when the water is pumped out of the pipes. AVVs typically employ a floater design that passively closes an exhaust/intake port as the water level inside the valve rises, which then reopens when the water level recedes. Currently, water pipeline systems are usually engineered with AVVs distributed along an adductor according to the AWWA M51 standard (301), being placed in the highest elevation points along adductors, after a long horizontal section, or when small slopes are present – situations of evident potential for air accumulation. A study by McPherson (302) proposes a more comprehensive approach, based on the use of full dynamic hydraulic models to evaluate the correct size and positioning of air valves. Developing such models poses a complex problem due to the inherent compressible and biphasic flow regimens, and the frequent failure of poorly maintained air valves exacerbates the issue.

Incorrectly sized or inoperative air valves can expose the hydraulic system to pressure loading surges that can lead to the mechanical failure of pipes and fittings, possibly resulting in leakages and system downtime (303). Thus, proper management of air entering and leaving the system is essential to operate hydraulic systems in desirable safety conditions. Despite their importance, in-depth studies on the dynamics of AVVs for their proper sizing and positioning are scarce and, aside from annual scheduled maintenance and inspections, pipeline operators employ no online or real-time monitoring to ensure their proper operation (304). Furthermore, air valve performance data provided by suppliers is often inaccurate, leading to potentially harmful design decisions (305). While research aimed at deepening the knowledge on the mechanics of such air/water systems continues to find its way into the specialized literature (304-306), there is still a distinct gap in developing effective AVVs monitoring strategies. Systemic monitoring and maintenance programs need to be developed, as well as comprehensive design procedures that consider the individual requirements of each valve and its location.

Considering this context, this study aimed to address the lack of real-time remote monitoring solutions for AVVs by proposing and validating through experimentation an all-optical monitoring setup using a fiber Bragg grating (FBG) sensor embedded into a 3D-printed flexible polymer casing. The casing was fixed to the AVV exhaust/intake port with the help of a 3D printed support adapter and allowed to bend in response to the airflow. The FBG then operated as a fiber optics strain gauge that responded to the applied flexural load. Results

obtained with the FBG approach were then compared to reference data from a traditional orifice plate setup.

6.3.1 Materials and methods

FBG probes fabricated in-house were encased into 200 mm long thermoplastic polyurethane (TPU) casings (2 mm x 10 mm rectangular cross-section) by 3D-printing, using a filament printer (AiP-A3, Sethi 3D) according to the procedures detailed in Manzo *et al.* (307). Encasing the fiber adds an extra layer of both protection against mechanical shock and handling and against environmental conditions (308). A support piece was also 3D-printed using polylactide (PLA) filament to secure the encased fiber sensor to the AAV exhaust/intake port, allowing it to bend in response to the airflow pressure loading. The TPU encased sensor was then secured to the support using a pair of 3D-printed PLA clamps (Figure 85). The distance between fixtures was set at 90 mm, and the backside of the PLA support was fitted with a threaded pipe adaptor that allows to fasten the support to the AVV exhaust/intake port. Thus, air is allowed to flow freely through the holes in the center of the support and adapter.

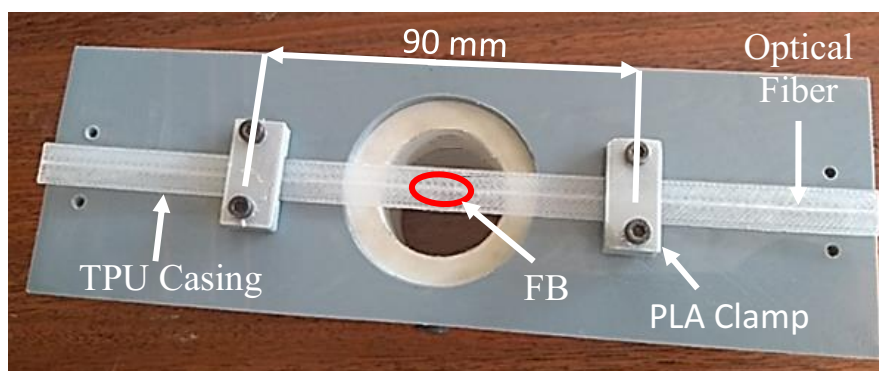


Figure 85 – 3D-printed TPU encased FBG sensor secured to the 3D-printed PLA support (257).

TPU was selected for this application for its flexibility, which produces a clear and detectable mechanical response even for relatively low-pressure loads during air intake through the AVV. The adequacy of its mechanical properties for this application can be better shown by looking at the results from the tensile stress-strain testing done with dog-bone shaped test specimens, following the guidelines and recommendations of the ISO 37 standard (309). The tensile test was conducted using a universal testing machine with a displacement speed of up to 50 mm/min and a 10 kN load cell. Figure 86 presents the tensile stress-strain curve for the 3D-

printer filament grade TPU, while Table 4 summarizes the test results. As can be observed, TPU exhibits a rubber like behavior, reaching over 140 % strain before failure with a fairly low Young's modulus of 44.79 MPa.

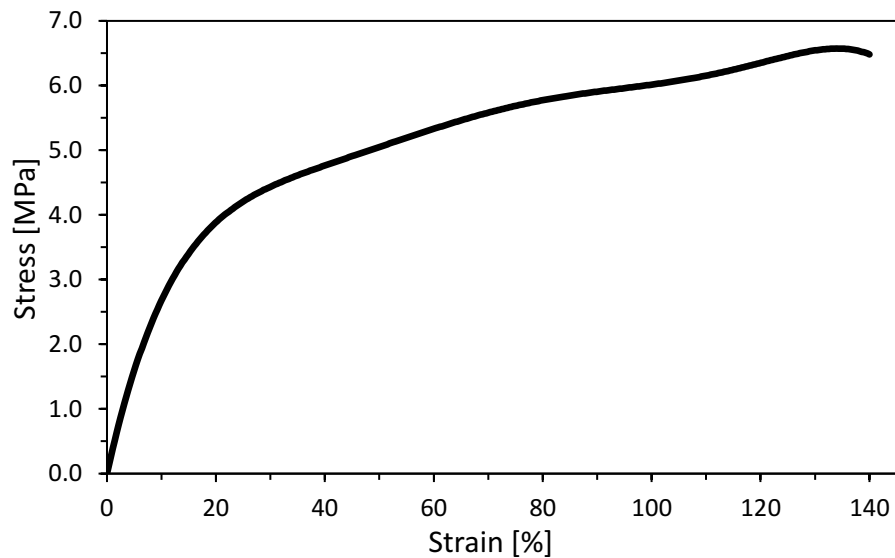


Figure 86 – Stress-Strain curve of 3D-printer filament grade TPU (257).

Table 4 – Physical properties of the TPU polymer (257).

Material	Thermoplastic Polyurethane (TPU)
Young's modulus	44.79 MPa
Maximum stress	6.76 MPa
Strain at break	143 %
Stress at break	6.48 MPa

To simulate the loading and discharging operation of a real water adductor piping system for the AVV monitoring tests, a test bench (Figure 87) was assembled with cast iron pipes and fittings of 150 mm nominal diameter, gate valves, two AVVs, and a fixed speed centrifugal pump assembly with the following characteristics: engine power of 25 hp (18.6 kW), 22 mH₂O (215 kPa) manometric head and 180 m³/h nominal flow rate at 1750 RPM. Both gate valves (V1 and V2) are at ground level, and the pump and drain are connected to the municipal water supply network. For this experiment, only the AVV at the highest point (2.4 m from ground level) in the hydraulic test bench was instrumented. A more in-depth discussion of this setup can be found in (306).

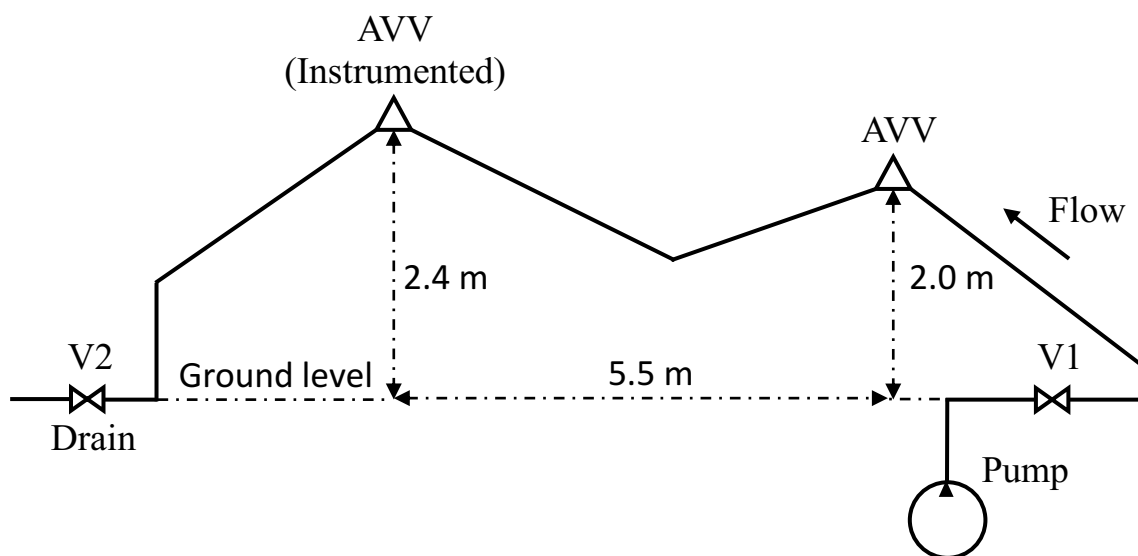


Figure 87 – Schematic drawing of hydraulic test bench. V1, V2 = gate valves. AVV = air/vacuum valve (257).

To compare the results obtained with the FBG, a 900 mm long pipe section (28 mm diameter) with a concentric orifice plate (14.6 mm orifice diameter) was attached to the AVV as a reference, with the plate positioned 300 mm from the AVV intake/exhaust port. Electronic pressure sensors were placed at one diameter upstream of the orifice plate and half a diameter downstream (306). The concentric orifice plate assembly was chosen for this application based on a previous study by Aquino *et al.* (310). In that study the authors tested the adequacy of vane anemometers, pitot tube and orifice plates for monitoring AVVs, with the conclusion that both the anemometer and pitot tube were unable to produce accurate results due to the mixed water/air flow and relatively high air velocities during purging events. As the orifice plate assembly is too bulky to be used on real air valve installations, this also highlights the importance of developing a compact monitoring setup capable of reliably monitoring their operational status. Since the airflow velocity, and thus the pressure gradient between sensors, is much higher for air purging events than air intake, sensors with distinct operating ranges were utilized to maximize the sensitivity for both scenarios: For air purge 0-200 kPa dynamic range sensors (Hokushin DPF100.3) were used, and for air intake 0-29 kPa dynamic range sensors (Siemens D-76181). Operation the test bench is relatively simple, for purge tests, the drain valve V2 is closed while the pump valve V1 is open, then the pump is turned on until the pipeline is completely filled. Afterwards the pump is turned off, V1 is closed, and then V2 is opened to let the pipe discharge for the intake test. The limitation of this setup is the impossibility of installing both the orifice plate and the encased FBG sensor in series at the AVV exit port; thus, tests with

each sensing approach were conducted separately. To account for this limitation and obtain comparable datasets, experimental conditions were kept as uniform as possible (controlled room temperature and humidity), the same hydraulic test bench was used for all tests, and every test followed the same experimental procedures. Furthermore, data for three purge and intake events were recorded for both the orifice plate and FBG. The datasets were then combined by averaging and computing the standard deviation using a t-distribution to obtain the confidence intervals of the data before presenting a comparison in scatter plots with interpolating lines. The combination of these measures as the best metrological practice available in this situation and is expected to provide reliable results.

6.3.2 Results and discussion

As previously discussed, the air flow leaving or entering the AVV will impart a pressure loading over the TPU beam with encased FBG sensor. This will cause the TPU casing to bend in the direction of the flow, resulting in tensile or compressive internal stresses that increase with the distance from the neutral bending axis (311). As the FBG acts as a unidirectional strain gauge and the optical fiber is offset from the neutral axis, it is sensitive to these effects as described in back in Chapter 3, Equation (3.3). The working principle is illustrated in Figure 88, where it is evident that the FBG sensor will detect tensile strain for air purge events, compressive strain for air intake events, and no strain when the valve is closed. Effectively, by observing the sign and the magnitude of the strain measured with the FBG via its spectral shift it is possible to determine the operation regimen of the AVV and the duration of the purge/intake events. Experiments with the electronic pressure sensors and encased FBG sensor were conducted separately, as discussed in the previous section. Firstly, the pipe extension with orifice plate was installed to the AVV and the pressure difference between sensors placed upstream and downstream (ΔP) of the flow was recorded for three consecutive purge and intake events. Afterwards the extension is removed and the 3D-printed TPU support is secured to the AVV, following with data collection of three other sets of air purging and intake events. Performing all tests in quick succession under controlled laboratory conditions eliminated concerns regarding the FBG cross-sensitivity with temperature. Data collected with the FBG is expressed in terms of the observed Bragg wavelength shift ($\Delta\lambda_B$), in response to the applied pressure load.

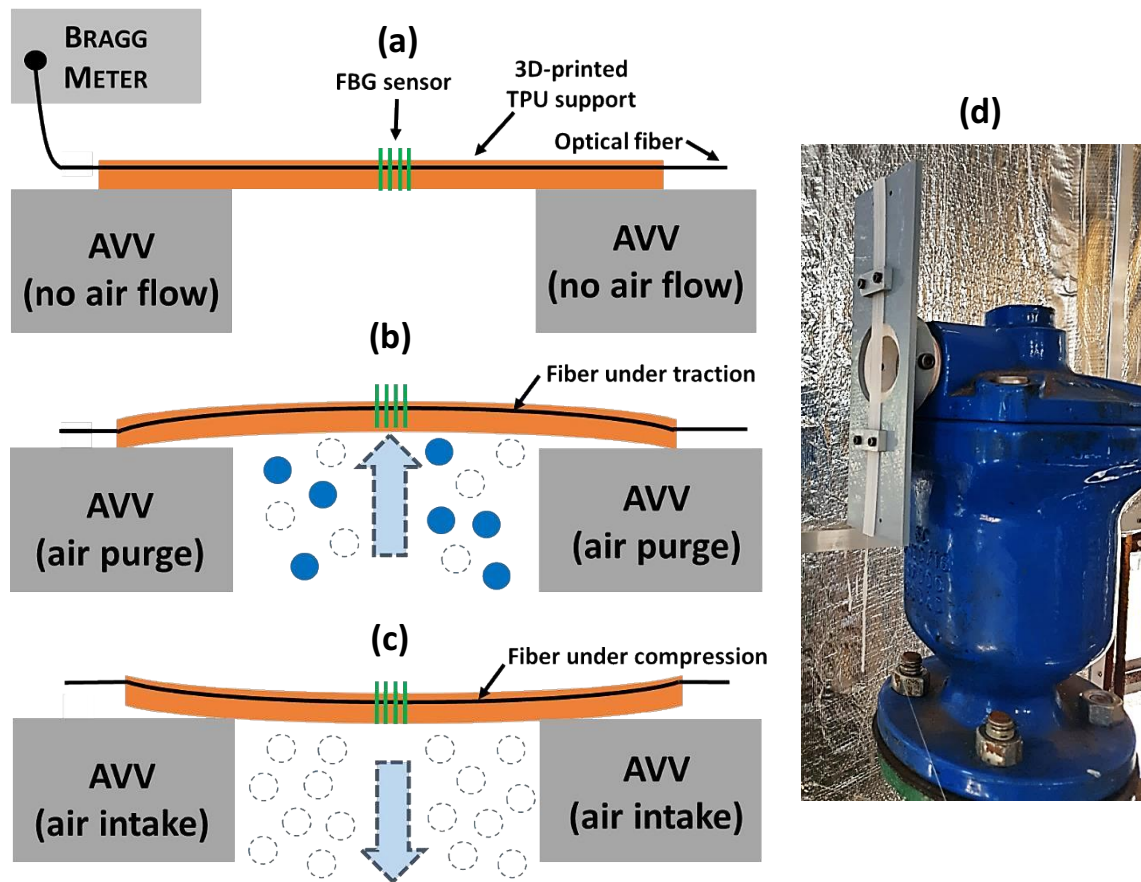


Figure 88 – Schematic drawing of the optical fiber sensor working principle. (a): Sensor at rest (no air flow). (b): Bending of the sensor due to the air and water droplets flow in a purging event. (c): Bending of the sensor during an air intake event. (d): PLA support and encased FBG sensor secured to the AVV (257).

Figure 89 summarizes the results as scatter plots, with the air purge data presented in Figure 89a, and air intake in Figure 89b. The green dots are the averaged ΔP values in kPa for the 3 events, while the red dots are the averaged $\Delta\lambda_B$ values in pm. Sensor data was collected at a rate of 1 sample/s for both sensor types, which corresponds to the maximum acquisition rate of the Portable BraggMETER FBG interrogation unit used here. As shown in Figure 89, the agreement between the ΔP and $\Delta\lambda_B$ curves for both types of airflow through the AVV is very good. The encased FBG sensor was able to clearly detect the slight bending under the lower pressure loads during air intake (Figure 89b), and the $\Delta\lambda_B$ curve also shifts from positive values during air purge, to negative values during air intake, as expected. As both events have relatively long durations (8 to 12 seconds) and no abrupt transients, the 1 sample/s limit of the FBG interrogator posed no issue for airflow monitoring. The good agreement between curves is interesting as it suggests the possibility of utilizing the FBG based sensor to obtain calibration curves of AVVs. This can be of particular interest to manufacturers, as previous research suggests that the development of standardized procedures for characterizing AVVs is necessary

as performance curves presented on datasheets are often unreliable (305). But this was beyond the scope of this work, which aimed to provide a proof-of-concept of a novel setup capable of reliably monitoring the operational state of AVVs (“closed”, “intake” or “air purge” state) and would require further testing with precisely controlled air flows. For the purposes of this work the main concern was the limit of detection, given the air flow during intake events is very subtle (peak ΔP measured between electronic pressure sensors ~ 4 kPa, Figure 89b). The proposed optical approach can clearly detect this subtle flow, and a detectable response can be seen on the FBG signal even for ΔP 's in the range of ~ 1 kPa (Figure 89b).

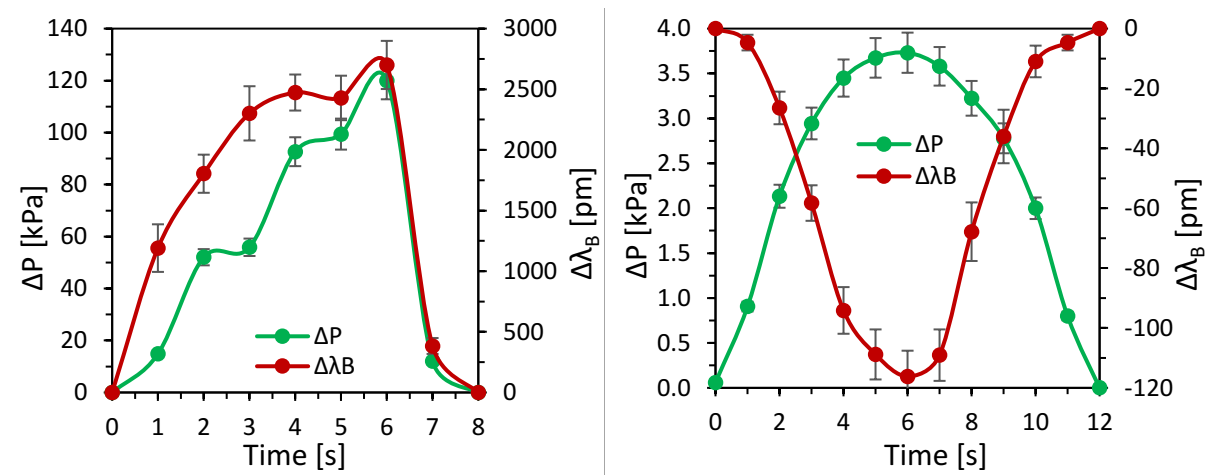


Figure 89 – Response curves of the FBG sensor (red dots) and electronic pressure sensors (green dots). (a): During air purging events. (b): During air intake events (257).

Although the orifice plate also proved to be effective in this experiment, it presents drawbacks that limit its application on the field. Most notably is its bulkiness, since it requires extending a straight pipe section out of the AVV, which is often unfeasible due to the prevalence of confined spaces in piping systems. Orifice plates are also subject to clogging and accumulating water, which is expelled in small quantities before the valve completely shuts off during purging events. Electrical safety and corrosion are also cause for concern. It is worth noting, however, that orifice plates or other methods are not utilized in the industry to monitor air valves. As discussed in the Introduction, visual inspection during scheduled maintenance is the only monitoring strategy currently employed. In this study, the orifice plate was used only for validation purposes. While a single fiber with one inscribed FBG was used to monitor an AVV in this study, monitoring multiple AVVs on field applications can be achieved by means of multiplexing sensors. This can be realized by writing multiple FBGs along a single fiber or by concatenating signals from multiple fibers. Future research will focus on making the sensor

“field-ready,” such as developing strategies to compensate for temperature, testing new approaches for encasing the FBG (encasing material and casing mechanical design) that are more robust than TPU without sacrificing sensitivity, and modeling the relation between flexural load observed in the encased FBG and the volumetric air flow through the AVV.

7 CONCLUSIONS

Several novel optical fiber probes with low-cost interrogation setups based on specklegram recording or intensity-based demodulation were presented to assess physical and chemical variables. The setups mostly consisted of a single He-Ne laser to excite the fiber probes, a pair of objective lenses to launch fiber to and from the fiber, and a cheap ~20 USD webcam for recording the speckle patterns, a significant improvement in both cost and complexity in relation to competing setups needing broadband light sources and optical spectrum analyzers such as SPR based sensors, or interferometric setups that need fine alignment of all optical components and expensive laser sources with longer coherence lengths. Despite the use of lower cost equipment and simple optical setups, the sensors exhibited a performance comparable or superior to said solutions reported in the specialized literature, as detailed at the end of each individual section in chapters 4 and 5, posing as viable alternatives to current commercial optical fiber sensing solutions. Further developments will focus mainly on expanding the capabilities of the proposed probes and enhancing their performance.

For the evaporation probe described in section 4.1 one avenue currently being explored to improve the stability of the probe's response and shield it from external factors is to introduce a Germanium doped glass rod fixed to the inner wall of the glass microtube, preventing light launched in the Ge doped rod from leaking into the glass tube, strongly limiting the interaction between guided modes and the external medium to the interface between the rod and the fluid contained inside the capillary. Developing an appropriate evaporation model for the capillary fibers also opens the possibility of using the probe for assessing fluid properties such as viscosity, vapor pressure and effective diffusivity. For the concatenated fiber structured proposed in section 4.2 there is good opportunity to develop strategies to compensate for temperature crosstalk and to encapsulate the fiber probe for practical measurements. The capabilities of the exposed core fiber sensor detailed in section 4.3 can be enhanced by using the EZNCC approach for increased dynamic range, the response of the probe to external refractive index can also be better characterized by employing a more diverse array of fluids to cover the gaps between air ($n \approx 1.0$) and water ($n = 1.3330$), and between water and ethanol ($n = 1.3632$). The fundamental mechanisms behind the hysteresis observed in the opto-magnetic probes (section 4.4) needs further investigation, other proposed developments for this study

include experimenting with core/cladding fibers instead of the no-core structure and investigating the effects of magnetic saturation of the Tb^{3+} ions on the dynamic range of the probe.

Regarding the agarose-based waveguides, the main improvement opportunities come from exploring new waveguide compositions, such as including glycerol in the agarose mix to improve probe stability, though care must be taken to use biocompatible materials when exploring *in-vivo* applications and biochemical measurements. The structured agarose probe from section 5.1 can be exploited as an optical sensor and growth medium for microorganisms. Both excitation and fluorescent lights can be guided through the structured fiber core, making it simple to evaluate the spectral response under different environmental conditions. The waveguide may be designed as a disposable sample unit containing the necessary nutrients and immobilized cells, which could be promptly coupled to the optical instrumentation (spectrometer or microscope) for practical analyses. Moreover, the fiber can also be used as a substrate for cell immobilization and as a growth medium, so the biochemical properties can be assessed through the interaction between the sample and the transmitted light. Exploring other hydrogels and additives is also important for the pH probe detailed in section 5.3, as the fluorescent properties of the nanoparticles is affected by the medium encapsulating them through solvatochromism, suggesting this as a possible path for enhancing the probe sensitivity and linearity. As before, the doped hydrogel waveguide can also be used as a medium for growing cells, reducing the risk of causing cell death during measurements. Finally, the performance of the reusable memory effect probe detailed in section 5.2, overall performance can be improved by revisiting the cladding material for a better index contrast with the ABS core, while a tensile testing machine to enable complete control of the applied stress and strain rate along with securing the fiber to a robust substrate, such as a standard tensile test specimen, will also significantly improve tensile test results by inhibiting necking along the fiber. The observed spikes in the transmission loss after relief-reload cycles present an interesting possibility of utilizing the proposed POF sensor as a fatigue life indicator of critical components in mechanical systems and smart structures.

Lastly, new application cases for fiber Bragg gratings for optical anemometers, characterization of multiphase flow in reduced size channels, and for the monitoring of air valves in water adductor systems were also demonstrated. Even though the FBG based pitot device in section 6.1 was not presently able to properly detect airflow speeds lower than 20 m/s, it is worth noticing that the dynamic range can be extended by changing the diaphragm design

by increasing the square membrane dimensions, reducing the thickness, or choosing a material with adequate E and ν values. Another approach consists in using of OFSs with higher bending sensitivity, such as in-fiber interferometers, surface-core fibers, and fiber specklegram sensors, but there is a tradeoff between the measurement capabilities and the robustness of such devices. Miniaturization of the interrogation unit into an embedded hardware is another avenue that can be explored in future developments. Regarding the multiphase flow device based on a tilted FBG in section 6.2, one of the main advantages demonstrated in this study was the demonstration that the probe interrogation can be achieved by monitoring transmitted intensity for a single wavelength, considerably reducing costs over traditional FBG interrogators based on broadband lasers and detailed optical spectrum analysis. Temperature crosstalk of the FBG can be compensated using the Bragg reflection peak (λ_B), which is insensitive to the external refractive index, therefore one may implement a dual-wavelength scheme to assess λ and λ_B simultaneously and correct the calibration curve in real-time, so no reference fibers are required with such setup, which would still be a simpler and more cost-effective approach than traditional FBG interrogation schemes. Presently the air/vacuum valve monitoring setup detailed in section 6.3 still employs traditional FBG interrogators, but the system cost is mitigated when considering the high multiplexing capability for monitoring multiple valves across several km of pipelines. It is also important to note that an approach based on traditional electronic pressure sensors are often not possible due to space constraints and electrical safety concerns. Future research will focus on making the sensor “field-ready,” such as developing strategies to compensate for temperature, testing new approaches for encasing the FBG (encasing material and casing mechanical design) that are more robust than TPU without sacrificing sensitivity, and modeling the relation between flexural load observed in the encased FBG and the volumetric air flow through the AVV, as the volume of air flowing through the piping systems is also of interest to evaluate the performance of the air valves and their optimal positioning on water adductor systems.

The collection of studies presented here represent a small yet impactful push on the boundaries of the collective scientific and technical knowledge developed around fiber optic sensors, most notably when pertaining to the viability and potential of specklegram sensors as low-cost and highly sensitive alternatives for the sensing of numerous quantities of interest. To illustrate the great flexibility of fiber optic sensors, this work has presented optical probes for measuring refractive index, temperature, liquid level (or bathed length), pH, evaporation of fluids, magnetic field intensity, mechanical strain, and fluid flow speed and flow rates.

References

- 1 HERZBERGER, M. Optics from Euclid to Huygens. **Applied Optics**, v.5, n.9, p.1383-1393, 1966.
- 2 DOUGLASS, W. T.; GEDYE, N. G. Lighthouse. In: HUGH, Chisholm (Ed.). **Encyclopædia Britannica**. Cambridge University Press, 1911. v.16, p.627-651.
- 3 DU, Y.; CHEN, W.; CUI, K.; GUO, Z.; WU, G.; REN, X. An exploration of the military defense system of the Ming Great Wall in Qinghai Province from the perspective of castle-based military settlements. **Archaeological and Anthropological Sciences**, v.13, article 46, 2021.
- 4 POLYBIUS. In: PATON, W. R. (Translation), WALBANK, F. W.; HABICHT, C. (Revision). **The Histories, Volume IV: Books 9-15**. Loeb Classical Library 159. Cambridge, MA: Harvard University Press, 2011.
- 5 REHMAN, S. U.; ULLAH, S.; CHONG, P. H. J.; YONGCHAREON, S.; KOMOSNY, D.; Visible Light Communications: A System Perspective – Overview and Challenges. **Sensors (Basel)**, v.19, n.5, article 1153, 2019.
- 6 DUNNINGTON, G. W. **Carl Friedrich Gauss: Titan of Science**. New York: Hafner Publishing, 1955. Reprint: The Mathematical Association of America, Washington, 2004.
- 7 MCGRAIL, S. **Boats of the World: From the Stone Age to Medieval Times**. New York: Oxford University Press, 2004.
- 8 MARTIN, L. C. Surveying and navigational instruments from the historical standpoint. **Transactions from the Optical Society**, v.24, n.5, 1923.
- 9 DREYER, J. L. E. On the invention of the Sextant. **Astronomical Notes**, v.115, n.3, p.33-35, 1886.
- 10 GOODE, S. Mance's Heliograph, or Sun-Telegraph. **Royal United Services Institution Journal**, v.19, n.83, 1875.

- 11 MIMS III, F. M. Alexander Graham Bell and the Photophone: The Centennial of the Invention of Light-Wave Communications, 1880 – 1890. **Optics News**, v.6, n.1, p.8-16, 1980.
- 12 BALLATO, J.; DRAGIC, P. Glass: The Carrier of Light – A Brief History of Optical Fiber. **International Journal of Applied Glass Science**, v.7, n.4, p.413-422, 2016.
- 13 COLLADON, D. On the reflections of a ray of light inside a parabolic liquid stream. **Comptes Rendus**, v.15, p.800-802, 1842.
- 14 BABINET, J. Note on the transmission of light by sinuous canals. **Comptes Rendus**, v.15, p.802, 1842.
- 15 THYAGARAJAN, K.; GHATAK, A. **Fiber Optic Essentials**. Hoboken: John Wiley & Sons, 2007.
- 16 MAINMAN, T. Stimulated Optical Radiation in Ruby. **Nature**, v.187, p.493-494, 1960.
- 17 KAO, K. C.; HOCKHAM, G. A. Dielectric-fiber surface waveguides for optical frequencies. **Proceedings of the Institution of Electrical Engineers**, v.113, n.7, p.1151-1158, 1966.
- 18 UDD, E.; SPILLMAN JR, W. B. **Fiber Optic Sensors: And Introduction for Engineers and Scientists**. New Jersey: John Wiley & Sons, 2011.
- 19 UDD, E. Fiber Optic Smart Structures. **Proceedings of the IEEE**, v.84, n.6, p.884-894, 1996.
- 20 KEISER, G. **Comunicações por Fibras Ópticas**. Porto Alegre: AMGH, 2014.
- 21 SENIOR, J. M. **Optical Fiber Communications – Principles and Practice**. Harlow: Pearson Education, 2009.
- 22 WENG, Y.; HE, X.; PAN, Z. Space division multiplexing optical communication using few-mode fibers. **Optical Fiber Technology**, v.36, p.155-180, 2017.

- 23 OTO, M.; KIKUGAWA, S.; SARUKURA, N.; HIRANO, M.; HOSONO, H. Optical fiber for deep ultraviolet light. **IEEE Photonics Technology Letters**, v.13, n.9, p.978-980, 2001.
- 24 SAVELII, I.; DESEVEDAVY, F.; JULES, J.-C.; GADRET, G.; FATOME, J.; KIBLER, B.; KAWASHIMA, H.; OHISHI, Y.; SMEKTALA, F. Management of OH absorption in tellurite optical fibers and related supercontinuum generation. **Optical Materials**, v.35, n.8, p.1595-1599, 2013.
- 25 LIN, A.; ZHANG, A.; BUSHONG, E. J.; TOULOUSE, J. Solid-core tellurite glass fiber for infrared and nonlinear applications. **Optics Express**, v.17, n.19, p.16716-16721, 2009.
- 26 BALLATO, J.; E.-HEIDEPRIEM, H.; ZHAO, J.; PETIT, L.; TROLES, J. Glass and Process Development for the Next Generation of Optical Fibers: A Review. **MDPI Fibers**, v.5, n.1, article 11, 2017.
- 27 HEALY, N.; GIBSON, U.; PEACOCK, A. C. A review of materials engineering in silicon-based optical fibres. **Semiconductor Science and Technology**, v.33, n.2, article 023001, 2018.
- 28 KIEU, K.; SCHNEEBELI, L.; NORWOOD, R. A.; PEYGHAMBARIAN, N. Integrated liquid-core optical fibers for ultra-efficient nonlinear liquid photonics. **Optics Express**, v.20, n.7, p.8148-8154, 2012.
- 29 TRAVERS, J. C.; CHANG, W.; NOLD, J.; JOLY, N. Y.; RUSSEL, P. ST. J. Ultrafast nonlinear optics in gas-filled hollow-core photonic crystal fibers [Invited]. **Journal of the Optical Society of America B**, v.28, n.12, p.A11-A26, 2011.
- 30 MARKOS, D. J.; IPSON, B. L.; SMITH, K. H.; SCHULTZ, S. M.; SELFRIDGE, R. H.; MONTE, T. D.; DYOTT, R. B.; MILLER, G. Controlled core removal from a D-shaped optical fiber. **Applied Optics**, v.42, n.36, p.7121-7125, 2003.
- 31 BIAZOLI, C. R.; SILVA, S.; FRANCO, M. A. R.; FRAZÃO, O.; CORDEIRO, C. M. B. Multimode interference tapered fiber refractive index sensors. **Applied Optics**, v.51, n.24, p.5941-5945, 2012.
- 32 KOSHIBA, M.; SAITOH, K.; TAKENAGA, K.; MATSUO, S. Multi-core fiber design and analysis: coupled-mode theory and coupled-power theory. **Optics Express**, v.19, n.26, p.B102-B111, 2011.

- 33 ADAM, J. L.; TROLES, J.; BRILLAND, L.; COULOMBIER, Q.; CHARTIER, T. Photonic crystal fibers based on chalcogenide glasses. In: **Proc. SPIE 7839, 2nd Workshop on Specialty Optical Fibers and Their Applications (WSOF-2)**, Oaxaca, Mexico, 2010.
- 34 KUMAR, V. V. R. K.; GEORGE, A. K.; KNIGHT, J. C.; RUSSEL, P. ST. J. Tellurite photonic crystal fiber. **Optics Express**, v.11, n.20, p.2641-2645, 2003.
- 35 BUCZYŃSKI, R.; KLIMCZAK, M.; PYSZ, D.; STĘPNIEWSKI, G.; SIWICKI, B.; CIMEK, J.; KUJAWA, I.; PIECHAL, B.; STĘPIEŃ, R. Soft glass photonic crystal fibres and their applications. In: **Proc. SPIE 9507, Micro-structured and Specialty Optical Fibres IV**, Prague, Czech Republic, 2015.
- 36 KAISER, P.; ASTLE, H. W. Low-Loss Single-Material Fibers Made From Pure Fused Silica. **The Bell System Technical Journal**, v.53, n.6, p.1021-1039 1974.
- 37 FRAZÃO, O.; SILVA, R. M.; FERREIRA, M.S.; SANTOS, J. L.; RIBEIRO, A. B. L. Suspended-core Fibers for Sensing Applications. **Photonic Sensors**, v.2, n.2, p.118-126, 2012
- 38 KNIGHT, J. C.; BIRKS, T. A.; RUSSEL, P. S. J.; ATKIN, D. M. All-silica single-mode optical fiber with photonic crystal cladding. **Optics Letters**, v.21 n.19, p.1547-1549, 1996.
- 39 LÆGSGAARD, J.; BJARKLEV, A. Microstructured Optical Fibers – Fundamentals and Applications. **Journal of the American Ceramic Society**, v.89, n.1, p.2-12, 2005.
- 40 STAWSKA, H. I.; POPENDA, M. A.; B.-PAWLIK, E. Anti-Resonant Hollow Core Fibers with Modified Shape of the Core for the Better Optical Performance in the Visible Spectral Region – A Numerical Study. **MDPI Polymers**, v.18, n.10, article 899, 2018.
- 41 JU, J.; JIN, W. Photonic Crystal Fiber Sensors for Strain and Temperature Measurements. **Journal of Sensors**, v.2009, article 476267, 2009.
- 42 BIRKS, T. A.; KNIGHT, J. C.; RUSSEL, P. ST. J. Endlessly single-mode photonic crystal fiber. **Optics Letters**, v.22, n.13, p.961-963, 1997.
- 43 YAKASAI, I. K.; ABAS, PG. E.; BEGUM F. Review of porous core photonic crystal fibers for terahertz waveguiding. **Optik**, v.229, article 166284, 2021.

- 44 REEVES, W. H.; KNIGHT, J. C.; RUSSEL, P. ST. J.; ROBERTS, P. J. Demonstration of ultra-flattened dispersion in photonic crystal fibers. **Optics Express**, v.10, n.14, p.609-613, 2002.
- 45 KIANG, K. M.; FRAMPTON, K.; MONRO, T. M.; MOORE, R.; TUCKNOTT, J.; HEWAK, D. W.; RICHARDSON, D. J.; RUTT, H. N. Extruded singlemode non-silica glass holey optical fiber. **Electronics Letters**, v.38, n.12, p.546-547, 2002.
- 46 TREVOR, D. J.; BISE, R. T. Sol-gel derived microstructured fiber: fabrication and characterization. In: **OFC/NFOEC Technical Digest. Optical Fiber Communication Conference 2005**, Anaheim, USA, 2005.
- 47 RUSSEL, P. ST. J. Photonic crystal fibers: Basics and applications. In: KAMINOW, Ivan P.; LI, Tingye; WILLNER, Alan E. (Eds.). **Optical Fiber Telecommunications V A**. Cambridge: Academic Press, 2008. Chapter 14, p.485-522.
- 48 TALAITASONG, W.; ISMAEEL, R.; MARQUES, T. H. R.; MOUSAVI, S. A.; BERESNA, M.; GOUVEIA, M. A.; SANDOGHCHI, S. R.; LEE, T.; CORDEIRO, C. M. B.; BRAMBILLA, G. Mid-IR Hollow-core microstructured fiber drawn from a 3D printed PETG preform. **Scientific Reports**, v.8, article 8113, 2018.
- 49 POLETTI, F.; PETROVICH, M. N.; RICHARDSON, D. J. Hollow-core photonic bandgap fibers: technology and applications. **Nanophotonics**, v.2, n.5-6, p.315-340, 2013.
- 50 HARTOG, A. H. **An Introduction to Distributed Optical Fiber Sensors**. Boca Raton: CRC Press, 2017.
- 51 FANG, Z.; CHIN, K.; QU, R.; CAI, H. In: CHANG, Kai (Ed.). **Fundamentals of Optical Fiber Sensors**. Hoboken: John Wiley & Sons, 2012.
- 52 WANG, X.-D.; WOLFBEIS, O. S. Fiber-Optic Chemical Sensors and Biosensors (2015-2019). **Analytical Chemistry**, v.92, n.1, p.397-430, 2020.
- 53 RAMAKRISHNAN, M.; RAJAN, G.; SEMENOVA, Y.; FARREL, G. Overview of Fiber Optic Sensors Technologies for Strain/Temperature Sensing Applications in Composite Materials. **Sensors (Basel)**, v.16, n.1, article 99, 2016.

- 54 YE, X. W.; SU, Y. H.; HAN, J. P. Structural Health Monitoring of Civil Infrastructure Using Optical Fiber Sensing Technology: A Comprehensive Review. **The Scientific World Journal**, v.2014, article 652329, 2014.
- 55 LI, J. A review: Development of novel fiber-optic platforms for bulk and surface refractive index sensing applications. **Sensors and Actuators Reports**, v.2, n.1, article 100018, 2020.
- 56 SILVA, R. M.; MARTINS, H.; NASCIMENTO, I.; BAPTISTA, J. M.; RIBEIRO, A. L.; SANTOS, J. L.; JORGE, P.; FRAZÃO, O. Optical Current Sensors for High Power Systems: A Review. **Applied Sciences**, v.2, n.3, p.602-628, 2012.
- 57 LIU, C.; SHEN, T.; WU, H.-B.; FENG, Y.; CHEN, J.-J. Applications of magneto-strictive, magneto-optical, magnetic fluid materials in optical fiber current sensors and optical fiber magnetic field sensors: A review. **Optical Fiber Technology**, v.65, article 102634, 2021.
- 58 ZHANG, C.-L.; GONG, C.-Y.; GONG, Y.; RAO, Y.-J.; PENG, G.-D. Optical Fiber Microfluidic Sensors Based on Opto-physical Effects. In: Peng, Gang-Ding (Ed.). **Handbook of Optical Fibers**. Singapore: Springer, 2019.
- 59 BINU, S.; PILLAI, V. P. M.; CHANDRASEKARAN, N. Fibre optic displacement sensor for the measurement of amplitude and frequency of vibration. **Optics & Laser Technology**, v.39, n.8, p.1537-1543, 2007.
- 60 KUANG, K. S. C.; QUEK, S. T.; KOH, C. G.; CANTWELL, W. J.; SCULLY, P. J. Plastic Optical Fibre Sensors for Structural Health Monitoring: A Review of Recent Progress. **Journal of Sensors**, v.2009, article 312053, 2009.
- 61 RORIZ, P.; RAMOS, A.; SANTOS, J. L.; SIMÕES, J. A. Fiber Optic Intensity-Modulated Sensors: a Review in Biomechanics. **Photonic Sensors**, v.2, n.4, p.315-330, 2012.
- 62 DE ACHA, N.; S.-LENÁROZ, A. B.; ELOSÚA, C.; MATÍAS, I. R. Trends in the Design of Intensity-Based Optical Fiber Biosensors (2010-2020). **Biosensors**, v.11, article 197, 2021.
- 63 SOARES, M. C. P.; VIT, F. F.; SUZUKI, C. K.; DE LA TORRE, L. G.; FUJIWARA, E. Perfusion Microfermentor Integrated into a Fiber Optic Quasi-Elastic Light Scattering Sensor for Fast Screening of Microbial Growth Parameters. **Sensors**, v.19, n.11, article 2493, 2019.

- 64 SOARES, M. C. P.; RODRIGUES, M. S.; SCHENKEL, E. A.; PERLI, G.; SILVA, W. H. A.; GOMES, M. K.; FUJIWARA, E.; SUZUKI, C. K. Evaluation of Silica Nanofluids in Static and Dynamic Conditions by an Optical Fiber Sensor. **Sensors**, v.20, n.3, article 707, 2020.
- 65 YANG, L.; SHEN, Y.; HE, K.; ZHANG, T.; XU, R.; ZHAO, S.; CHEN, L.; XU, S. An optical fiber temperature sensor based on fluorescence intensity ratio used for real-time monitoring of chemical reactions. **Ceramics International**, v.47, n.23, p.33537-33543, 2021.
- 66 YU, Q.; ZHOU, X. Pressure Sensor Based on the Fiber-Optic Extrinsic Fabry-Perot Interferometer. **Photonic Sensors**, v.1, n.1, p.72-83, 2011.
- 67 XU, J.; WANG, X.; COOPER, K. L.; WANG, A. Miniature all-silica fiber optic pressure and acoustic sensors. **Optics Letters**, v.30, n.24, p.3269-3271, 2005.
- 68 AREF, S. H.; LATIFI, H.; ZIBAILI, M. I.; AFSHARI, M. Fiber optic Fabry-Perot pressure sensor with low sensitivity to temperature changes for downhole applications. **Optics Communications**, v.269, n.2, p.322-330, 2007.
- 69 ISLAM, MD. R.; ALI, M. M.; LAI, M.-H.; LIM, K.-S.; AHMAD, H. Chronology of Fabry-Perot Interferometer Fiber-Optic Sensors and Their Applications: A Review. **Sensors**, v.14, n.4, p.7451-7488, 2014.
- 70 SANBORN, E. E.; SANG, A. K.; WESSON, E.; WIGENT, D. E., LUCIER, G. Distributed Fiber Optic Strain Measurement Using Rayleigh Scatter in Composite Structures. In: PROULX, TOM (Ed.) **Experimental and Applied Mechanics, Volume 6. Conference Proceedings of the Society for Experimental Mechanics Series**. New York: Springer, 2011.
- 71 LEFÈVRE, H. C. The fiber-optic gyroscope, a century after Sagnac's experiment: The ultimate rotation-sensing technology? **Comptes Rendus Physique**, v.15, n.10, p.851-858, 2014.
- 72 KASSANI, S. H.; KHAZAEINEZHAD, R.; JUNG, Y.; KOBELKE, J.; OH, K. Suspended Ring-Core Photonic Crystal Fiber Gas Sensor With High Sensitivity and Fast Response. **IEEE Photonics Journal**, v.7, n.1, article 2700409, 2015.

- 73 NEMECEK, T.; KOMANEC, M.; MARTAN, T.; AHMAD, R.; ZVANOVEC, S. Suspended-core microstructured fiber for refractometric detection of liquids. **Applied Optics**, v.54, n.30, p.8899-8903, 2015.
- 74 JUNG, Y.; KIM, S.; LEE, D. S.; OH, K. Compact three segmented multimode fiber modal interferometer for high sensitivity refractive-index measurement. In: **Proc. SPIE 5855, 17th International Conference on Optical Fibre Sensors**, Bruges, Belgium, 2005.
- 75 JORGENSON, R. C.; YEE, S. S. A fiber-optic chemical sensor based on surface plasmon resonance. **Sensors and Actuators B: Chemical**, v.12, n.3, p.213-220, 1993.
- 76 KASHYAP, R.; CHAKRABORY, S.; ZENG, W.; SWARNAKAR, S.; KAUR, S.; DOLEY, R.; MONDAL, B. Enhanced Biosensing Activity of Bimetallic Surface Plasmon Resonance Sensor. **Photonics**, v.6, n.4, article 108, 2019.
- 77 SAVIN, S.; DIGONNET, M. J. F.; KINO, G. S.; SHAW, H. J. Tunable mechanically induced long-period fiber gratings. **Optics Letters**, v.25, n.10, p.710-712, 2000.
- 78 KASHYAP, R. **Fiber Bragg Gratings**. Cambridge: Academic Press, 1999.
- 79 KERSEY, A. D.; DAVIS, M. A.; PATRICK, H. J.; LEBLANC, M.; KOO, K. P., ASKINS, C. G.; PUTNAM, M. A.; FRIEBELE, E. J. Fiber Grating Sensors (Invited Paper). **Journal of Lightwave Technology**, v.14, n.8, p.1442-1463, 1997.
- 80 CARVALHO, J. P.; ANUSZKIEWICZ, A.; S.-BARABACH, G.; BAPTISTA, J. M.; FRAZÃO, O.; MERGO, P.; SANTOS, J. L.; URBANCZYK, W. Long period gratings and rocking filters written with a CO₂ laser in highly-birefringent boron-doped photonic crystal fibers for sensing applications. **Optics Communications**, v.285, n.3, p.264-268, 2012.
- 81 MAJUMDER, M.; GANGOPADHYAY, T. K.; CHAKRABORTY, A. K.; DASGUPTA, K.; BHATTACHARYA, D. K. Fibre Bragg gratings in structural health monitoring – Present status and applications. **Sensors and Actuators A: Physical**, v.147, n.1, p.150-164, 2008.
- 82 SAHOTA, J. K.; GUPTA, N. DHAWAN, D. Fiber Bragg grating sensor for monitoring of physical parameters: a comprehensive review. **Optical Engineering**, v.59, n.6, article 060901, 2020.

- 83 KINET, D.; MÉGRET, P.; GOOSSEN, K. W.; QIU, L.; HEIDER, D.; CAUCHETEUR, C. Fiber Bragg Grating Sensors toward Structural Health Monitoring in Composite Materials: Challenges and Solutions. **Sensors**, v.14, n.4, p.7394-7419, 2014.
- 84 FRAZÃO, O.; FERERIRA, L. A.; ARAÚJO, F. M.; SANTOS, J. L. Applications of Fiber Optic Grating Technology to Multi-Parameter Measurement. **Fiber and Integrated Optics**, v.24, n.3-4, p.227-244, 2005.
- 85 SILVEIRA, P. C.; DANTE, A.; KELEY, M. M.; CARVALHO, C.; ALLIL, R.; MOK, R.; GARÇÃO, L.; WERNECK, M. Experimental Evaluation of low-cost interrogation techniques for FBG sensors. In: **Proc. 2018 IEEE International Instrumentation and Measurement Technology Conference (I2MTC)**, Houston, USA, 2018.
- 86 DARWICH, D.; YOUSSEF, A.; ZARAKET, H. Low-cost multiple FBG interrogation technique for static applications. **Optics Letters**, v.45, n.5, p.1116-1119, 2020.
- 87 DIAZ, C. A. R.; LEITÃO, C.; MARQUES, C. A.; DOMINGUES, M. F.; ALBERTO, N.; PONTES, M. J.; FRIZERA, A.; RIBEIRO, M. R. N.; ANDRÉ, O. S. B.; ANTUNES, P. F. C. Low-Cost Interrogation Technique for Dynamic Measurements with FBG-Based Devices. **MDPI Sensors**, v.17, n.10, article 2414, 2017.
- 88 WU, S.; YIN, S.; YU, F. T. S. Sensing with fiber specklegrams. **Applied Optics**, v.30, n.31, p.4468-4470, 1991.
- 89 FUJIWARA, E.; RI, Y.; WU, Y. T.; FUJIMOTO, H.; SUZUKI, C. K. Evaluation of image matching techniques for optical fiber specklegram sensor analysis. **Applied Optics**, v.57, n.33, p.9845-9854, 2018.
- 90 SPILLMAN, W. B.; KLINE, B. R.; MAURICE, L. B.; FUHR, P. L. Statistical-mode sensor for fiber optic vibration sensing. **Applied Optics**, v.28, n.15, p.3166-3176, 1989.
- 91 HILL, K. O.; TREMBLAY, Y.; KAWASAKI, B. S. Modal noise in multimode fiber links: theory and experiment. **Optics Letters**, v.5, n.6, p.270-272, 1980.
- 92 FUJIWARA, E.; DA SILVA, L. E.; DE FREITAS, H. E.; WU, Y. T.; CORDEIRO, C. M. B. Optical Fiber Chemical Sensor Based on the Analysis of Fiber Specklegrams Characteristics. In: **Proc. 2018 SBFoton IOPC**, Campinas, Brazil, 2018.

- 93 T SUJI, T.; ASAKURA, T.; FUJII, H. Variation of the speckle contrast in a graded-index fibre by misalignment of the incident beam. **Optical and Quantum Electronics**, v.16, p.9-18, 1984.
- 94 ETCHEPAREBORDA, P.; FEDERICO, A.; KAUFMANN, G. H. Sensitivity evaluation of dynamic speckle activity measurements using clustering methods. **Applied Optics**, v.49, n.19, p.3753-3761, 2010.
- 95 FUJIWARA, E.; WU, Y. T.; CORDEIRO, C. M. B. Entropy analysis of optical fiber specklegram sensors. **Results in Optics**, v.5, article 100155, 2021.
- 96 CUEVAS, A. R.; FONTANA, M.; R.-COBO, L.; LOMER, M.; L.-HIGUERA, J. M. Machine Learning for Turning Optical Fiber Specklegram Sensor into a Spatially-Resolved Sensing System. Proof of Concept. **Journal of Lightwave Technology**, v.36, n.17, p.3733-3738, 2018.
- 97 YU, F. T. S.; WEN, M.; YIN, S.; UANG, C. M. Submicrometer displacement sensing using inner-product multimode fiber speckle fields. **Applied Optics**, v.32, n.15, p.4685-4689, 1993.
- 98 FUJIWARA, E.; DOS SANTOS, M. F. M.; SUZUKI, C. K. Optical fiber specklegram sensor analysis by speckle pattern division. **Applied Optics**, v.56, n.6, p.1585-1590, 2017.
- 99 FUJIWARA, E.; WU, Y. T.; SUZUKI, C. K.; Vibration-based specklegram fiber sensor for measurement of properties of liquids. **Optics and Lasers in Engineering**, v.50, n.12, p.1726-1730, 2012.
- 100 FUJIWARA, E.; WU, Y. T.; DOS SANTOS, M. F. M.; SCHENKEL, E. A.; SUZUKI, C. K. Development of a tactile sensor based on optical fiber specklegram analysis and sensor data fusion technique. **Sensors and Actuators A: Physical**, v.263, p.677-686, 2017.
- 101 L.-JUNIOR, A. G.; FRIZERA, A.; MARQUES, C.; PONTES, M. J. Optical Fiber Specklegram Sensors for Mechanical Measurements: A Review. **IEEE Sensors Journal**, v.20, n.2, pp.569-576, 2020.
- 102 EFENDIOGLU, H. S. A Review of Fiber-Optic Modal Modulated Sensors: Specklegram and Modal Power Distribution Sensing. **IEEE Sensors Journal**, v.17, n.7, p.2055-2064, 2017.

- 103 WANG, J.-J., YAN, S.-C.; RUAN, Y.-P.; XU, F.; LU, Y.-Q. Fiber-Optic Point-Based Sensor Using Specklegram Measurement. **Sensors**, v.17, n.10, article 2429, 2017.
- 104 FUJIWARA, E.; DA SILVA, L. E.; MARQUES, T. H. R.; CORDEIRO, C. M. B. C. Polymer optical fiber specklegram strain sensor with extended dynamic range. **Optical Engineering**, v.57, n.11, article 116107, 2018.
- 105 CABRAL, T. D.; DA SILVA, L. E.; FUJIWARA, E.; CORDEIRO, C. M. B. Fiber Specklegram Analysis for Monitoring Evaporation Inside a Capillary-like Optical Fiber. In: **Proc. LAWOFS 2019**, Rio de Janeiro, Brazil, 2019.
- 106 FUJIWARA, E.; CABRAL, T. D.; CORDEIRO, C. M. B. Optical Fiber Specklegram Sensors for Measurement of Liquids (Invited Paper). In: **Proc. 2019 SBFoton IOPC**, São Paulo, Brazil, 2019.
- 107 FUJIWARA, E.; DA SILVA, L. E.; CABRAL, T. D.; DE FREITAS, H. E.; WU, Y. T.; CORDEIRO, C. M. B. Optical Fiber Specklegram Chemical Sensor for Based on a Concatenated Multimode Fiber Structure. **Journal of Lightwave Technology**, v.37, n.19, p.5041-5047, 2019.
- 108 CABRAL, T. D.; FUJIWARA, E.; WARREN-SMITH, S. C.; EBENDORFF-HEIDPRIEM, H.; CORDEIRO, C. M. B. Multimode exposed core fiber specklegram sensor. **Optics Letters**, v.45 n.12, p.3212-3215, 2020.
- 109 SMITH, D.L.; NGUYEN, L.V.; OTTAWAY, D.J.; CABRAL, T.D.; FUJIWARA, E.; CORDEIRO, C.M.B.; WARREN-SMITH, S.C. Machine learning for sensing with a multimode exposed core fiber specklegram sensor. **Optics Express**, v.30, n.7, p.10443-10455, 2022.
- 110 CABRAL, T. D.; FRANCO, D. D.; FUJIWARA, E.; NALIN, M.; CORDEIRO, C. M. B. Magnetic Field Fiber Specklegram Sensor Based on Tb³⁺ Doped Magneto-Optical Glass Fibers with Very High Verdet Constants. **IEEE Sensors Journal**. – UNDER REVIEW.
- 111 NILSON, R. H.; GRIFFITHS, S. K.; TCHIKANDA, S. W. Axially Tapered Microchannels of High Aspect Ratio for Evaporative Cooling Devices. **Journal of heat Transfer ASME**, v.126, p.453-462, 2004.

- 112 VELEV, O. D.; GUPTA, S. Materials Fabricated by Micro-and Nanoparticle Assembly – The Challenging Path from Science to Engineering. **Advanced Materials**, v.21, n.10, p.1897-1905, 2009.
- 113 ARIF, M. F. H.; HOSSAIN, M. M.; ISLAM, N.; KHALED, S. M. A nonlinear photonic crystal fiber for liquid sensing applications with high birefringence and low confinement loss. **Sensing and Bio-Sensing Research**, v.2, article 100252, 2019.
- 114 OSÓRIO, J. H.; CHESINI, G.; SERRÃO, V. A.; FRANCO, M. A. R.; CORDEIRO, C. M. B. Simplifying the design of microstructured optical fibre pressure sensors. **Scientific Reports**, v.7, article 2990, 2017.
- 115 GOUVEIA, M. A.; AVILA, P. D.; MARQUES, T. H. R. M.; TORRES, M. C.; CORDEIRO, C. M. B. Morphology dependent polymeric capillary optical resonator hydrostatic pressure sensor. **Optics Express**, v.23, n.8, p.10643-10652, 2015.
- 116 ZHAO, J.-R.; HUANG, X.-G.; HE, W.-X.; CHEN, J.-H. High-resolution and temperature-insensitive fiber optic refractive index sensor based on Fresnel reflection modulated by Fabry-Perot interference. **Journal of Lightwave Technology**, v.28, n.19, p.2799–2803, 2010.
- 117 MENG, H.; SHEN, W.; ZHANG, G.; TAN, C.; HUANG, X. Fiber Bragg grating-based fiber sensor for simultaneous measurement of refractive index and temperature. **Sensors and Actuators B: Chemical**, v.150, n.1, p.226–229, 2010.
- 118 GARG, R.; TRIPATHI, S. M.; THYAGARAJAN, K.; BOCK, W. J. Long period fiber grating based temperature-compensated high performance sensor for bio-chemical sensing applications. **Sensors and Actuators B: Chemical**, v.176, p.1121–1127, 2013.
- 119 KIM, J. A.; HWANG, T.; DUGASANI, S. R.; AMIN, R.; KULKARNI, A.; PARK, S. H.; KIM, T. Graphene based fiber optic surface plasmon resonance for bio-chemical sensor applications. **Sensors and Actuators B: Chemical**, v.187, p.426-433, 2013.
- 120 OLIVEIRA, R.; MARQUES, T. H. R.; BILRO, L.; NOGUEIRA, R.; CORDEIRO, C. M. B. Multiparameter POF Sensing Based on Multimode Interference and Fiber Bragg Grating. **Journal of Lightwave Technology**, v.35, n.1, p.3-9, 2017.

- 121 WANG, P.; BRAMBILLA, G.; DING, M.; SEMENOVA, Y.; WU, Q.; FARREL, G. High-sensitivity, evanescent field refractometric sensor based on a tapered, multimode fiber interference. **Optics Letters**, v.36, n.12, p.2233-2235, 2011.
- 122 CUBILLAS, A. M.; UNTERKOFER, S.; EUSER, T. G.; ETZOLD, B. J. M.; JONES, A. C.; SADLER, P. J.; WASSERSCHIED, P.; RUSSEL, P. ST. J. Photonic crystal fibres for chemical sensing and photochemistry. **Chemical Society Reviews**, v.42, n.22, p.8629-8648, 2013.
- 123 WANG, B.; HUANG, C.; GUO, R.; YU, F. T. S. A novel fiber chemical sensor using inner-product multimode fiber speckle fields. In: **Proc. SPIE 5206, Optical Science and Technology, SPIE's 48th Annual Meeting**, San Diego, United States, 2003.
- 124 FENG, F.; CHEN, W.; CHEN, D.; LIN, W.; CHEN, S.-C. In-situ ultrasensitive label-free DNA hybridization detection using optical fiber specklegram. **Sensors and Actuators B: Chemical**, v.272, n.1, p.160-165, 2018.
- 125 JUNG, Y.; KIM, S.; LEE, D.; OH, K. Compact three segmented multimode fibre modal interferometer for high sensitivity refractive-index measurement. **Measurement Science and Technology**, v.17, n.5, article 1129, 2006.
- 126 MOHAMMED, W. S.; SMITH, P. W. E.; GU, X. All-fiber multimode interference bandpass filter. **Optics Letters**, v.31, n.17, p.2547-2549, 2006.
- 127 OLIVEIRA, R.; ARISTILDE, S.; OSÓRIO, J. H.; FRANCO, M. A. R.; BILRO, L.; NOGUEIRA, R. N.; CORDEIRO, C. M. B. Intensity liquid level sensor based on multimode interference and fiber Bragg grating. **Measurement Science and Technology**, v.27, n.12, article 125104, 2016.
- 128 LI, C.; NING, T.; ZHANG, C.; LI, J.; WEN, X.; PEI, L.; GAO, X.; LIN, H. Liquid level measurement based on a no-core fiber with temperature compensation using a fiber Bragg grating. **Sensors and Actuators A: Physical**, v.245, p.49-53, 2016.
- 129 MICKELSON, A. R.; WEIERHOLT, A. Modal noise-limited signal-to-noise ratios in multimode optical fibers. **Applied Optics**, v.22, n.19, p.3084-3089, 1983.
- 130 MEHTA, A.; MOHAMMED, W.; JOHNSON, E. G. Multimode interference-based fiber-optic displacement sensor. **IEEE Photonics Technology Letters**, v.15, n.8, p.1129-1131, 2003.

- 131 TAKAHARA, H. Visibility of speckle patterns: effect of the optical guide length in coherent light. **Applied Optics**, v.15, n.3, p.609-610, 1976.
- 132 R.-COBO, L.; LOMER, M.; COBO, A.; L.-HIGUERA, J.-M. Optical fiber strain sensor with extended dynamic range based on specklegrams. **Sensors and Actuators A: Physical**, v.203, p.341-345, 2013.
- 133 LI, E. Temperature compensation of multimode-interference-based fiber devices. **Optics Letters**, v.32, n.14, p.2064-2066, 2007.
- 134 KIM, Y. H.; PARK, S. J.; JEON, S.-W.; JU, S.; PARK, C.-S.; HAN, W.-T.; LEE, B. H. Thermo-optic coefficient measurement of liquids based on simultaneous temperature and refractive index sensing capability of a two-mode fiber interferometric probe. **Optics Express**, v.20, n.21, p.23744-23754, 2012.
- 135 ZHANG, Y.; TIAN, X.; XUE, L.; ZHANG, Q.; YANG, L.; ZHU, B. Super-High Sensitivity of Fiber Temperature Sensor Based on Leaky-Mode Bent SMS Structure. **IEEE Photonics Technology Letters**, v.25, n.8, p.560-563, 2013.
- 136 HOO, Y. L.; JIN, W.; SHI, C.; HO, H. L.; WANG, D. N.; RUAN, S. C. Design and modeling of a photonic crystal fiber gas sensor. **Applied Optics**, v. 42, n.18, p.3509-3515, 2003.
- 137 COX, F. M.; LWIN, R.; LARGE, M. C. J.; CORDEIRO, C. M. B. Opening up optical fibers. **Optics Express**, v.15, n.19, p.11843-11848, 2007.
- 138 W-SMITH, S. C.; E.-HEIDPRIEM, H.; FOO, T. C.; MOORE, R.; DAVIS, C.; MONRO, T. M. Exposed-core microstructured optical fibers for real-time fluorescence sensing. **Optics Express**, v.17, n.21, p.18533-18542, 2009.
- 139 BACHHUKA, A.; HENG, S.; VASILEV, K.; KOSTECKI, R.; ABELL, A.; E.-HEIDPRIEM. Surface Functionalization of Exposed Core Glass Optical Fiber for Metal Ion Sensing. **Sensors**, v. 19, n.8, article 1829, 2019.
- 140 KLANTASAVA, E.; FRANÇOIS, A.; E.-HEIDPRIEM, H.; HOFFMANN, P.; MONRO, T. M. Surface Plasmon Scattering in Exposed Core Optical Fiber for Enhanced Resolution Refractive Index Sensing. **Sensors**, v.15, n.10, p.25090-25102, 2015.

- 141 DOHERTY, B.; THIELE, M.; W.-SMITH, S.; SCHATNER, E.; E.-HEIDPRIEM, H.; FRITZCHE, W.; SCHMIDT, M. A. Plasmonic nanoparticle-functionalized exposed-core fiber – an optofluidic refractive index sensing platform. **Optics Letters**, v.42, n.21, p.4395-4398, 2017.
- 142 LI, X.; NGUYEN, L. V.; BECKER, M.; PHAM, D.; E.-HEIDPRIEM, H.; W.-SMITH, S. C. Simultaneous measurement of temperature and refractive index using an exposed core microstructured optical fiber. **IEEE Journal of Selected Topics in Quantum Electronics**, v.25, n.4, article 5600107, 2019.
- 143 REDDING, B.; POPOFF, S. M.; CAO, H. All-fiber spectrometer based on speckle pattern reconstruction. **Optics Express**, v.21, n.5, p.6584-6600, 2013.
- 144 R.-COBO, L.; LOMER, M.; L.-HIGUERA, J. M. Fiber specklegram-multiplexed sensor. **Journal of Lightwave Technology**, v.33, n.12, p.2591-2597, 2015.
- 145 W.-SMITH, S. C.; KOSTECKI, R.; NGUYEN, L. V.; MONRO, T. M. Fabrication, splicing, Bragg grating writing, and polyelectrolyte functionalization of exposed-core microstructured optical fibers. **Optics Express**, v.22, n.24, p.29493-29504, 2014.
- 146 SODRÉ JR, A. C; Recent progress and novel applications of photonic crystal fibers, **Reports on Progress in Physics**. v.73, n.2, Article ID 024401, 2010.
- 147 RUSSEL, P. Photonic Crystal Fibers. **Science**, v.299, n.5605, p.358-362, 2003.
- 148 W.-SMITH, S. C.; VAHID, S. A.; MONRO, T. M. Theoretical study of liquid-immersed exposed-core microstructured optical fibers for sensing. **Optics Express**, v.16, n.12, p.9034-9045, 2008.
- 149 JOINT COMMITTEE FOR GUIDES ON METROLOGY (BIPM, IEC, IFCC, ILAC, IUPAC, IUPAP, ISO, OIML). **International Vocabulary of Metrology (VIM) - Basic and general concepts and associated terms**. 2012. 108p. Available online (free download) in: <http://www.bipm.org/vim>
- 150 MONTGOMERY, D. C.; RUNGER, G. C. **Applied Statistics and Probability for Engineers**. Hoboken: John Wiley and Sons, 2010.

- 151 LIU, P. Y.; CHIN, L. K.; SER, W.; CHEN, H. F.; HSIEH, C.-M.; LEE, C.-H.; SUNG, K.-B.; AYI, T. C.; YAP, P. H.; LIEBERG, B.; WANG, K.; BOUROUINA, T.; LEPRINCE-WANG, Y. Cell refractive index for cell biology and disease diagnosis: past, present and future. **Lab on a Chip**, v.16, n.4, p.634-644, 2016.
- 152 DANAIE, M.; KIANI, B. Design of a label-free photonic crystal refractive index sensor for biomedical applications. **Photonics and Nanostructures – Fundamentals and Applications**, v.31, p.89-98, 2018.
- 153 YAROSLAVKSY, A. N.; PATEL, R.; SALOMATINA, E.; LI, C.; LIN, C.; AL-ARASHI, M.; NEEL, V. High-contrast mapping of basal cell carcinomas. **Optics Letters**, v.37, n.4, p.644-646, 2012.
- 154 LIU, S.; DENG, Z.; LI, J.; WANG, J.; HUANG, N.; CUI, R.; ZHANG, Q.; MEI, J.; ZHOU, W.; ZHANG, C.; YE, Q.; TIAN, J. Measurement of the refractive index of whole blood and its components for a continuous spectral region. **Journal of Biomedical Optics**, v.24, n.3, 2019.
- 155 SHIOWAKA, N.; MIZUNO, Y.; TSUCHIYA, H.; TOKUNAGA, E. Sagnac interferometer for photothermal deflection spectroscopy. **Optics Letters**, v.37, n.13, p.2655-2657, 2012.
- 156 LEVITON, D.; FREY, B. J. Temperature-dependent absolute refractive index measurements of synthetic fused silica. In: **Proc. of SPIE 6273**, article 62732K, 2008.
- 157 VILLATORO, J.; FINAZZI, V.; BADENES, G.; PRUNERI, V. Highly Sensitive Sensors Based on Photonic Crystal Fiber Modal Interferometers. **Journal of Sensors**, v.2012, Article ID 747830, 2009.
- 158 ZHANG, T.; ZHENG, Y.; WANG, C.; MU, Z.; LIU, Y.; LIN, J. A review of photonic crystal fiber sensor applications for different physical quantities. **Applied Spectroscopy Reviews**, v.53, n.6, p.486-502, 2018.
- 159 SUN, L.; JIANG, S.; MARCIANTE, J. R.; All-fiber optical magnetic-field sensor based on Faraday rotation in highly terbium-doped fiber. **Optics Express**, v.18, n.6, p.5407-5412, 2010.

- 160 NASCIMENTO, I. M.; CHESINI, G.; BAPTISTA, J. M.; CORDEIRO, C. M. B.; JORGE, P. A. S. Vibration and Magnetic Field Sensing Using a Long-Period Grating. **IEEE Sensors Journal**, v.17, n.20, p.6615-6621, 2017.
- 161 SU, G.-H.; SHI, J.; XU, D.-G.; ZHANG, H.-W.; XU, W.; WANG, Y.-Y.; FENG, J.-C.; YAO, J.-Q. Simultaneous Magnetic Field and Temperature Measurement Based on No-Core Fiber Coated With Magnetic Fluid. **IEEE Sensors Journal**, v.16, n.23, p.8489-8493, 2016.
- 162 GAO, R.; JIANG, Y.; ABDELAZIZ, S. All-fiber magnetic field sensors based on magnetic fluid-filled photonic crystal fibers. **Optics Letters**, v.38, n.9, p.1539-1541, 2013.
- 163 RAMPRASAD, B. S.; RADHA BAI, T. S. Speckle-based fibre-optic current sensor. **Optics & Laser Technology**, v.16, n.3, p.156-159, 1984.
- 164 DANDRIDGE, A.; TVETEN, A. B.; SIGEL, G. H.; WEST, E. J.; GIALLORENZI, T. G. Optical fiber magnetic field sensors. **Electronics Letters**, v.16, n.11, p.408-409, 1980.
- 165 BOLSHAKOV, M. V.; ERSHOV, A. V.; KUNDIKIVA, N. D. Optical method for detecting variations of the magnetic field strength. **Optics and Spectroscopy**, v.110, p.624-629, 2011.
- 166 KUZMIN, D. A.; BYCHKOV, I. V.; SHAVROV, V. G. Influence of graphene coating on speckle-pattern rotation of light in gyrotropic optical fiber. **Optics Letters**, v.40, n.6, p.890-893, 2015.
- 167 ANAND, A.; TRIVEDI, V.; MAHAJAN, S.; CHHANIWAL, V. K.; ZALEVSKY, Z.; JAVIDI, B. Speckle-Based Optical Sensor for Low Field Faraday Rotation Measurement. **IEEE Sensors Journal**, v.13, n.2, p.723-727, 2012.
- 168 FRANCO, D. F.; FERNANDES, R. G.; FELIX, J. F.; MASTELARO, V. R.; ECKERT, H.; AFONSO, C. R. M.; MESSADDEQ, Y.; MESSADDEQ, S. H.; MORENCY, S.; NALIN, M. Fundamental studies of magneto-optical borogermanate glasses and derived optical fibers containing Tb^{3+} . **Journal of Materials Research and Technology**, v.11, p.312-327, 2021.
- 169 FRANCO, D. F.; LEDEMI, Y.; CORRER, W.; MORENCY, S.; AFONSO, C. R. M.; MESSADDEQ, S. H.; MESSADDEQ, Y.; NALIN, M. Magneto-optical borogermanate glasses and fibers containing Tb^{3+} . **Scientific Reports**, v.11, article 9906, 2021.

- 170 GAO, G.; W.-BECKMANN, A.; SURZHENKO, O.; DUBS, C.; DELLITH, J.; SCHMIDT, M. A.; WONDRAKZEK, L. Faraday rotation and photoluminescence in heavily Tb³⁺-doped GeO₂-B₂O₃-Al₂O₃-Ga₂O₃ glasses for fiber-integrated magneto-optics. **Scientific Reports**, v.5, article 8492, 2015.
- 171 QIU, X.; WU, B.; LIU, Y.; WEN, F. Study on mode coupling characteristics of multimode magneto-optical fibers. **Optics Communications**, v.456, article 124704, 2020.
- 172 BABKINA, A.; KULPINA, E.; SGIBNEV, Y.; FEDOROV, Y.; STOROBOR, A.; PALASHOV, O.; NIKONOROV, N.; IGNATIEV, A.; ZYRYANOVA, K.; ORESHKINA, L.; ZHIZHIN, E.; PUDI KOV, D. Terbium concentration effect on magneto-optical properties of ternary phosphate glass. **Optical Materials**, v.100, article 109692, 2020.
- 173 MOLLAEI, M.; ZHU, X.; JENKINS, S.; ZONG, J.; TEMYANKO, E.; NORWOOD, R.; C.-PIRSON, A.; LI, M.; ZELMON, D.; PEYGHAMBARIAN, N. Magneto-optical properties of highly Dy³⁺ doped multicomponent glasses. **Optics Express**, v.28, n.8, p.11789-11796, 2020.
- 174 FERNANDES, R. G.; FRANCO, D. F.; MASTELARO, V. R.; CARDINAL, T.; TOULEMONDE, O.; NALIN, M. Thermal and structural modification in transparent and magnetic germanoborate glasses induced by Gd₂O₃. **Ceramics International**, v.46, n.14, p.22079-22089, 2020.
- 175 CHEN, Q.; MA, Q.; WANG, H.; CHEN, Q. Diamagnetic tellurite glass and fiber based magneto-optical current transducer. **Applied Optics**, v.54, n.29, p.8664-8669, 2015.
- 176 KRUR, A.; WAJLER, A.; MRÓZEK, M.; ZYCH, L.; GAWLIK, W.; BRYLEWSKI, T. Transparent yttrium oxide ceramics as potential optical isolator materials. **Optica Applicata**, v.45, n.4, p.585-594, 2015.
- 177 DARSCHT, M. Y.; KATAEVSKAYA, I. V.; KUNDIKOVA, N. D.; ZEL'DOVICH, B. Y. Magnetic rotation of the speckle pattern of light transmitted through an optical fiber. In: **Proc. SPIE 2800, Nonlinear Optical Interactions and Wave Dynamics**, St. Petersburg, Russian Federation, 1995.
- 178 WASILEWSKI, P. J. Magnetic hysteresis in natural materials. **Earth and Planetary Science Letters**, v.20, n.1, p.67-72, 1973.

- 179 PRIETO, J. L.; AROCA, C.; LOPEZ, E.; SANCHEZ, M. C., SANCHEZ, P. Reducing hysteresis in magnetorestrictive-piezoelectric magnetic sensors. **IEEE Transactions on Magnetics**, v.34, n.6, p.3913-3915, 1998.
- 180 FETISOV, Y. K.; CHASIN, D. V.; BURDIN, D. A.; EKONOMOV, N. A.; FETISOV, L. Y. Elimination of hysteresis in magnetoelectric DC magnetic field sensors. In: **Proc. 2017 IEEE International Magnetics Conference (INTERMAG)**, Dublin, Ireland, 2017.
- 181 FUJIWARA, E.; CABRAL, T. D.; SATO, M.; OKU, H.; CORDEIRO, C. M. B. Agarose-based structured optical fibre. **Scientific Reports**, v.10, n.1, article 7035, 2020.
- 182 CABRAL, T. D.; DA SILVA, L. E.; FUJIWARA, E.; NG, A. K. L.; EBENDORFF-HEIDEPRIEM, H.; CORDEIRO, C. M. B. Reusable polymer optical fiber strains sensor with memory capability based on ABS crazing. **Applied Optics**, v.58, n.20, p.9870-9875, 2019.
- 183 AMATO, F.; SOARES, M. C. P.; CABRAL, T. D.; FUJIWARA, E.; CORDEIRO, C. M. B.; CRIADO, A.; PRATO, M.; BARTOLI, J. R. Agarose-Based Fluorescent Waveguide with Embedded Silica Nanoparticle-Carbon Nanodot Hybrids for pH Sensing. **ACS Applied Nano Materials**, v.4, n.9, p.9738-9751, 2021.
- 184 CHOI, M; HUMAR, M.; KIM, S.; YUN, S.-H. Step-Index Optical Fiber Made of Biocompatible Hydrogels. **Advanced Materials**, v.27, n.27, p.4081-4086, 2015.
- 185 C.-GINISTRELLI, E.; PUGLIESE, D.; BOETTI, N. G.; NOVAJRA, G.; AMBROSONE, A.; LOUSTEAU, J.; V.-BROVARONE, C.; ABRATE, S.; MILANESE, D. Novel biocompatible and resorbable UV-transparent phosphate glass based optical fiber. **Optical Materials Express**, v.6, n.6, p.2040-2051, 2016.
- 186 SHAN, D.; ZHANG, C.; KALABA, S.; MEHTA, N.; KIM, G. B.; LIU, Z.; YANG, J. Flexible biodegradable citrate-based polymeric step-index optical fiber. **Biomaterials**, v.143, p.142-148, 2017.
- 187 JAIN, A.; YANG, A. H. J.; ERICKSON, D. Gel-based optical waveguides with live cell encapsulation and integrated microfluidics. **Optics Letters**, v.37, n.9, p.1472-1474, 2012.

- 188 CHOI, M.; CHOI, J. W.; KIM, S.; NIZAMOGLU, S.; HAHN, S. K.; YUN, S. H. Light-guiding hydrogels for cell-based sensing and optogenetics synthesis *in vivo*. **Nature Photonics**, v.7, p.987-994, 2013.
- 189 SHABAHANG, S.; KIM, S.; YUN, S.-H. Light-Guiding Biomaterials for Biomedical Applications. **Advanced Functional Materials**, v.28, n.24, article 1706635, 2018.
- 190 NAZEMPOUR, R.; ZHANG, Q.; FU, R.; SHENG, X. Biocompatible and Implantable Optical Fibers and Waveguides for Biomedicine. **MDPI Materials**, v.11, n.8, article 1283, 2018.
- 191 FU, R.; LUO, W.; NAZEMPOUR, R.; TAN, D.; DING, HE.; ZHANG, K.; YIN, L.; GUAN, J.; SHENG, X. Implantable and Biodegradable Poly(L-lactic acid) Fibers for Optical Neural Interfaces. **Advanced Optical Materials**, v.6, n.3, article 1700941, 2018.
- 192 TAO, H.; KAPLAN, D. L.; OMENETTO, F. G. Silk Materials – A Road to Sustainable High Technology. **Advanced Materials**, v.24, n.21, p.2824-2837, 2012.
- 193 GUO, J.; ZHOU, M.; YANG, C. Fluorescent hydrogel waveguide for on-site detection of heavy metal ions. **Scientific Reports**, v.7, article 7902, 2017.
- 194 YETISEN, A. K.; JIANG, N.; FALLAHI, A.; MONTELONGO, Y.; R.-ESPARZA, G. U.; TAMAYOL, A.; ZHANG, Y. S.; MAHMOOD, I.; YANG, S.-A.; KIM, K. S.; BUTT, H.; KHADEMHOSEINI, A.; YUN, S.-H. Glucose-Sensitive Hydrogel Optical Fibers Functionalized with Phenylboronic Acid. **Advanced Materials**, v.29, n.15, article 1606380, 2017.
- 195 GUO, J.; LIU, X.; JIANG, N.; YETISEN, A. K.; YUK, H.; YANG, C.; KHADEMHOSEINI, A.; ZHAO, X.; YUN, S.-H. Highly Stretchable, Strain Sensing Hydrogel Optical Fibers. **Advanced Materials**, v.28, n.46, p.10244-10249, 2016.
- 196 ZARRINTAJ, P.; MANOUCHEHRI, S.; AHMADI, Z.; SAEB, M. R.; URBANSKA, A. M.; KAPLAN, D. L.; MOZAFARI, M. Agarose-based biomaterials for tissue engineering. **Carbohydrate Polymers**, v.187, p.66-84, 2018.
- 197 OKU, H.; UJI, T.; ZHANG, Y.; SHIBAHARA, K. Edible fiducial marker made of edible retroreflector. **Computers & Graphics**, v.77, p.156-165, 2018.

- 198 MONOCCHI, A. K.; DOMACHUK, P.; OMENETTO, F. G.; YI, H. Facile fabrication of gelatin-based biopolymeric optical waveguides. **Biotechnology and Bioengineering**, v.103, n.4, p.725-732, 2009.
- 199 KOU, L.; LABRIE, D.; CHYLEK, P. Refractive indices of water and ice in the 0.65- to 2.5- μm spectral range. **Applied Optics**, v.32, n.19, p.3531-3540, 1993.
- 200 JIANG, N.; AHMED, R.; RIFAT, A. A.; GUO, J.; YIN, Y.; MONTELONGO, Y.; BUTT, H.; YETISEN, A. K. Functionalized Flexible Soft Polymer Optical Fibers for Laser Photomedicine. **Advanced Optical Materials**, v.6, n.3, article 1701118, 2018.
- 201 HAYASHI, A.; KANZAKI, T. Swelling of agarose gel and its related changes. **Food Hydrocolloids**, v.1, n.4, p.317-325, 1987.
- 202 EUSER, T. G.; CHEN, J. S. Y.; SCHARRER, M.; RUSSEL, P. ST. J.; FARRER, N. J.; SADLER, P. J. Quantitative broadband chemical sensing in air-suspended solid-core fibers. **Journal of Applied Physics**, v.103, n.10, article 103108, 2008.
- 203 SAXL, T.; KHAN, F.; FERLA, M.; BIRCH, D.; PICKUP, J. A fluorescent lifetime-based fibre-optic glucose sensor using glucose/galactose-binding protein. **Analyst**, v.136, n.5, p.968-972, 2011.
- 204 ABOLGHASEMI, M. M.; SOBHI, M.; PIRYAEI, M. Preparation of a novel green optical pH sensor based on immobilization of red grape extract on bioorganic agarose membrane. **Sensors and Actuators B: Chemical**, v.224, p.391-395, 2016.
- 205 NAKAMURA, K.; HUSDI, I. R.; UEHA, S. Memory effect of POF distributed strain sensor. **Proc. of SPIE**, v.5502, 2004.
- 206 FUKUMOTO, T.; NAKAMURA, K.; UEHA, S. A POF-based distributed strain sensor with intrinsic memory effect. **Proc. of SPIE**, v.6770, article 67700P, 2007.
- 207 MINAKWA, K.; HAYASHI, N.; MIZUNO, Y.; NAKAMURA, K. Thermal memory effect in polymer optical fibers. **IEEE Photon. Technol. Lett.**, v.27, n.13, p.1394-1397, 2015.
- 208 NARANGEREL, T. **Solvent crazing as a means to prepare poly(ethylene terephthalate) composite fibers**. PhD dissertation, Aachen University, 2015.

- 209 WANG, T. T.; MATSUO, M.; KWEI, T. K. Criteria of Craze Initiation in Glassy Polymers. **Journal of Applied Physics**, v.42, n.11, p.4188-4196, 1971.
- 210 ARGON, A. S.; HANNOOSH, J. G.; SALAMA, M. M. Initiation and Growth of Crazes in Glassy Polymers. **Fracture**, v.1, p.445-470, 1977.
- 211 XIAO, Z. M.; LIM, M. K.; LIEW, K. M. Micromechanics analysis of crazing phenomenon in polymers. **Journal of Materials Processing Technology**, v.48, p.437-443, 1995.
- 212 GUNEL, E. M.; BASARAN, C. Stress Whitening Quantification of Thermoformed Mineral Filled Acrylics. **Journal of engineering Materials and Technology**, v.132, 2010.
- 213 LIU, Y.; KENNARD, C. H. L.; TRUSS, R. W.; CALOS, N. J. Characterization of stress-whitening of tensile yielded isotactic polypropylene. **Polymer**, v.38, n.11, p.2797-2805, 1997.
- 214 RADLEY, E.; LOWE, C.; GETHIN, D. Stress Whitening in Polyester Melamine Coatings. **Johnson Matthey Technol. Rev.**, v.62, n.3, p.331-349, 2018.
- 215 SHOULBER, R. H.; LANG, E. R. Stress Whitening of Polymer Blends as a Tool for Experimental Stress Analysis. **Experimental Mechanics**, v.2, p.271-273, 1962.
- 216 PAE, K. D.; CHU, H.-C.; LEE, J. K.; KIM, J.-H. Healing of Stress-Whitening in Polyethylene and Polypropylene at or Below Room Temperature. **Polymer Engineering and Science**, v.40, n.8, p.1783-1795, 2000.
- 217 LEE, Y. W.; KUNG, S. H. Elimination of stress whitening in high-molecular-weight polyethylene. **Journal of Applied Polymer Science**, v.46, n.1, p.9-18, 1992).
- 218 CALLISTER, W. D.; RETHWISCH, D. G. **Materials Science and Engineering: An Introduction**. Hoboken: John Wiley and Sons, 2009.
- 219 JUNG, M. R.; HORGAN, F. D.; ORSKI, S.V.; RODRIGUEZ, C.V.; BEERS, K. L.; BALAZS, G. H.; JONES, T. T.; WORK, T. M.; BRIGNAC, K. C.; ROYER, S.-J.; HYRENBACH, K. D.; JENSEN, B. A.; LYNCH, J. M. Validation of ATR FT-IR to identify polymers of plastic marine debris, including those ingested by marine organisms. **Marine Pollution Bulletin**, v.127, p.704-716, 2018.

- 220 HAVNER, K. S. On the onset of necking in the tensile test. **International Journal of Plasticity**, v.20, p.965-978, 2004.
- 221 ZHOU, M.; GUO, J.; YANG, C. Ratiometric fluorescence sensor for Fe³⁺ ions detection based on quantum dot-doped hydrogel optical fiber. **Sensors and Actuators B: Chemical**, v.264, p.52-58, 2018.
- 222 ĐORĐEVIĆ, L.; ARCUDI, F.; D'URSO, A.; CACIOPPO, M.; MICALI, N.; BÜRGI, T.; PURRELO, R.; PRATO, M. Design principles of chiral carbon nanodots help convey chirality from molecular to nanoscale level. **Nature Communications**, v.9, article 3442, 2018.
- 223 ARCUDI, F.; ĐORĐEVIĆ, L. PRATO, M. Rationally Designed Carbon Nanodots towards Pure White-Light Emission. **Angewandte Chemie**, v.56, n.15, p.4170-4173.
- 224 SUN, Y.-P.; ZHOU, B.; LIN, Y.; WANG, W.; FERNANDO, K. A. S.; PATHAK, P.; MEZIANI, M. J.; HARRUFF, B. A.; WANG, X.; WANG, H.; LUO, P. G.; YANG, H.; KOSE, M. E.; CHEN, B.; VECA, L. M.; XIE, S.-Y. Quantum-Sized Carbon Dots for Bright and Colorful Photoluminescence. **Journal of the American Chemical Society**, v.128, n.24, p.7756-7757, 2006.
- 225 YUAN, F.; LI, S.; FAN, Z.; MENG, X.; FAN, L.; YANG, S. Shining carbon dots: Synthesis and biomedical and optoelectronic applications. **Nano Today**, v.11, n.5, p.565-586, 2016.
- 226 WANG, F.; HU, A. Carbon quantum dots: synthesis, properties and applications. **Journal of Materials Chemistry C**, v.2, n.34, p.6921-6939, 2014.
- 227 HUANG, X.; ZHANG, F.; ZHU, L.; CHOI, K. Y.; GUO, N.; GUO, J.; TACKETT, K.; ANILKUMAR, P.; LIU, G.; QUAN, Q.; CHOI, H. S.; NIU, G.; SUN, Y.-P.; LEE, S.; CHEN, X. Effect of Injection Routes on the Biodistribution, Clearance, and Tumor Uptake of Carbon Dots. **ACS Nano**, v.7, n.7, p.5684-5693, 2013.
- 228 ARCUDI, F.; ĐORĐEVIĆ, L.; PRATO, M. Synthesis, Separation, and Characterization of Small and Highly Fluorescent Nitrogen-Doped Carbon NanoDots. **Angewandte Chemie**, v.55, n.6, p.2107-2112, 2016.

- 229 WANG, X.; QU, K.; XU, B.; REN, J.; QU, X. Microwave Assisted One-Step Green Synthesis of Cell-Permeable Multicolor Photo-luminescent Carbon Dots without Surface Passivation Reagents. **Journal of Materials Chemistry**, v.21 n.8, p.2445-2450, 2011.
- 230 PAN, D.; GUO, L.; ZHANG, J.; XI, C.; XUE, Q.; HUANG, H.; LI, J.; ZHANG, Z.; YU, W.; CHEN, Z.; LI, Z.; WU, M. Cutting Sp^2 Clusters in Graphene Sheets into Colloidal Graphene Quantum Dots with Strong Green Fluorescence. **Journal of Materials Chemistry**, v.22, n.8, p.3314-3318, 2012.
- 231 ZHU, S.; ZHANG, J.; QIAO, C.; TANG, S.; LI, Y.; YUAN, W.; LI, B.; TIAN, L.; LIU, F.; HU, R.; GAO, H.; WEI, H.; ZHANG, H.; SUN, H.; YANG, B. Strongly Green-Photoluminescent Graphene Quantum Dots for Bioimaging Applications. **Chemical Communications**, v.47, n.24, p.6858-6860, 2011.
- 232 SUPPAN, P. Invited Review Solvatochromic Shifts: The Influence of the Medium on the Energy of Electronic States. **Journal of Photochemistry and Photobiology A: Chemistry**, v.50, n.3, p.293-330, 1990.
- 233 FILIPPINI, G.; AMATO, F.; ROSSO, C.; RAGAZZON, G.; VEGA-PENALOZA, A.; COMPANYÓ, X.; DELL'AMICO, L.; BONCHIO, M.; PRATO, M. Mapping the Surface Groups of Amine-Rich Carbon Dots Enables Covalent Catalysis in Aqueous Media. **Chem**, v.6, n.11, p.3022-3037, 2020.
- 234 CHOI, Y.; JO, S.; CHAE, A.; KIM, Y. K.; PARK, J. E.; LIM, D.; PARK, S. Y.; IN, I. Simple Microwave-Assisted Synthesis of Amphiphilic Carbon Quantum Dots from A_3/B_2 Polyamidation Monomer Set. **ACS Applied Materials & Interfaces**, v.9, n.33, p.27883-27893, 2017.
- 235 GONG, X.; MA, W.; LI, Y.; ZHONG, L.; LI, W.; ZHAO, X. Fabrication of High-Performance Luminescent Solar Concentrators Using N-Doped Carbon Dots/PMMA Mixed Matrix Slab. **Organic Electronics**, v.63, p.237-243, 2018.
- 236 AMATO, F.; CACIOPPO, M.; ARCUDI, F.; PRATO, M.; MITUO, M.; FERNANDES, E.; CARREÑO, M.; PEREYRA, I.; BARTOLI, J. Nitrogen-Doped Carbon Nanodots/PMMA Nanocomposites for Solar Cells Applications. **Chemical Engineering Transactions**, v.74, p.1105-1110, 2019.

- 237 SOARES, M. C. P.; PERLI, G.; BARTOLI, J. R.; BERTUZZI, D. L.; TAKETA, T. B.; BATAGLIOLI, R. A.; SUZUKI, C. K.; ORNELAS, C.; FUJIWARA, E. Fast Microwave-Assisted Synthesis of Green-Fluorescent Carbon Nanodots from Sugarcane Syrup. **In: Proc. 2019 SBFoton International Optics and Photonics Conference (SBFoton IOPC)**, São Paulo, Brazil, 2019.
- 238 MARTINDALE, B. C. M.; HUTTON, G. A. M.; CAPUTO, C. A.; REISNER, E. Solar Hydrogen Production Using Carbon Quantum Dots and a Molecular Nickel Catalyst. **Journal of the American Chemical Society**, v.137, n.18, p.6018– 6025, 2015.
- 239 SCIORTINO, A.; MARINO, E.; VAN DAM, B.; SCHALL, P.; CANNAS, M.; MESSINA, F. Solvatochromism Unravels the Emission Mechanism of Carbon Nanodots. **Journal of Physical Chemistry Letters**, v.7, n.17, p.3419–3423, 2016.
- 240 BANO, D.; KUMAR, V.; SINGH, V. K.; CHANDRA, S.; SINGH, D. K.; YADAV, P. K.; TALAT, M.; HASAN, S. H. A Facile and Simple Strategy for the Synthesis of Label Free Carbon Quantum Dots from the Latex of *Euphorbia Mili* and Its Peroxidase-Mimic Activity for the Naked Eye Detection of Glutathione in a Human Blood Serum. **ACS Sustainable Chemistry & Engineering**, v.7, n.2, p.1923–1932, 2019.
- 241 CHANDRA, S.; SINGH, V. K.; YADAV, P. K.; BANO, D.; KUMAR, V.; PANDEY, V. K.; TALAT, M.; HASAN, S. H. Mustard Seeds Derived Fluorescent Carbon Quantum Dots and Their Peroxidase-like Activity for Colorimetric Detection of H₂O₂ and Ascorbic Acid in a Real Sample. **Analytica Chimica Acta**, v.1054, p.145–156, 2019.
- 242 REICHARDT, C. Polarity of Ionic Liquids Determined Empirically by Means of Solvatochromic Pyridinium *N*-Phenolate Betaine Dyes. **Green Chemistry**, v.7, n.5, p.339–351, 2005.
- 243 REICHARDT, C. Solvatochromic Dyes as Solvent Polarity Indicators. **Chemical Reviews**, v.94, n.8, p.2319–2358, 1994.
- 244 ILER, R. K. **The Chemistry of Silica**. New York: John Wiley and Sons, 1979.
- 245 GÖTZE, J.; MÖCKEL, R. **Quartz: Deposits, Mineralogy and Analytics**. New York: Springer, 2012.
- 246 JIANG, K.; WANG, Y.; LI, Z.; LIN, H. Afterglow of Carbon Dots: Mechanism, Strategy and Applications. **Materials Chemistry Frontier**, v.4, n.2, p.386–399, 2020.

- 247 SOARES, M. C. P.; GOMES, M. K.; SCHENKEL, E. A.; RODRIGUES, M. D. S.; SUZUKI, C. K.; TORRE, L. G. DE LA; FUJIWARA, E. Evaluation of Silica Nanoparticle Colloidal Stability With a Fiber Optic Quasi-Elastic Light Scattering Sensor. **Brazilian Journal of Chemical Engineering**, v.36, n.4, p.1519–1534, 2019.
- 248 CANNAS, M.; CAMARDA, P.; VACCARO, L.; AMATO, F.; MESSINA, F.; FIORE, T.; AGNELLO, S.; GELARDI, F. M. Luminescence Efficiency of Si/SiO₂ Nanoparticles Produced by Laser Ablation. **Physica Status Solidi A**, v.216, n.3, article 1800565, 2019.
- 249 LAKOWICZ, J. R. **Principles of Fluorescence Spectroscopy**. New York: Springer, 2006.
- 250 ZHANG, T.; DONG, S.; ZHAO, F.; DENG, M.; FU, Y.; LÜ, C. Tricolor Emissive Carbon Dots for Ultra-Wide Range pH Test Papers and Bioimaging. **Sensors and Actuators B: Chemical**, v.298, article 126869, 2019.
- 251 CHEN, Y.; ZHAO, C.; WANG, Y.; RAO, H.; LU, Z.; LU, C.; SHAN, Z.; REN, B.; WU, W.; WANG, X. Green and High-Yield Synthesis of Carbon Dots for Ratiometric Fluorescent Determination of pH and Enzyme Reactions. **Materials Science and Engineering: C**, v.117, article 111264, 2020.
- 252 WANG, L.; LI, M.; LI, W.; HAN, Y.; LIU, Y.; LI, Z.; ZHANG, B.; PAN, D. Rationally Designed Efficient Dual-Mode Colorimetric/Fluorescence Sensor Based on Carbon Dots for Detection of pH and Cu²⁺ Ions. **ACS Sustainable Chemistry & Engineering**, v.6, n.10, p.12668–12674, 2018.
- 253 SKOOG, D.; WEST, D.; HOLLER, F. J.; CROUCH, S. **Fundamentals of Analytical Chemistry**. Belmont: Cengage Learning, 2014.
- 254 ASTM INTERNATIONAL. **Standard Test Method for pH of Aqueous Solutions With the Glass Electrode; ASTM E70-19**. West Conshohocken: ASTM International, 2019.
- 255 FUJIWARA, E.; DELFINO, T. S.; CABRAL, T. D.; CORDEIRO, C. M. B. All-Optical Fiber Anemometer Based on the Pitot-Static Tube. **IEEE Transactions on Instrumentation and Measurement**, v.69, n.4, p.1805-1811, 2019.
- 256 ARISTILDE, S.; SOARES, M. C. P.; CABRAL, T. D.; RODRIGUES, G.; FUJIWARA, E.; FRUETT, F.; CORDEIRO, C. M. B. Measurement of Multiphase Flow by Tilted Optical Fiber Bragg Grating Sensor. **IEEE Sensors Journal**, v.21, n.2, p.1534-1539, 2021.

- 257 DE AQUINO, G. A.; DE LUCCA, Y. F. L.; CABRAL, T. D.; LAZARI, P. M.; MARTIM, A. L. S. S.; FUJIWARA, E.; CORDEIRO, C. M. B.; DALFRÉ FILHO, J. G. All-optical real-time monitoring of air/vacuum valves in water pipeline systems using fiber Bragg gratings. **Journal of the Brazilian Society of Mechanical Sciences and Engineering**, v.44, article 5, 2022.
- 258 PATRICK, H.; GILBERT, S. L.; LIDGARD, A.; GALLAGHER, M. D. Annealing of Bragg gratings in hydrogen-loaded optical fiber. **Journal of Applied Physics**, v.78, n.5, p.2940-2945, 1995.
- 259 KLOPFENSTEIN JR., R. Air Velocity and flow measurement using a Pitot tube. **ISA Transactions**, v.37, n.4, p.257-263, 1998.
- 260 AL-GARNI, A. M. Low speed calibration of hot-wire anemometers. **Flow Measurement and Instrumentation**, v.18, n.2, p.95-98, 2007.
- 261 BRUSCHI, P.; DEI, M.; PIOTTO, M. A Low-Power 2-D Wind Sensor Based on Integrated Flow Meters. **IEEE Sensors Journal**, v.9, n.12, p.1688-1696, 2009.
- 262 CHUANG, P. Y.; SAW, E. W.; SMALL, J. D.; SHAW, R. A.; SIPPERLEY, C. M.; PAYNE, G. A.; BACHALO, W. D. Airborne Phase Doppler Interferometry for Cloud Microphysical Measurements. **Aerosol Science and Technology**, v.42, n.8, p.685-703, 2007.
- 263 VILLANUEVA, J. M. M.; CATUNDA, S. Y. C.; TANSCHKEIT, R. Maximum-Likelihood Data Fusion of Phase-Difference and Threshold-Detection Techniques for Wind-Speed Measurements. **IEEE Transactions on Instrumentation and Measurement**, v.58, n.7, p.2189-2195, 2009.
- 264 OVEJAS, V. J.; CUADRAS, A. Multimodal piezoelectric wind energy harvesters. **Smart Materials and Structures**, v.20, n.8, article 085030, 2011.
- 265 CHO, L.-H.; LU, C.; ZHANG, A. P.; TAM, H.-Y. Fiber Bragg Grating Anemometer With Reduced Pump Power-Dependency. **IEEE Photonics Technology Letters**, v.25, n.24, p.2450-2453, 2013.
- 266 WANG, X.; DONG, X.; ZHOU, Y.; LI, Y.; CHENG, J.; CHEN, Z. Optical fiber anemometer using silver-coated fiber Bragg grating and bitaper. **Sensors and Actuators A: Physical**, v.214, p.230-233, 2014.

- 267 ZUBIA, J.; ARESTI, O.; ARRUE, J.; L.-AMO, M. Barrier sensor based on plastic optical fiber to determine the wind speed at a wind generator. **IEEE Journal of Selected Topics in Quantum Electronics**, v.6, n.5, p.773-779, 2000.
- 268 LEE, C.-L.; LEE, C.-F.; LI, C.-M.; CHIANG, T.-C.; HSIAO, Y.-L. Directional anemometer based on an anisotropic flat-clad tapered fiber Michelson interferometer. **Applied Physics Letters**, v.101, n.2, article 023502, 2012.
- 269 ZHAO, Y.; HU, H.-F.; BI, D.-J.; YANG, Y. Research on the optical fiber gas flowmeters based on intermodal interference. **Optics and Lasers in Engineering**, v.82, p.122-126, 2016.
- 270 LIU, Y.; PENG, W.; ZHANG, X.; LIANG, Y.; GONG, Z.; HAN, M. Fiber-Optic Anemometer Based on Distributed Bragg Reflector Fiber Laser Technology. **IEEE Photonics Technology Letters**, v.25, n.13, p.1246-1249, 2013.
- 271 HUANG, J.; ZHOU, Z.; WEN, X.; ZHANG, D. A diaphragm-type fiber Bragg grating pressure sensor with temperature compensation. **Measurement**, v.46, n.3, p.1041-1046, 2013.
- 272 ALLWOOD, G.; WILD, G.; LUBANSKY, A.; HINCKLEY, S. A highly sensitive fiber Bragg grating diaphragm pressure transducer. **Optical Fiber Technology**, v.25, p.25-32, 2015.
- 273 FIGLIOLA, R. S.; BEASLEY, D. E. **Theory and Design for Mechanical Measurements**. Hoboken: John Wiley & Sons, 2011.
- 274 TIMOSHENKO, S. P.; W.-KRIEGER, S. **Theory of Plates and Shells**. Singapore: McGraw-Hill, 1959.
- 275 SIMCHAREION, W.; AMNUAIKIT, T.; BOONME, P.; TAWEEPRED, W.; PICHAYAKORN, W. Characterization of Natural Rubber Latex Film Containing Various Enhancers. **Procedia Chemistry**, v.4, p308-312, 2012.
- 276 HILL, K. O.; MELTZ, G. Fiber Bragg grating technology fundamentals and overview. **Journal of Lightwave Technology**, v.15, n.8, p.1263-1276, 1997.

- 277 GAO, S.; ZHANG, A. P.; TAM, H.-Y.; CHO, L. H.; LU, C. All-optical fiber anemometer based on laser heated fiber Bragg gratings. **Optics Express**, v.19, n.11, p.10124-10130, 2011.
- 278 SNOEK, C. W.; A selection of new developments in multiphase flow measurement techniques. **Experimental Thermal and Fluid Science**, v.3, n.1, p.60-73, 1990.
- 279 YAN, Y.; WANG, L.; WANG, T.; WANG, X.; YONGHUI, H.; DUAN, Q. Application of soft computing techniques to multiphase flow measurement: A review. **Flow Measurement and Instrumentation**, v.60, p.30-43, 2018.
- 280 WU, J.; GU, M.; Microfluidic sensing: state of the art fabrication and detection techniques. **Journal of Biomedical Optics**, v.16, n.8, article 080901, 2011.
- 281 ZHU, Y.; FANG, Q. Analytical detection techniques for droplet microfluidics – A review. **Analytica Chimica Acta**, v.787, p.24-35, 2013.
- 282 LEE, B. Review of the present status of optical fiber sensors. **Optical Fiber Technology**, v.9, n.2, p.57-79, 2003.
- 283 LIM, H.-J.; CHANG, K.-A.; SU, C. B.; CHEN, C.-Y. Bubble velocity, diameter, and void fraction measurements in a multiphase flow using fiber optic reflectometer. **Review of Scientific Instruments**, v.79, n.12, article 125105, 2008.
- 284 VEJRAŽKA, J.; VEČEŘ, M.; ORVALHO, S.; SECHET, P.; RUZICKA, M. C.; CARTELLIER, A. Measurement accuracy of a mono-fiber optical probe in a bubbly flow. **International Journal of Multiphase Flow**, v.36, n.7, p.533-548, 2010.
- 285 HSIEH, Y.-W.; WANG, A.-B.; LU, X.-Y.; WANG, L. A. High-throughput on-line multi-detection for refractive index, velocity, size, and concentration measurements of micro-two-phase flow using optical microfibers. **Sensors and Actuators B: Chemical**, v.237, p.841-848, 2016.
- 286 EUSER, T. G.; GARBOS, M. K.; CHEN, J. S. Y.; RUSSEL, P. ST. J. Precise balancing of viscous and radiation forces on a particle in liquid-filled photonic bandgap fiber. **Optics Letters**, v.34, n.23, p.3674-3676, 2009.

- 287 NIELSEN, K.; NOORDEGRAAF, D.; SØRENSEN, T.; BJARKLEV, A.; HANSEN, T. P. Selective filling of photonic crystal fibres. **Journal of Optics A: Pure and Applied Optics**, v.7, n.8, article L13, 2005.
- 288 ZAMARRENO, C. R.; MARTELLI, C.; BARONCINI, V. H. V.; DOS SANTOS, E. N.; DA SILVA, M. J.; MORALES, R. E. M.; ZUBIATE, P.; ARREGUI, F. J.; MATIAS, I. R. Single and Multiphase Flow Characterization by Means of an Optical Fiber Bragg Grating Grid. **Journal of Lightwave Technology**, v.33, n.9, p.1857-1862, 2015.
- 289 DAVID, N.; DJILALI, N.; WILD, P. Fiber Bragg grating sensor for two-phase flow in microchannels. **Microfluidics and Nanofluidics**, v.13, p.99-106, 2012.
- 290 CHIN, L. K.; LIU, A. Q.; ZHANG, J. B.; LIM, C. S.; SOH, Y. C. An on-chip liquid tunable grating using multiphase droplet microfluidics. **Applied Physics Letters**, v.93, n.16, article 164107, 2008.
- 291 ALBERT, J.; SHAO, L.-Y.; CAUCHETEUR, C. Tilted fiber Bragg grating sensors. **Lasers & Photonics Reviews**, v.7, n.1, p.83-108, 2013.
- 292 GUO, T.; LIU, F.; GUAN, B.-O.; ALBERT, J. [INVITED] Tilted fiber grating mechanical and biochemical sensors. **Optics & Laser Technology**, v.78, p.19-33, 2016.
- 293 LIU, X.; SHEN, C.; XIAO, Y.; GONG, J.; WANG, J.; LANG, T.; ZHAO, C.; HUANG, C.; JIN, Y.; DONG, X.; ZHANG, Y.; JING, Z.; PENG, W.; SEMENOVA, Y. Liquid surface tension and refractive index sensor based on a tilted fiber Bragg grating. **Journal of the Optical Society of America B**, v.35, n.6, p.1282-1287, 2018.
- 294 SHEN, C.; LIAN, X.; KAVUNGAL, V.; ZHONG, C.; LIU, D.; SEMENOVA, Y.; FARRELL, G.; ALBERT, J.; DONEGAN, J. F. Optical spectral sweep comb liquid flow rate sensor. **Optics Letters**, v.43, n.4, p.751-754, 2018.
- 295 SHEN, C.; LIU, D.; LIAN, X.; LANG, T.; ZHAO, C.; SEMENOVA, Y.; ALBERT, J. Microfluidic flow Direction and rate vector sensor based on a partially gold-coated TFBG. **Optics Letters**, v.45, n.10, p.2776-2779, 2020.
- 296 KRAUS, T.; GÜNTHER, A.; DE MAS, N.; SCHMIDT, M. A.; JENSEN, K. F. An integrated multiphase flow sensor for microchannels. **Experiments in Fluids**, v.36, p.819-832, 2004.

- 297 BAROUD, C. N.; GALLAIRE, F.; DANGLA, R. Dynamics of microfluidic droplets. **Lab on a Chip**, v.10, n.16, p.2032-2045, 2010.
- 298 ANGELI, P.; HEWITT, G. F. Flow structure in horizontal oil-water flow. **International Journal of Multiphase Flow**, v.26, n.7, p.1117-1140, 2000.
- 299 XU, J. H.; LI, S. W.; TAN, J.; LUO, G. S. Correlations of droplet formation in T-junction microfluidic devices: from squeezing to dripping. **Microfluidics and Nanofluidics**, v.5, n.6, p.711-717, 2008.
- 300 C.-HERNÁNDEZ, O. E.; F.-MIQUEL, V. S.; M.-MELIÁ, D.; SALGUEIRO, Y. Quasi-static Flow Model for Predicting the Extreme Values of Air Pocket Pressure in Draining and Filling Operations in Single Water Installations. **MDPI Water**, v.12, n.3, article 664, 2020.
- 301 AMERICAN WATER WORKS ASSOCIATION (AWWA). **Air Release, Air/Vacuum, and Combination Air Valves: Manual of Water Supply Practices M51**. Denver: AWWA, 2016.
- 302 McPHERSON, D. L. Air Valve Sizing and Location: A prospective. In: **Proc. Pipelines Specialty Conference 2009**, San Diego, USA, 2009.
- 303 MALEKPOUR, A.; KARNEY, B. W. Complex interactions of water, air and its controlled removal during pipeline filling operations. **Fluid Mechanics Research International Journal**, v.3, n.1, p.4-15, 2019.
- 304 RAMEZANI, L.; KARNEY, B.; MALEKPOUR, A. The Challenge of Air Valves: A Selective Critical Literature Review. **Journal of Water Resources Planning and Management**, v.141, n.10, 2015.
- 305 TASCA, E. S. A.; DALFRÉ FILHO, J. G.; LUVIZOTTO JR., E.; AQUINO, G. A. The problem with air valves inaccurate air mass flow versus differential pressure curves. In: **Proc. 1st International WDSA / CCWI 2018 JOINT CONFERENCE**, Kingston, Canada, 2018.
- 306 AQUINO, G. A.; DE LUCCA, Y. F. L.; DALFRÉ FILHO, J. G. The importance of experimental tests on air valves for proper choice in a water supply project. **Journal of the Brazilian Society of Mechanical Sciences and Engineering**, v.40, article 403, 2018.

- 307 MANZO, N. R.; CALLADO, G. T.; CORDEIRO, C. M. B.; VIEIRA JR., L. C. M. Embedding optical Fiber Bragg Gratings (FBG) sensors in 3D printed casings. **Optical Fiber Technology**, v.53, article 102015, 2019.
- 308 DE SOUZA, K. R.; OSÓRIO, J. H.; CARVALHO, J. B.; LIMA, B. M.; CORDEIRO, C. M. B. 3D Printing Technology for Tapered Optical Fiber Protection With Gas Sensing Possibilities. **Photonic Sensors**, v.10, n.4, p.298-305, 2020.
- 309 INTERNATIONAL ORGANIZATION FOR STANDARDIZATION (ISO). **ISO 37:2017 Rubber, vulcanized or thermoplastic – Determination of tensile stress-strain properties**. Vernier: ISO, 2017.
- 310 AQUINO, G. A.; DE LUCCA, Y. F. L.; DALFRÉ FILHO, J. G. Medição de vazão de ar em válvulas ventosas. In: **Proc. XXI Simpósio de Recursos Hídricos ABRHidro**, Brasília, Brazil, 2015.
- 311 HIBBELER, R. C. **Mechanics of Materials**. London: Pearson, 2016.